UNIVERSITY OF SOUTHAMPTON

On the Applicability of a Conventional Microwave Marine Radar System to Quantitative Measurements of the Ocean Surface Roughness and Oceanographic Applications

by

Christine Pascale GOMMENGINGER

Doctor of Philosophy

Department of Oceanography, Faculty of Science

October 1997

UNIVERSITY OF SOUTHAMPTON

ABSTRACT

FACULTY OF SCIENCE

OCEANOGRAPHY

Doctor of Philosophy

On the Applicability of a Conventional Microwave Marine Radar System to Quantitative Measurements of the Ocean Surface Roughness and Oceanographic Applications

by Christine Pascale GOMMENGINGER

This thesis examines the capabilities of a conventional X-band marine radar associated with a digital capture board for quantitative measurement of ocean surface roughness, and to provide a useful tool for oceanographic research. For the first time, the detection performances of a conventional marine radar system are established and found particularly suitable to sea clutter measurements at low grazing angles. Similarly, the definition of the system's radiometric resolution reveals that data quality is comparable to that of traditional research microwave radars.

The study of the relation between the ocean backscatter and operational parameters establishes the dominant influence of ocean wave crest scattering and shadowing processes at low grazing angles. A composite shadowing model is proposed and found to provide a satisfactory method to estimate the range of ocean backscatter extinction in a wide range of operational and environmental conditions. Examples of the positive contribution of the system in particular investigations establish the great potential of this type of instrument in oceanographic research.

List of Contents

List of Figures

List of Tables

Acknowledgements

I would like to express my thanks to Simon Boxall for being my supervisor and giving me the opportunity to study in the UK.

I would also like to acknowledge the indispensable assistance of Ray Ibbetson, Mike Barnard and Mike Hensby of Racal Decca Marine Ltd, New Malden, in providing technical support and facilities for the calibration of the marine radar system.

Dr John Scott and Peter Dovey of DRA Portland (now DERA Winfrith) were of immense help by granting me access to the DRA base at Portland, by giving me the chance to participate in their oil deployment experiments and by providing the meteorological and oceanographic data.

I would also like to record my thanks to the technical support staff at the Department of Oceanography, University of Southampton, in particular Gary Fisher and Bob Stringer.

My thanks also to Dave Woolf for providing a friendly scientific ear and a stimulating source of ideas. Finally, many grateful thanks to Nick Ward, without whose insight and expertise much of this work would not have taken place.

Chapter 1

Introduction and Aims

1.1 - Introduction

Over the past decade, microwave remote sensing has become an area of great interest for academic and industrial oceanographers. Airborne and satellite-based microwave radars have now clearly proven their ability to image the distribution of the sea surface roughness over large areas. For example, DeLoor (1981) detected underwater bathymetric features from airborne Real Aperture Radar (RAR) images under suitable tidal conditions. Similarly, the detection of natural or anthropogenic surface slicks and internal waves signatures using microwave radar systems is also commonly reported (Vesecky and Stewart, 1982).

Microwave radar systems encountered in the research literature mostly fall into two categories: (i) airborne and satellite-borne systems benefiting from a wide spatial coverage, with good spatial and radiometric resolution, and (ii) fixed-platform based systems concentrating on the temporal evolution of radar scattering within one antenna footprint. These two types of highly sophisticated systems give complementary information for the overall study of radar scattering from the ocean. However, when routine monitoring of a particular area is required or where transitory oceanographic processes are being studied, they fail to provide the requisite measurement repetitivity and extended spatial coverage.

In comparison, shore or ship-based conventional marine radars are only occasionally used for scientific applications as they are generally considered unsuitable as investigative tools for oceanographic research, despite being inexpensive and readily available. This is partly related to the marine radar technology being optimised for the detection of ships and buoys for which signals from the sea surface are treated as noisy clutter to be suppressed. In

addition, the propagation of radar waves over the ocean at near-horizontal angles is more complex than that at steeper viewing angles. Consequently, the interest of oceanographers has focused on remote-sensing applications linked with airborne and satellite-based radar systems, with the simpler marine radar systems remaining largely neglected.

1.2 - History of marine radar applications to oceanography

Until recently, the recording of marine radar data involved the lengthy processing of photographs of the radar display screens (Kerry, 1984). The intensity of the radar returns was represented at best as 2 bit data (black/white and 2 grey levels) which limited the intensity resolution of those instruments. In spite of this, scientific benefit has been demonstrated, for example in the imaging of gravity and internal waves (Watson and Robinson, 1990).

The advent in recent years of digital capture board technology has made marine radar backscatter data more easily accessible and reproducible. Radar echoes can be digitised in real-time to produce 8 bit images (256 grey levels) with spatial resolutions comparable to that of more expensive airborne and satellite-based systems.

Taking advantage of the instrument's reasonably extended spatial coverage, its high measurement repetitivity and the newly acquired high intensity and spatial resolution, marine radars became a popular method for producing unambiguous directional wave spectra using the information in both time and space domains (Young *et al.*, 1985, Buckley, 1994). Other uses of digital marine radar images for oceanographic purposes include the study of wave refraction in the coastal zone (Boalch *et al*, 1989) and the detection of oil spills at sea (Atanassov *et al.*, 1991, van Hasselma and Teeuwen, 1992).

However, most marine radar studies reported in the literature have restricted their interest to the qualitative exploitation of the information in the images. At present, the only accessible example of a fully calibrated marine radar applied to oceanography is that reported by Trizna (1988) at the Naval Research Laboratory (NRL) where a high-performance military radar was employed to investigate the statistics of sea clutter. But, to the best of the author's

knowledge, no *conventional* marine radar system has ever been calibrated and hence their capabilities for quantitative measurements have never been investigated.

It is difficult to assess the potential of conventional marine radar systems for the quantitative study of ocean processes as essential information on the dynamic range and radiometric resolution of those instruments is lacking. The definition of these performances will show the potential of these marine radar systems as an inexpensive technique to produce reliable quantitative measurements for a wide range of oceanographic features which may be able to fill the gap left by other radar systems for operational monitoring in a given area.

1.3 - Aims of the thesis

The prime objective of this thesis is to establish the technical performances of conventional marine radar systems for the production of quantitative ocean backscatter measurements. The dynamic range and radiometric resolution of these systems is estimated from the results of the calibration and error analysis for a standard marine radar associated with an off-the-shelf digital capture board. Hardware modification is kept to a minimum as the aim of the study is to give a representative view of the technical performances of a standard system.

The second objective of this thesis is to illustrate the usefulness of quantitative marine radar images for oceanographic applications. For this purpose, the importance of operational and environmental parameters on the ocean backscatter is investigated to assess the range of conditions for which this type of radar is an effective measuring device. Then using experimental evidence and literature reports on the radar signature of oceanographic features, the extensive range of oceanographic applications which can be quantitatively studied with this system is demonstrated.

1.4 - Structure of the thesis

The thesis is divided into two parts to reflect these dual aims. Part 1 (Chapter 2 to 5) is concerned with the definition of the radar system, its calibration and the determination of its

performance. Part 2 (Chapter 6 to 8) investigates the properties of the radar backscatter obtained at near-horizontal incidences with the radar system and its oceanographic application. The content of each chapter is as follows:

Part 1 - Instrumentation, Calibration and Performance

Chapter 2 provides background information on the parameters quantifying the electromagnetic properties of a medium and describes the electromagnetic properties of the sea surface at microwave frequencies. A brief review of statistical parameters commonly used to describe the sea surface roughness is given. Some vocabulary specific to microwave remote sensing is introduced and the fundamental properties of microwave remote sensing are recalled.

Chapter 3 introduces the marine radar and the technical specifications and mechanism for the radar data capture by the digital board. The spatial and temporal resolution of the radar images is determined in relation to the various parameters in the digital capture board set-up register. The optimal register to be used throughout the study are established for each pulse setting. Also, a new electronic device, named the "Electronic Flywheel", is introduced to improve the radar antenna heading accuracy of the system. Details of its working principle and evidence of its efficiency are presented.

Chapter 4 concerns the normalisation of the raw echo intensity images into radar backscatter coefficient images representative of the physical properties of the sea surface. The successive calibration steps towards the determination of the system's end-to-end transfer function are presented in detail, including an attempt at an absolute calibration using navigational buoys.

Chapter 5 presents the error analysis which estimates the error associated with each variable in the normalisation equations used to calculate the ocean radar backscatter coefficient and defines the system's radiometric accuracy. Also, the dynamic range of the instrument in which the measurement error is minimised is derived.

Part 2 - Ocean Backscatter at Low Grazing Angles

Chapter 6 gives a review of the theoretical background to microwave backscatter from a random rough surface. Particular attention is given to the search for a radar backscatter model suitable for the prediction of microwave backscatter from the sea surface at near-horizontal incidence.

Chapter 7 investigates the influence of operational parameters on the radar backscatter. In particular, the impact of antenna height and emitted pulse length on the nature of the sea clutter are examined. Models for the evolution with antenna height of radar backscatter at near-horizontal incidence are compared with experimental results in order to quantify the effect of antenna height on the performances of the radar system.

Chapter 8 examines the effect of environmental conditions on the radar backscatter from the sea surface using experimental results from a long-term deployment on the Isle of Portland, UK. The principal environmental parameters affecting the backscatter coefficient are determined from the experimental evidence. The range of conditions for which radar backscatter is expected to give satisfactory ocean backscatter measurements is established. Examples of oceanographic applications are introduced and discussed based on the radar's performances and the features' radar signatures.

Finally, Chapter 9 summarises the principal results and concludes on the suitability of marine radar systems for the quantitative study of oceanographic processes. Areas of work in future oceanographic applications are identified.

Part 1

Instrumentation, Calibration and System Performances

Chapter 2

Background Knowledge on Microwave Remote Sensing of the Sea Surface

In this chapter, the background information needed in the subsequent chapters is provided. First, the quantities characterising the electromagnetic properties of a medium are defined and the properties of sea water at microwave frequencies are examined. A brief overview of parameters used to describe the sea surface roughness is provided and some vocabulary specific to microwave remote sensing is given. The fundamental properties of the microwave remote sensing technique are summarised.

2.1 - Electromagnetic theory

2.1.1 - Maxwell's equations

All electromagnetic waves obey the Maxwell equations which describe the propagation and interactions of the electric field $\vec{E}$ and magnetic field $\vec{H}$ in a medium. These equations relate the electric field $\vec{E}$ and magnetic field $\vec{H}$ via the electric permittivity ε, the magnetic permeability μ and the conductivity σ which characterise the medium.

Maxwell's equations can be rearranged to accept a plane wave solution of the form $\vec{E}(\vec{r},t) = \vec{E}_0 . e^{-i(\vec{k}\vec{r}-\omega t)}$ with $\vec{E}_0$ a constant amplitude vector, $\vec{k} = k.\hat{k}$ the electromagnetic (e.m.) wave vector with $\hat{k}$ the unit vector along the direction of propagation of the wave, $|\vec{k}| = k$ the wave number equal to $2\pi/\lambda$, λ the wavelength and ω the angular frequency of the wave.

A corollary of these equations is that $\vec{E}$ and $\vec{H}$ are perpendicular to each other and to the direction of propagation of the wave. This fact is sometimes represented by introducing the wave intrinsic impedance Z defined as:

$$Z = \sqrt{\frac{\mu}{\varepsilon}} \qquad \text{Equation 2. 1}$$

which enable $\vec{E}$ and $\vec{H}$ to be related by:

$$Z\vec{H} = \hat{k} \wedge \vec{E} \qquad \text{Equation 2. 2}$$

It follows that the intrinsic impedance Z represents the ratio of the absolute magnitudes of E to H in the medium.

The temporal and spatial characteristics of the e.m. wave are related via the dispersion relation obtained by applying the plane wave solution to the original equations. The relation can be written:

$$k^2 = \varepsilon\mu\omega^2 - i\mu\omega\sigma \qquad \text{Equation 2. 3}$$

The complex nature of the wave number k indicates the attenuation of the e.m. wave amplitude by the medium. From Equation 2.3, it follows that the complex velocity of the electromagnetic wave in the medium is:

$$v = \frac{\omega}{k} = \frac{1}{\sqrt{\varepsilon\mu\left(1 - \frac{i\sigma}{\omega\varepsilon}\right)}} \qquad \text{Equation 2. 4}$$

2.1.2 - Electromagnetic properties of a medium

In free space, the electric permittivity and magnetic permeability take constant values $\varepsilon_0 = 8.8545\times10^{-12}$ F.m^{-1} and $\mu_0 = 4\pi\times10^{-7}$ H.m^{-1} and in absence of source charges, the conductivity σ equals 0. Hence, the velocity of electromagnetic waves in free space is real and equal to the speed of light:

$$c = \frac{\omega}{k} = \frac{1}{\sqrt{\varepsilon_0 \mu_0}} \approx 3.10^8 m.s^{-1} \qquad \text{Equation 2. 5}$$

The relative electric permittivity, $\varepsilon_r = \varepsilon / \varepsilon_0$, and magnetic permeability, $\mu_r = \mu/\mu_0$, are two complex quantities which represent the effect of the medium on an e.m. field in comparison with its propagation in free space. For natural media like the atmosphere or the ocean which possess no magnetic properties, the magnetic permeability μ_r is usually taken equal to 1 so that $\mu = \mu_0$.

The ratio of the velocity of the e.m. wave in free space to its velocity in a medium defines the complex index of refraction n of the medium which reads as a function of ε_r as:

$$n = \frac{c}{v} = \sqrt{\varepsilon_r - \frac{i\sigma}{\varepsilon_0 \omega}} \qquad \text{Equation 2. 6}$$

The dielectric function or "constant", K, of a medium is then defined as the square of its index of refraction. The attenuation of the e.m. wave in the medium can be expressed by rewriting the complex index of refraction n as:

$$n = \eta + i\chi \qquad \text{Equation 2. 7}$$

where the real part η represents the reduction of the e.m. wave propagation velocity in the medium with respect to the speed of light and the imaginary part χ characterises the attenuation of the electromagnetic wave as it propagates through the medium. The wave number k can be rewritten as:

$$k = \omega n/c = \omega\eta/c + i\omega\chi/c \qquad \text{Equation 2. 8}$$

and the electric field magnitude can then be expressed as:

$$E = E_0 \exp(-i(kx - \omega t)) = E_0 \exp(\kappa x) \exp\left(-i\left(\frac{\omega\eta}{c}x - \omega t\right)\right) \qquad \text{Equation 2. 9}$$

which clearly introduces the attenuation coefficient κ as

$$\kappa = \omega\chi/c \qquad \text{Equation 2. 10}$$

Another parameter characterising the electromagnetic properties of a medium is given by the skin depth, d, defined as the distance travelled by the e.m. wave in the medium before its amplitude is reduced to 1/e of its original value. The skin depth is defined as the inverse of the attenuation coefficient κ:

$$d = \frac{1}{\kappa} = \frac{c}{\omega\chi} \qquad \text{Equation 2. 11}$$

2.1.3 - Electromagnetic properties of sea water at microwave frequencies

The e.m. properties of a medium depend on the frequency of the e.m. radiation. In the present study, the radar radiation being used belongs to the range of microwave frequencies and is close to 10^{10} Hz (or 10 GHz). The equivalent radiation wavelength in the atmosphere is equal to 3 centimetres.

The dielectric constant of sea water, K, is given by the empirical Debye formula derived from laboratory measurements on pure water with a contribution due to the sea water's conductivity:

$$K = K_R + i \cdot K_I = K_\infty + \frac{K_S(T,S) - K_\infty}{1 - i\omega\, t_k(T,S)} + \frac{i\sigma(T,S)}{\omega\varepsilon_0} \qquad \text{Equation 2. 12}$$

where T is the temperature, S is the salinity, K_∞ is the dielectric constant at infinite frequency ($\omega = 2\pi f \to \infty$), K_S is the static dielectric constant ($\omega = 2\pi f \to 0$) and t_k is a relaxation time. The analytic expressions for these coefficients as functions of salinity and temperature can be found for example in Stewart (1985).

The effect of salinity and temperature on the real and imaginary part of the dielectric constant at microwave frequencies is shown in Figure 2.1. For frequencies greater than 5 GHz, the influence of salinity can be considered negligible. Similarly, the influence of temperature on the dielectric constant can be ignored over the normal range of oceanic temperatures.

The e.m. conductivity of the sea water σ increases the complex part of the dielectric constant and thus causes strong attenuation of the e.m. field in the sea water. The result is a weak penetration in the water column resulting in very thin skin depths. For an e.m. frequency of 10 GHz for example, the skin depth of 20 ° C sea water at 35 psu is approximately equal to 1.3 millimetres.

Hence, at microwave frequencies, the scattering will originate almost exclusively from the first few millimetre of the water column. Unlike the scattering of visible light by the ocean, the scattering of microwave radiation does not include any signal from the water column but is only affected by the surface properties of the sea water.

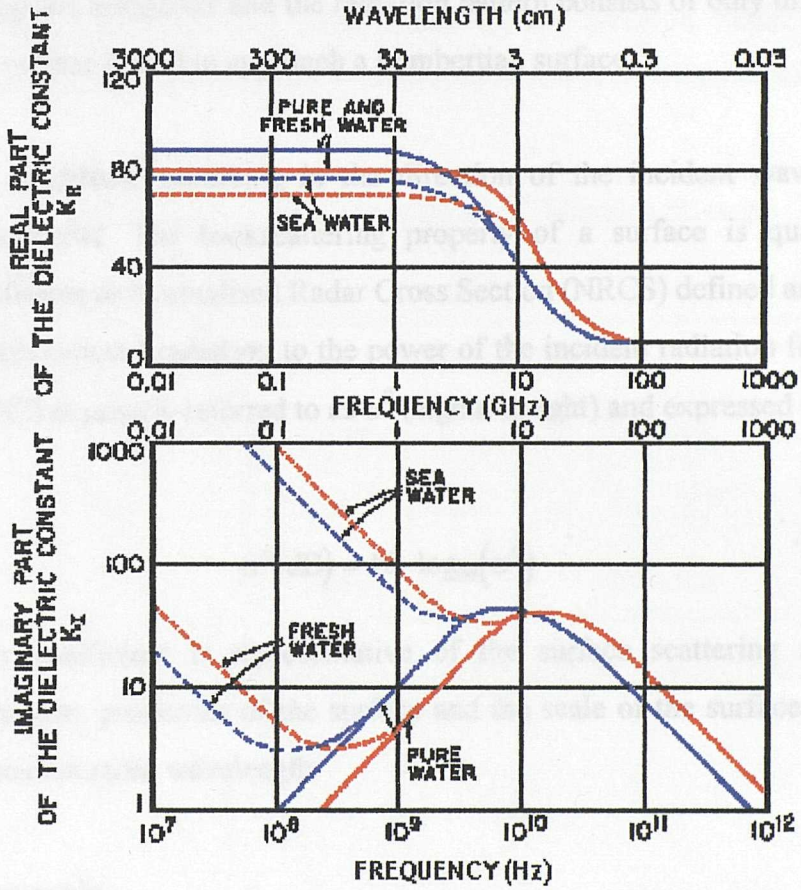

Figure 2. 1 - Complex dielectric constant of pure, fresh and sea water at 0 (blue) and 20 (red) degrees C (after Fiuza, 1990)

2.2 - Concepts of microwave remote sensing

2.2.1 - Surface scattering and Normalised Radar Cross Section (NRCS)

An e.m. wave impinging on a perfectly smooth and conducting surface at an angle θ from the vertical is entirely reflected in a direction equal and opposite (- θ) referred to as the specular direction. For a rough surface, the e.m. wave is partly reflected in the specular direction (coherent component) and partly scattered in all directions (diffuse component). The magnitude of the coherent component decreases for rougher surfaces while the diffuse component increases with surface roughness. For very rough surfaces, the specular component disappears altogether and the radiation pattern consists of only diffuse scattering. In this case, the surface is said to approach a Lambertian surface.

The proportion of diffuse scattering in the direction of the incident wave is called the backscatter component. The backscattering property of a surface is quantified by the backscatter coefficient or Normalised Radar Cross Section (NRCS) defined as the ratio of the power of the backscattered radiation to the power of the incident radiation for a unit area of surface. The NRCS is usually referred to as σ^0 (sigma-naught) and expressed in decibels (dB) as:

$$\sigma^0(\mathrm{dB}) = 10 \cdot \log_{10}\left(\sigma^0\right) \qquad \text{Equation 2. 13}$$

The backscatter coefficient is representative of the surface scattering and is strongly dependent on the e.m. properties of the surface and the scale of the surface roughness with respect to the incident radar wavelength.

2.2.2 - Incidence angle

One particularly important parameter in microwave remote sensing is the angle of incidence of the electromagnetic radiation to the sea surface. This angle is measured with respect to the local vertical at the scattering point. Small incidence angles correspond to near-vertical viewing angles while large incidence angles refer to near-horizontal viewing angles.

For coastal or ship-based radars, incidence angles are generally large and it is more convenient to talk in terms of grazing angles defined with respect to the local horizontal. The terms small and large grazing angles are then employed to describe respectively near-horizontal and near-vertical viewing angles.

2.2.3 - Radar frequency nomenclature

As mentioned earlier, microwave radiations correspond to centimetric wavelengths and frequencies around 10^{10} Hz. The frequency is generally expressed in gigahertz or GHz (10^{9} Hz). During World War II, some radar frequency bands acquired specific denominations which are still commonly used to date. The nomenclature for the radar frequency bands most frequently encountered in microwave remote sensing are given in Table 2.1. The radar system used in the present study is shown to belong to the class of X-band radars.

Radar frequency band	Frequency range (GHz)	Wavelength range (cm)
L	0.390 - 1.550	76.9 - 19.3
C	3.90 - 6.20	7.7 - 4.8
X	5.20 - 10.90	5.7 - 2.7
K	10.90 - 36.00	2.7 - 0.8

Table 2. 1 - Radar frequency bands (adapted from Stewart, 1985)

2.2.4 - Polarisation

The e.m. wave is also characterised by its polarisation which indicates the orientation of the electric field with regards to the wave's plane of incidence. The horizontal polarisation corresponds to the case where the electric field is perpendicular to the plane of incidence. The vertical polarisation corresponds to the electric field being parallel to the plane of incidence. It should be noted that while the electric field is indeed horizontal at horizontal

polarisation, the electric field in the vertical polarisation is not necessarily vertical.

The capacity of a radar system to emit and receive electromagnetic waves of a particular polarisation is determined by the properties of the radar antenna. Where a system emits and receives in the horizontal polarisation, the mode of operation is referred to as HH. Similarly, the mode is known as VV when emitting and receiving vertically polarised waves.

In some cases, the polarisation of the radiation can change after reflection from the surface. This phenomenon is known as "depolarisation". Only systems with two antennas or with an antenna able to switch polarisation rapidly are able to record the depolarised component of the backscatter. The modes of operation are then referred to as HV or VH where the first and second letter respectively indicate the polarisation of the emitted and received radiation.

2.3 - Description of the sea surface

2.3.1 - Decorrelation time and correlation length

The elevation of the sea surface $\eta(t)$ above its mean level may be represented as the superposition of an infinite number of weakly interacting independent sinusoidal waves with amplitude a_j , frequency ω_j and wavenumber k_j. For a one-dimensional profile along an O/X axis, the surface elevation reads:

$$\eta(x,t) = \sum_j a_j \cdot \exp\left(i\left(k_j \cdot x - \omega_j \cdot t\right)\right) \qquad \text{Equation 2. 14}$$

The autocorrelation function of the surface elevation indicates the randomness of the sea surface by giving a measure of the degree of change in time and space between the surface elevation at a time t and position x and at a time $t+\Delta t$ and position $x+\Delta x$. Adopting the bracket notation <q> to indicate the averaging of a quantity q over N samples, the surface elevation autocorrelation is given as:

$$\rho(\Delta x, \Delta t) = \left\langle \eta(x+\Delta x, t+\Delta t).\eta(x,t) \right\rangle \qquad \text{Equation 2. 15}$$

The autocorrelation function is maximal for Δt and Δx equal to 0, when it corresponds to the surface height variance or mean square height H^2. The surface variance or mean square height of the surface is then given as:

$$H^2 = \rho(0,0) = \langle \eta^2(x,t) \rangle \qquad \text{Equation 2. 16}$$

where H is also known as the root-mean-square (rms) height.

The decorrelation time and the correlation length are two quantities derived from the autocorrelation function to characterise the surface. They correspond respectively to the time and distance for which the autocorrelation function is equal to 1/e times its maximal value H^2. The surface correlation length and decorrelation time estimates the distance and duration for two samples to be statistically independent.

The zero-crossing period is another temporal quantity derived statistically from the wave height time series directly. It is defined as the mean time between two successive upcrossings of the mean level by the surface elevation.

2.3.2 - Power spectral density

The power spectral density $S(\omega)$ gives the distribution of the wave energy among the different wave modes present in the wave field. It can be obtained by computing the Fourier transform of the temporal autocorrelation function of the surface elevation η (Apel, 1987) measured at a fixed point in space. The power spectral density is usually normalised in order for the total energy in the wave field to be equal to the surface mean square height H^2 as follows:

$$H^2 = \frac{1}{2\pi} \int_{-\infty}^{+\infty} S(\omega)\, d\omega \qquad \text{Equation 2. 17}$$

In practice, the power density spectrum obtained from Waverider buoys is discretised and expressed as a series of energy density coefficients per frequency bandwidth Δf_i as:

$$H^2 = \sum_i S_i \cdot \Delta f_i \qquad \text{Equation 2. 18}$$

where the frequency bandwidth Δf_i is defined by the upper and lower frequencies f_i^{up} and f_i^{low} in the band as:

$$\Delta f_i = f_i^{up} - f_i^{low} \qquad \text{Equation 2. 19}$$

and where the wave frequencies f_i are related to the angular frequencies ω_i by:

$$f_i = \frac{\omega_i}{2\pi} \qquad \text{Equation 2. 20}$$

The energy density coefficients S_i are expressed in $m^2.s^{-1}$ and permit the calculation of the wave energy in the corresponding frequency band. The mean energy in a frequency band can then be equated to the square of the amplitude a_i of the waves in that band (Komen and Hasselmann, 1994):

$$S_i \cdot \Delta f_i = a_i^2 \qquad \text{Equation 2. 21}$$

Hence, within the limits of the linear wave theory, it is possible to calculate the amplitude of the individual waves in the wave field and recreate the surface elevation from the power spectral density function.

The significant wave height $H_{1/3}$ is another quantity derived from the power spectral density used to indicate the total amount of energy present in the ocean wave field. It corresponds to the average of the heights of the highest one-third of the waves in a wave height time-series and for a Gaussian surface is related to the root mean square height by (Apel, 1987):

$$H_{1/3} \approx 4 \cdot H \qquad \text{Equation 2. 22}$$

2.3.3 - Surface mean square slope

The sea surface roughness is often defined in terms of the statistics of the surface slope instead of surface height. In 1 dimension, the slope along the O/X axis is given as:

$$\zeta(x,t) = \frac{\partial}{\partial x}\left(\eta(x,t)\right) = \sum_j k_j \cdot a_j \cdot \exp\left(i(k_j \cdot x - \omega_j \cdot t)\right) \qquad \text{Equation 2. 23}$$

The mean square slope s^2 for the surface is then equal to:

$$s^2 = \left\langle \zeta^2(x,t) \right\rangle = \frac{1}{2}\sum_j a_j^2 \cdot k_j^2 \qquad \text{Equation 2. 24}$$

The wavenumber k_j is related to the angular frequency ω_j by the dispersion relation issued from the linear wave theory. The general dispersion relation reads as:

$$\omega^2 = g \cdot k \cdot \tanh(k \cdot d) \qquad \text{Equation 2. 25}$$

where d represents the water depth in meters. Two approximate relations can be deduced when the water depth is much larger and much smaller than the ocean wavelength. In the deep water approximation, the relationship reads:

$$\omega^2 = g \cdot k \qquad \text{Equation 2. 26}$$

with g the gravitational acceleration. When the water depth becomes equal to less than half the ocean wavelength, the dispersion relation in the shallow water approximation leads to:

$$\omega^2 = g \cdot k^2 \cdot d \qquad \text{Equation 2. 27}$$

Following Equation 2.21, the mean square slope can be calculated from the power spectral density coefficients S_j as:

$$s^2 = \frac{1}{2}\sum_j S_j \cdot \Delta\omega_j \cdot k_j^2 \qquad \text{Equation 2. 28}$$

2.4 - Properties of X-band microwave remote sensing

2.4.1 - Day/night operation

Unlike most other remote-sensing techniques, microwave radar systems are not affected by

the intensity of solar radiation or the distribution of the cloud cover. Hence, they are not impaired by diurnal variations and can perform equally well by day and night.

2.4.2 - Atmospheric particle scattering

The scattering of an e.m. radiation by particles in the atmosphere depends on the dimension of the particles with respect to the e.m. wavelength. For particles much smaller than the wavelength, the scattering is referred to as Rayleigh scattering for which the backscattered power is proportional to the sixth power of the particles diameter. Hence higher microwave frequencies are more likely to be perturbed by hydrometeors (e.g. rain, snow) than lower frequencies.

Centimetric X-band radiations are however largely unaffected by the smaller types of hydrometeors like fog, mist or drizzle. For example, the attenuation rate for a 3 cm wavelength in conditions of light rain is estimated to be about 10^{-2} dB/km (Skolnik, 1980) resulting in a 0.2 dB contribution to the NRCS of a target located at 10 km from the radar. Larger particles like snow, sleet or cases of heavy rain can strongly interfere with an X-band radiation and totally obscure the returns from the sea surface. In this case, measurement of the sea surface NRCS is impossible as most of the radar backscatter originates from the atmosphere between the radar and the surface.

2.4.3 - Spatial resolution

The spatial resolution is an important criteria in remote-sensing as it determines the smallest observable features with a given technique. At radar frequencies, the dimension across the propagation path of the sampling cell is determined by the radiation wavelength λ and the aperture of radar antenna. The spatial resolution in azimuth can be approximated by λ/L, where L is the physical length of the antenna. Hence, for a given antenna length, high microwave frequencies produce a better resolution in azimuth than at lower frequencies.

2.5 - Conclusion

The study of the electromagnetic properties of sea water has revealed that at X-band radar frequencies, the sea water behaves like a perfect conductor and the microwave radiation cannot penetrate further than a few millimetres into the water column. The parameters describing the electromagnetic properties of sea water at X-band have been found to be independent of temperature and salinity in the range found in oceanic waters. Consequently, the ocean NRCS measured at X-band is primarily a measure of the physical roughness of the sea surface.

Microwave remote sensing at X-band offers a good compromise between spatial resolution and sensitivity to atmospheric attenuation by hydrometeors. X-band radars can operate successfully in a large variety of weather conditions and can be used night and day. These properties make the X-band radar an ideal tool for marine surveillance and monitoring.

Chapter 3

Instrumentation and Digital Radar Image Capture Procedure

This chapter presents the technical specifications of the radar system used in this thesis and explains the principle of radar image collection by the digital capture board. The role of the data capture set-up parameters in defining the properties of the radar images is established. The optimal set-up registers are determined in view of the ultimate oceanographic applications of the radar images. A new electronic device, named the "Flywheel", is introduced to improve the heading accuracy of the antenna. Its working principle and the improvement in heading accuracy it induces are demonstrated.

3.1 - Description of the radar system

3.1.1 - Operational set-up of the system

The radar system consists of a marine radar associated with a digital capture board based on a personal computer. Figure 3.1 gives a schematic representation of the system's operational set-up. The two elements of the system are connected via three data links which are discussed in detail later.

The system is compact and mobile as the electric power can be supplied by a portable power generator. Set-up time is typically less than half an hour for two people upon arrival on site.

The system is occasionally deployed from boats but the pitch and roll motion adds to the complexity of the problem of accurately measuring the ocean backscatter coefficient. Hence,

in this study, the radar system was deployed exclusively from coastal sites with at least 180 degrees coverage in azimuth of the sea.

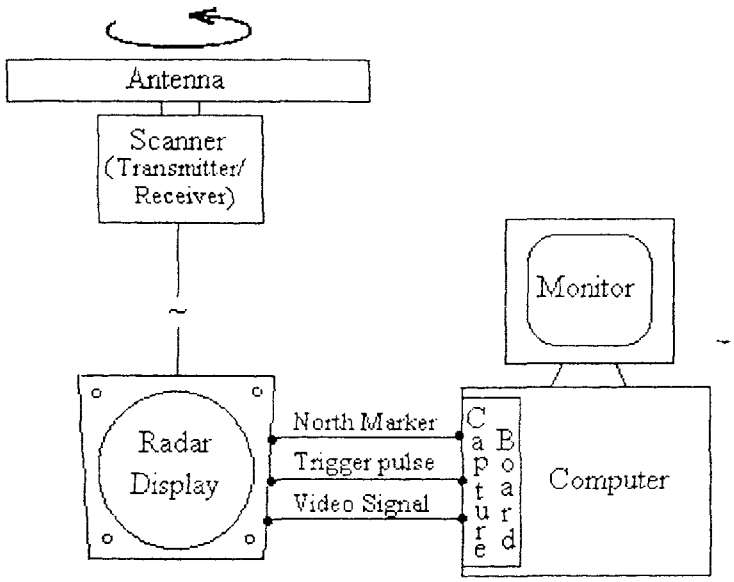

Figure 3. 1- Radar and capture board set-up

Additional requirements for the site are an elevated unobstructed location where the rotating antenna can be secured and a dry workspace for the set-up of the computer equipment. The workspace also doubles as shelter from the microwave radiation for the operators. Examples of sites have included Coast-Guards look-out towers, disused light-houses and Portacabins on beaches and cliff tops. More often though the system is simply deployed from a vehicle parked in a suitable coastal location thus providing an adaptable and mobile base for a wide range of applications.

3.1.2 - Marine radar technical specifications

Radar antenna

The radar is a standard panoramic X-band Racal Decca 1070A marine radar fitted with a linear 1.8m rotating antenna. The antenna rotates at 25 revolutions per minute (RPM) equivalent to a period of about 2.4 seconds. As for most marine radars, the polarisation is horizontal (HH).

The properties of the antenna are defined by the antenna gain pattern which depicts the antenna gain in azimuth and elevation. The characteristic parameters are the antenna beam width defined as the width of the main lobe at half power i.e. when the gain equals -3 dB, and the gain of the side lobes which determines the percentage of power received from unwanted targets and surroundings lying at angles outside the main lobe.

As in most marine radars, the aerial is specifically designed for the accurate detection and location of point targets at all ranges regardless of the boat motion. To this end, the antenna gain pattern is narrow in the horizontal plane for accurate azimuth determination and wide in the vertical plane to provide a uniform antenna gain with range and insensitivity to the boat's pitch and roll.

The horizontal beam width at half power (-3 dB) is equal to about 1.3 degrees so that the dimension in azimuth of the antenna footprint at 500 meters from the radar is approximately equal to 10 meters.

The nominal value of the maximum gain of the antenna is provided by the manufacturer and is equal to 28 dB. The relative gain of the highest side lobe with respect to the main lobe is less than -23 dB thus indicating a strongly directional antenna. Any contribution to the signal from side lobes can therefore be neglected.

The vertical beam width of the antenna is approximately 25 degrees centred on the horizon. It ensures a constant gain at all but the closest range. The vertical beam width determines the closest range for sea clutter measurements as:

$$R_{min} = \frac{h}{\sin\alpha} \qquad \text{Equation 3. 1}$$

where h is the height of the antenna above sea level and α is equal to approximately 12.5 degrees.

Radar radiation

The microwave radiation is emitted in the X-band at a frequency centred around 9.41 GHz. The radiation wavelength is approximately 3.2 centimetres.

The frequency tuning of the radar receiver is carried out manually before each data capture to account for the slight shift in emitted frequency caused by the effect of temperature and humidity variations on the magnetron. Tuning is achieved by adjusting the tuning control on the radar display unit until the intensity of faint echoes from fixed targets are maximised on the radar screen. This operation is essential in minimising the error between measurements from different data capture sessions and must therefore be performed with great care.

The microwave energy is emitted as rectangular pulses of varying temporal lengths τ. Three pulse lengths settings are available: short ($\tau = 0.08\mu s$), medium ($\tau = 0.3\mu s$) or long ($\tau = 1\mu s$) producing nominal antenna footprints respectively 12, 45 or 150 meters long in the radial direction. On the present system, the pulse length is selected by adjusting the range selector and setting the "Short/Long" pulse switch according to the information in Table 3.1.

Range selector in Nautical Miles (NM)	Nominal Pulse Length (μs)	
	Short	Long
0.25 - 1.5	0.08	0.3
3	0.3	1.0
6 - 96	1.0	1.0

Table 3. 1 - Pulse length as a function of range selector and "Short/Long" switch settings.

The different pulse length settings are characterised by the Peak Power Pt (W), which represents the amplitude of the pulses emitted, and the Pulse Repetition Rate PRR (Hz), which represents the frequency of repetition of the pulses. The nominal values of the Peak Power and the PRR associated with each pulse length setting are shown in Table 3.2. It

shows how the peak power is higher for longer pulse length settings to allow the detection of signals from greater distances, while the PRR is lower to leave enough time between two pulses to be able to determine the range of remote targets without ambiguity.

Pulse Setting	Nominal pulse length (μs)	Peak Power (kW)	PRR (Hz)	Antenna Footprint Radial Length (m)
Short	0.08	> 6	2400	12
Medium	0.3	> 8	1200	~ 45
Long	1	> 8	600	150

Table 3. 2 - Emitted pulse characteristics for different pulse length settings.

Radar receiver

The radar receiver records the returned echoes incoherently i.e. only the amplitude of the signals is recorded and phase information is ignored. After reception, the signals are shifted in frequency from GHz to MHz to enable subsequent amplification by the radar logarithmic amplifier. The amplified signals are then sent to the radar Video Display Unit (VDU) to produce a 360 degrees polar representation of the distribution of backscatter on the screen.

The radar display unit is fitted with rain and sea clutter filters which are designed to reduce sea clutter and optimise the detectability of buoys and ships on the radar screen when used for navigational purposes. These filters should be turned off during sea clutter measurements to visualise the sea clutter on the video screen. However, these controls do not affect the gain of the receiver and have no influence on the intensity of the signals received at the radar.

Technical specification summary

X-band Racal Decca 1070A marine radar			
Aerial type		Linear end-fed slotted wave guide	
Aperture		1.8 meters (6 ft)	
Rotation speed		25 rpm (150 deg/s)	
Horizontal beam width (at -3 dB)		1.3 degrees	
Vertical beam width		25 degrees approximately	
Side lobes		< -23 dB outside ± 10 degrees of main lobe	
Aerial gain		28 dB approximately	
Polarisation		HH	
Frequency		9380 - 9344 MHz	
Peak power		10 kW nominal	
PRR and Pulse length	Short	2400 Hz	0.08 μs
	Medium	1200 Hz	0.3 μs
	Long	600 Hz	1.0 μs
Amplification		Logarithmic	

3.1.3 - Digital Capture Board

The data capture is performed by a Wavex digital capture board built by MIROS Ltd. Little information was available with regards to the hardware and the processing occurring in the Wavex board as co-operation on the part of the manufacturer was minimal. Consequently, the principle of the data capture and the signal processing inside the board was deduced by means of trial and error.

The capture board is based on a PC and interfaced to the radar via three links as shown on Figure 3.1. The North Marker pulse indicates the position of the antenna heading reference point determined by the orientation of the radar scanner with respect to North. The Trigger pulse marks each microwave pulse emitted by the magnetron and has consequently a frequency equal to the Pulse Repetition Rate (PRR). The Video Signal consists of the radar echoes captured from the radar at the output of the radar logarithmic amplifier.

The principle of the data collection by the capture board and the role of the set-up parameters are described hereafter. Practical details of the experimental set-up and the computer operations can be found in the "Southampton University Wavex System" manual (1992) and MIROS's "Operation Manual For Wavex Radar Data Capture System" (1991).

3.2 - Principle of the digital data capture

Various input parameters are needed by the capture board to collect radar data. These set-up registers determine the properties of the final radar images. These parameters are listed in Table 3.3 with the range of their possible values.

3.2.1 - Spatial resolution in the radar image

Resolution in Azimuth

The **Azimuth Step** represents the number of pulses integrated for every azimuth bin in the radar image and is equivalent to the concept of "number of looks" encountered in satellite and airborne radar remote sensing. Together with the **Pulse Repetition Rate (PRR)** and the antenna rotation speed, it determines the dimension in azimuth of the pixels in the radar image.

The resolution in azimuth (deg) is calculated as:

$$\text{AngularResolution} = \frac{\text{AzimuthStep} * \text{RotationSpeed}}{\text{PRR (Hz)}} \qquad \text{Equation 3. 2}$$

where the antenna rotation speed (deg/s) is defined in relation to the **Time per revolution** (s) as:

$$\text{RotationSpeed} = \frac{360}{\text{TimePerRevolution}} \qquad \text{Equation 3. 3}$$

For each azimuth bin, the capture board integrates a number of returned echoes equal to the Azimuth Step. It then samples and digitises the resulting composite echo to produce radar backscatter values represented in 16-bits. The digital data are subsequently compressed to 8 bits (256 grey levels) for storage on PC. The **Mux Control** controls the position of the 8 bit offset to adjust it in relation to the intensity of the data and maximise the dynamic range. The usual practice recommended by the manufacturer is to set the Mux Control in accordance with the value of the Azimuth Step. Typically, for an Azimuth Step value of 2^n, the Mux control is set to n.

Set-up Registers	Range of values
Azimuth Step	1 - 256
Mux Control	0 - 7
Azimuth Start Angle	0.9 - 357.3 ± 1.8 degrees
Azimuth Interval	1.8 - 180 ± 1.8 degrees
Sampling Rate	2.5, 5, 10, 20 MHz
Initial Delay	0.6 - 25.4 μs
Burst Duration	0.2 - 51.0 μs
Number of Images	1 - 256
PRR	2400, 1200, 600 Hz
Time per revolution	2.4 s

Table 3. 3 - Set-up registers for the digital capture board

Resolution in range

The amplified echoes collected at the output of the logarithmic amplifier are sampled at a **Sampling Rate** which can be set to 20, 10, 5 or 2.5 MHz. Figure 3.2 represents the emitted and received pulses at the transmitter and receiver respectively and their defining parameters.

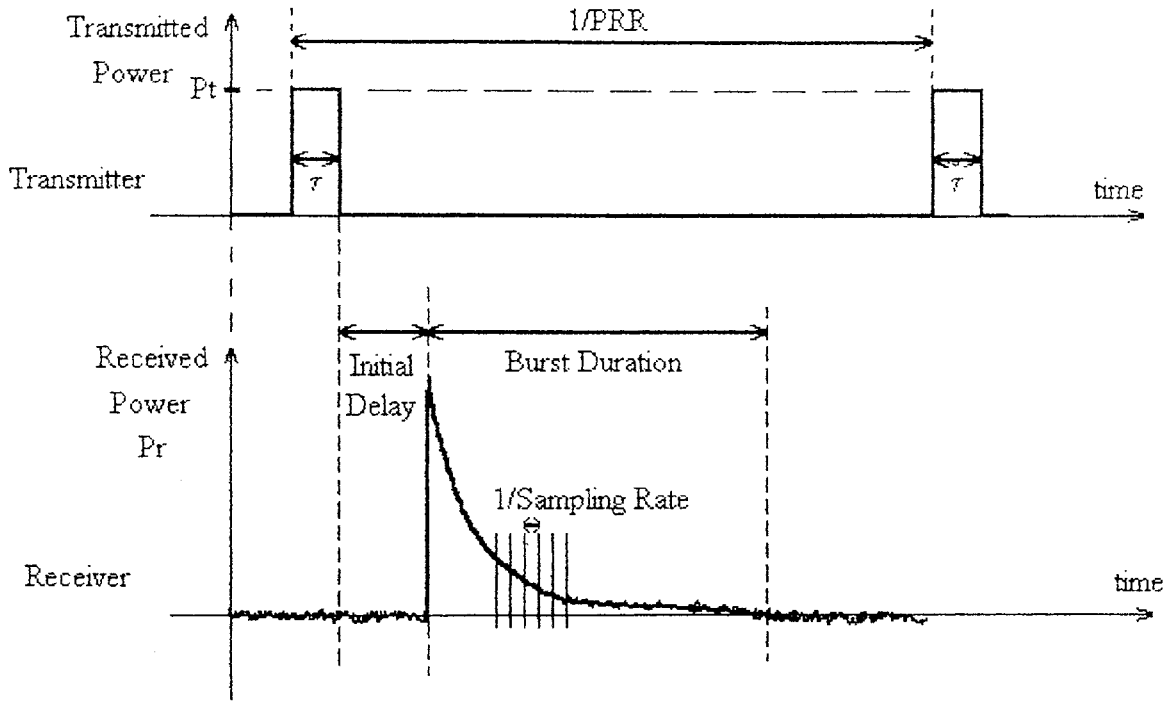

Figure 3. 2 - Pulse parameters at the transmitter and receiver (power levels for transmitter and receiver are not to scale)

The Sampling Rate determines the radial dimension of the pixels in the image which is calculated as:

$$\text{Radial Resolution} = \frac{c}{2 * \text{SamplingRate}} \qquad \text{Equation 3. 4}$$

where c is the speed of light (3.10^8 m/s). Hence, the radial resolution associated with the above values for the Sampling Rate is equal to 7.5, 15 , 30 or 60 meters respectively.

3.2.2 - Geographical definition of the sea area

Geographical location in azimuth

The co-ordinates in azimuth of the geographical area to be imaged are determined by the **Azimuth Start Angle** and the **Azimuth Interval** as shown on Figure 3.3. The Azimuth Start Angle represents the start of data recording by the board and is given with respect to the North Marker heading. The Azimuth Interval determines the end of data capture and is determined with respect to the Azimuth Start Angle.

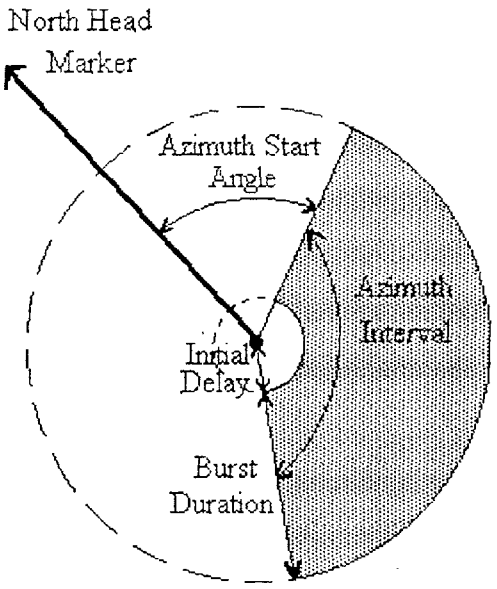

Figure 3. 3 - Geometrical definition of the sea area imaged by the radar

The capture board estimates the start and end of capture times, associated respectively with the Azimuth Start Angle and the Azimuth Interval Angle, by counting the number of emitted pulses in the Trigger signal. Assuming a constant antenna rotation speed, the board deduces the Angular Resolution for the image using Equation 3.2 and the capture parameters setting. From the value of the Azimuth Step, it determines how many pulses to integrate per azimuth bin and from this, can deduce how many azimuth bins to skip between the North Marker and the Azimuth Start Angle. Hence, the number of azimuth bins skipped before the start of data capture is:

$$StartAzimuthBin = \frac{AzimuthStartAngle}{AzimuthResolution} \qquad \text{Equation 3. 5}$$

Similarly, the end of capture is deduced by estimating the total number of azimuth bins to be collected during the Azimuth Interval, as defined by:

$$TotalAzimuthBin = \frac{AzimuthInterval}{AzimuthResolution} \qquad \text{Equation 3. 6}$$

Geographical extent in range

The definition of the location in range of the image is determined by the **Initial Delay** and the **Burst Duration** (μs) as shown in Figure 3.3. The **Initial Delay** determines the time delay between the end of the emitted pulse and the start of the data recording (see also Figure 3.2). It defines the closest range in the image and its minimal value is set to 0.6 μs, (90 meters) to avoid damage to the system from strong echoes at close proximity. The **Burst Duration** is the length of time after the Initial Delay during which the capture board is recording. It usually defines the maximum range interval in the image although this is ultimately determined by the Sampling Rate and the limitation of the capture board's buffer.

The maximum number of pixels in range is limited by the capacity of the capture board's buffer. The 512 pixel buffer capacity advertised by the manufacturer should not be used as it has been observed to cause the last twenty pixels in range in the images to overflow and reach saturation. This problem is resolved when the data capture is limited to 510 pixels in range. Hence, the maximum capacity of the buffer should be taken to be 510 pixels and the maximum range interval for an image is therefore the minimum of:

$$MaxRangeInterval = \frac{c * BurstDuration}{2} \qquad \text{Equation 3. 7}$$

and

$$MaxRangeInterval = \frac{c * 510}{2 * SamplingRate} \qquad \text{Equation 3. 8}$$

For example, the maximum range interval for an image sampled at 20 MHz with a Burst

Duration set equal to 51 μs is limited to a maximum range interval of 3825 meters (or 2.1 nautical miles).

3.2.3 - Resolution in time

The capture board is able to collect up to 256 images consecutively and produce time-series of radar images for a particular area. It is therefore possible to study the statistics of radar backscatter in time. Post-processing can produce average radar images which present at every pixel the average radar backscatter value calculated for this pixel over several antenna rotations. Similarly, images featuring the standard deviation or the skewness can also be obtained.

On short pulse setting, the system can collect data on consecutive rotations separated on the present instrument by 2.4 seconds. On medium and long pulse settings, the radar only transmits every two and four revolutions respectively to avoid any possible ranging ambiguity from far range echoes. This characteristic cannot be modified and time series images for medium and long pulse are consequently separated by 4.8 and 9.6 seconds respectively.

3.3 - Optimisation of the digital capture parameters

3.3.1 - Image resolution in azimuth

Nominal Azimuth Step

The optimal azimuth resolution of the radar system is set by the horizontal beam width of the system's antenna. It determines the smallest feature that can be imaged in the azimuth direction. The angular resolution in the images was shown to be directly related to the Azimuth Step (Equation 3.2). Due to the intrinsic speckle in radar signals, the number of "looks" should be chosen so that the image resolution in azimuth equals the dimension in azimuth of the antenna beam footprint.

For the present system, the antenna horizontal beam width is equal to just over 1 degree and the antenna's angular rotation speed is 150 degrees per second. Hence, the nominal Azimuth Step, corresponding to a resolution in azimuth of 1 degree, can be calculated from Equation 3.2 for short, medium and long pulse setting using PRR values respectively equal to 2400, 1200 and 600 Hz. The nominal Azimuth Step values for short, medium and long pulse setting are found respectively equal to 16, 8 and 4 pulses.

Oversampling

When the Azimuth Step is chosen larger than the recommended nominal value for a given pulse setting, the resolution in azimuth of the image deteriorates by becoming larger than the effective physical resolution of the antenna. The result is indistinct blurry radar images.

If the Azimuth Step is chosen smaller than the nominal value, the resolution in azimuth is artificially improved by sampling several times within the same antenna footprint. Although this type of oversampling could potentially enhance the clarity of the images, it results in fewer pulses being integrated per azimuth bin and increases the radar speckle. Consequently, the radar images will preferably be collected with an optimal azimuth resolution set to 1 degree per azimuth bin.

3.3.2 - Image resolution in range

Smallest distinguishable feature in range

The radial resolution of the marine radar is determined by the selected pulse length which determines the size in range of the sea patch contributing to the radar backscatter. This dimension defines the size of the smallest distinguishable feature by the system in the radial direction. The radial size of the sea patch was found equal to 12, 45 and 150 meters for short, medium and long pulse respectively.

The radial resolution in the digital image is determined by the Sampling Rate used to digitise the returned signals. The equivalent dimension in range of the image pixels was found equal

to 7.5, 15, 30 and 60 meters for sampling rates equal to 20, 10, 5 and 2.5 MHz respectively.

The radial resolution in the image should in principle be matched with the radial resolution of the radar for a given pulse setting. However, in contrary to what happens when oversampling in azimuth, there is no increase in speckle when oversampling the returned pulses in range as the number of pulses integrated and the size of the sea patch area contributing to the scattering are unchanged. It is therefore possible to sample medium or long pulse images at high frequency to enable for example pixel to pixel comparison with images collected on short pulse. However, the dimension of the smallest distinguishable feature in range is ultimately determined by the maximum of the radar pulse length and the image radial resolution.

Image range interval

Given the limit in the storage capacity of the capture board buffer to 510 pixels, the choice of the digital sampling rate is usually the result of a compromise between the dimension of the smallest feature to be imaged and the desired extent of the image's range interval.

Hence, if small features such as ocean waves are to be imaged, the radar should be set to Short Pulse and the Sampling Rate set to its highest value (20 MHz) so that ocean wavelengths equal to 12 m and greater can be detected in the images. In this case, the maximum range interval is limited by the buffer capacity to a maximum of 3825 meters (Equation 3.8). If instead the emphasis lies on imaging an area as large as possible, the Sampling Rate should be lowered to below 10 MHz. The dimension for the smallest detectable feature then becomes 15 meters.

At this stage, it should be noted that Sampling Rates less than 10 MHz are rarely employed as the maximum permitted Burst Duration value is equal to 51 μs. The largest possible images can therefore be sampled at 10 MHz without over-running the 510 pixel capacity of the buffer. The lower Sampling Rate values are only rarely used when a smoothing effect performed by averaging over large sea areas is pursued.

3.3.3 - Choice of pulse length

If coverage of a large area is required and the imaging of small features is unimportant, the choice of the pulse length setting should be made in accordance with the level of radar backscatter from the sea surface. In conditions of low to moderate backscatter, the pulse length can be set to medium or long pulse for which the higher level of emitted power should enable backscatter coefficient measurements for larger ranges from the radar.

3.3.4 - Summary of the optimal capture set-up

For all pulse length settings, the image resolution in azimuth will always be optimised to coincide with the 1 degree resolution of the antenna and reduce radar speckle. The choice of the remaining capture parameters will be made as a function of the final applications for the radar images and the backscatter conditions. The optimal capture parameters for each application are detailed in Table 3.4.

Set-up register	Optimal values for high resolution images	Optimal values for large coverage images	
Azimuth Step	16 pulses	8 pulses	4 pulses
Mux Control	4	3	2
Sampling Rate	20 MHz	10 MHz	10 MHz
Initial Delay	0.6 - 25.0 μs	0.6 - 25.0 μs	0.6 - 25.0 μs
Burst Duration	25.0 μs	51.0 μs	51.0 μs
Pulse setting	Short	Medium	Long
PRR	2400 Hz	1200 Hz	600 Hz
Time per revolution	2.4 s	2.4 s	2.4 s

Table 3. 4 - Optimal set-up parameters for different applications

3.4 - Radar images representation

The rotating antenna configuration of the marine radar system causes data to be collected in a radial geometry. In contrast, the digital radar data are recorded column after column in a rectangular matrix, each column consisting of the pixels obtained for all ranges at a particular azimuth bin.

Ideally, the radar data should be displayed in a radial projection to represent the sea surface backscatter in a geographically corrected (or geo-corrected) frame of reference and facilitate comparison with charts and other sources of information. The transformation from a rectangular to a radial representation does however have implications for the quality of the data.

The major problem originates in the rectangular matrix database providing the same number of data points to represent the area at close and at far ranges. Thus, in radial projection, the area near the radar is described by many data points while at far ranges there are large gaps where no data points are available, requiring a combination of averaging (near field) and interpolation (far field) to reproduce a regular spatial data grid.

An alternative solution is to use the simple Cartesian projection of the data matrix as a rectangular image. An example of the two type of projections is given for comparison in Figure 3.4 for an area in the Bay of Christchurch on the south coast of England. The Cartesian image is simply plotted as range versus azimuth bins regardless of the orientation of the area with regards to the true geographical North. This type of representation is particularly useful when accurate data values are needed and for the application of pixel-by-pixel correction. It also provides a faster way to assess the content of an image.

Throughout this study, both types of projections will be used. Where images are employed for the definition of instrumental characteristics or for the general study of radar backscatter, the more convenient Cartesian projection will be applied. Where the underlying geographical circumstances are relevant to the argumentation and for images used in oceanographic

applications, the radar data will be converted to a radial projection and displayed in a geographical frame of reference. The geo-correction will be undertaken using an in-house conversion routine.

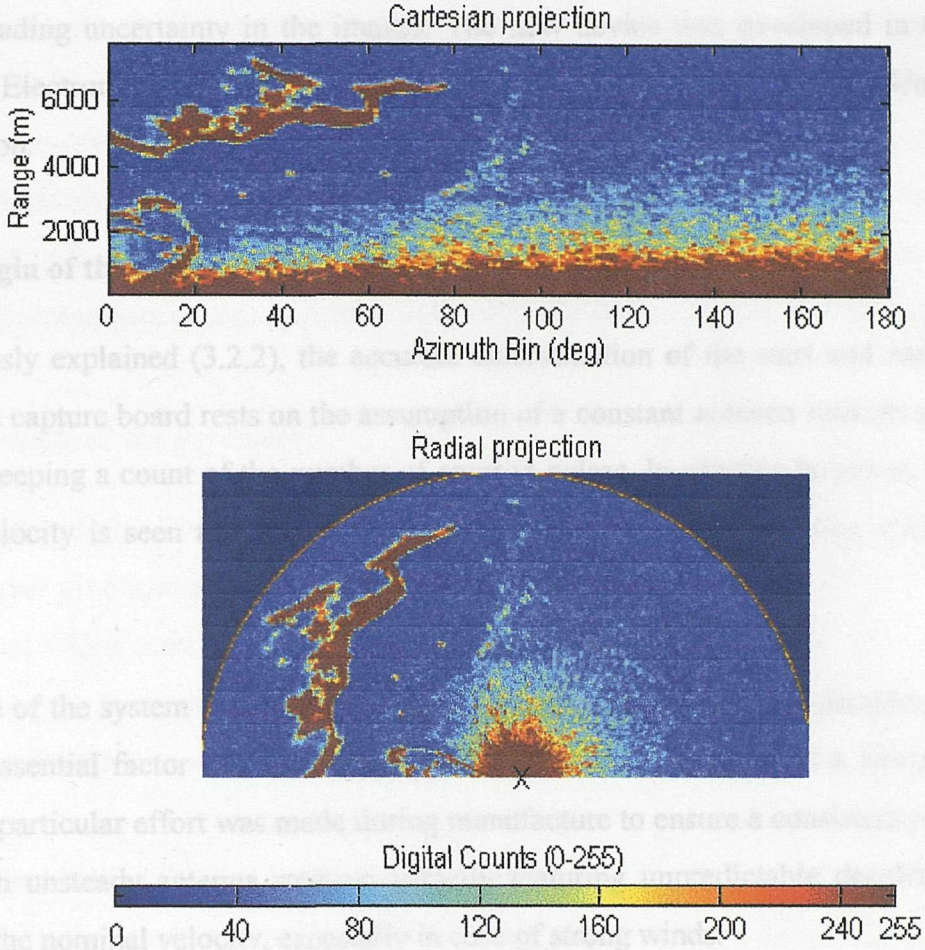

Figure 3. 4 - Cartesian and radial representation of a raw radar image collected in Christchurch Bay on the south coast of England.

3.5 - Antenna heading improvement: the "Flywheel"

From an early stage, it appeared that consecutive images collected as a time-series were regularly offset by a few degrees in azimuth and thus rarely represented exactly the same geographical area. One important consequence of these sequences of non-overlapping images was the loss of the potential reduction in measurement error through averaging over several antenna rotations.

The origin of the problem was rapidly identified as the irregular antenna rotation velocity. After carefully analysing how the antenna heading is estimated by the digital board, a new electronic device named the "Flywheel" was designed and implemented to reduce the antenna heading uncertainty in the images. The new device was developed in conjunction with the Electronic workshop of the Department of Oceanography, University of Southampton.

3.5.1 - Origin of the heading error

As previously explained (3.2.2), the accurate determination of the start and end of capture time by the capture board rests on the assumption of a constant antenna rotation speed and is based on keeping a count of the number of emitted pulses. In practice however, the antenna rotation velocity is seen to vary by over 10 %, often visibly decelerating within a single rotation.

The failure of the system to produce a regular antenna rotation speed is understandable as it is not an essential factor in the normal application of marine radars as a navigational aid. Hence, no particular effort was made during manufacture to ensure a consistent rotation. The result is an unsteady antenna rotation velocity featuring unpredictable decelerations with respect to the nominal velocity, especially in case of strong winds.

3.5.2 - Harmful effects on image capture

As a consequence of the above, the number of pulses emitted per degree of azimuth varies randomly and the antenna heading is therefore inaccurate. This has several detrimental effects on the radar images quality.

The most noticeable problem arises in the erroneous determination of the start of capture time which is based on counting the number of emitted pulses with respect to the North Marker reference heading. Given that the antenna speed does not control the emitted pulse repetition rate, when the antenna speed is lower than its nominal value, the capture board reaches the pulse count associated with the start time earlier than planned i.e. for a true

antenna heading smaller than the specified Azimuth Start Angle. This may result in a loss of control over the area for which data are being collected.

Also, as these antenna decelerations occur randomly, the start time will be slightly different from one antenna rotation to the next. Consequently, the time-series of radar images represent non-overlapping areas all starting at different headings. Average images subsequently produced by averaging several images of the time-series pixel-to-pixel appear smeared and unfocused. In extreme cases, some features are visible at several locations in an image and point targets echoes appear as linear features by being stretched in azimuth.

3.5.3 - Principle of the Flywheel

The principle of the Electronic Flywheel is based on the availability of a true antenna heading signal produced as standard by the marine radar. This Heading Marker consists of a pulsed signal which marks every 1 degree scanned in azimuth by the antenna. The signal is obtained directly from monitoring the physical displacement of a disk at the base of the antenna and therefore records all the irregularities in the antenna velocity.

The basic idea behind the Flywheel is to regulate the flow of returned echoes and ensure the integration by the capture board of an exact and fixed number of pulses between two Heading Marker pulses. The regulation of the flow of pulses received by the capture board is made possible by the particular characteristic of the capture board to remain on stand-by whenever the flow of the Trigger pulse signal is interrupted and to record data to the next azimuth bin only after receiving the exact number of pulses stipulated by the Azimuth Step. Hence, the Flywheel starts to count the number of incoming pulses after each Heading Marker pulse, interrupts the flow of incoming pulses when the correct number of pulses is reached, and then waits until the next Heading Marker pulse comes up.

3.5.4 - Limitations of the Flywheel

It is clear that the principle of the Flywheel can only work when the number of pulses per degree of azimuth is larger or equal to the Azimuth Step which corresponds to an antenna

speed lower than the nominal value. Experimental evidence seems to confirm that the antenna rotation speed is generally lower than the nominal value, although data capture with the Flywheel had to be temporarily postponed on some rare occasions of very strong wind.

The electronic Flywheel is a small box inserted at the links between the radar and the capture board. It takes two input signals from the radar (one from the radar Trigger Pulse, one from the radar Heading Marker) and has one output link to the capture board "Trigger Pulse" input. It also features a "Number of Pulses" manual switch and an audible alarm which triggers when it fails to count the required number of emitted pulses between two Heading Marker pulses.

The development of the Flywheel was carried out on a minimum budget. The restrictions this imposed on the quality of some of the hardware components employed have given rise to some limitations of the Flywheel's performances.

Additional delay in range

The Flywheel is known to introduce a time delay of approximately 2 microseconds, which was detected by comparing the positions in range of fixed buoys in no-Flywheel and with-Flywheel images. This delay is related to the relatively poor quality of its electronic microchips which cannot match the rapid response of the electronic components in the radar. The delay introduces a 360 meters offset of the closest measurable range in the image and prevents the collection of data at very close range.

A second characteristic of this additional delay is the slight variation of its duration. Transects across fixed navigational buoys have helped to estimate the variation at a few tenths of a microsecond, sufficient to introduce an uncertainty in range of a few meters. Figure 3.5 represents the profile in range of echoes from the same navigational buoy over several consecutive rotations for images collected with and without the Flywheel. The position in range of the peak of the echo is clearly shown to shift over several pixels from one image to the next. Also, the overall profile of the buoy echo changes from rotation to rotation in images collected with the Flywheel while remaining absolutely identical in shape

in non-Flywheel images. This observation indicates that the wobble in range occurs for every emitted pulse and that the change in the buoy's shape results from the integration of several pulses with slightly different delays.

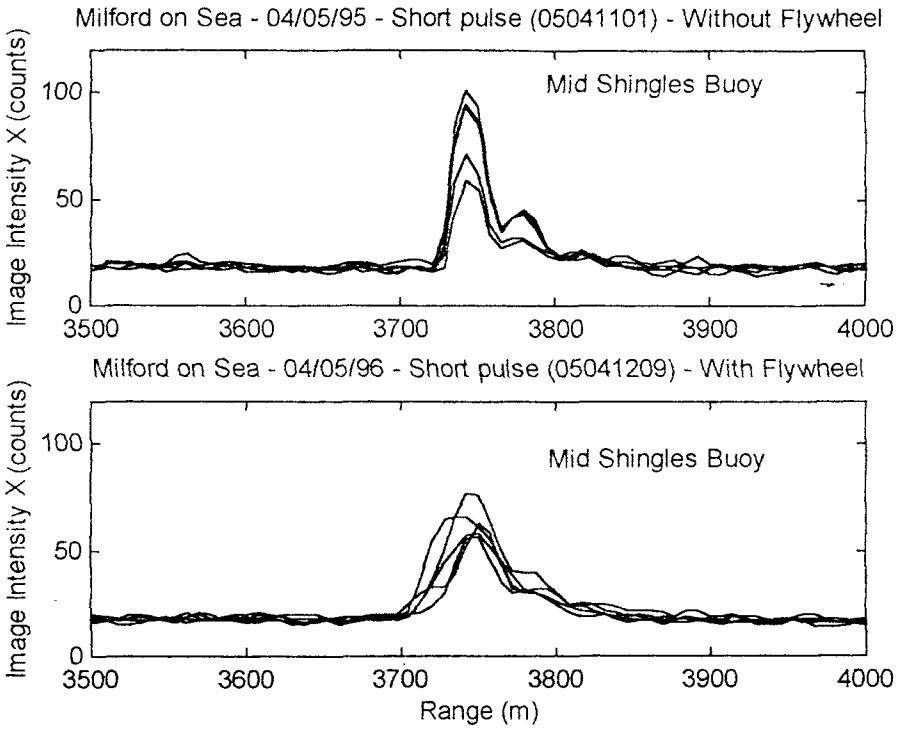

Figure 3. 5 - Buoy echoes on successive rotations for non-Flywheel images (top) and with-Flywheel images (bottom)

Hence, this wobble in range can strongly degrade the intensity of discrete targets such as buoys and images collected with the Flywheel should therefore not be used for the accurate measurement of the echo intensity and range of point targets. In contrast, these fluctuations in range have no serious implications for the measurement of ocean backscatter and are less damaging than the wobble in azimuth experienced without the Flywheel.

Manual dial restrictions

The second Flywheel hardware limitation is related to the restriction on the selector dial for the "number of pulses to be integrated" on the Flywheel. The dial can only be set to odd values between 3 and 13. This parameter determines the number of pulses counted by the Flywheel between two successive Heading Marker pulses and therefore affects the images'

resolution in azimuth.

Hence, the new resolution needs to be determined and the capture parameters modified in accordance. For the sake of brevity, only the case of short pulse images collected with the optimal digital capture registers is considered. The result are generalised to the other pulse length settings later.

3.5.5 - New image resolution in azimuth

On short pulse setting, the optimal number of pulses to be integrated per azimuth bin is equal to 16 pulses and results in the nominal resolution in azimuth of 1 degree. The closest value on the Flywheel manual dial is equal to 13. Figure 3.6 illustrates the Flywheel mechanism under these circumstances by showing the input and output signals.

In Figure 3.6, the top plot represents the Heading Marker and indicates every degree of azimuth scanned by the antenna. The middle plot represents the incoming Trigger Pulse signal from the radar. The bottom graph represent the Trigger pulse sequence at the output of the Flywheel as seen by the capture board.

The 16 consecutive pulses integrated for each azimuth bin by the capture board are indicated in individual colours. It becomes immediately clear that the discrepancy between the Azimuth Step and the Flywheel "Number of Pulses" setting results in the radar data being collected over an azimuth angle larger than 1 degree.

From Figure 3.6, it is clear that the resolution in azimuth would be equal to exactly 1 degree if the capture board could be set to integrate 13 pulses only per azimuth bin instead of 16. However, following the conditions on the definition of the Mux Control (3.2.1), the value of the Azimuth Step must be a power of 2 and can therefore not be set to 13.

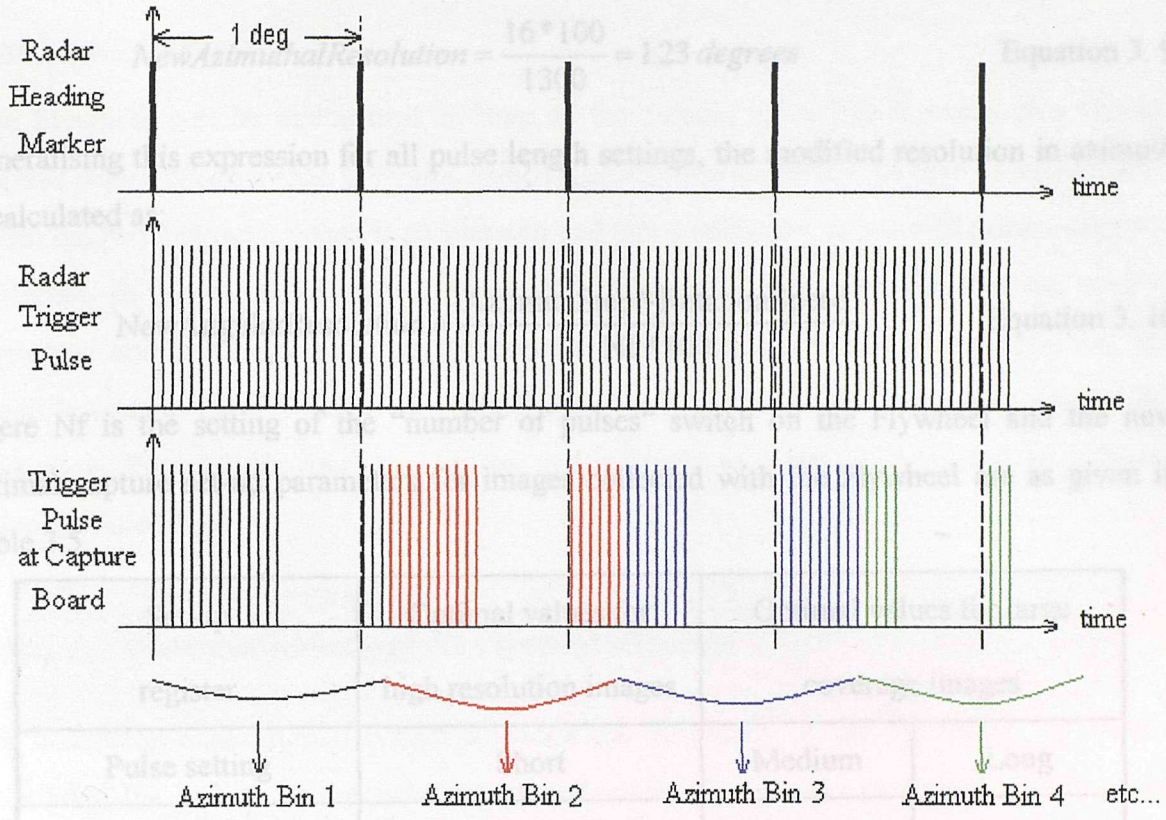

Figure 3. 6 - Input and output signals for the Flywheel when the Azimuth Step is equal to 16 and the Flywheel "number of pulses" selector is set to 13.

New capture registers

The angular resolution for short pulse images collected with the optimal set-up registers is given by Equation 3.2 and is equal to $\frac{16*150}{2400} = 1$ degree. If only 13 pulses are integrated per azimuth bin, it can be shown that the same 1 degree resolution in azimuth can be achieved by arbitrarily changing the PRR value to 1300 Hz and the RotationSpeed to 100 degrees per second, so that $\frac{13*100}{1300} = 1$ degree. This artefact is admissible simply because the capture board has no internal time clock and uses the PRR and RotationSpeed information only to determine the number of pulses per degree.

From this equivalence and from the resolution in azimuth suggested graphically in Figure 3.6, the expression for the new resolution in azimuth for Flywheel images can be deduced using Equation 3.2 and the new capture registers as:

$$NewAzimuthalResolution = \frac{16*100}{1300} = 1.23\ degrees \qquad \text{Equation 3. 9}$$

Generalising this expression for all pulse length settings, the modified resolution in azimuth is calculated as:

$$\text{NewAngularResolution} = \frac{\text{AzimuthStep} * \text{RotationSpeed}}{\text{Nf} * 100} \qquad \text{Equation 3. 10}$$

where Nf is the setting of the "number of pulses" switch on the Flywheel and the new optimal capture set-up parameters for images collected with the Flywheel are as given in Table 3.5.

Set-up register	Optimal values for high resolution images	Optimal values for large coverage images	
Pulse setting	Short	Medium	Long
Azimuth Step	16	8	4
Mux Control	4	3	2
Initial Delay	2.6 to 27.0 μs	2.6 to 27.0 μs	2.6 to 27.0 μs
New artificial PRR	1300 Hz	700 Hz	300 Hz
Nf	13	7	3
New artificial Time per Revolution	3.6 s	3.6 s	3.6 s
Resolution in Azimuth	1.23 degree	1.14 degree	1.33 degree

Table 3. 5 - Modified optimal capture registers for radar images collected with the Flywheel.

It follows that the new angular resolution in Flywheel images is slightly degraded in comparison to the earlier 1 degree resolution. However, this angular resolution is still smaller than the real beam width of the antenna (1.3 degrees). Hence, the Flywheel does not reduce the system imaging capabilities in azimuth when the "Number of Pulses" switch is chosen as close as possible to the value of the Azimuth Step.

Conditions of operation

The Flywheel will be operational as long as the number of pulses between two Heading Marker pulses is larger than the value selected on its manual switch. In case of strong winds, it can happen that the antenna is accelerated and that a sufficient number of pulses cannot be collected. In these conditions, the Flywheel alarm will sound to signify that the data are corrupted and collection must be interrupted. If data need however to be collected, it is possible to turn the "Number of Pulses" selector down to a lower value to enable data collection. The angular resolution in the image would however be degraded as estimated using Equation 3.10.

3.5.6 - Experimental evidence of the Flywheel efficiency

The following experimental results illustrate the efficiency of the electronic Flywheel in improving the quality of the radar image collection. The images presented in this section were collected with and without the Flywheel a short interval apart. All images were captured using the appropriate optimal capture registers.

Figure 3.7 illustrates the improvement of the Azimuth Start Angle accuracy. Each figure includes four single rotation views extracted from a 64 rotations time-series. The two time-series were collected at 10 minutes interval in calm wind conditions so that any heading error is due to the inherent rotation speed irregularities of the system. The images are represented in Cartesian projection with azimuth angle represented along the X axis and range running along the Y axis.

The improvement in heading accuracy is clearly demonstrated when comparing the azimuth bearing fluctuations in the time-series obtained without Flywheel (top section) and with Flywheel (bottom section) of the headland on the left-hand side of the images and the buoy echo at 3100 meters. Note how the azimuth error for the position of the headland reaches up to 15 degrees in the time-series without Flywheel while being less than 1 degree in the time-series obtained with the Flywheel.

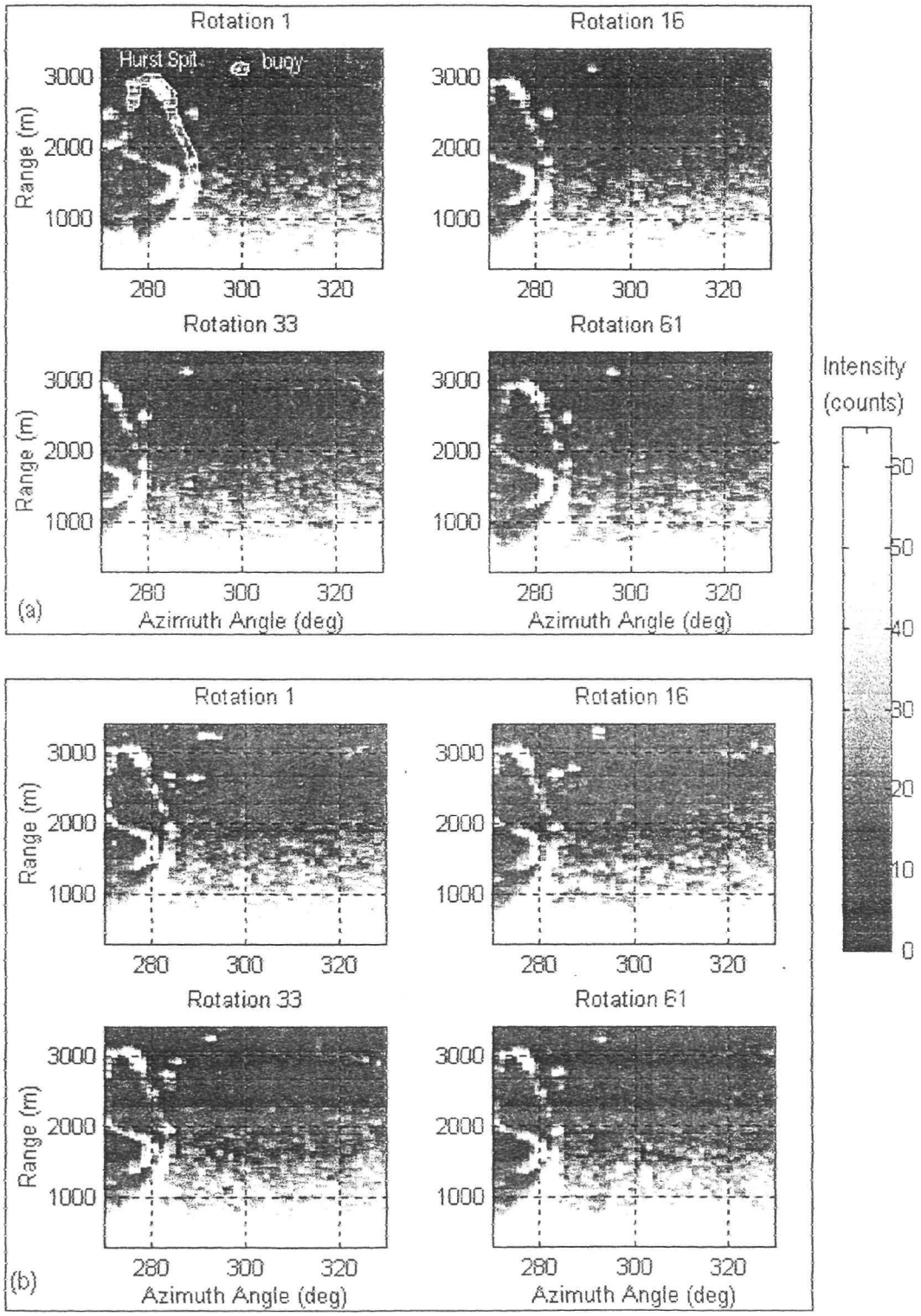

Figure 3. 7 - Rotation 1, 16, 33 and 61 extracted from a 64 rotation time-series obtained without Flywheel (a) and with Flywheel (b). Note how the azimuth bearing of the headland and buoy highlighted in the top-left image fluctuates by over 15 degrees in the time-series obtained without Flywheel.

The azimuth accuracy can be determined exactly in both instances by plotting the position in azimuth of a fixed target. Figure 3.8 presents the position of the navigational buoy highlighted in Figure 3.7.a, plotted for every rotation of the time-series without Flywheel (top) and with Flywheel (bottom). The standard deviation of the position in azimuth over the time-series is found equal to nearly 3.5 degrees in the non-Flywheel images and less than 0.5 degrees with the Flywheel, thus clearly indicating the considerable improvement in heading accuracy.

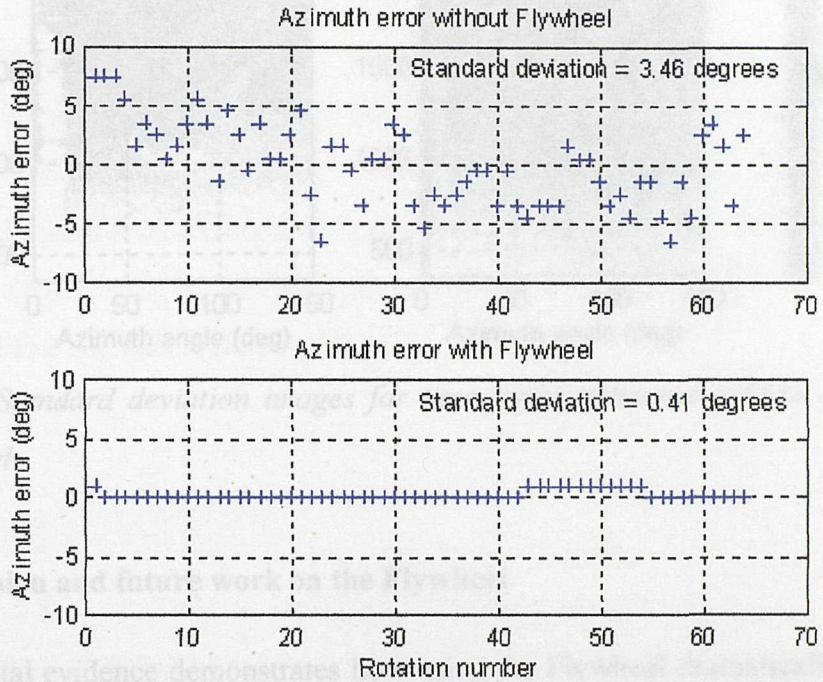

Figure 3. 8 - Azimuth position error of a fixed navigational buoy in non-Flywheel (top) and with-Flywheel (bottom) images.

Finally, the deviation image which represents the standard deviation of the backscatter intensity at every pixel was also computed for both time-series. The results are shown in Figure 3.9. The mean standard deviation in a typical area was calculated for both images and found respectively equal to 27.4 and 24.3 digital counts for non-Flywheel and with-Flywheel images. The values of the standard deviation are therefore clearly larger on the non-Flywheel images as the non-overlapping of successive images introduces further fluctuations in the backscatter signal.

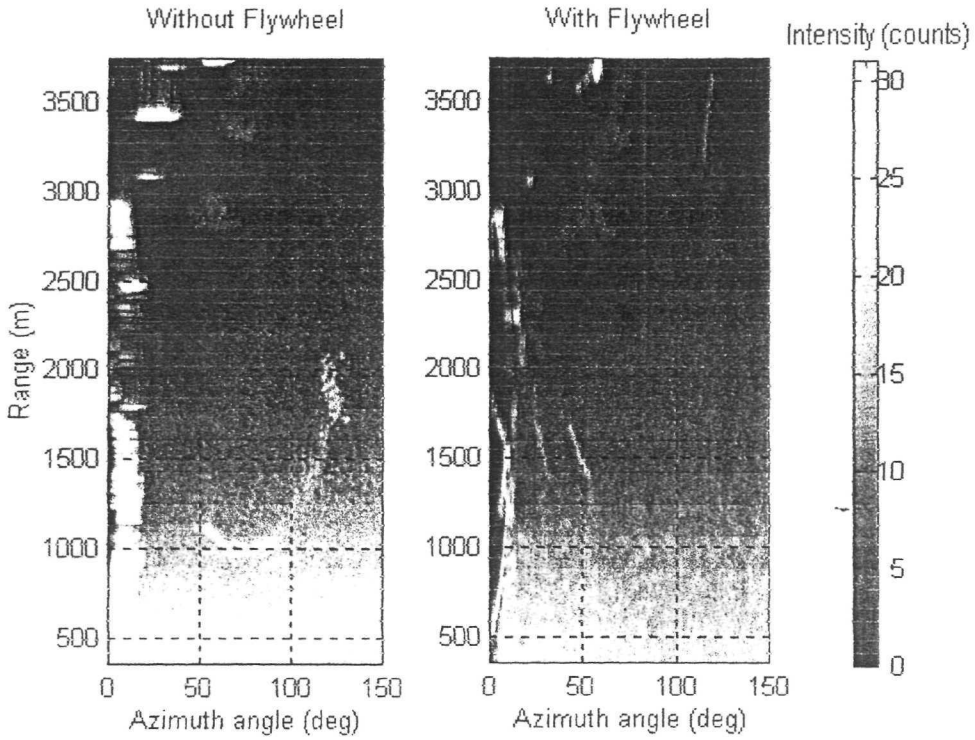

Figure 3. 9 - Standard deviation images for time-series collected without (left) and with (right) Flywheel.

3.5.7 - Conclusion and future work on the Flywheel

The experimental evidence demonstrates how using the Flywheel dramatically improves the heading accuracy of the capture board and rectifies the image capture problems linked to the irregular antenna rotation speed. The accuracy of the start and finish azimuth angles delimiting the area of interest and the heading accuracy of fixed targets is now better than 1 degree, this improved error being attributable to the uncertainty in the North Marker signal. The possibility of perfectly overlapping image time-series now enables the computation of the real sea clutter statistics and the attainment of good signal to noise ratio in the averaged images.

The hardware limitations of the Flywheel have proven to be of minor importance for the collection of sea backscatter data with only intensity measurements for point targets being degraded. These problems should however be considered for future work to be able to make use of the improved heading accuracy under all circumstances.

3.6 - Conclusion

The marine radar system constitutes a cheap, simple and versatile tool for obtaining microwave backscatter measurements in the coastal zone. The system benefits from the facility to choose between three different pulse lengths thus allowing the spatial resolution and the backscatter sensitivity to be adapted in accordance with the application and the scattering conditions.

The marine radar system also provides a unique opportunity to obtain time-series over an extended spatial area and study both the temporal and spatial evolution of the ocean backscatter distribution. This capability is further exploited with the use of the electronic Flywheel which guarantees the accurate location and reliability of backscatter measurements and enables the monitoring of oceanographic phenomena in a particular area over time scales ranging from a few seconds to hours or days.

Chapter 4

Image Normalisation and Instrument Calibration

This chapter describes the procedure for the normalisation of the raw radar images to produce representations of the sea surface roughness distribution. The relationship between the intensity of the backscatter in the image and the received power leads to the calibration of the instrument. Several calibration methods are investigated and are explained in detail. An attempt at an absolute calibration of the Normalised Radar Cross Section in dB of the sea surface is also presented.

4.1 - Image normalisation

The radar backscatter intensity in every pixel represents the power received at the antenna from the sea area illuminated by the antenna at this particular range. The normalisation enables "pretty pictures" to be turned into real measurements of the sea surface roughness independently of range, sea surface area or operational set-up.

4.1.1 - Normalised Radar Cross Section

The Normalised Radar Cross Section (NRCS), σ^0, of a target is related to the power received at the antenna, Pr, by the Radar Equation (Ulaby *et al.*, 1982):

$$Pr = \frac{Pt.\ g(\theta,\phi).\ Ae.\ \sigma^0.\ Ar}{(4\Pi)^2.\ R^4} \qquad \text{Equation 4. 1}$$

where R is the range of the target (m), Pt the transmitted power emitted by the radar magnetron (W), $g(\theta,\phi)$ the antenna gain pattern in azimuth (θ) and elevation (ϕ), Ae the effective area of the antenna (m^2) and Ar the physical area of the target (m^2). Due to the

strong directionality of the antenna in the present case, the gain $g(\theta,\phi)$ can be approximated hereafter by the maximum antenna gain $G = g(0,0) = 28$ dB.

From the theory of antennas, the antenna's effective area is known to be related to the maximum gain of the antenna G (Wheeler, 1963) by:

$$Ae = \frac{G.\lambda^2}{4\pi} \qquad \text{Equation 4. 2}$$

where λ is the wavelength of the radar radiation (m). Replacing Ae in Equation 4.1 leads to the NRCS in dB:

$$\sigma^0(dB) = 10\log_{10}\sigma^0 = 10\log_{10}\Pr + 10\log_{10}R^4 - 10\log_{10}Ar - 10\log_{10}K$$

Equation 4. 3

showing the NRCS as a function of the received power, range, physical area of the target and a scaling factor, K, which characterises the properties of the radar magnetron and antenna and can be evaluated as:

$$K = \frac{Pt \cdot G^2 \cdot \lambda^2}{(4\pi)^3} \qquad \text{Equation 4. 4}$$

4.1.2 - Sea clutter area Ar_s

For distributed targets like the sea surface, the physical area of the target Ar is given by the size of the antenna beam footprint on the sea surface. At high angles of incidence, the antenna footprint of the pulsed radar is determined by the horizontal beam width of the antenna ω and the temporal length of the radiated pulse τ as shown in Figure 4.1.

The equivalent spatial length of the radar pulse p is given in meters by:

$$p = c.\tau / 2 \qquad \text{Equation 4. 5}$$

where c is the speed of light ($c = 3.10^8$ m.s^{-1}) and τ is the radar pulse length (s). From Figure

4.1 follows the rigorous expression for the vertical beam width Φ of the pulsed radar beam (radians):

$$\Phi = \arccos\left(\frac{h}{R+p}\right) - \arccos\left(\frac{h}{R}\right) \qquad \text{Equation 4. 6}$$

where h is the height of the radar antenna (m).

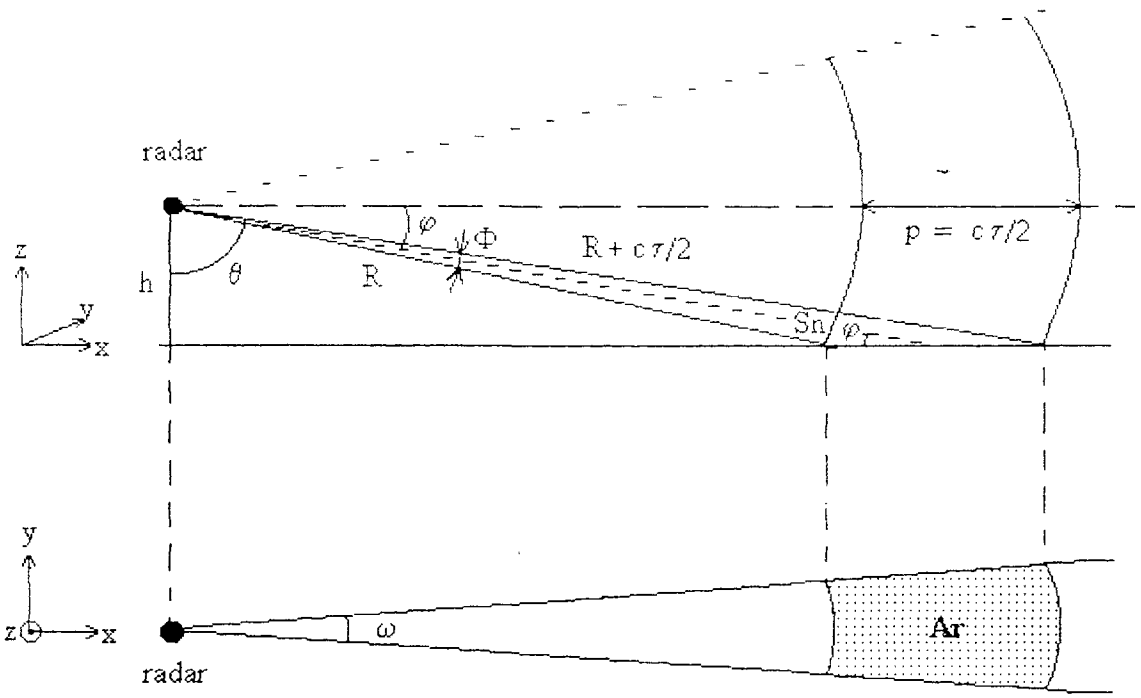

Figure 4. 1 - Geometry of the pulsed radar beam and antenna footprint

The solid angle of the pulsed radar antenna beam, Ω (rad^2), is then given by $\Omega = \Phi.\omega$ and the surface area normal to the incident radiation is $S_n = R^2.\Omega$ (m^2). Given the expression for the grazing angle, φ = arcsin(h/R) in radians, the sea clutter area Ar_s (m^2) becomes:

$$Ar_s = \frac{S_n}{\sin\varphi} = \frac{R^2.\Phi.\omega}{\sin\varphi} = \frac{R^3.\Phi.\omega}{h} \qquad \text{Equation 4. 7}$$

4.1.3 - Received power Pr

The radar backscatter intensity in the images is related to the received power Pr by the radar

system transfer function. This relationship comprises the radar's amplification function and the digital capture board transfer function. To define this relationship requires the calibration of the radar system.

4.2 - External calibration

Most modern marine radars are fitted with a logarithmic amplifier designed to increase the detectability of ships and buoys at sea. Unlike its predecessor - the linear amplifier - a logarithmic amplifier increases the dynamic range of the instrument thus extending the maximum range of target detection and reducing the risk of losing targets in strong sea clutter at close ranges.

4.2.1 - External calibration formulation

In first approximation, the amplification function may be assumed perfectly logarithmic. The relation between received power and intensity can therefore be expressed in a logarithmic scale as a linear function of the form:

$$X = A \,.\, \log_{10} Pr + B \qquad \text{Equation 4. 8}$$

where X is the image intensity, and A and B two constants defining the amplification function. Equation 4.3 and Equation 4.8 lead to:

$$10\log_{10} Pr = 10\log_{10}(\sigma^0 \,.\, Ar) + 10\log_{10} K - 10\log_{10} R^4 \qquad \text{Equation 4. 9}$$

$$10\log_{10} Pr = 10\left(\frac{X - B}{A}\right) \qquad \text{Equation 4. 10}$$

which after equating produce the following relationship:

$$10\log_{10} R^4 = C \,.\, X + D \qquad \text{Equation 4. 11}$$

with $$C = -\frac{10}{A} \qquad \text{Equation 4. 12}$$

$$D = \frac{10 \cdot B}{A} + 10 \cdot \log_{10}(\sigma^0 \cdot Ar) + 10 \cdot \log_{10}(K)$$ Equation 4. 13

4.2.2 - Empirical definition of the system transfer function

The numerical values of C and D can be determined experimentally by plotting $10.\log_{10}R^4$ against intensity (X) for echoes of targets of known radar cross section $\sigma_t = \sigma_t^0.Ar_t$. These empirically determined coefficients are hereafter referred to as C_t and D_t to indicate that they were obtained from measurements over point targets. Analytically these coefficients are equal to:

$$C_t = -\frac{10}{A}$$ Equation 4. 14

$$D_t = \frac{10 \cdot B}{A} + 10 \cdot \log_{10}(\sigma_t) + 10 \cdot \log_{10}(K)$$ Equation 4. 15

The empirical determination of the numerical values of C_t and D_t provides the mean to characterise the end-to-end transfer function of the radar system. By replacing Equation 4.8 in the expression for the NRCS (Equation 4.3) and given the analytical expressions for C_t and D_t, the sea surface NRCS in dB, σ_s^0, finally reads as a function of image intensity X as:

$$\sigma_s^0(dB) = -C_t.X + -D_t + 10\log_{10}(\sigma_t) + 10\log_{10}R^4 - 10\log_{10}Ar_s$$

Equation 4. 16

where C_t and D_t are the coefficients measured empirically from point targets, σ_t is the radar cross section of the point targets (m^2), R the range (m) and Ar_s the sea surface area (m^2) irradiated by the radar antenna.

4.2.3 - Experimental results

The coefficients C_t and D_t were determined experimentally using radar images collected in Christchurch Bay, UK. This area features numerous marker buoys defining the safe

navigation channel for ship traffic between the Isle of Wight and the mainland. Figure 4.2 shows the area imaged by the radar and the position of the navigational buoys located at various ranges and azimuth with regards to the radar position.

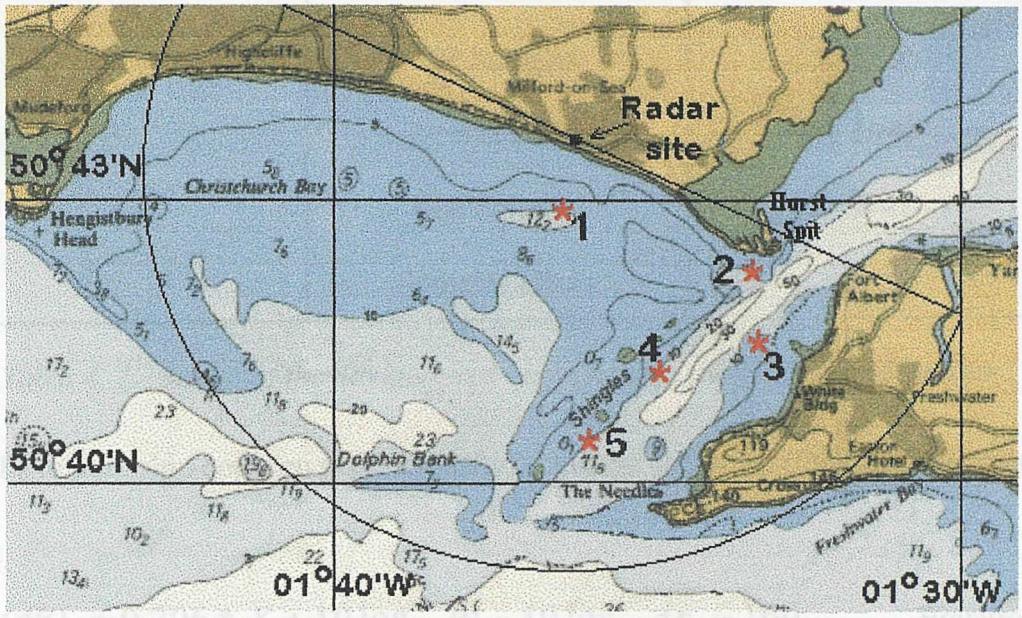

Figure 4. 2 - Location of the radar station and the five navigational buoys used for the external calibration experiment in Christchurch Bay (adapted from Admiralty Chart 2219)

The buoys used in this study are maintained by Trinity House Lighthouse Services and are fitted with 16 inch octahedral Speckter type radar reflectors with a radar cross section $\sigma_t = \sigma_t^0.Ar_t = 10m^2$ (Simmons, 1994). The name and range to the radar for each navigational buoys is given in Table 4.1 against the reference number found in Figure 4.2. The range from the buoys to the radar was measured from the position of the buoys echo peaks in high resolution radar images.

The intensities of the returns from the buoys X_t, were measured from the average images obtained from 16 consecutive antenna rotations. These intensities were then plotted against $10*\log10R_b^4$, with R_b given in Table 4.1. This preliminary examination of the system's transfer function was carried out for medium pulse only. The coefficients C_t and D_t were found equal to -0.206 and 170 respectively.

Buoy reference number in Figure 4.2	Buoy name	Buoy range (m)
1	North Head	1020
2	NE Shingles	3120
3	Warden	3690
4	Mid Shingles	3742
5	Shingles Elbow	5430

Table 4. 1 - Range of the navigational buoys used in the external calibration

Hence, the relationship between pixel intensity X and the sea surface NRCS is directly given by:

$$\sigma_s^0(dB) = 0.206 * X + 10\log_{10} R^4 - 10\log_{10} Ar_s - 160 \qquad \text{Equation 4. 17}$$

and represents the end-to-end transfer function of the radar system for medium pulse setting.

4.2.4 - Validation

Validation was sought by applying these preliminary results to a set of radar images collected over this same area in Christchurch Bay for three very different wind and sea conditions. The dataset used here for the external calibration validation is independent of that used for the definition of the empirical coefficients.

The radar system was deployed from a coastal car park in Milford-on-Sea on three successive days. The antenna was situated approximately 7 meters above the mean sea level, the change in tidal elevation being negligible in this area. Wind and sea conditions were calm on the first day (wind speed W ~ 3 m/s), but increased suddenly overnight to result in a much rougher sea on the second day (W ~ 8 - 10 m/s) which gradually abated on day 3 (W ~ 5 m/s).

The surface roughness was assumed to be spatially uniform over selected parts of the images

where the coast does not affect the wind distribution over the sea surface. As the dominant wind direction was from the south-west, the sea surface roughness in the western half of the images could be assumed to be unaffected by the surrounding coast. The NRCS in this area is then expected to be either constant or decaying slightly with range due to possible shadowing of the sea surface at very small grazing angles by large wave crests.

The radar images collected on medium pulse setting were first averaged over 16 rotations then calibrated using Equation 4.17. Representative transects from the calibrated images obtained on the three days are presented in Figure 4.3.

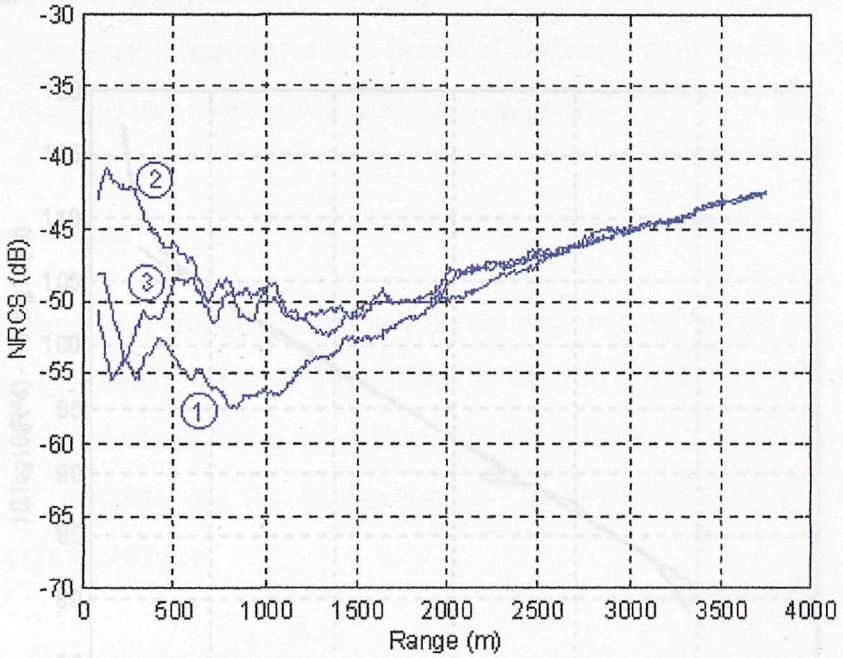

Figure 4. 3 - Transects from externally calibrated radar images collected on medium pulse setting in Milford-on-Sea on day 1 to 3.

The transects indicate that the computed NRCS increase steadily with range in disagreement with the anticipated behaviour. As this trend occurs regardless of environmental conditions, it cannot be related to an effective increase in sea surface roughness in this region but is likely to be of instrumental origin. Further examination revealed that this increase in NRCS corresponds to areas of low levels of received power for which the hypothesis of a perfect logarithmic amplification may be unfounded. Indeed, at low levels of power, the amplifier output may diverge from the perfect logarithmic form by stabilising towards the system's

internal noise level.

The hypothesis of a non-logarithmic behaviour of the amplifier at low power levels was later confirmed by sea surface backscatter images collected from the Isle of Wight overlooking the English Channel. The quantity $10*\log_{10}(R^4) - 10*\log_{10}Ar_s$ was plotted against intensity (X) for every pixel of 30 radial transects taken from a radar image collected over an area of uniform sea surface roughness. Figure 4.4 shows the behaviour of this quantity when averaged over the 30 transects. The discrepancy seen in the data around intensity X = 170 is attributed to the presence of a zone of reduced backscatter in the image and should therefore be disregarded.

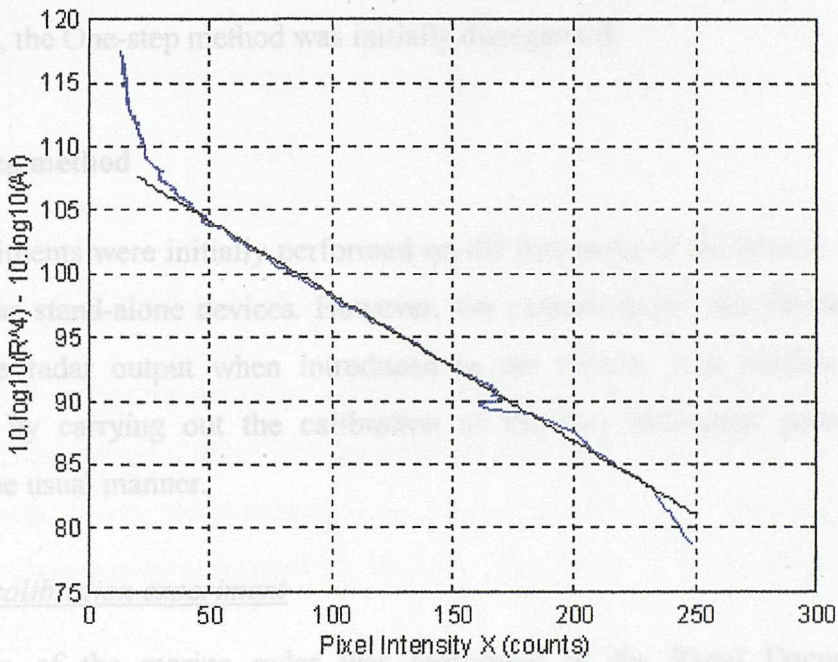

Figure 4. 4 - Evidence of the radar amplifier's non-logarithmic behaviour at low and high image intensity. The straight line corresponds to the perfect logarithmic amplification case

If the amplification function is perfectly logarithmic, Equation 4.16 predicts the plot to be linear. Instead, the data clearly deviate from the logarithmic function at high and low intensities. The assumption of a perfect logarithmic function therefore introduces discrepancies which cause the NRCS to be respectively over- and under-estimated at low and high power levels.

4.3 - Internal Calibration

In the absence of a perfect logarithmic amplification function, a simple external calibration approach is not satisfactory. An internal calibration is therefore required to accurately determine the radar system transfer function especially at low and high power levels.

Two methods of calibration were envisaged for the internal determination of the system's transfer function: a "Two-step" procedure where the radar and the capture board are calibrated separately and their respective transfer functions are subsequently combined, and a "One-step" method whereby the composite "radar + board" system is calibrated as a whole in one single experiment. Because of the practical difficulties of implementation of the second method, the One-step method was initially disregarded.

4.3.1 - Two-step method

The two experiments were initially performed on the two parts of the system independently of each other as stand-alone devices. However, the capture board was found to lower the voltages at the radar output when introduced in the circuit. This electric loading was accounted for by carrying out the calibration of the two individual parts while being connected in the usual manner.

Marine radar calibration experiment

The calibration of the marine radar was performed at the Racal Decca Marine Ltd laboratories in New Malden, UK. A calibrated microwave generator was provided to generate the microwave pulses of well-defined power levels to be injected into the radar receiver.

Firstly, the opportunity was taken to carry out a few tests on the performance specifications of the marine radar. The transmitting properties of the radar were measured and compared with the nominal values set by the manufacturer to assess the quality of the instrument. The emitted power levels, the duration of the emitted pulse length and the pulse repetition rate were measured for the three pulse settings. The results are summarised in Table 4.2.

The quality of the radar receiver was also examined by checking the response in time of the receiver to injected microwave pulses. The pulses appeared distorted indicating the existence of a strong capacitance effect which introduces a delay in the pulses reaching their maximum value. A fault in an auxiliary circuit in the display unit was found to be responsible for this and was immediately repaired. The discovery of this fault does not affect the reliability of the earlier sea surface measurements taken with the system. It however invalidates any measurements of point targets echoes intensity made previously and signifies that the results of the external calibration can only be used from a qualitative point of view.

Pulse length setting	Transmitted power Pt (kW)		Emitted pulse duration (μs)		Pulse Repetition Rate (Hz)	
	nominal	measured	nominal	measured	nominal	measured
Short	> 6	7.0	0.08	0.065	2400	2250
Medium	> 8	10.0	0.3	0.22	1200	1125
Long	> 8	11.5	1	0.86	600	560

Table 4. 2 - Technical characteristics of the marine radar transmitter

The experimental set-up for the radar calibration is shown in Figure 4.5. For each level of injected power, the output voltage was recorded at the amplifier with an oscilloscope. The microwave power levels were measured in dBm defined as the power relative to one milliwatt and subsequently expressed in decibels. The power level in dB is related to the value in dBm by:

$$\text{Power(dBm)} = 10 \cdot \log_{10}\left(\frac{\text{Power(W)}}{10^{-3}}\right)$$

and hence:

$$\text{Power(dB)} = \text{Power(dBm)} - 30$$

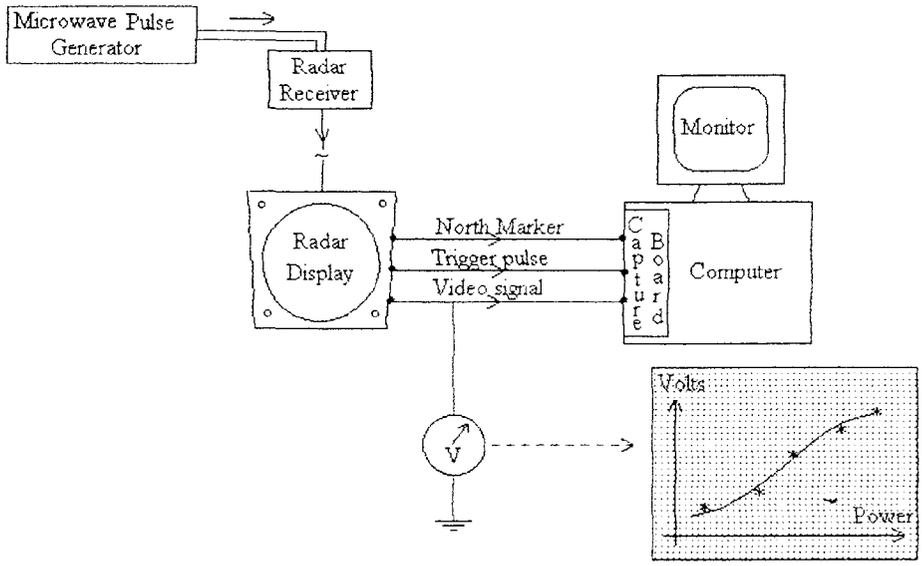

Figure 4. 5 - Experimental set-up for the calibration of the radar in the Two-step procedure

All voltages were measured from the lower limit of the ground noise level to the upper limit of the pulse as shown in Figure 4.6 to minimise the reading error from the oscilloscope display. All voltage readings therefore included the instrumental noise voltage. The internal noise voltage appeared to be independent of the power level of the injected pulses and was therefore determined by measuring the voltage in the absence of injected pulses. This internal noise voltage was subsequently subtracted from all voltage readings to give the true voltage.

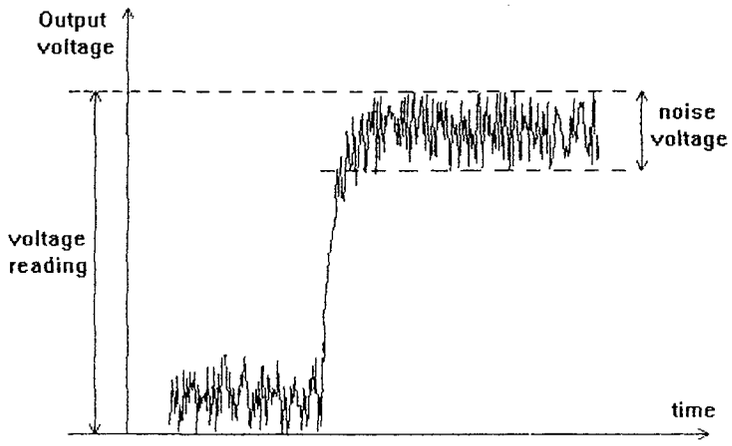

Figure 4. 6 - Voltage readings for the calibration of the marine radar

Capture board calibration experiment

The calibration of the data capture board was performed at the Electronic workshop in the Department of Oceanography, University of Southampton. An AC/DC pulse generator was used to generate pulses of determined voltage to be injected into the data capture board Video signal link as shown on Figure 4.7.

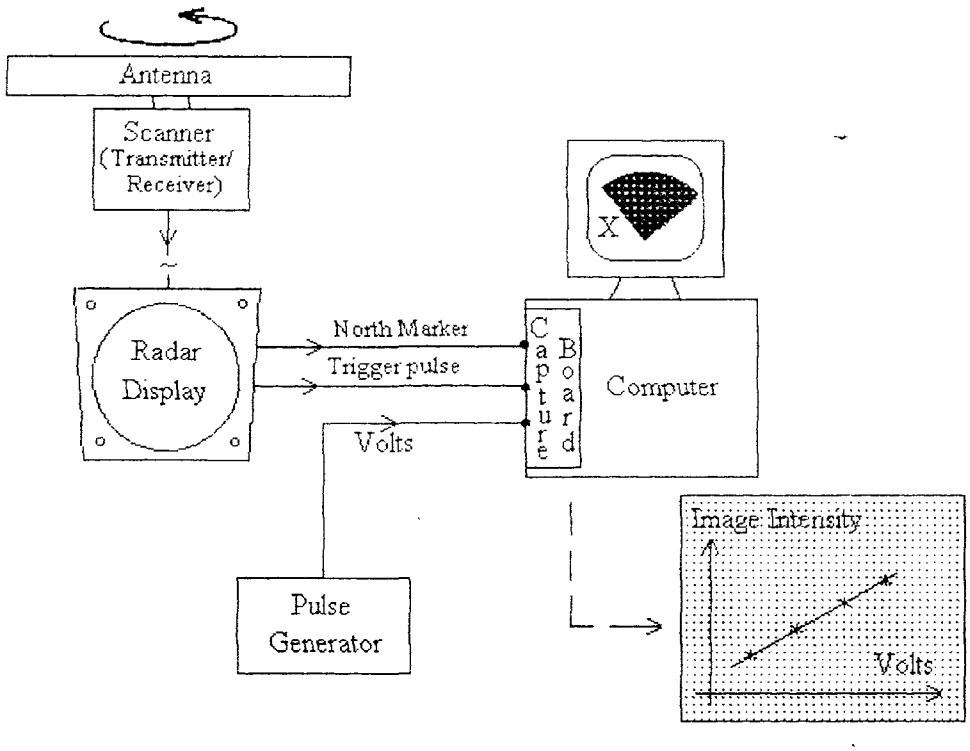

Figure 4. 7 - Experimental set-up for the calibration of the capture board in the Two-step procedure

The capture board was linked to the radar via the North Marker and Trigger Pulse connections to enable the capture of "images" for each voltage level. The set-up registers for the image capture were set to the nominal values for each particular pulse setting. In particular, the radial resolution was set to the optimal 7.5 meters cell size. Both DC and AC pulses of different frequencies and pulse duration were employed but no changes were observed in the final results.

Radar calibration results

The values of the experimental measurements (Pr, V) for the radar calibration can be found in appendix A. The relationship between received power Pr in dB and amplifier output voltage V was determined by fitting the experimental measurements in a least square method with a third degree polynomial as follows:

$$Pr(dB) = 10.\log10(Pr) = \alpha.V^3 + \beta.V^2 + \gamma.V + \delta \qquad \text{Equation 4. 18}$$

The values of α, β, γ and δ found on the short pulse setting are respectively equal to 8.778, -35.27, 75.04 and -130.8. The medium and long pulse settings were found to share the same amplification function. The coefficients α, β, γ and δ for medium/long pulse are respectively equal to 7.008, -28.38, 66.50 and -132.8. The precision in the fitted coefficients was determined as the point where no further significant improvement in the value of the χ^2 could be observed. The relationship between received power Pr and output voltage V further confirmed the non-logarithmic behaviour of the radar amplifier at low and high power levels.

Capture board calibration results

The results of the experimental measurements (V,X) for the digital capture board calibration can be found in appendix A. The function relating input voltage (V) to image intensity (X) was obtained by fitting a linear function to the experimental measurements by a least square criterion. The resulting relationship reads:

$$V\ (volts) = 6.6.10^{-2}\ X - 1.2.10^{-1} \qquad \text{Equation 4. 19}$$

where the coefficients' precision was once again determined by χ^2 testing. The calibration of the data capture board established the linearity of the digital capture board's transfer function over the whole range of voltages issued from the marine radar. Also, the range of input voltages accepted by the data capture board was found to correspond to the lower half of the range of output voltages generated by the radar. The dynamics of the total system are consequently determined by the noise level of the radar and the saturation level of the data capture board.

Composite transfer function

The complete system's transfer functions for short and medium/long pulses are obtained by combining the results of the two calibration experiments. The amplification functions read:

for short pulse;

$$10.\log10(Pr) = 2.567.10^{-6}.X^3 - 1.691.10^{-3}.X^2 + 5.560.10^{-1}.X - 1.402.10^{2} \quad \text{Equation 4. 20}$$

for medium and long pulse;

$$10.\log10(Pr) = 2.049.10^{-6}.X^3 - 1.360.10^{-3}.X^2 + 4.880.10^{-1}.X - 1.411.10^{2} \quad \text{Equation 4. 21}$$

These functions are plotted in Figure 4.8 for comparison with the external calibration function obtained previously for medium pulse. The comparison can however only be qualitative as the internal calibration functions do not include the antenna and transmitter properties.

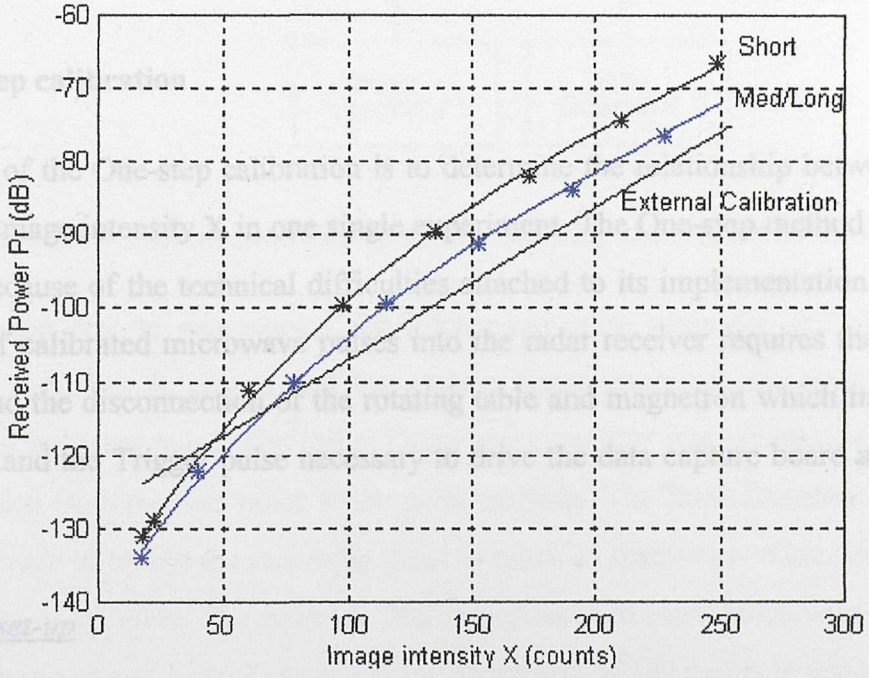

Figure 4. 8 - Composite Two-step transfer function for short and medium/long pulse setting compared with the perfectly logarithmic transfer function found in the external calibration for medium pulse.

At intermediate intensities, the slope of the Two-step function for medium/long pulse is in agreement with that of the external calibration function. The 5 dB difference between the short and medium/long pulse functions has been attributed to the presence of an additional

amplifier on medium/long pulse setting.

At low intensities however, the Two-step function starts to diverge from the perfect logarithmic law around an image intensity values of 125. This result is in clear conflict with the experimental observations in Figure 4.4 where the non-logarithmic behaviour of the amplifier only appears for intensities less than 50.

After reviewing the validity of this experimental approach, it was suggested that the digital capture board may affect the video signal in a way that cannot be reproduced by combining the results of two independent calibration experiments. It was decided that an accurate transfer function could only be guaranteed by calibrating the system in experimental conditions as close as possible to the normal conditions of data capture.

4.3.2 - One-step calibration

The objective of the One-step calibration is to determine the relationship between received power Pr and image intensity X in one single experiment. The One-step method was initially disregarded because of the technical difficulties attached to its implementation. Indeed, the introduction of calibrated microwave pulses into the radar receiver requires the removal of the antenna and the disconnection of the rotating table and magnetron which imply that the North Marker and the Trigger pulse necessary to drive the data capture board are no longer generated.

Experimental set-up

To resolve this problem, the amplitude and frequency of the radar North Marker and Trigger pulse signals were determined with the help of an oscilloscope. Two AC/DC pulse generators signals were then set-up to simulate signals of similar characteristics. These two pseudo-radar control signals were then fed into the data capture board input links and allowed the radar antenna and magnetron to be disconnected. The microwave pulse generator could then be set up at the radar receiver end for the generation of the calibrated microwave pulses. As before, the microwave pulse generator was supplied by Racal Decca Marine Ltd.

The experimental set-up for the One-step calibration is shown in Figure 4.9. In this instance, the only connection between the radar and the capture board is the Video link which carries the calibrated microwave pulses.

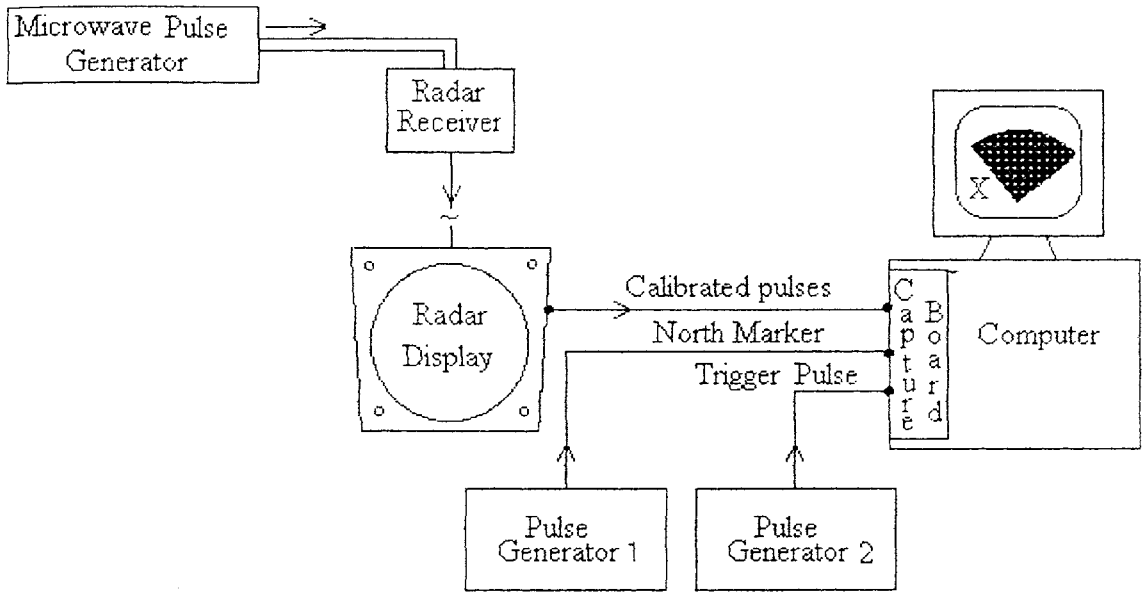

Figure 4. 9 - Experimental set-up for the One-step calibration method

One essential step was to synchronise the microwave pulse generator and the "pseudo-Trigger" pulse generator to ensure that the capture board intercepts the same part of the incoming pulses for every pulse. The Initial Delay set-up register was adjusted to collect data over the transition from receiver noise to the pulse intensity. The Burst Duration register was chosen long enough to enable the incoming pulse to reach its maximum value while allowing a Sampling Rate of 20 MHz. The Azimuth Step was chosen in accordance with the nominal register guidelines and each image contained the equivalent of 180 pixels in azimuth.

Artificial images of the applied pulses were collected for incremented power levels. All radial transects in the images were averaged in azimuth to provide a clear profile of the incoming pulse intensity. Figure 4.10 shows the azimuth-averaged transects from artificial images obtained on short pulse for incremental power levels between -100 and -35 dBm.

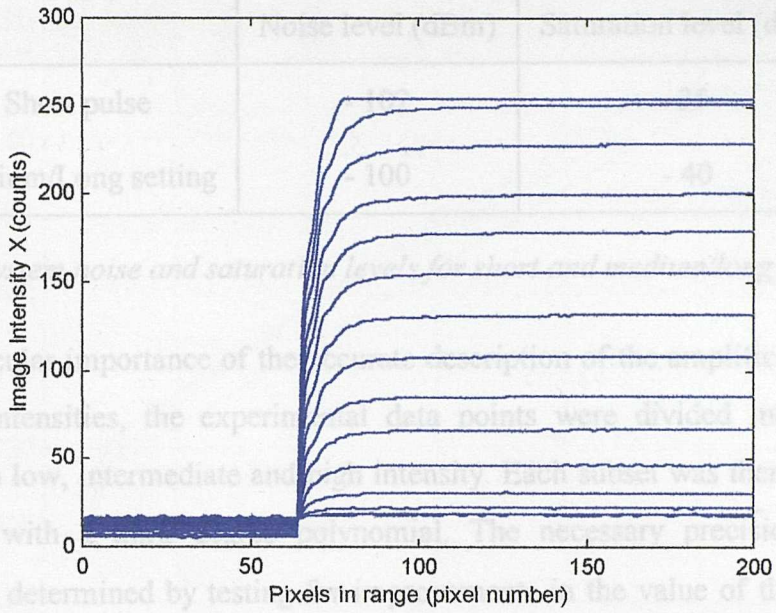

Figure 4. 10 - Azimuth-averaged transects in artificial images obtained on short pulse setting in the One-step calibration experiment for incremental power levels between -100 and -35 dBm.

This experiment also enabled the precise definition of the system's noise and saturation levels. The system noise level was defined as the input power level for which the incoming pulse could not be distinguished from the background radar noise. The saturation level was associated with the power level for which the digital capture board reaches saturation (i.e. X= 255).

Experimental results

The intensity X associated with each power level is obtained by averaging over the section of the transects for which the pulse has reached its maximum value. Consequently, the experimental measurement error was minimal as the standard deviation of the intensity measurements was systematically found to be better than 1 count in these sections. The values of the experimental data points can be found in appendix A. The noise and saturation levels of the system for short and medium pulse are summarised in Table 4.3.

	Noise level (dBm)	Saturation level (dBm)
Short pulse	- 102	-35
Medium/Long setting	- 100	- 40

Table 4. 3 - System noise and saturation levels for short and medium long pulse settings

Due to the particular importance of the accurate description of the amplification function at low and high intensities, the experimental data points were divided into three subsets corresponding to low, intermediate and high intensity. Each subset was then fitted in a least square method with a third degree polynomial. The necessary precision in the fitted coefficients was determined by testing for improvements in the value of the χ^2. Extra care was taken to ensure continuity at the boundaries of each subset. The relationships derived between the received power Pr in dB and the image intensity X in counts for each pulse setting and intensity range read as follows:

Short pulse

$18 < X \leq 31$ $\quad Pr\,(dB) = f_s(X) = 2.678.10^{-3}.X^3 - 2.813.10^{-1}.X^2 + 9.783.X - 2.326.10^2$

$31 < X \leq 251$ $\quad Pr\,(dB) = f_s(X) = 1.097.10^{-6}.X^3 - 6.300.10^{-4}.X^2 + 3.250.10^{-1}.X - 1.292.10^2$

$251 < X < 255$ $\quad Pr\,(dB) = f_s(X) = 6.8152.10^{-4}.X^3 - 4.6199.10^{-1}.X^2 + 1.0414.10^2.X - 7.8814.10^3$

Medium/long pulse

$18 < X \leq 25$ $\quad Pr\,(dB) = f_{ml}(X) = 6.84.10^{-3}.X^3 - 6.32.10^{-1}.X^2 + 1.91.10^1.X - 3.09.10^2$

$25 < X \leq 245$ $\quad Pr\,(dB) = f_{ml}(X) = 1.49.10^{-6}.X^3 - 7.30.10^{-4}.X^2 + 3.03.10^{-1}.X - 1.27.10^2$

$245 < X < 255$ $\quad Pr\,(dB) = f_{ml}(X) = 1.0194.10^{-4}.X^3 - 6.6737.10^{-2}.X^2 + 1.4685.10^1.X - 1.1656.10^3$

These functions are plotted in Figure 4.11. Once again, the slopes of the external calibration and the One-step internal calibration functions for medium pulse compare well in the intermediate range of intensities. At lower and higher intensities, the One-step amplification functions clearly diverge from the perfectly logarithmic function. The non-logarithmic behaviour appears for intensities around 50 in perfect agreement with the experimental observations in Figure 4.4.

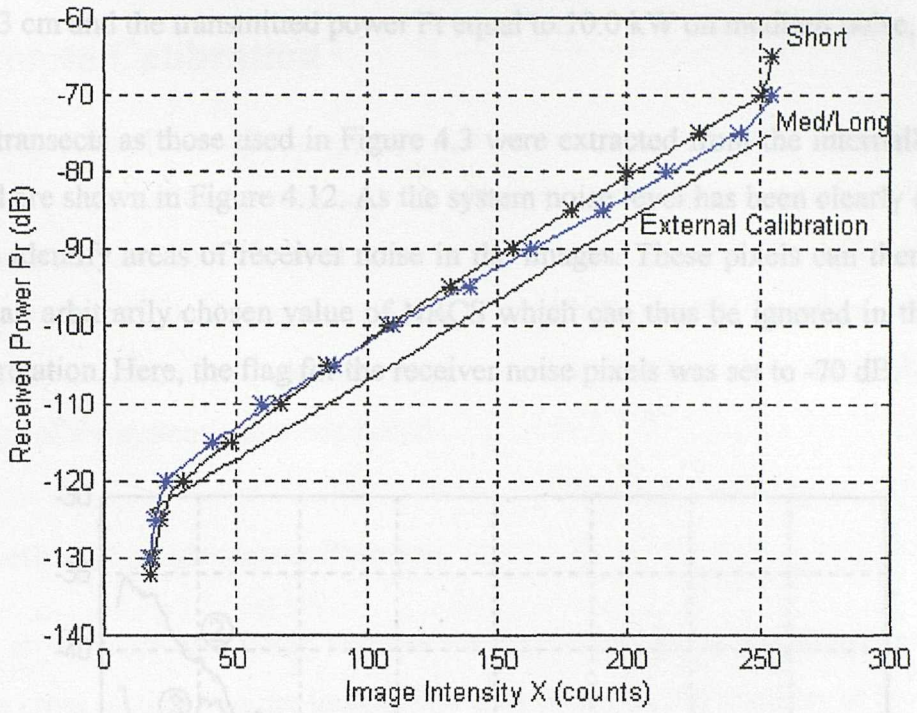

Figure 4. 11 - One-step calibration transfer functions for short and medium/long pulse setting and external transfer function for medium pulse

Validation of the One-step calibration

Following Equation 4.3, the expression of NRCS in dB becomes:

$$\sigma^0(dB) = f_{s,ml}(X) + 10\log_{10} R^4 - 10\log_{10} Ar_s - 10\log_{10} K \qquad \text{Equation 4. 22}$$

with f_s and f_{ml} the amplification functions for short and medium/long pulse shown in Figure 4.11, R the range (m), Ar_s the sea patch area and K the scaling factor characterising the properties of the radar magnetron and antenna.

The validation of the One-step calibration results was undertaken by calculating the NRCS for the same set of images as used previously to validate the external calibration method. The radar images were averaged over 16 rotations and normalised using the internal calibration results given in Equation 4.22. The coefficient K representing the quality of the antenna and magnetron was estimated using the manufacturer's technical specifications. The coefficient K is found equal to 32.5 dB for a maximum antenna gain G of 28 dB, a radiation wavelength

λ equal to 3 cm and the transmitted power Pt equal to 10.0 kW on medium pulse,

The same transects as those used in Figure 4.3 were extracted from the internally calibrated images and are shown in Figure 4.12. As the system noise level has been clearly defined, it is possible to identify areas of receiver noise in the images. These pixels can then be flagged and set to an arbitrarily chosen value of NRCS which can thus be ignored in the following data interpretation. Here, the flag for the receiver noise pixels was set to -70 dB.

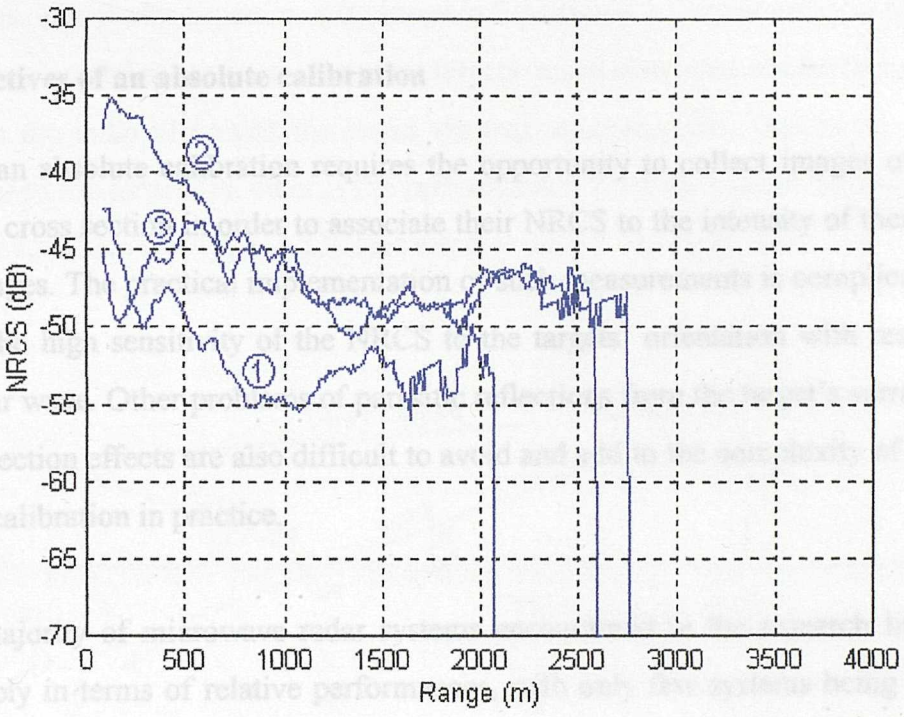

Figure 4. 12: Validation dataset for the One-step calibration on day 1 to 3.

In contrast to the external calibration results, the NRCS is found to vary little with range beyond a region 1000m from the shore as expected for a uniformly rough sea surface. The decay of the NRCS at close range may be associated with the steeper incidence angle of the radar wave on the sea or a possible increase of the sea surface roughness near shore. This particular characteristic of the NRCS is investigated later in Chapter 7.

4.4 - Absolute Calibration

So far, the properties of the radar magnetron and antenna were estimated from the laboratory measurements of the emitted power and the maximum antenna gain provided in the radar technical specifications. This nominal value of the antenna gain may be different in reality. The scaling factor K in the calculation of the NRCS should therefore be measured experimentally to determine whether these calculated values are acceptable for the determination of the system's dynamic range.

4.4.1 - Objectives of an absolute calibration

To perform an absolute calibration requires the opportunity to collect images of targets of known radar cross section in order to associate their NRCS to the intensity of their echoes in the radar images. The practical implementation of such measurements is complicated chiefly because of the high sensitivity of the NRCS to the targets' orientation with respect to the incident radar wave. Other problems of parasitic reflections from the target's surroundings or multiple reflection effects are also difficult to avoid and add to the complexity of performing an absolute calibration in practice.

The large majority of microwave radar systems encountered in the research literature are defined simply in terms of relative performances, with only few systems being sufficiently advanced to justify the extra cost and investment associated with performing an absolute calibration. High-resolution radars with small antenna beam widths of the order of a few square meters are usually calibrated in anechoic chambers to simulate measurements in free space and minimise parasitic reflections. Systems with larger antenna footprints need specially designed large scale facilities to carry out the measurements. SIR-C/X-SAR for example used specifically designed land-based radar reflectors which are re-orientated to the path of the Space Shuttle before each data take (Zink, 1995).

For marine radars, absolute calibrations are seldom performed aside from research and development projects designed to improve the performances of radar systems as navigational aids. For these research purposes, radar manufacturers have developed specific sites featuring

arrays of pole-mounted radar reflectors set up at various heights above the sea level. Unfortunately there was no opportunity to access such a facility within the time-scale of this study. Instead, better use was made of the radar corner reflectors mounted on the navigational buoys previously used in the external calibration experiment.

4.4.2 - Multiple scattering

The problem of measuring echoes from navigational buoys is different from measuring sea surface returns. The Radar Equation introduced in Equation 4.1 is valid only for point targets in free space or located at sea level. For point targets raised above the sea surface, the energy radiated from the radar arrives at the target via two separate paths. One is the direct path from the radar to the target, the other is the path reflected from the surface between the radar and the target as shown on Figure 4.13. This effect is called "multiple scattering" or "forward scatter".

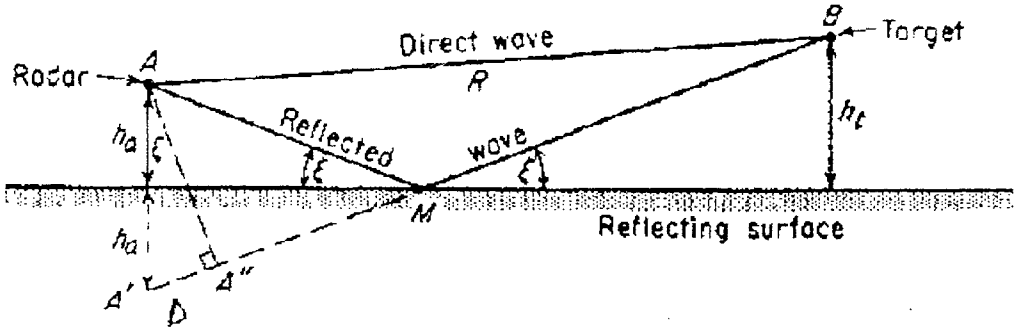

Figure 4. 13 - Propagation over a plane reflecting surface (from Skolnik, 1980)

Hence, the magnitude of the resultant echo is determined by the relative amplitude and the phase difference between the direct and the reflected radiation. The amplitude of the reflected radiation is determined by the reflection properties of the surface. In the case of a smooth sea surface, the reflection of a horizontally polarised X-band radiation at small grazing angles is nearly total and undergoes no significant change in amplitude (Skolnik, 1980).

In these conditions, it is possible to quantify the effect of the surface on the target echo by estimating the power ratio η^4 at the radar between the power in presence of the surface and

the power in free space (Skolnik, 1970):

$$\eta^4 = 16.\sin^4\left(\frac{2\pi h_a h_t}{\lambda R}\right) \qquad \text{Equation 4. 23}$$

where h_a is the height of the radar antenna, h_t is the height of the target above the mean sea level, λ is the radiation wavelength and R is the distance from the radar to the target via the direct path.

From this expression, it appears that the power ratio can vary between 0 and 16 for different configuration of antenna height, target height and target range. The presence of the reflecting surface thus causes the continuous elevation coverage of the radar to break up into a lobed structure, the magnitude of the received power from a given target depending strongly on its location with respect to the maximum lobes.

The Radar Equation describing the received echo power must therefore be modified to account for this propagation factor. The new expression for the received power for point targets in presence of the reflective sea surface may be rewritten and approximated for small grazing angles by:

$$Pr = \eta^4 \cdot \frac{Pt \cdot G^2 \cdot \lambda^2 \cdot \sigma}{(4\pi)^3 \cdot R^4} \approx \frac{4\pi \cdot Pt \cdot G^2 \cdot \sigma \cdot (h_a h_t)^4}{\lambda^2 \cdot R^8} \qquad \text{Equation 4. 24}$$

It follows that the new expression for the Normalised Radar Cross Section of a target in presence of a reflecting surface is given by:

$$\sigma^0(dB) = 10 \cdot \log_{10} Pr + 10 \cdot \log_{10} R^8 - 10 \cdot \log_{10} Ar - 10 \cdot \log_{10} K' \qquad \text{Equation 4. 25}$$

with Pr the received power at the radar (W), R the target range (m) and Ar the physical area of the target (m^2). The coefficient K′ is a new scaling factor which can be estimated by:

$$K' = \frac{4\pi \cdot Pt \cdot G^2 \cdot (h_a h_t)^4}{\lambda^2} \qquad \text{Equation 4. 26}$$

4.4.3 - New formulation for the absolute calibration

The impact of multiple scattering on the intensity of sea surface echoes is negligible and the equations for the normalisation of ocean backscatter images are therefore unchanged. Hence, the scaling factor to be determined to achieve the absolute calibration of the system is still the coefficient K as defined in Equation 4.4.

From their respective definitions, the scaling factor K can be related to the intermediate coefficient K′ with the following relationship:

$$K = \frac{K' \cdot \lambda^4}{(4\pi)^4 \cdot (h_a h_t)^4} \qquad \text{Equation 4. 27}$$

The scaling factor K can therefore be obtained from the determination of the coefficient K′. The latter can be found by combining experimental measurements of navigational buoys intensity as performed in the external calibration and results from the internal calibration.

New formulation for the buoy intensity measurements

Following the same procedure as employed for the external calibration but based on the new Radar Equation, the radar system transfer function can be reduced to an equation of the form:

$$10 \cdot \log_{10} R^8 = C' \cdot X + D' \qquad \text{Equation 4. 28}$$

with

$$C' = -\frac{10}{A'} \qquad \text{Equation 4. 29}$$

$$D' = \frac{10 \cdot B'}{A'} + 10 \cdot \log_{10}(\sigma^0 \cdot Ar) + 10 \cdot \log_{10} K' \qquad \text{Equation 4. 30}$$

where R is the range of the target, X is the intensity of the echo in the radar image, A′ and B′ are two constants defining the radar's logarithmic amplification function and $\sigma = \sigma^0.Ar$ is the target radar cross section.

The system's end-to-end transfer function can then be determined empirically by defining the coefficients C'_t and D'_t in a least square fitting of echo intensity of targets of known radar cross section $\sigma_t = \sigma^0.Ar_t$ plotted as $10.\log_{10}R^8$ versus X.

Finally, as was demonstrated for the external calibration, the expression of the NRCS for any target can be shown to read:

$$\sigma^0(\mathrm{dB}) = -C'_t \cdot X - D'_t + 10 \cdot \log_{10}\sigma_t + 10 \cdot \log_{10} R^8 - 10 \cdot \log_{10} Ar_t \qquad \text{Equation 4. 31}$$

Formulation for the calculation of the scaling factor K

The empirical approach and the internal calibration procedure result in two expressions of the Normalised Radar Cross Section σ^0(dB) given respectively in Equation 4.31 and Equation 4.25. In the range of intermediate intensities where the internal and external calibration functions were shown to give qualitatively comparable results, it is possible to write for any given pixel with an intermediate intensity X that:

$$\underbrace{10 \cdot \log_{10} \mathrm{Pr} - 10 \cdot \log_{10} K'}_{\text{internal calibration}} = \underbrace{-C'_t.X - D'_t + 10.\log 10(\sigma_t)}_{\text{external calibration}} \qquad \text{Equation 4. 32}$$

where $\sigma_t = \sigma_t^0.Ar_t$ is the radar cross section of the target used for the empirical definition of C'_t and D'_t.

Since the only function of X on the left hand side of the equality sign is included in the internal calibration function, the coefficient - C'_t must be equal to the slope of the internal calibration amplification function $10.\log_{10}Pr = f(X)$ in the intermediate intensity range. From the results of the internal calibration experiment, the amplification functions for short and medium/long pulse settings can be linearly approximated in the intermediate intensity range by:

Short Pulse $\quad 10.\log_{10}(Pr) = 0.223.X - 125 \qquad$ Equation 4. 33

Medium/Long Pulse $\quad 10.\log_{10}(Pr) = 0.201.X - 123 \qquad$ Equation 4. 34

Equating the empirical coefficient C'_t to -0.223 and -0.201 for short and medium/long pulse respectively, the experimental points in the $10.\log_{10}R^8$ versus X plots can then be fitted in a least squares manner by adjusting the offset D'_t.

After the empirical definition of D'_t for short, medium and long pulse, the coefficient K′ can be calculated for the three pulse settings as:

$$K'_{short}(dB) = 10 \cdot \log_{10}(K'_s) = 0.223 \cdot X - 125 - 0.223 \cdot X + D'_{ts} - 10 \cdot \log_{10}\sigma_t \quad \text{Equation 4. 35}$$

$$K'_{med}(dB) = 10 \cdot \log_{10}(K'_m) = 0.201 \cdot X - 123 - 0.201 \cdot X + D'_{tm} - 10 \cdot \log_{10}\sigma_t \quad \text{Equation 4. 36}$$

$$K'_{long}(dB) = 10 \cdot \log_{10}(K'_l) = 0.201 \cdot X - 123 - 0.201 \cdot X + D'_{tl} - 10 \cdot \log_{10}\sigma_t \quad \text{Equation 4. 37}$$

and the scaling factor K can finally be determined using equation 4.27.

4.4.4 - Experimental set-up for the buoys intensity measurements

The "K-coefficient" experiment was carried out in Milford-on-Sea overlooking Christchurch Bay. The geographical location of the radar and the radar image area are the same as those used for the external calibration and are shown in Figure 4.2. A new set of radar images was collected for the measurement of the buoys intensities as the data collected on previous occasions were known to be affected by the capacitance effect detected during the internal calibration of the instrument.

Despite the evident measurement uncertainty associated with the motion of the buoys, the errors were minimised by carrying out the experiment in very calm wind and sea conditions (Beaufort 0-1 c. 0 - 3 m/s). The pitch-and-roll motion of the buoys and the contribution of the surrounding sea to the radar backscatter measurement were consequently strongly reduced.

The radar image spatial resolution was optimised to 7.5m to measure the buoys' echo intensities as accurately as possible. Time-series of radar images were collected over a large number of antenna rotations. The irregular rotation speed of the radar antenna resulted in the

position of the buoys being shifted significantly in azimuth from one image to the next. The time-series of the echo intensity for each buoy could not therefore be extracted by simply selecting the same position in every image of the time-series. The use of the electronic Flywheel (Chapter 3) was not possible either because of the reduction of the intensity of sharp features resulting from the slight fluctuations in range.

The intensity of the targets was therefore measured from non-Flywheel images by manually locating and recording the peak intensity value for each buoy in every antenna rotation in the time-series and for the three pulse settings. For each buoy and pulse setting, a time series of 250 intensity measurements was obtained for statistical analysis. The buoys intensity time-series are presented in Figure 4.14, 4.15 and 4.16 for short, medium and long pulse respectively with the associated normalised histograms.

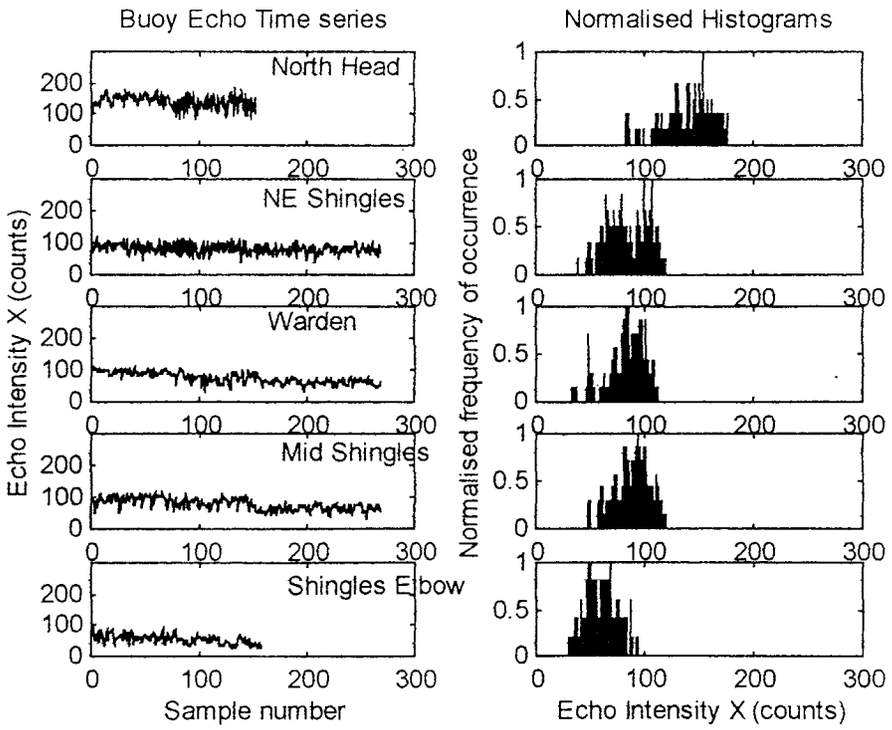

Figure 4. 14 - Time series and normalised histograms for the buoys on short pulse

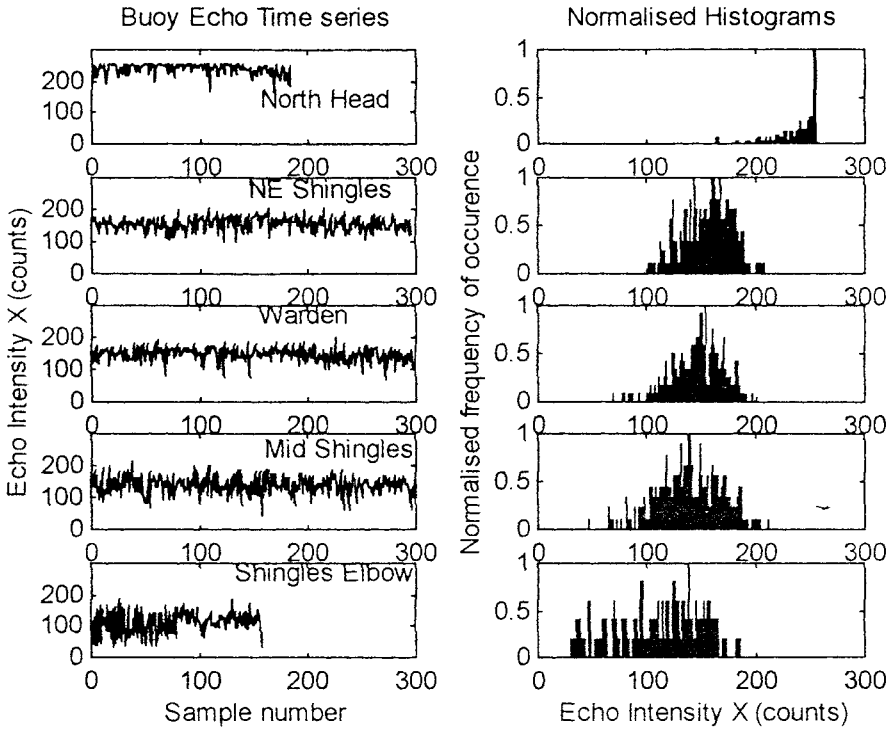

Figure 4. 15 - Time series and normalised histograms for the buoys on medium pulse

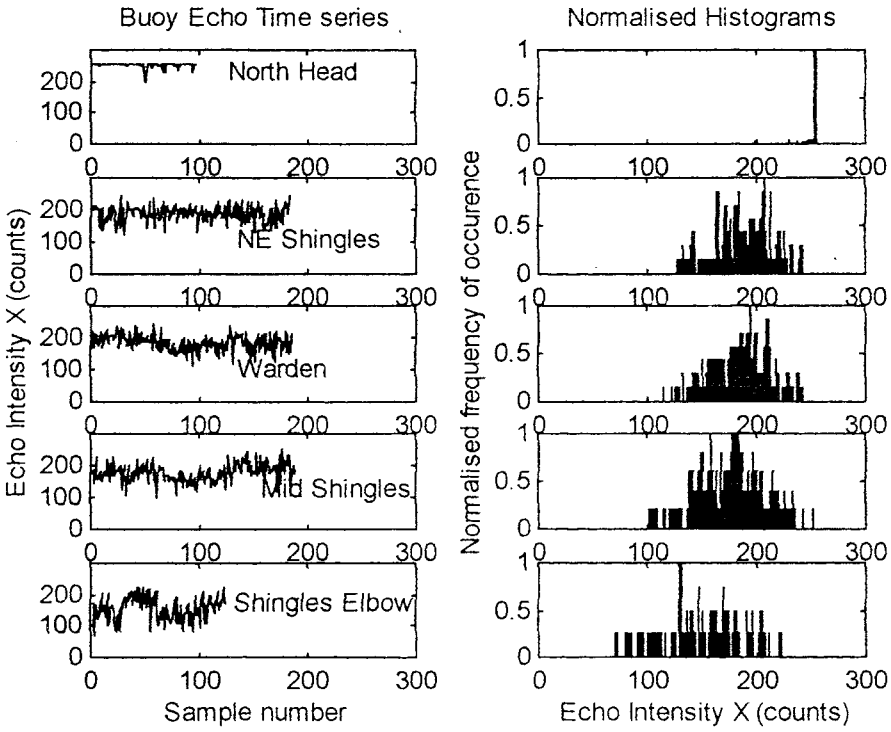

Figure 4. 16 - Time series and normalised histograms for the buoys on long pulse

Although the images in the time-series were collected closely in time, some sections show distinctly lower average intensity values. This was associated with the passage of ships in the nearby navigation channel which temporarily roughened the sea and increased the amplitude of the buoys motion. These lower intensity sections were consequently discarded from the statistical analysis.

The time-series were also purged of high echoes originating from passing ships collocated with the buoys. These unwanted echoes were identified using the images time-series to follow the tracks of passing traffic.

4.4.5 - Statistical analysis

As expected for a series of independent measurements, the histograms of the buoys intensity generally resemble a Gaussian distribution. The performances of the buoy-based radar reflectors are well defined in view of their extreme importance for navigation safety. Regular research is carried out by Trinity House Lighthouse Service to monitor and improve the performances of radar reflectors in various sea conditions. Their latest investigation (Ward and Vennings, 1989) reports a series of trials where the statistics of the NRCS for different types of radar reflectors are investigated in relation to their tilt angle. The 16 inch octahedral Speckter radar reflectors mounted on the buoys used here have been reported to produce echoes larger or equal to their nominal $10m^2$ radar cross section for 30% of the time for tilt angles between 0 and 10 degrees from the vertical.

Given the very calm conditions encountered during this experiment, the buoys inclination was assumed to be contained within this range of 0 to 10 degrees. The intensity corresponding to 30% of all echo occurrences in the cumulative histograms of the intensity time-series was chosen to represent the intensity associated with the 10 m^2 radar cross section. This intensity, $X_{30\%}$, was determined for each buoy and each pulse length setting and the results are summarised in Table 4.4.

Buoy name	Buoy range (m)	Short Pulse	Medium Pulse	Long Pulse
North Head	1020	156	251	255
NE Shingles	3120	99	168	206
Warden	3690	95	160	200
Mid Shingles	3742	97	155	193
Shingles Elbow	5430	68	138	169

Table 4. 4 - Upper 30 % occurrence intensity for the navigational buoys and three pulse length settings in the Absolute calibration experiment

4.4.6 - Validation of the intensity measurements

Validity of the North Head buoy measurements

The results for the closest buoy, North Head, are much lower than anticipated. Examination of the radar images revealed that the buoy is located exactly at the range where the receiver gain of the radar is known to dip. The "black line" is indeed clearly visible on Figure 4.16 at around 1000 meters range going through the echo from the North Head buoy and clearly reducing its intensity.

In order to rectify this, a set of radar images previously obtained for the area from a site 0.5 km to the east were utilised. As this deployment was concerned with imaging ocean waves, only short pulse images were available.

The position of the North Head buoy in the supplementary dataset lay outside the "black line" zone at a range of 1130 meters. Despite only 16 images being available, the 30% occurrence intensity value for North Head was confirmed to be higher and found equal to $X_{30\%} = 188$ on short pulse. Given the significant increase in $X_{30\%}$ for short pulse compared to the results in Table 4.4, the intensity $X_{30\%}$ for North Head on medium and long pulse images are expected to overrun the system's saturation level (i.e. $X_{30\%} > 255$).

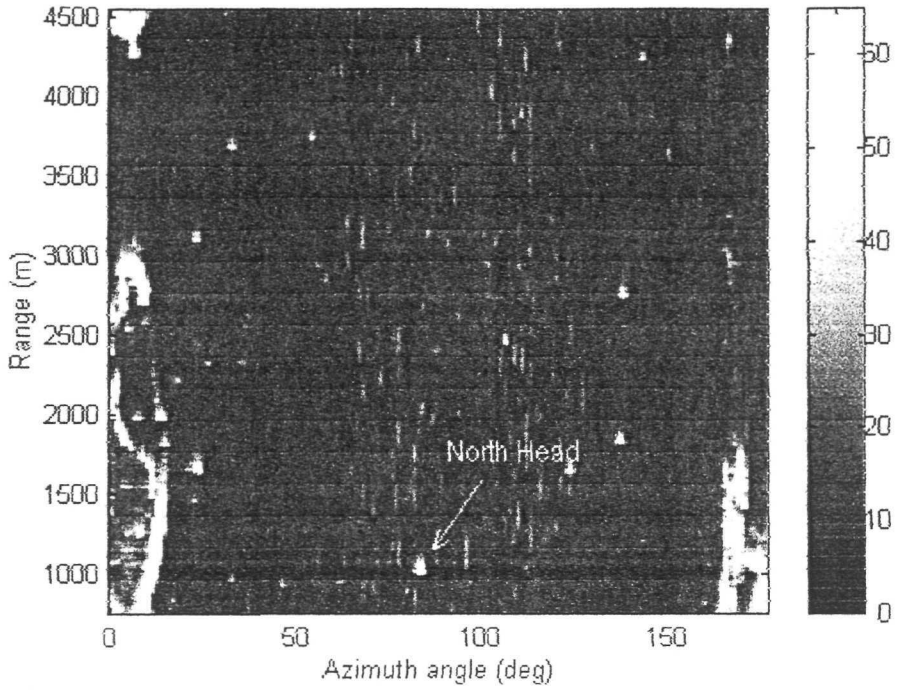

Figure 4. 17 - "Black line" at 1000 meters range related to a transitory drop in receiver gain at this time delay.

Validity of all the buoy intensity measurements

For point targets such as buoys, the shape and duration of the radar echo should be similar and of equal duration to that of the emitted pulse. The examination of transects across the buoys echoes revealed that their dimension in range is larger than the length of the emitted pulse, and that the rectangular shape of the emitted pulse is not preserved. Figure 4.18 represent transects across the NE Shingles buoy for short, medium and long pulse images.

The change in shape of the buoy echoes for increasing pulse length suggests the presence of a capacitor in the receiver which introduces a delay in the response of the system to sharp changes of echo intensity. This delay is particularly evident in the shape of the buoy echoes obtained on long pulse image. This problem is addressed in the next section.

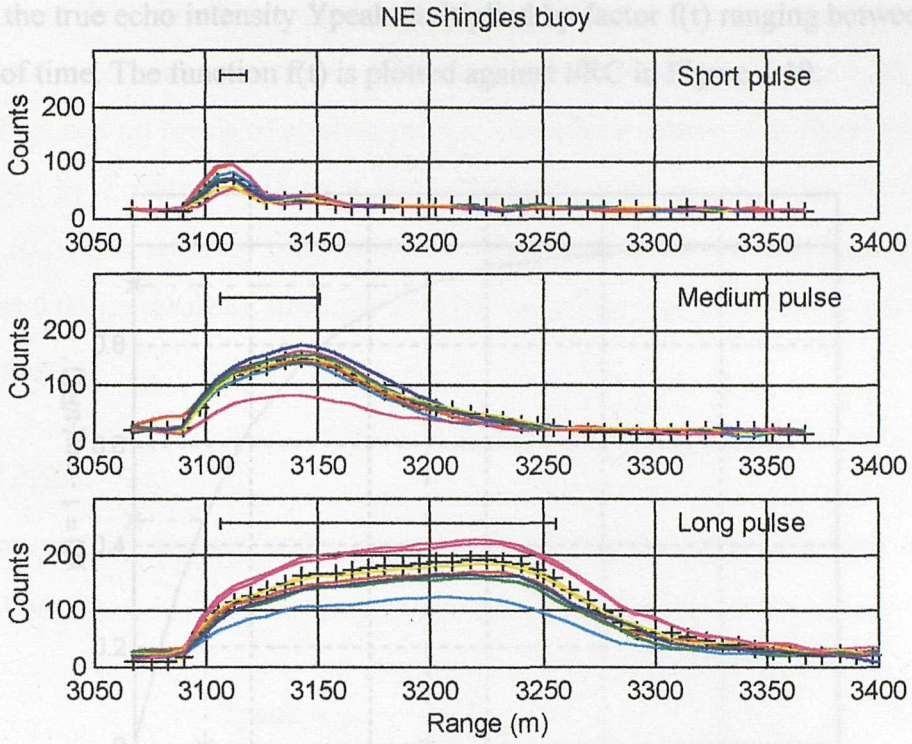

Figure 4. 18 - Transects across the NE Shingles buoy on short, medium and long pulse. Ticks along the transects represent the size of the digital pixel. The horizontal bar above the echoes gives the dimension of the emitted pulse.

4.4.7 - Receiver time factor correction

Receiver time response

The capacitor is characterised by a time constant which determines the delay between the beginning of the pulse rise and the point where the pulse finally stabilises. In first approximation, the response of a capacitor can be represented as an exponential function. From the shape of the buoys echoes, the echo intensity measured by the receiver can be described by:

$$Y(t) = Ypeak * \left(1 - \exp\left(-\frac{t}{RC}\right)\right) = Ypeak * f(t) \qquad \text{Equation 4. 38}$$

where Ypeak represents the maximum intensity of the echo after stabilisation and RC characterises the capacitor's time constant. The echo intensity Y(t) can be interpreted as the

product of the true echo intensity Ypeak multiplied by factor f(t) ranging between 0 and 1 as a function of time. The function f(t) is plotted against t/RC in Figure 4.19.

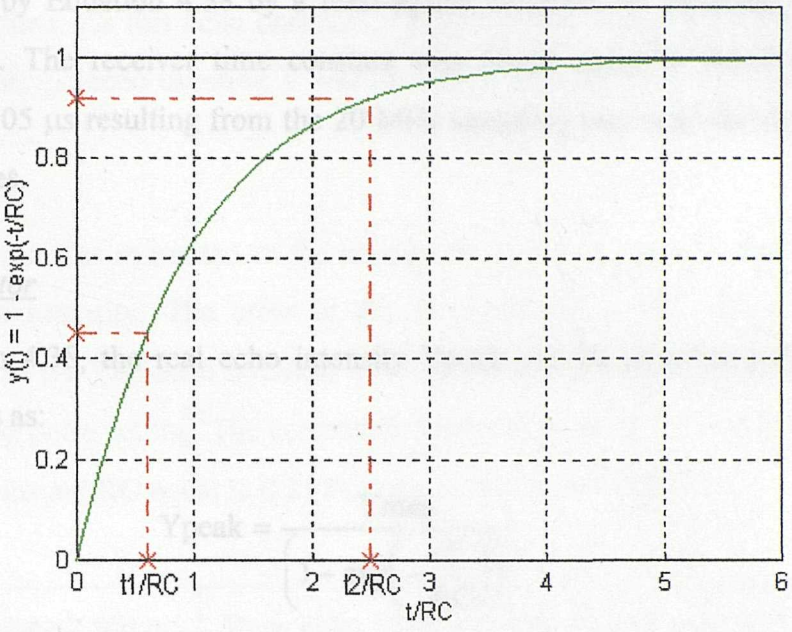

Figure 4. 19 - Time function in the measurements of buoy intensity

From Figure 4.19, the measured intensity for an echo depends strongly on its duration with respect to the receiver rise time. For example, echoes of duration equal to the receiver time constant produce intensity measurements reduced to approximately 60% of their maximum intensity.

The reduction of the measured intensity is significant for all echoes shorter than 3 times the time constant RC. Clearly this error increases exponentially as echoes get shorter and therefore unequally affects intensity measurements on different pulse length settings.

Experimental measurement of the receiver time constant

The time constant of the receiver was determined experimentally from the artificial images collected for the One-step internal calibration. The transition from receiver noise to the intensity of the injected pulse shown previously in Figure 4.10 represents the time response of the receiver.

The intensity of the azimuth-averaged transects in the artificial images were normalised with respect to the maximum intensity in each transect and plotted in Figure 4.20 for all pulse length settings and all levels of applied power. The whole dataset was fitted with a function f(t) described by Equation 4.38 by a least-square criterion on adjusting the time constant parameter RC. The receiver time constant was found equal to 0.217 μs with an error estimated at 0.05 μs resulting from the 20 MHz sampling rate used for the collection of the artificial images.

Correction factor

From Equation 4.38, the real echo intensity Ypeak can be calculated from the measured intensity Ymes as:

$$Ypeak = \frac{Ymes}{\left(1 - \exp\left(-\frac{T}{RC}\right)\right)} \qquad \text{Equation 4. 39}$$

where T represents the duration of the echo and RC is the receiver time constant.

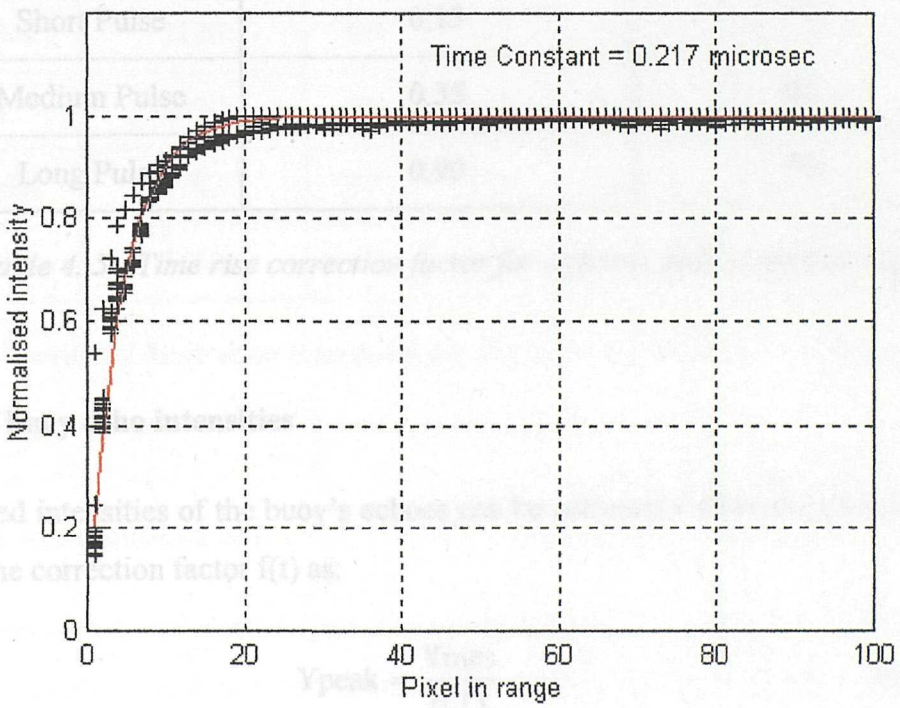

Figure 4. 20 - Normalised intensity transects from artificial images for various input power levels and pulse length settings.

The duration T of the buoy echo should theoretically be equal to the duration of the emitted pulse as measured during the internal calibration of the instrument. However, the echo duration from the buoys observed in the transects is longer than the emitted pulses, possibly due to multipathing. As this echo duration T plays an important role in the estimate of the correction factor, the echo duration T was measured directly from the transects across each buoy.

The echo duration was estimated as the time between the start of the intensity rise and the maximum echo intensity. The error in the measurement of the echo duration is again estimated at 0.05 μs. The echo duration was found to be constant in all images and for all buoys on a given pulse setting. The correction factor associated with each pulse setting and a receiver time constant RC equal to 0.217 μs are summarised in Table 4.5.

Pulse length setting	Buoy echo duration T (μs)	Correction factor f(T) in %
Short Pulse	0.15	50
Medium Pulse	0.35	80
Long Pulse	0.90	98

Table 4. 5 - Time rise correction factor for different pulse length settings

4.4.8 - New buoy echo intensities

The corrected intensities of the buoy's echoes can be calculated from the measured intensity Ymes and the correction factor f(t) as:

$$Ypeak = \frac{Ymes}{f(T)} \qquad \text{Equation 4. 40}$$

The conceptual echo intensities Ypeak and Ymes used so far were expressed with respect to a noise intensity which was assumed to be equal to 0. The average noise intensity in the radar

images however is offset to a value equal to 19 digital counts. The intensities Y(t) are therefore related to the intensity in the radar images y(t) by:

$$y(t) = Y(t) + 19 \qquad \text{Equation 4. 41}$$

The corrected echo intensities ypeak for the navigational buoys are therefore calculated from the intensities measured in the images ymes by:

$$ypeak = \frac{(ymes - 19)}{f(T)} + 19 \qquad \text{Equation 4. 42}$$

The new echo intensities are summarised in Table 4.6.

Buoy name	Buoy range (m)	Short Pulse		Medium Pulse		Long Pulse	
		Old	**New**	Old	**New**	Old	**New**
North Head	1020	188	**255**	255	**255**	255	**255**
NE Shingles	3120	99	**179**	168	**205**	206	**210**
Warden	3690	95	**171**	160	**195**	200	**204**
Mid Shingles	3742	97	**175**	155	**189**	193	**197**
Shingles Elbow	5430	68	**117**	138	**168**	169	**172**

Table 4. 6 - Corrected buoy echo intensities for the absolute calibration buoy echo intensity measurements

4.4.9 - Empirical definition of D'_t

The new intensities X are plotted against range as $10*\log10R_b^8$ in Figure 4.21 for all buoys and all pulse lengths. The data points for each pulse setting were fitted with a function of the form $10 \cdot \log_{10} R^8 = C'_t \cdot X + D'_t$ with C'_t equal to -0.223 and -0.201 for short and medium/long pulse respectively. The function was fitted by a least-mean square criterion on

adjusting the coefficient D'_t, ignoring the values of the nearest buoy which were always saturated. The values of D'_t for short, medium and long pulse were found equal to 323, 325.5 and 326.5.

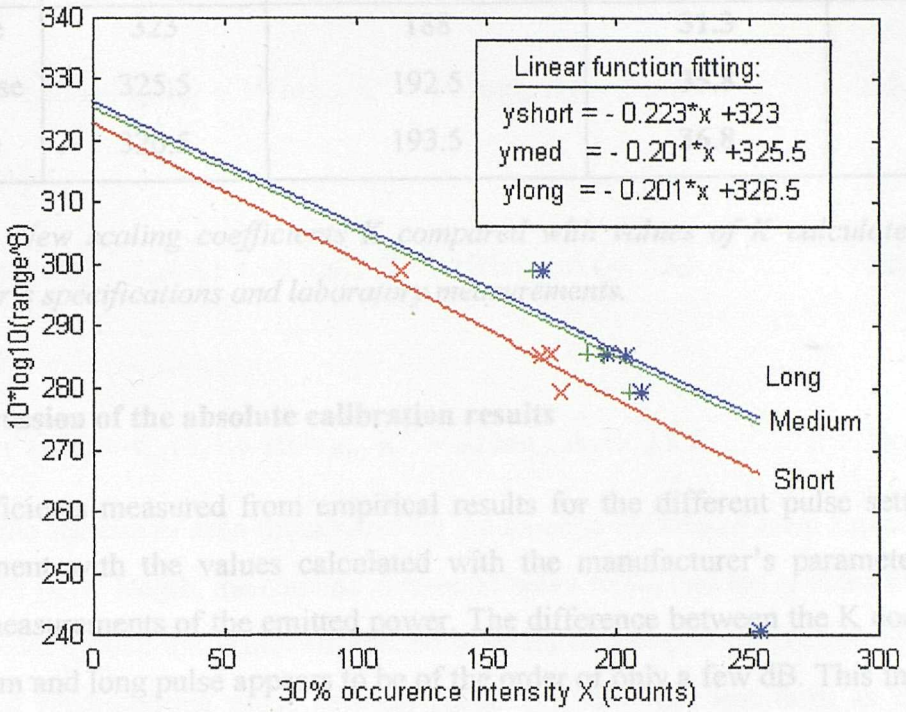

Figure 4. 21 - New buoy echo intensity plotted versus $10.\log_{10}R^8$ for the five navigational buoys. The slope of the fitted curves is determined from the internal calibration results and the least square fitting criterion in on the zero-crossing coefficient D'_t. The data points for the closest buoy reaching saturation are ignored for all pulse lengths.

4.4.10 - Results for the scaling factor K

Using equations 4.35 to 4.37, the intermediate coefficient K′ was calculated for short, medium and long pulse. The scaling factor K was then determined from the values of K′ using Equation 4.38 and values for the radiation wavelength λ equal to 0.032 m, the antenna height h_a equal to 7 meters and the target height h_t equal to 3 meters above the mean sea level. The numerical results of these calculations are summarised in Table 4.7.

Pulse length setting	Empirical coefficient D't	Intermediate scaling factor K' (dB)	**Scaling factor measured K (dB)**	Scaling factor calculated Kcalc (dB)
Short Pulse	323	188	**31.3**	31.6
Medium Pulse	325.5	192.5	**35.8**	33.1
Long Pulse	326.5	193.5	**36.8**	33.7

Table 4. 7 - New scaling coefficients K compared with values of K calculated from the manufacturer's specifications and laboratory measurements.

4.4.11 - Discussion of the absolute calibration results

The K coefficients measured from empirical results for the different pulse settings are in good agreement with the values calculated with the manufacturer's parameters and the laboratory measurements of the emitted power. The difference between the K coefficients at short, medium and long pulse appears to be of the order of only a few dB. This indicates that the difference in the emitted power levels at different pulse length plays only a minor role in the potential disparities in sea surface NRCS values on different settings.

Despite the good agreement with the calculated values, these empirical coefficients should not be used directly for the normalisation of the radar images as the accuracy of these results is debatable. The main source of concern may be readily identified as the 20% uncertainty attached to the estimation of the receiver time constant and a potential 30% error in the estimation of the buoys echo duration. Both parameters are known to be of critical importance for the final result and cast doubt on the reliability of this approach for an absolute calibration.

These results do nevertheless indicate that the technical specifications provided by the manufacturer give a realistic estimate of the system's capabilities. It is therefore the calculated values of the scaling factor K that will hereafter be used for the normalisation of the radar images.

4.5 - Normalisation equations

The final expression of the NRCS in dB for a pixel of intensity X in counts at a range R is:

on short pulse:

$$\sigma^0(\mathrm{dB}) = f_s(X) + 10\log_{10} R^4 - 10\log_{10} Ar - 31.6 \qquad \text{Equation 4. 43}$$

on medium pulse:

$$\sigma^0(\mathrm{dB}) = f_{ml}(X) + 10\log_{10} R^4 - 10\log_{10} Ar - 33.1 \qquad \text{Equation 4. 44}$$

on long pulse:

$$\sigma^0(\mathrm{dB}) = f_{ml}(X) + 10\log_{10} R^4 - 10\log_{10} Ar - 33.7 \qquad \text{Equation 4. 45}$$

where Ar is the sea clutter area illuminated by the antenna calculated from Equation 4.7 as a function of the pulse length, the antenna horizontal beam width and the antenna height, f_s and f_{ml} are the radar system amplification functions found by internal calibration of the system for short and medium/long pulse settings (page 67), and the last term is the absolute calibration scaling factor obtained by measurements on external calibrated targets.

4.6 - Conclusions

An internal calibration of the marine radar system has been implemented via a Two-step and a One-step method. The comparison of the two methods has highlighted the importance of treating the radar system as a whole rather than two independent parts. It was suggested that the processes occurring in the digital capture board may not be reproduced by combining the individual transfer functions of the marine radar and capture board. Although the One-step method imposes more challenging experimental conditions, the One-step amplification functions have been successfully validated by the radar data, while the results of the Two-step method were clearly unacceptable.

The accuracy of the absolute calibration is debatable mainly because of the poor temporal resolution used in the determination of the receiver time constant. There may also be concern

about the use of unsteady buoy-based radar reflectors and the statistical determination of the echo intensity associated with the target's radar cross section. The measurements were however obtained over several hundred samples and very calm conditions to reduce the risk of error. Also, the statistical analysis of the echo time-series made use of research results from a reliable source into the radar cross section performances of the reflectors used in this study.

It was nevertheless decided that the scaling factor values calculated from the manufacturer's specifications and the laboratory measurements should be used for the normalisation of radar images as they seemed to be the most reliable.

Chapter 5

Error Analysis and Radar System Performances

In this chapter, the various sources of error in the measurements of the Normalised Radar Cross Section (NRCS) are identified and estimated. The error analysis is performed theoretically as there was no opportunity for repeatable measurements over a static rough surface. At this stage, only the relative error can be estimated as the error attached to the absolute calibration presented in the previous chapter is difficult to quantify. Knowledge of the relative error alone does however allow the radar data quality and the system's performances to be defined.

5.1 - Error Analysis

The Normalised Radar Cross Section of the sea surface for a given pixel is a function of the pixel intensity X via its relation to the received power Pr, the transmitted power Pt, the maximum gain of the antenna G, the range of the pixel R, the height of the radar antenna h and the radiation wavelength λ. These variables are all defined with a greater or lesser error.

Measurement errors can be divided into two categories - systematic or constant errors and random errors. Systematic errors are caused by incorrect methods of measurement, unsuitable calibration procedures or overlooked secondary effects. They bias the results in a particular direction and can only be resolved by a critical analysis of the measuring technique and of the instrument. This type of error does not usually affect the internal consistency of the measurements, but becomes critical when comparing measurements with results from other experiments.

Random errors are caused by interference with the measurements so that the repeated measurements do not give exactly the same result. These errors are usually described statistically by a Gaussian probability distribution and characterised by the standard deviation of repeated measurements. The reliability of measurements affected by random errors can be improved by averaging over many realisations.

The following section classifies and quantifies the errors associated with each variable in the normalisation equations in view of estimating the total error in the NRCS. For random errors, the error is defined as the standard deviation of the normally distributed variable and is therefore expressed in the same unit as the variable. The calculation of the equivalent error in dB is carried out in the final section.

5.1.1 - Error in Pixel Intensity X

The error in the pixel intensity consists of the error in the measurement of the received power at the radar and of the digitisation error introduced during the determination of the instrument transfer function.

Instrumental noise

The error in the measured received power is the main source of error in the NRCS as it consists of the system's internal noise. This noise is mostly thermal in origin and is related to the agitation of electrons in the instrument. It is a random error and its statistics are directly related to the ambient temperature of the receiver (Wheeler, 1963). The random noise fluctuations are significantly reduced by averaging and the signal to noise power ratio is known to decrease as the inverse of the number of samples.

The thermal noise was determined experimentally for the present system owing to the ability of the digital capture board to collect radar images even without prior power transmission. In the absence of transmitted pulses, the measured echo consists of instrumental noise and ambient microwave noise. The natural level of energy at X band is generally considered negligible in comparison to the instrumental noise.

Thermal noise experiment

Experimental measurements of the thermal noise were carried out on several occasions characterised by different ambient temperatures to examine the stability of the system with temperature. On each occasion, a series of 64 images was collected for all three pulse settings using the optimum set-up registers. The resolution in range was maximised and 180 azimuth bins were collected. Since the noise measurement is independent of the heading of the antenna, the use of the Flywheel was not necessary.

Average and standard deviation images were produced for a variable number of antenna revolutions and for each time-series. The mean value of every average and standard deviation image was calculated over the whole image. The results for the three different temperature conditions are presented in Figure 5.1 for short, medium and long pulse. The mean noise level and noise standard deviation are expressed in digital counts (X) ranging between 0 and 255.

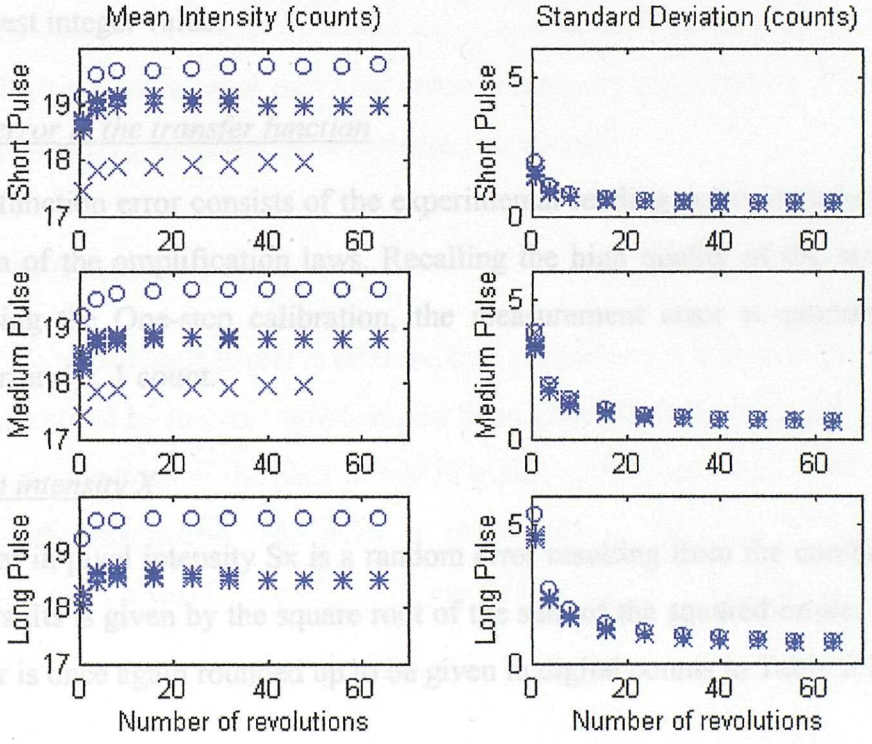

*Figure 5. 1 - Instrumental noise average and standard error against number of images for all pulse lengths and different temperatures (x =12 ° C, * = 15° C, o = 17 ° C)*

The average noise level is found to be largely independent of the number of revolutions and the pulse length but clearly depends on temperature. The 5 ^{o} C temperature difference between the datasets plotted as "x" and "o" in Figure 5.1 correspond to a 1.5 count increase in the mean noise level. The average noise level should rigorously be measured for every data capture session but can generally be assumed to be less than 25 counts in most environmental conditions.

The noise standard deviation (or standard error) is found to be independent of temperature but shows a clear $1/\sqrt{N}$ trend with N the number of images in the time series. The noise is larger for long and medium pulse settings which can probably be attributed to the smaller number of pulses integrated per azimuth bin (Azimuth Step) for longer pulse settings.

The thermal noise error for each pulse setting is summarised in Table 5.1 for a varying number of images. The decimal values of the noise average and standard error were rounded up to the closest integer value.

Digitisation error in the transfer function

The transfer function error consists of the experimental reading errors introduced during the determination of the amplification laws. Recalling the high quality of the artificial images obtained during the One-step calibration, the measurement error is estimated to be the digitisation error, i.e. 1 count.

Total error in intensity X

The total error in pixel intensity Sx is a random error resulting from the combination of two random errors. Its is given by the square root of the sum of the squared errors. The values of the total error is once again rounded up to be given in digital counts in Table 5.1.

Pulse setting	Number of revolutions	Thermal Noise Error in counts	Total Intensity Error Sx in counts
Short Pulse	$N < 4$	2	3
	$N \geq 4$	1	2
Medium Pulse	$N < 4$	4	5
	$4 \leq N < 16$	2	3
	$N \geq 16$	1	2
Long Pulse	$N < 4$	6	7
	$4 \leq N < 8$	3	4
	$8 \leq N < 24$	2	3
	$N \geq 24$	1	2

Table 5. 1 - Thermal noise error and total error in intensity expressed in digital counts as a function of pulse setting and number of antenna revolutions

5.1.2 - Error in transmitted power Pt

The value of the transmitted power is affected by a random error linked to the fluctuations in the magnetron caused by thermal agitation and fluctuations in the power supply. The random pulse to pulse fluctuations of the peak power Pt is one of the parameters used to characterise the quality of the magnetron. The pulse to pulse error is specified by the manufacturer (English Electronic Valves, Chelmsford, UK) to be less than ± 10% of the mean peak power at all pulse lengths.

Assuming that the ± 10% confidence criteria corresponds to 1 standard deviation in the probability distribution of the peak power, the standard deviation in Watts for single-pulse peak power values becomes:

$$S_1 = 0.1 * \overline{Pt} \qquad \text{Equation 5. 1}$$

where $\overline{Pt}$ is the mean peak power as measured during the internal calibration by Racal Decca. The mean peak power was then found equal to 7.0, 10.0 and 11.5 kW on short, medium and long pulse respectively.

The method of data collection with the digital capture board means that every pixel intensity obtained in a single rotation image is the result of integrating an Azimuth Step number "n_i" of successive pulses. The standard deviation of the peak power of n_i-integrated pulses is then known to be equal to the standard deviation of the single-pulse peak power distribution divided by the square-root of "n_i":

$$S_{n_i} = \frac{S_1}{\sqrt{n_i}} = \frac{0.1 * \overline{Pt}}{\sqrt{n_i}} \qquad \text{Equation 5. 2}$$

The same principle applies for the standard deviation of the peak power for radar images integrated over N antenna revolutions. The standard deviation or error in the peak power for images averaged over N rotations and an Azimuth Step value n_i then becomes:

$$S_{Pt} = \frac{S_{n_i}}{\sqrt{N}} = \frac{0.1 * \overline{Pt}}{\sqrt{N * n_i}} \qquad \text{Equation 5. 3}$$

The error S_{Pt} in the peak power in radar images can then be calculated for each pulse setting and a variable number of antenna revolutions. The Azimuth Step n_i is chosen according to the nominal capture parameters set-up for each pulse setting i.e. n_i equals 16, 8 and 4 for short, medium and long pulse respectively. The results for the error S_{Pt} are presented in Figure 5.2 as a function of the number of antenna rotations.

5.1.3 - Error in antenna gain G

The maximum antenna gain value used in the normalisation equations is taken from the technical specifications provided by the manufacturer. The error on the gain is a systematic error which is difficult to estimate. This absolute error should not affect the internal consistency of the data but may cause discrepancies when comparing results with

measurements obtained with other instruments. At this stage, this systematic error will be ignored as only the relative error is investigated.

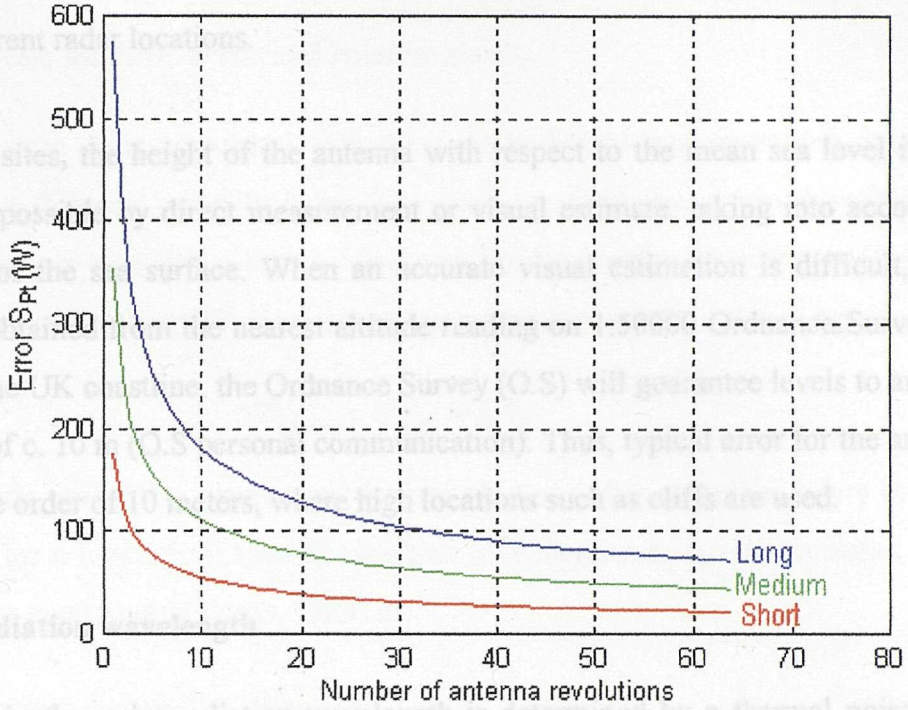

Figure 5. 2 - Error S_{Pt} in Watts in the peak power for short, medium and long pulse setting and a variable number of revolutions. The azimuth step ni is defined from the optimal set-up register.

5.1.4 - Error in range R

The error in the range of a fixed feature is a random error of very small magnitude determined by the accuracy in the measurement of the time delay between the emitted pulse and the reception of the echo. With the digitisation of the returned echoes, small variations in range can result in a feature appearing alternatively on two adjacent pixels. The error in range in a radar image can therefore be considered as a random error which magnitude is determined by the sampling rate used for the digitisation. Hence, the maximum error in range S_R in images collected with a sampling rate of 20 MHz is equal to 7.5 meters.

5.1.5 - Antenna height

The error on the antenna height is a systematic error that will bias all results for a given site in a particular direction. It is accountable for some of the discrepancies between results taken from different radar locations.

In coastal sites, the height of the antenna with respect to the mean sea level is determined whenever possible by direct measurement or visual estimate, taking into account any tidal elevation of the sea surface. When an accurate visual estimation is difficult, the antenna height is obtained from the nearest altitude reading on 1:50000 Ordnance Survey maps. For much of the UK coastline, the Ordnance Survey (O.S) will guarantee levels to an accuracy of the order of c. 10 m (O.S personal communication). Thus, typical error for the antenna height S_h is of the order of 10 meters, where high locations such as cliffs are used.

5.1.6 - Radiation wavelength

The error in the radar radiation wavelength is determined by a thermal noise error in the magnetron causing small frequency fluctuations and a larger systematic error linked to the variability in the mean frequency with temperature and humidity. The interval of frequency emitted by the radar is specified by the manufacturer as ranging from 9.380 to 9.440 GHz. The corresponding radiation wavelength is therefore defined as 0.0319 meters $\pm$ 6.10^{-5} meters. Given the very small magnitude of even the larger systematic error, the error in the radiation wavelength is assumed negligible.

5.2 - Radiometric resolution

From the error analysis of the variables in the normalisation equation, the total error is found to consist of random errors in the intensity X, the emitted peak power Pt and the range of the pixel R and a systematic error in the height of the antenna h. The error in radiation wavelength λ is assumed negligible and the absolute error in the antenna gain G is ignored. The dependence of NRCS on these variables can then be re-written as:

$$\sigma^0(\text{dB}) = W\left(X, Pt, R, h, \overline{\lambda}, \overline{G}\right) \qquad \text{Equation 5. 4}$$

where the overlined terms indicate the mean values of the variables.

5.2.1 - System intrinsic error and relative error

The systematic error associated with the antenna height intervenes only when comparing results from different radar locations. The system's relative error can therefore be separated into an intrinsic error δW_{intr} which represents the measurement accuracy within a given site and the systematic error δW_h issued from the uncertainty on the antenna height.

$$\delta W_{relative} = \delta W_{intr} + \delta W_h \qquad \text{Equation 5. 5}$$

The intrinsic error δW_{intr} represents the contributions of the random errors in X, Pt and R. The error for a function of several variables with random errors is calculated following the law of error combination (Boas, 1983) as:

$$\delta W_{intr} = \sqrt{\left(\delta W_X\right)^2 + \left(\delta W_{Pt}\right)^2 + \left(\delta W_R\right)^2} \qquad \text{Equation 5. 6}$$

where the terms δW_X, δW_{Pt}, ... represent the errors in dB associated with each variable.

5.2.2 - Errors δW_x in dB

In general terms, where W is a function of x and y, the errors can be estimated easily as:

$$\delta W_x = \left|W(\overline{x}, \overline{y}) - W(\overline{x} + S_x, \overline{y})\right| \qquad \text{Equation 5. 7}$$

$$\delta W_y = \left|W(\overline{x}, \overline{y}) - W(\overline{x}, \overline{y} + S_y)\right| \qquad \text{Equation 5. 8}$$

where the overlined quantities indicate the mean values and S_x and S_y are the standard deviations of the variables x and y. Here, the calculation of these errors is simplified by noting that the NRCS function of several variables can be expressed as:

$$\sigma^0(\text{dB}) = W_1(X) + W_2(Pt, \overline{\lambda}, \overline{G}) + W_3(R, h) \qquad \text{Equation 5. 9}$$

where

$$W_1(X) = f_{s,ml}(X) \qquad \text{Equation 5. 10}$$

is the amplification function for short or medium/long pulse setting obtained in the internal calibration

$$W_2(Pt,\lambda,G) = -10\cdot\log_{10}\left(\frac{Pt\cdot G^2\cdot\lambda^2}{(4\pi)^3}\right) \qquad \text{Equation 5. 11}$$

and

$$W_3(R,h) = 10\cdot\log_{10}R^4 - \underbrace{10\cdot\log_{10}\left(\frac{R^3\cdot\Phi(R,h,\overline{p})\cdot\overline{\omega}}{h}\right)}_{Ar_s} \qquad \text{Equation 5. 12}$$

with $\Phi(R,h)$ the vertical beam width given in Equation 4.6, $\overline{p}$ the physical dimension of the emitted pulse and $\overline{\omega}$ the antenna horizontal beam width. The errors for the NRCS random variables are therefore given as:

$$\delta W_X = \left|W_1(\overline{X}) - W_1(\overline{X}+S_X)\right| \qquad \text{Equation 5. 13}$$

$$\delta W_{Pt} = \left|W_2(\overline{Pt},\overline{\lambda},\overline{G}) - W_2(\overline{Pt}+S_{Pt},\overline{\lambda},\overline{G})\right| \qquad \text{Equation 5. 14}$$

$$\delta W_R = \left|W_3(\overline{R},\overline{h},\overline{p}) - W_3(\overline{R}+S_R,\overline{h},\overline{p})\right| \qquad \text{Equation 5. 15}$$

while the systematic error on height is expressed as:

$$\delta W_h = \left|W_3(\overline{R},\overline{h},\overline{p}) - W_3(\overline{R},\overline{h}+S_h,\overline{p})\right| \qquad \text{Equation 5. 16}$$

5.2.3 - Estimation of δW_X

The error δW_X in dB on the pixel intensity X in a radar image is a function of the number of antenna revolutions averaged and the pulse length setting via their influence on the error

standard deviation. The error in the intensity X also depends on the value of the mean intensity $\overline{X}$ as the amplification function f(X) is a non-linear function of X. This effect is illustrated in Figure 5.3 where the error bars indicate the magnitude of the error associated with a standard deviation S_X equal to 3 counts on short pulse setting.

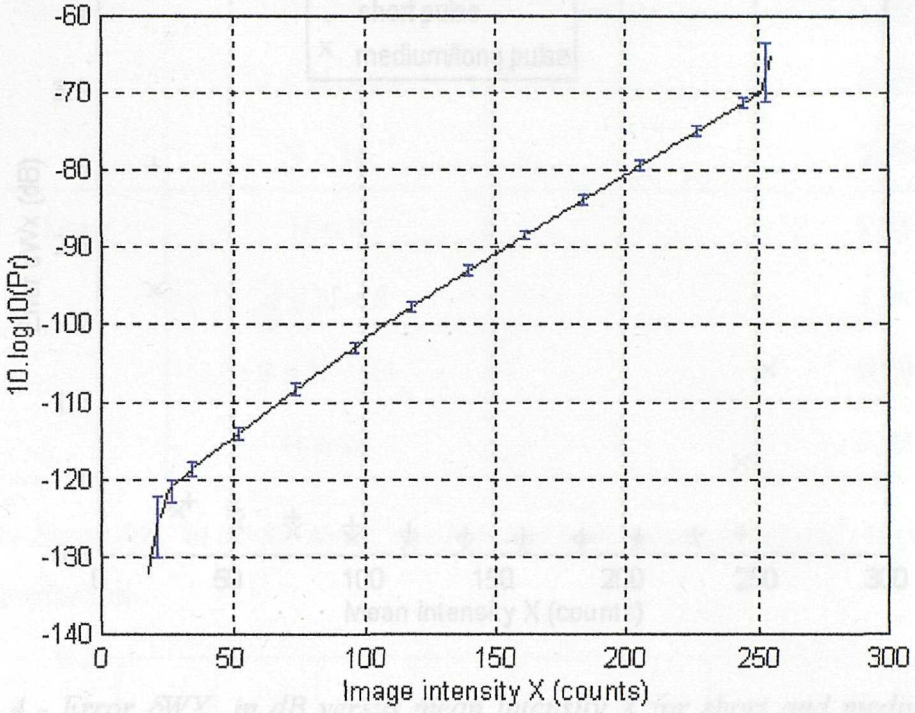

Figure 5. 3 - Error δW_X in dB versus $\overline{X}$ on short pulse setting for S_X = 3 counts.

The magnitude of the error δW_X versus $\overline{X}$ is shown more clearly on Figure 5.4 for the same standard deviation S_X = 3 counts at short and medium/long pulse. The error δW_X in dB becomes very large at low and high pixel intensity. The data in these zones are consequently highly unreliable and should not be used for quantitative measurements. For the largest part of the dynamic range however, the error is significantly lower and one can identify an intermediate range of intensities between 30 and 245 where the error is reasonably stable with intensity.

The representative error δW_X for a given number of antenna revolutions and pulse setting is chosen as the maximum of the error δW_X in the intermediate range of intensities. This error δW_X has been estimated for all combinations of number of antenna revolutions and pulse

length settings using the standard deviation given in Table 5.1. The results for δW_X are summarised in Table 5.2.

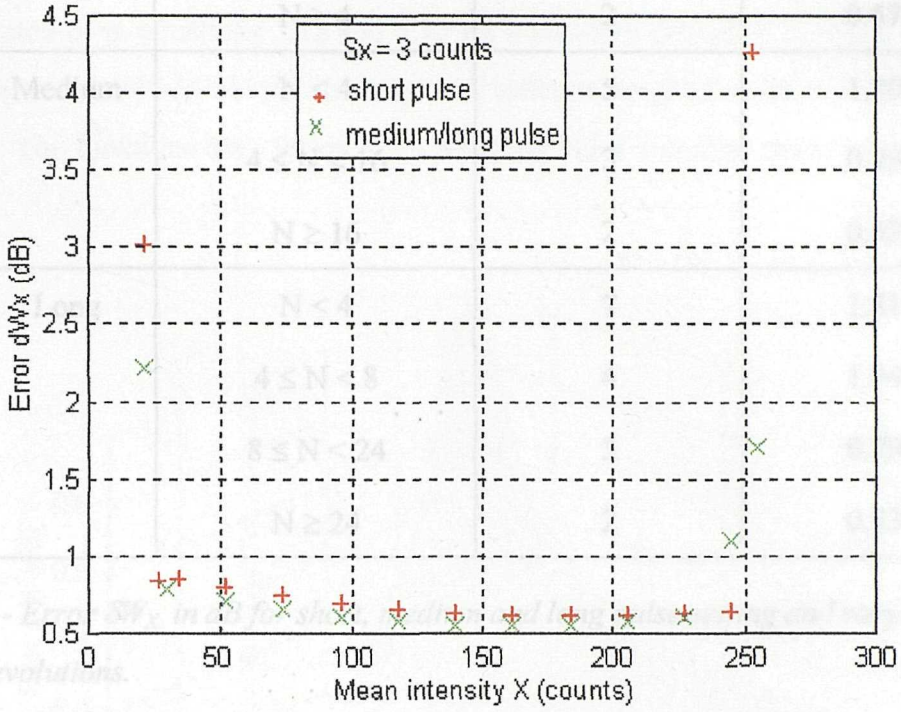

Figure 5. 4 - Error δWX in dB versus mean intensity X for short and medium/long pulse settings and a standard deviation SX = 3 counts.

5.2.4 - Estimation of δW_{pt}

The error δW_{pt} associated with the emitted peak power is estimated from the peak power standard deviation S_{pt} as a function of the number of antenna revolutions N and the pulse setting which determines the mean value of the peak power and the Azimuth Step n_i. Assuming the Azimuth Step to be chosen in accordance with the recommendations for the nominal capture parameters set-up, the error δW_{pt} is calculated using Equations 5.11 and 5.14. The mean value for the wavelength radiation λ is 0.0319 meters, and the gain G is taken equal to 28 dB. The results for δW_{pt} are plotted in Figure 5.5.

Pulse setting	Number of revolutions N	Standard deviation S_X (counts)	Random error in X δW_X (dB)
Short	$N < 4$	3	0.85
	$N \geq 4$	2	0.57
Medium	$N < 4$	5	1.30
	$4 \leq N < 16$	3	0.79
	$N \geq 16$	2	0.53
Long	$N < 4$	7	1.81
	$4 \leq N < 8$	4	1.04
	$8 \leq N < 24$	3	0.79
	$N \geq 24$	2	0.53

Table 5. 2 - Error δW_X in dB for short, medium and long pulse setting and varying number of antenna revolutions.

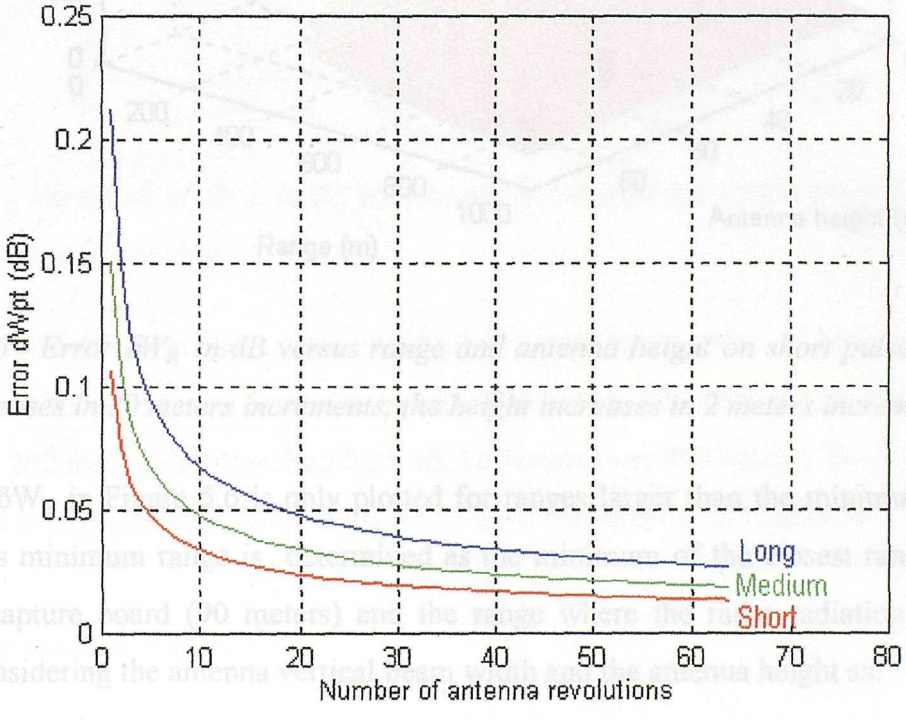

Figure 5. 5 - Error δW_{Pt} in dB for short, medium and long pulse setting and increasing number of antenna revolutions.

5.2.5 - Estimation of δW_R

The function $W_3(R,h)$ is a non-linear function of range. The error δW_R therefore depends on the mean value $\overline{R}$ as well as being a function of the mean antenna height $\overline{h}$. The error δW_R was calculated from equations 5.12 and 5.15 for a standard deviation S_R equal to 7.5 meters. The results are plotted in 3D versus range and antenna height for the short pulse setting in Figure 5.6. The functions δW_R for medium and long pulse a similar shape at a slightly lower magnitude.

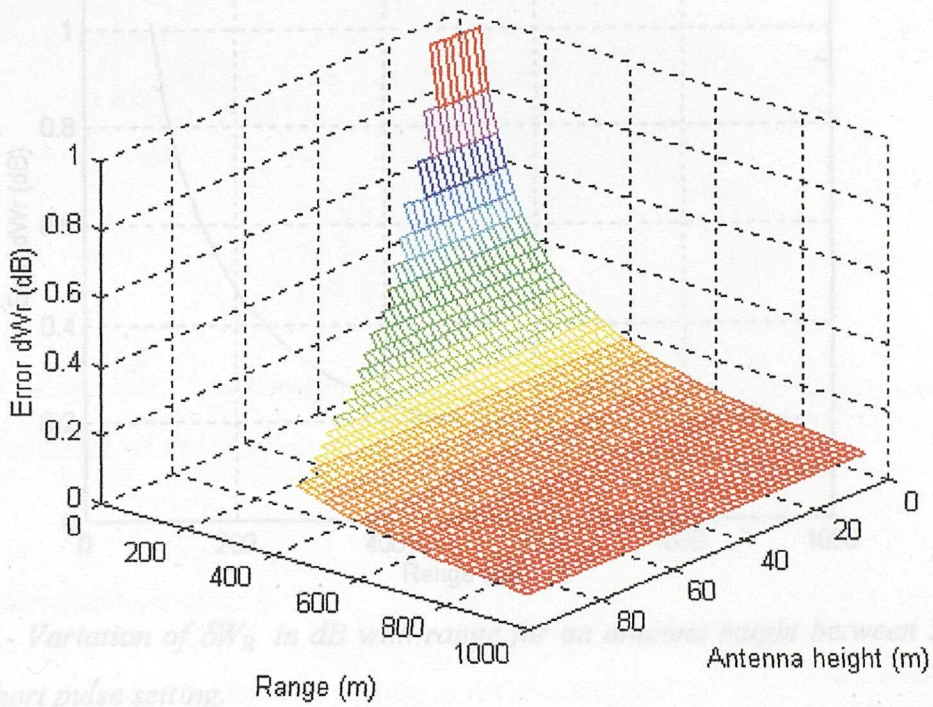

Figure 5. 6 - Error δW_R in dB versus range and antenna height on short pulse setting. The range increases in 20 meters increments, the height increases in 2 meters increments.

The error δW_R in Figure 5.6 is only plotted for ranges larger than the minimum detectable range. This minimum range is determined as the minimum of the closest range selectable with the capture board (90 meters) and the range where the radar radiation hits the sea surface considering the antenna vertical beam width and the antenna height as:

$$R_{min} = \min\left(90, \frac{h}{\sin(12.5^{o})}\right) \qquad \text{Equation 5. 17}$$

In Figure 5.6, the error δW_R drops rapidly with increasing range and increasing antenna height. However, the apparent decrease in δW_R with antenna height within the 200 m range area is linked entirely to the increase in R_{min} with increasing antenna height. Hence, the error δW_R is independent of antenna height and the error δW_R can then be plotted against range only by taking the cross section of the plot in Figure 5.6 along the range axis. The variation of δW_R with range for the short pulse setting is shown in Figure 5.7.

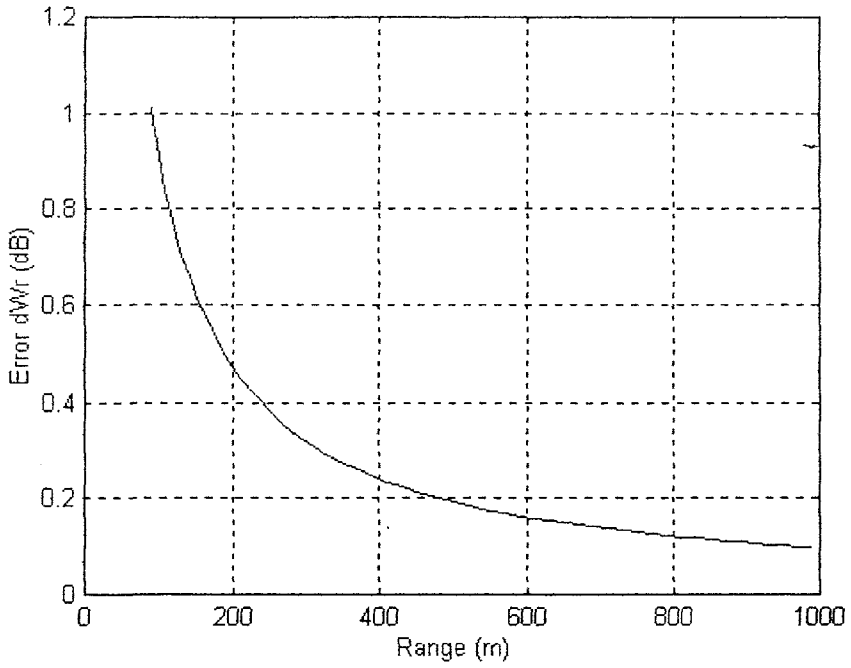

Figure 5. 7 - Variation of δW_R in dB with range for an antenna height between 5 and 100 meters on short pulse setting.

Hence, the error δW_R on short pulse setting has a maximum value of just over 1 dB for ranges under 100 meters and decreases rapidly with range. The error is less than 0.5 dB for ranges over 200 meters and less than 0.25 dB for ranges over 400 meters. Error estimates on medium and long pulse settings are found to be of the same order of magnitude.

5.2.6 - Estimation of δW_h

The error δW_h is a function of range, antenna height and pulse length. It was calculated from the expressions in equations 5.12 and 5.16 and plotted in 3D in the same manner as δW_R. The results for δW_h are shown for short pulse in Figure 5.8. The error δW_h for medium and

long pulse shows the same shape at a slightly lower magnitude.

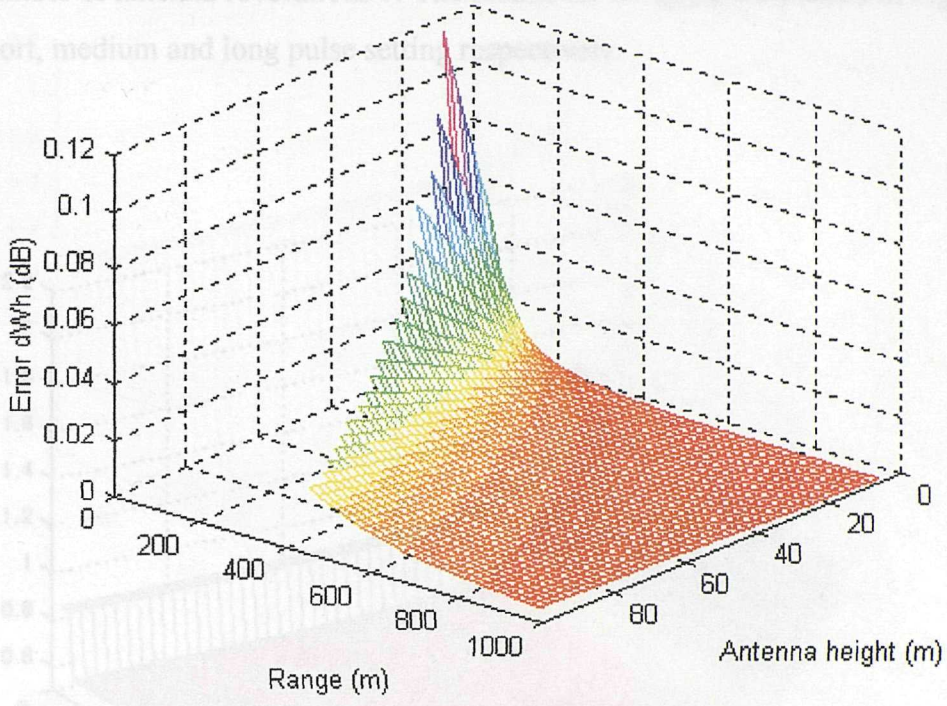

Figure 5. 8 - Error δW_h in dB against range and antenna height. The range increases in 20 meters increments and the antenna height increases in 2 meters increments.

5.2.7 - Total relative error

From equation 5.5 and 5.6, the total relative error is calculated as:

$$\delta W_{relative} = \sqrt{(\delta W_X)^2 + (\delta W_{Pt})^2 + (\delta W_R)^2} + \delta W_h \qquad \text{Equation 5. 18}$$

The errors δW_X and δW_{Pt} are functions of the pulse setting and the number of antenna revolutions, δW_R is a function of range and the pulse setting and δW_h is a function of range, pulse setting and antenna height. The variation of δW_R and δW_h with range can be represented by the transect across their maximum value with antenna height, thus eliminating the need to consider the effect of antenna height in the final error.

The total relative error can therefore be calculated for each pulse setting against range and a variable number of antenna revolutions N The results for $\delta W_{relative}$ are plotted in Figure 5.9 to 5.11 for short, medium and long pulse setting respectively.

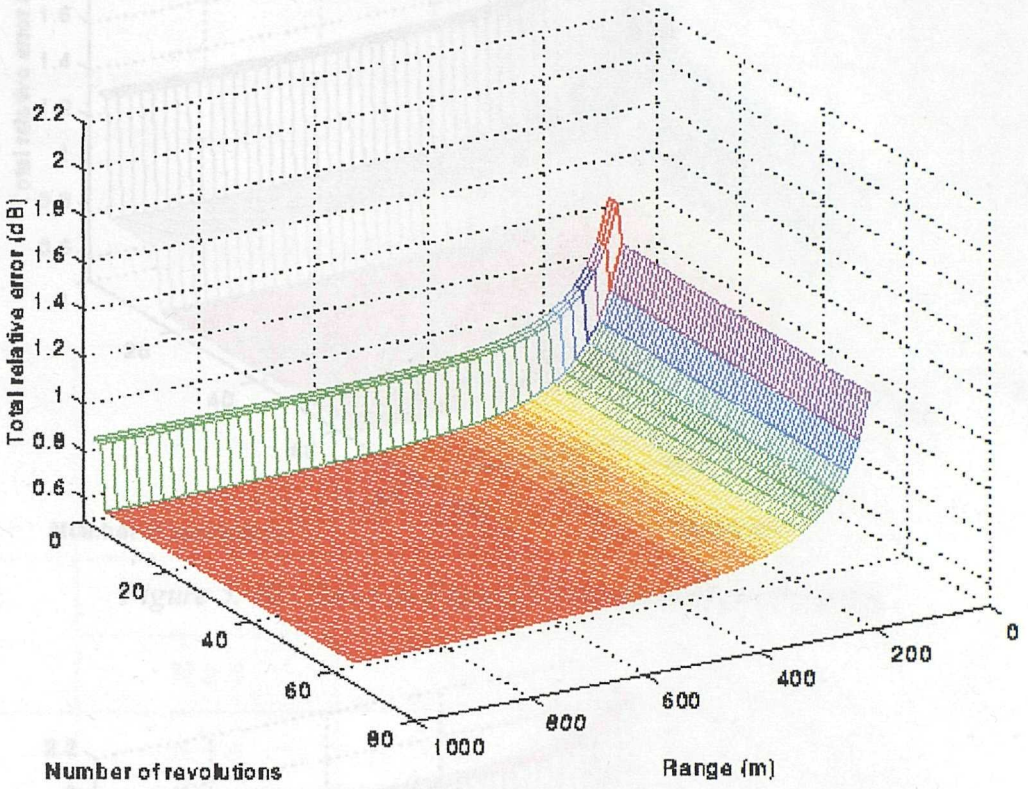

Figure 5. 9 - Total relative error in dB versus range and number of antenna revolutions on short pulse setting

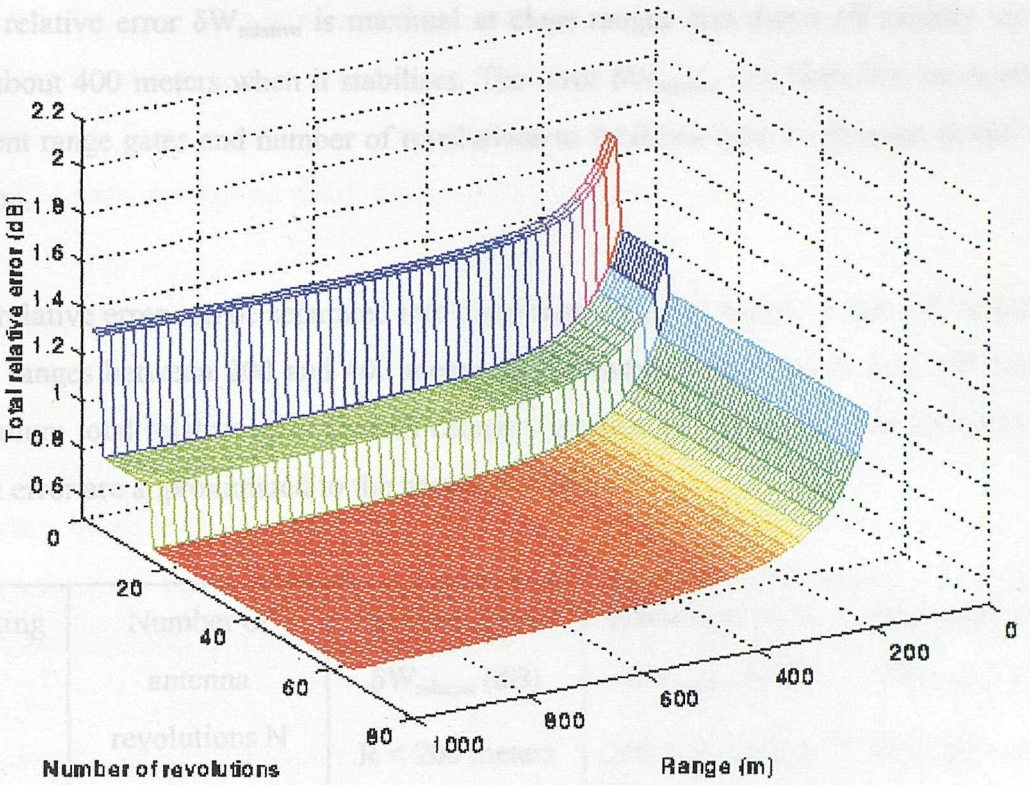

Figure 5. 10 - Same as Figure 5.9 on medium pulse setting

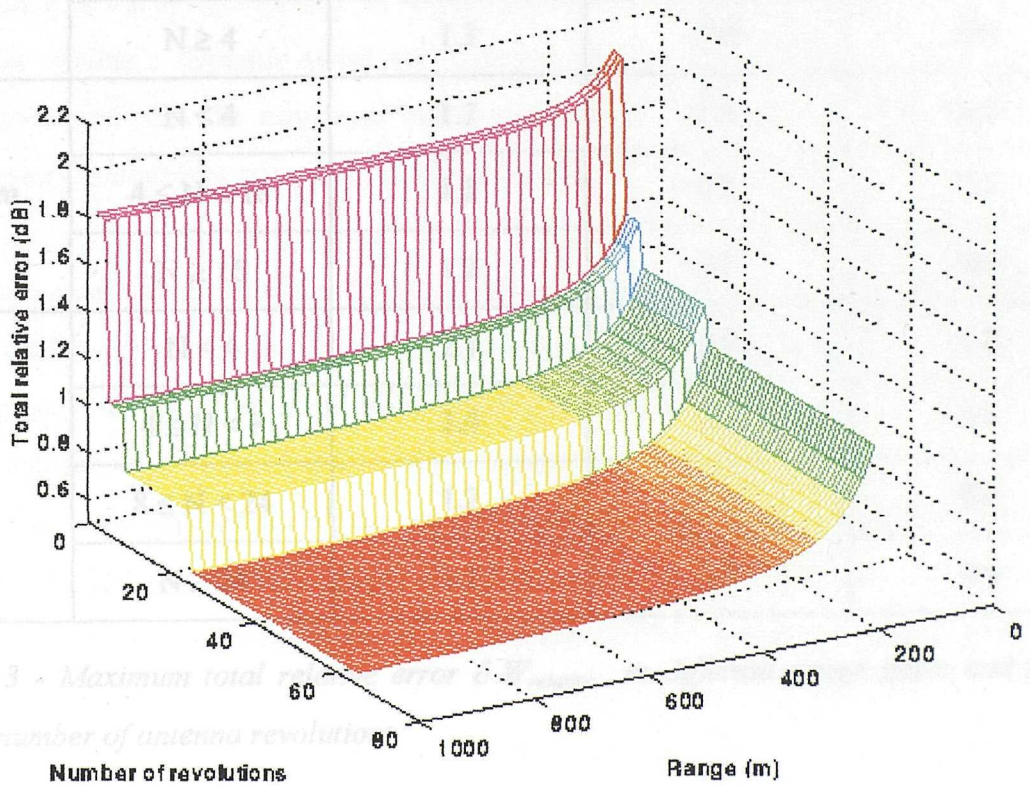

Figure 5. 11 - Same as Figure 5.9 on long pulse setting

The total relative error $\delta W_{relative}$ is maximal at close ranges and drops off rapidly up to a range of about 400 meters when it stabilises. The error $\delta W_{relative}$ can therefore be estimated for different range gates and number of revolutions to facilitate future reference to the error information.

The total relative error can be separated into three range regions: ranges within 200 meters of the radar, ranges between 200 and 400 meters of the radar, ranges larger than 400 meters. The maximum total relative error in each category is given in Table 5.3. The values for the maximum error are approximated to the nearest 0.1 dB.

Pulse setting	Number of antenna revolutions N	Maximum error $\delta W_{relative}$ (dB) R < 200 meters	Maximum error $\delta W_{relative}$ (dB) 200 ≤ R < 400 m	**Maximum error $\delta W_{relative}$ (dB) R ≥ 400 meters**
Short	N < 4	1.5	1	**0.9**
	N ≥ 4	1.3	0.8	**0.6**
Medium	N < 4	1.7	1.4	**1.3**
	4 ≤ N < 16	1.3	0.9	**0.8**
	N ≥ 16	1.2	0.7	**0.6**
Long	N < 4	2.1	1.9	**1.8**
	4 ≤ N < 8	1.4	1.2	**1.1**
	8 ≤ N < 24	1.2	0.9	**0.8**
	N ≥ 24	1.1	0.7	**0.6**

Table 5. 3 - Maximum total relative error $\delta W_{relative}$ in different range gates and for a variable number of antenna revolutions

The error $\delta W_{relative}$ in the category of ranges larger than 400 meters is representative of the radiometric resolution over at least 90% of standard-sized radar images collected with the

capture board. The error over most of the radar images extent is therefore better than 1 dB on all pulse length settings given more or less averaging. It is clear that the radiometric resolution benefits from averaging as it can be reduced down to 0.6 dB by averaging as little as 4, 16 and 24 radar images on short, medium and long pulse respectively.

5.3 - Dynamic range

The radiometric dynamic range of the system defines the interval of measurable NRCS values. Its lower limit, known as the Minimum Detectable Signal (MDS), corresponds to the radar system's noise level and determines the lowest measurable value of NRCS. The upper limit of the dynamic range is determined by the data capture board's saturation level and similarly determines the saturation equivalent NRCS (SAT).

From the results of the instrumental noise error in the previous paragraph, the error associated with intensities in the near-noise and near-saturation domain has proven too large to be included in the system's range of reliable measuring capabilities. The lower and upper limit of the system's dynamic range are therefore chosen to coincide with the intensity interval associated with the minimum instrumental noise. The dynamic range in terms of image intensity is therefore comprised between 30 and 245 digital counts.

The system's minimum detectable NRCS (or MDS) is calculated by introducing the intensity value X equal to 30 in the normalisation equations 4.43 to 4.45 for short, medium and long pulse. Similarly, the maximum detectable NRCS (or SAT) is calculated in the same manner with an intensity value X equal to 245. The antenna height value was chosen between 5 and 100 meters and had little effect on the calculation of the MDS and the SAT. The choice of the antenna height is therefore irrelevant. The results for the MDS and the saturation equivalent NRCS are presented versus range in Figure 5.12 as the solid and the dotted lines respectively.

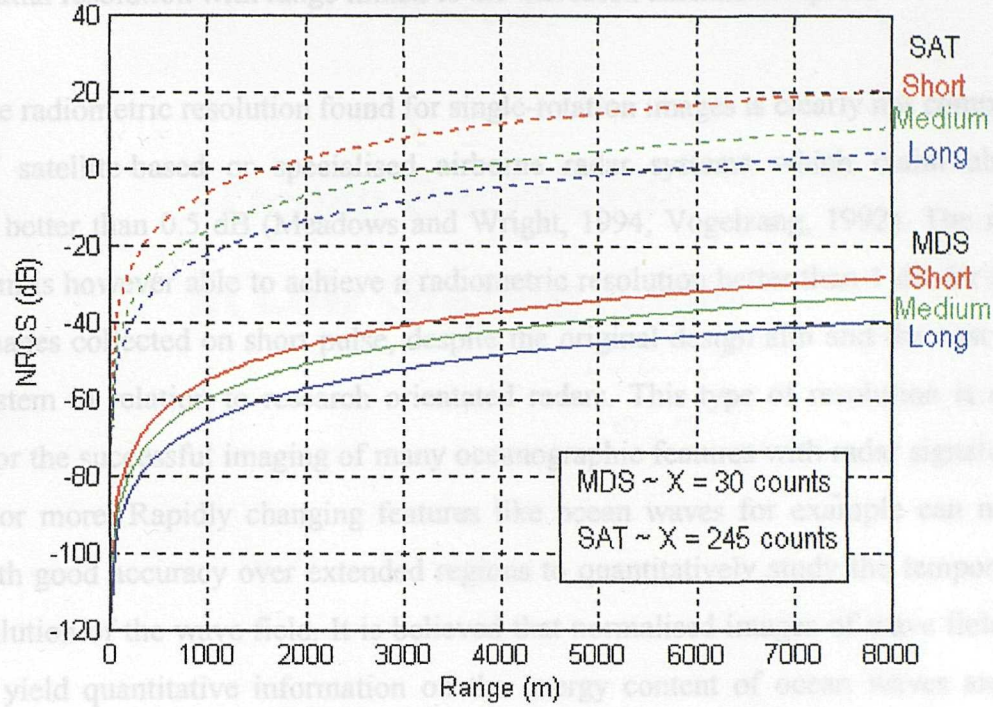

Figure 5. 12 - Minimum Detectable Signal and SATuration NRCS in dB on short (red), medium(green) and long(blue) pulse setting.

5.4 - Discussion

Being specifically designed for the effective detection of targets at far ranges, the dynamic range of the marine radar system is found to be well adapted to low-intensity backscatter measurements. Previous studies of grazing angle backscatter at X-band and HH polarisation have reported sea clutter NRCS to range between - 60 and - 10 dB under various environmental conditions (Daley et al, 1971, Trizna, 1985). The dynamic range of the radar system largely covers this range of NRCS values and therefore constitutes an ideal tool for the study of the weak ocean NRCS expected at near-horizontal incidence angles.

The Minimum Detectable Signal (MDS) on medium and long pulse setting is found lower than that on short pulse setting by 5 to 10 dB. Longer pulse settings are therefore better adapted to measuring NRCS in conditions of low backscatter conditions. Hence, some features may not be detectable on short pulse setting but be clearly visible on medium or long pulse images. This increased detection capability is however counterbalanced by a loss in the

images' spatial resolution with range linked to the increased antenna footprint.

The relative radiometric resolution found for single-rotation images is clearly not comparable to that of satellite-based or specialised airborne radar systems which claim absolute accuracies better than 0.5 dB (Meadows and Wright, 1994, Vogelzang, 1992). The marine radar system is however able to achieve a radiometric resolution better than 1 dB for single-rotation images collected on short pulse, despite the original design aim and the cost of the X-band system in relation to research orientated radars. This type of resolution is clearly adequate for the successful imaging of many oceanographic features with radar signatures of a few dB or more. Rapidly changing features like ocean waves for example can now be imaged with good accuracy over extended regions to quantitatively study the temporal and spatial evolution of the wave field. It is believed that normalised images of wave fields will ultimately yield quantitative information on the energy content of ocean waves and thus further our understanding on wave generation and evolution.

Where the detection of non-transitory oceanographic processes is concerned, the radiometric resolution of the marine radar system can be further improved by averaging over several antenna rotations down to a typical accuracy of 0.6 dB. Numerous medium (c. 1 hour) to long-term (c. days) oceanographic features can therefore be studied with very good accuracy and the evolution of their NRCS can be quantitatively linked to changes in environmental conditions. The relationship with environmental circumstances and the capabilities of the marine radar system for oceanographic applications are further investigated in Part 2 of this thesis.

Part 2

Ocean Backscatter at Low Grazing Angle

Chapter 6

Electromagnetic Scattering from a Rough Ocean Surface

In this chapter, the existing theories and models aimed at predicting the scattering of microwave radiation by the sea surface are examined. The basic theory of scattering from a perfectly smooth surface is briefly recalled before considering the problem of scattering from a random rough surface. The various radar backscatter models available to date are presented and examined in view of their applicability to scattering at low grazing angles. Finally, the particular issue of the origin of radar backscatter from the sea surface at grazing angles is examined.

6.1 - Scattering from a perfectly smooth surface

6.1.1 - Fresnel laws

An electromagnetic radiation impinging on a perfectly smooth interface must satisfy the boundary conditions derived from the Maxwell equations applied at the interface. In general, the incident electromagnetic (e.m.) wave is partly reflected and partly transmitted through the interface. The boundary conditions establish relationships between the electromagnetic fields and the properties of the media on either side of the interface.

The amplitude of the electric and magnetic fields reflected and transmitted at the interface are commonly expressed in terms of the Fresnel reflection and transmission coefficients which are defined as:

$$R = \frac{E_r}{E_i} \quad \text{and} \quad T = \frac{E_t}{E_i} \qquad \text{Equation 6. 1}$$

where Ei, Er and Et are the amplitudes of the incident, reflected and transmitted electric fields respectively. These coefficients are functions of the intrinsic impedances of the media on either side of the interface, the angle of incidence and the polarisation of the incident radiation. The reflection coefficient for horizontal and vertical polarisation are given by:

$$R_H(\theta) = -\frac{Z_1 / Z_2 \cos\theta_1 - \left[1-(k_1 / k_2)^2 \sin^2\theta_1\right]^{1/2}}{Z_1 / Z_2 \cos\theta_1 + \left[1-(k_1 / k_2)^2 \sin^2\theta_1\right]^{1/2}} \qquad \text{Equation 6. 2}$$

and

$$R_V(\theta) = \frac{Z_2 / Z_1 \cos\theta_1 - \left[1-(k_1 / k_2)^2 \sin^2\theta_1\right]^{1/2}}{Z_2 / Z_1 \cos\theta_1 + \left[1-(k_1 / k_2)^2 \sin^2\theta_1\right]^{1/2}} \qquad \text{Equation 6. 3}$$

where Z_1, Z_2 are the intrinsic impedances of the media and k_1, k_2 are the wave numbers of the radiation in the two media.

6.1.2 - Fresnel reflection coefficients for the sea surface

At microwave frequencies, the reflection coefficients for the sea surface behave very differently with incidence angle depending on the radiation's polarisation. Figure 6.1 shows the Fresnel coefficients at 10 GHz for both polarisations as a function of incidence angle.

At normal incidence ($\theta = 0$), the reflection coefficients R_H and R_V are equal and the polarisation of the e.m. radiation is irrelevant. For increasing incidence angles however, the reflection coefficient of sea water for horizontal polarisation increases steadily towards unity while the reflection coefficient for vertical polarisation decreases rapidly towards a minimum value near 83 degrees before rising rapidly to reach unity at 90 degree incidence from the vertical. The minimum value of R_V is called the Brewster angle and occurs only on vertical polarisation. Whenever microwave energy is reflected from the sea surface at small grazing

angles, the properties of the radar backscatter can be expected to behave quite differently depending on polarisation.

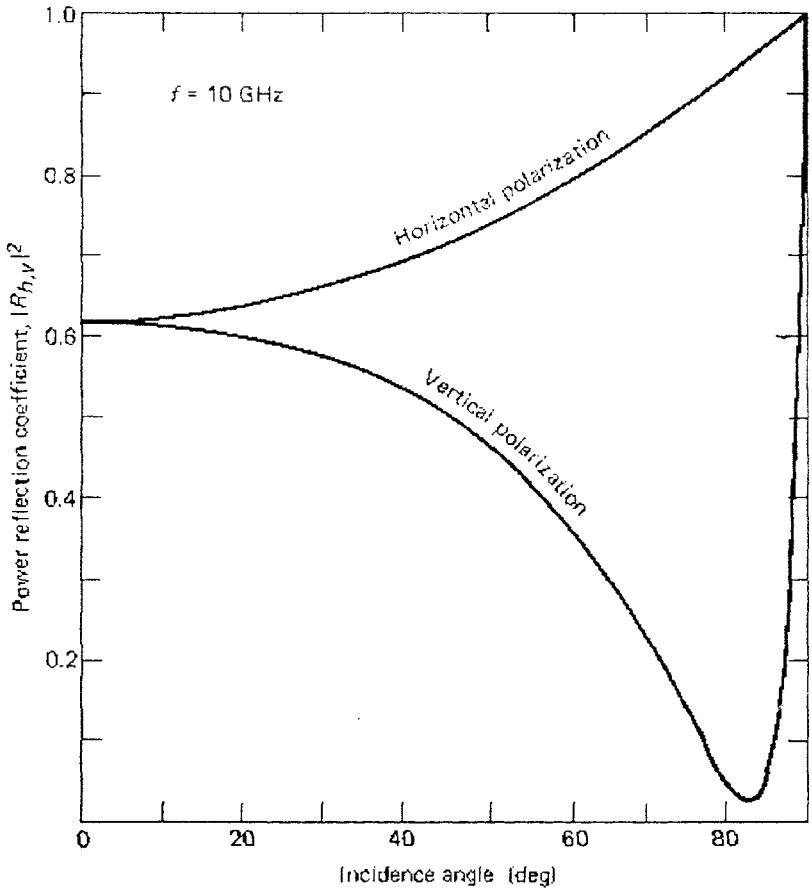

Figure 6. 1 - Squares of the Fresnel coefficients versus incidence angle for HH and VV polarisation at 10 GHz (from Apel, 1987)

6.2 - Scattering from a random rough surface

6.2.1 - Integral Equations

Given the existence of adequate boundary conditions, the theoretical expression of electromagnetic scattering from a rough surface is summarised by the Stratton and Chu Integral Equations (Beckmann and Spizzichino, 1963, Ogilvy, 1991):

$$\vec{E}_s = -\oiint_S \left[i\omega\mu_o \left(\vec{n} \times \vec{H}\right) G + \left(\vec{n} \times \vec{E}\right) \times \nabla G + \left(\vec{n} \cdot \vec{E}\right) \nabla G \right] dS \qquad \text{Equation 6. 4}$$

$$\vec{H}_s = \oiint_S \left[i\omega\varepsilon_o \left(\vec{n} \times \vec{E}\right) G - \left(\vec{n} \times \vec{H}\right) \times \nabla G - \left(\vec{n} \cdot H\right) \nabla G \right] dS \qquad \text{Equation 6. 5}$$

where $G = \exp(ikR)/4\pi R$ is the Green's function of free space, R is the range of the scattering point and $\vec{n}$ is the positive unit vector normal to the surface.

6.2.2 - Solutions to the Integral Equations

The resolution of this complex set of equations is difficult. Exact analytical solutions can only be obtained for simple bodies where a system of co-ordinates can be found for which the body surface coincides with one of the co-ordinates (i.e. a cube, sphere or infinite cylinder). This method of resolution has therefore not been able to yield tractable analytical solutions for the evaluation of scattering from complex objects like the rough sea surface.

The Integral Equations may be solved numerically. The emergence of high speed computers has enabled the implementation of integral equation matrix methods (Method of Moments) which estimate the scattered field by computing the current distribution on the surface (Knott and Shaeffer, 1985). When applied to the sea surface, the method requires an accurate description of the water profile. The Method of Moments has been applied to a rough water surface by Kwoh and Lake (1985) using laser-determined water profiles. The predictions were in good agreement with coincident high-resolution microwave radar measurements.

Numerical methods are however limited to small surfaces with respect to the radar wavelength. Typically, the surface must be sampled five to ten times per wavelength (Knott and Shaeffer, 1985). In the case of centimetric radar waves, should the method be applied to surfaces typical of the size of imaging radar cells, this level of sampling would rapidly produce matrices too large for computation.

6.3 - Approximate solutions and radar backscatter models

Approximate solutions to the Integral Equations can be found by using simplifying hypotheses on the roughness scale of the surface with respect to the radar wavelength. So far, approximate methods of resolution have been the most successful way of producing tractable radar backscatter models. Several models have thus emerged for the different cases of surface roughness scale in relation to the wavelength of the incident electromagnetic radiation.

6.3.1 - Sea surface roughness scale large compared to the radar wavelength

This approximation is applicable to surfaces with gentle undulations which average roughness scale is large compared with the electromagnetic wavelength. For statistical surfaces, the correlation length l must be larger than the radar wavelength and the surface's rms height H must be small enough so that the average radius of curvature is larger than the electromagnetic wavelength (Ulaby *et al.*, 1982). This means that even surfaces with large standards deviations (i.e. with high amplitude components) are acceptable if their correlation length is large enough to preserve an acceptable average radius of curvature.

Tangent Plane approximation

Whenever the surface roughness scale can be classified as slowly varying compared to the incident wavelength, the electromagnetic fields scattered by this surface may be approximated by the fields which would be present if an infinite tangent plane was introduced at each point of the surface. These facets must be more than one wavelength across so that diffraction effects do not dominate. Consequently, the laws of reflection and transmission from a perfectly smooth surface described earlier are applicable at the facets.

This method also known as the Kirchhoff First approximation or the Physical Optics (PO) theory was applied in the new model developed by Holliday et al (1986) and reported to produce good results for near vertical angles of incidence. The precise range of validity of this approximation is difficult to establish, but due to the conditions on the roughness scale, the Kirchhoff First approximation is usually confined to incidence angles between 0 and 45

degrees to the vertical (Valenzuela, 1985).

Specular Point model

This model derives from the Tangent Plane approximation applied to a finite conductive rough surface and considers that only those plane facets normal to the direction of the incident radiation contribute to the radar backscatter by pure specular reflection. The Normalised Radar Cross Section (NRCS) is dependent on the surface joint probability density of slope $p(\zeta_x, \zeta_y)$ as:

$$\sigma_{sp}(\theta) = \pi . \sec^4 \theta . p(\xi_x, \xi_y) . |R(0)|^2 \qquad \text{Equation 6. 6}$$

with θ the incidence angle and R(0) the Fresnel reflection coefficient at normal incidence.

This model is independent on polarisation and wavelength except through implicit dependencies in the Fresnel reflection coefficient. Comparison with experimental results have produced relatively good agreement at normal incidence. The discrepancies which appear when applied at larger incidence angles have lead to suggestions that the slope statistics of an ocean surface with slicks (i.e. without gravity-capillary and capillary waves) may be better suited (Valenzuela, 1978a). With this correction implemented, the Specular Point model produces reasonably good results for incidence angles between 0 and 20 degrees. For larger angles of incidence, the NRCS decreases rapidly in clear conflict with experimental evidence.

Curve Surface approximation

The Curve Surface approximation is based on the same principle as the Tangent Plane approximation with the difference that the rough surface is now approximated by curved facets instead of infinite planes. Consequently the resolution is more difficult and the approximation does not lead to an easy formulation. This method is rarely employed but it is believed to constitute a possible future way of development for a more exact analytical solution (Jeynes, 1989). To date, the validity of this model is difficult to evaluate.

Geometrical Optics

The Geometrical Optics theory is the high frequency extension of the Physical Optics. It estimates the scattering using the ray tracing technique familiar in Optics theory and assumes no diffraction by edge effects (Knott and Schaeffer, 1985). The scattering at a point in space is therefore obtained by the coherent summation of each ray accounting for amplitude, phase and polarisation (Valenzuela, 1978b).

This principle was applied to microwave radiations in a one-dimensional numerical phase summation model for the calculation of radar backscatter from a rough sea surface (Robinson and Ward, 1990). In this model, each point hit by the electromagnetic wave was assumed to behave like a secondary source and re-radiate isotropically above the sea surface (Huyghens principle in Optics). The amplitude of the reflected wave was simply determined by the Fresnel coefficient which introduces dependencies of the backscatter on the properties of the sea water and the polarisation of the radar wave. Comparison of the model's results with aircraft data show good agreement at low incidence angles (0-20 degrees). For larger incidences however, the model significantly over-estimates the values of the backscatter from the sea.

Geometrical Theory of Diffraction

The Geometrical Theory of Diffraction (GTD) is an extension of the Geometrical Optics to include diffraction effects. The GTD is a theory designed to account for the diffracted rays produced by edges, wedges and corner tips. The diffracted field is determined by the geometry of the scattering edge or tip, the direction of illumination, the position of the observer and the polarisation of the incident field (Ogilvy, 1991).

The GTD prediction of scattering from individual sharp-crested waves compared successfully with laboratory experiments in wave tanks (Kwoh and Lake, 1985). But the general application of this method to the ocean surface requires an accurate description of the wave field in terms of the number, spatial distribution, shape and size of the wave crests. Following the lack of experimental data in this matter, models based on the GTD are restricted by their reliance on assumptions about the statistical distribution of wedges in the

real sea.

6.3.2 - Sea surface roughness scale comparable to the radiation wavelength

When the surface roughness scale is of the same order than the radiation wavelength, the scattering from the surface can be solved using the Small Perturbation Theory (SPT). The theory was proposed by Lord Rayleigh in 1894 and extended by Rice (1951) to explain the scattering of plane acoustic or electromagnetic waves from "slightly rough surfaces".

These surfaces are defined as rough surfaces of gentle slopes and small surface heights compared to the electromagnetic wavelength. They must obey the Rayleigh criterion for roughness whereby the surface does not change the phase of the scattered wave by more than $\pi/2$ (Rees, 1990). In terms of the surface rms height H, the Rayleigh criterion reads as:

$$H < \frac{\lambda}{8.\cos(\theta)} \qquad \text{Equation 6. 7}$$

where θ is the angle of incidence of the radar wave.

The SPT assumes the scattered fields to be a superposition of plane waves of unknown amplitudes. The problem is resolved by applying the boundary conditions at the interface and expanding the electromagnetic field into a Taylor series. Tractable solutions have so far been obtained for series expanded to the first and second order.

Bragg Theory

From the first-order approximation, a simple model for the calculation of the NRCS of the sea surface was proposed. This model considers that the radar backscatter is entirely caused by a mechanism of constructive interference between the radar wave and the ocean waves. Moreover, the model assumes that only those ocean waves travelling parallel to the radar wave and whose wavelength satisfy the resonance with the radar wavelength contribute to the backscatter. This theory is commonly known as the Bragg theory after a similar resonant mechanism in crystals illuminated by X-rays discovered by Bragg in 1913.

The condition of resonance is expressed by:

$$\Lambda_w = \frac{\lambda}{2 \cdot \sin\theta} \qquad \text{Equation 6. 8}$$

where Λ_w is the ocean wavelength and λ is the radar wavelength. Hence, at near-horizontal incidence and X-band frequency for example, this theory predicts the radar backscatter to originate wholly from 1.5 cm ocean wavelengths.

For this model, the expression for the ocean NRCS is:

$$\sigma^0(\theta) = 16\pi \cdot k^4 \cdot \cos^4\theta \cdot g(\theta)^2 \, S(2k \sin\theta, 0) \qquad \text{Equation 6. 9}$$

where k is the radar wave number, $S(k_x,k_y)$ is the two-dimensional ocean wave spectral density function and $g(\theta)$ is the first order scattering coefficient. The coefficient $g(\theta)$ is a function of the radiation polarisation, the sea water dielectric constant ε_r and the incidence angle θ. It is calculated for horizontal and vertical polarisation respectively as:

$$g_{HH}(\theta) = \frac{\varepsilon_r - 1}{(\cos\theta + \sqrt{\varepsilon_r - \sin^2\theta})^2} \qquad \text{Equation 6. 10}$$

and

$$g_{VV}(\theta) = \frac{(\varepsilon_r - 1)[\varepsilon_r(1+\sin^2\theta) - \sin^2\theta]}{[\varepsilon_r \cos\theta + \sqrt{\varepsilon_r - \sin^2\theta}]^2} \qquad \text{Equation 6. 11}$$

The first-order coefficient $g(\theta)$ is responsible for the polarisation dependence of the Bragg scattering model. In particular, the model predicts that the scattering from the sea surface at horizontal polarisation is less than for vertical polarisation especially at larger incidence angles. Hence, the backscatter power ratio VV/HH is estimated to reach up to 40 dB for a perfectly conductive surface viewed at a grazing angle of 10 degrees.

Experimental evidence of a resonant interaction between electromagnetic radiations and ocean waves was first produced by Crombie (1955) with a coastal Doppler HF radar working at a radar wavelength of 22 meters. The Doppler shift of the peak of the backscattered signal

was found to correspond to the velocity of waves of wavelengths half that of the radar. He therefore deduced that the ocean waves acted as a diffraction grating array and that these ocean waves half the radar wavelength produced the largest contribution to the backscatter.

Crombie's observations were later extended to microwave radiations at low wind speeds. As the wind speed increased however, the microwave backscatter Doppler spectrum is found to broaden (Plant and Keller, 1990) and a particular backscatter peak can no longer be identified. This fact has been attributed to the growing contribution of the longer underlying waves by modulation of the resonant centimetre waves' amplitude. A modified Bragg model was introduced to incorporate the effects of longer waves on the small scale roughness. This model is known as the Two-Scale model.

Two Scale model

This Bragg-based model was developed by Wright (1968) to account for the imaging of long swell waves by centimetric radar waves. The model considers the surface to be composed of an infinite number of "slightly rough" patches modulated by the longer waves. Two components of the Bragg scattering modulation by the longer waves have been identified: a "tilt" modulation arising from the change in the local angle of incidence of the radar wave on the sea surface as the longer gravity waves travel through the short capillary waves, and a "hydrodynamic" modulation accounting for the larger number of capillary waves on the front face of long swell waves.

Assuming the microwave return from one rough patch to the next to be decorrelated, the resulting microwave backscatter can be approximated by averaging the first order Bragg backscatter for one patch calculated with the modified local incidence angle over the distribution of slopes of the dominant waves of the ocean (Valenzuela, 1985). Hence, the Two-Scale model expression for the NRCS reads :

$$\sigma^0_{sea}(\theta) = \iint \sigma^0(\theta_i).\, p(\tan\Psi, \tan\delta).d(\tan\Psi)\,d(\tan\delta) \qquad \text{Equation 6. 12}$$

where $\sigma^0(\theta_i)$ is the first order Bragg NRCS calculated from Equation 6.9, p is the joint

probability density of slopes of the large-scale roughness of the ocean and θ_i is the modified local angle of incidence given by:

$$\theta_i = \cos^{-1}[\cos(\theta + \psi).\cos\delta] \qquad \text{Equation 6. 13}$$

where ψ is the facet tilt angle in the plane of incidence and δ is the facet tilt angle in the plane perpendicular to the plane of incidence.

Extensive microwave radar datasets have been collected to validate the Two Scale model. Figure 6.2 presents a comparison of the model's output with experimental measurements carried out for a number of frequencies, polarisation and incidence angles by the US Naval Research Laboratory (Daley *et al.*, 1971).

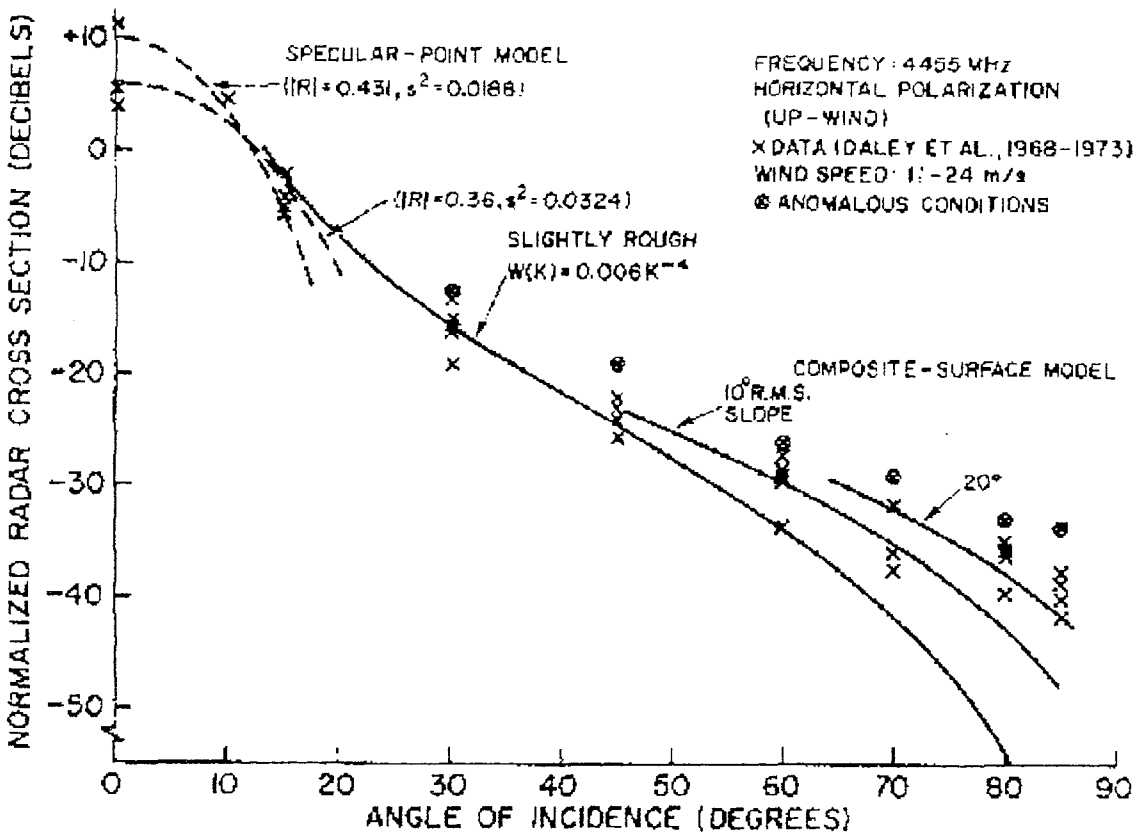

Figure 6. 2 - Comparison of the Two-Scale model predictions with experimental measurements at C-band frequency and horizontal polarisation (from Valenzuela, 1978a).

The Two Scale model is generally accepted to give satisfactory results for intermediate

incidence angles between 20 and 70 degrees. It also correctly reproduces the frequency and polarisation dependence observed experimentally including the reduction of the sea clutter NRCS on HH polarisation.

The discrepancies observed at low and high incidence angles have been attributed to contributions to the backscatter from other scattering mechanisms. The results at low incidence angles were subsequently adjusted by including the contribution from specular returns as calculated from the Specular Point model. The significant disparity observed mainly on horizontal polarisation between the model's predictions and the high NRCS measurements at large incidence angles have been attributed to propagation phenomena typical of electromagnetic waves travelling at low-grazing angles over a rough surface.

6.4 - Theoretical validity of the Two Scale model

The satisfactory performances of the Two Scale model at intermediate incidence angles have resulted in a widespread acceptance of the model in the oceanographic research community. There has however been concern about the validity of the model following examples of behaviour inconsistent with observations, raising questions as to the applicability of the model to the real sea surface.

6.4.1 - Model shortcomings

The most frequently acknowledged weakness of the Bragg-based models is their strong reliance on the spectral density function S chosen to estimate the wave energy at the ocean resonance frequency. In the case of microwave radiations, the relevant ocean wavelengths belong to the range of capillary centimetric waves. To date, the modelling of the wave spectrum at higher frequency is still an area of active research. Capillary waves are increasingly seen to play a fundamental role in the energy transfer from the atmosphere to the ocean and in wave growth. Little experimental data are available and the existing high-frequency spectrum models are generally based on theoretical assumptions.

Another problem often highlighted by critics of the Two Scale model is the necessity to

artificially divide the sea surface spectrum into large scale and small scale roughness, representing respectively the modulating long waves and the modulated short waves. The waves of the two groups are then assumed to be completely independent from one another. Critics have pointed out that the choice of the division in a continuous ocean wave spectrum is scientifically unjustifiable and entirely subjective (Jeynes, 1989). An example of a divided Two-Scale model is given by Pierson and Donelan (1987) who compared the model's predictions with experimental scatterometer data in a wide range of wind conditions and incidence angles. The modelled results were found to be systematically lower than the data over the whole range of incidence angles by amounts that could not be explained by measurement error alone. It has been suggested that the choice of the division parameter might be responsible for some of the inconsistencies of the results (Holliday et al, 1986).

6.4.2 - Applicability to the real sea surface

The main source of concerns is in the application of Bragg-based models to real sea surfaces in view of the potential conflict with the "slightly rough" condition imposed by the Small Perturbation Theory. Indeed, the open ocean surface is only expected to obey the Rayleigh criterion for roughness in very calm sea conditions.

A series of laboratory experiments established that the Small Perturbation Theory is indeed valid for low wind speeds up to 3 m/s (Kwoh and Lake, 1981, 1984, 1985). However, as the wind speed increases, the backscatter Doppler spectrum is found to broaden and become double-peaked. The Doppler shift of the new peak was later associated with the phase velocity of the wave crests. This contribution from wave crests constitutes a component of the total backscatter of similar or greater importance than the Bragg frequency peak and was discovered at its strongest at very high incidence angles. This new backscatter component has since been observed at all incidence angles and has been attributed to a wide range of processes from turbulence patches (Banner and Fooks, 1985) to specular reflections from steep wave crests on the verge of breaking (Lee et al, 1995).

6.4.3 - Conclusion

Despite an apparent aptitude for predicting the backscatter coefficients of the sea surface, the Two-Scale model fails to acknowledge the contributions of the specular facets, sharp crests and turbulent patches which characterise real ocean surfaces. It has become accepted that this additional scattering component is significant at all incidence angles and especially relevant at high grazing angles. New models have been proposed based on the Two-Scale model and including a scattering component from sharp-crested and breaking waves (Pierson and Donelan, 1987, Phillips, 1988, Trizna, 1989) although the exact feature responsible for this scattering remains uncertain.

6.5 - Grazing angles scattering

All models and theories examined so far have failed to provide a reliable method to predict microwave radar backscatter at grazing angles. The discrepancies between the Two Scale model and data at near horizontal incidence angle have been attributed to propagation phenomena specific to near-horizontal illumination and/or scattering from wave crests. Here, the current understanding of the possible origin of this additional scattering at low grazing angles is reviewed.

6.5.1 - Experimental evidence

Given its importance for navigation safety and defence purposes, the scattering of radar waves from the sea surface at low grazing angles attracted much interest from an early stage. The scattering at near horizontal incidence angles was rapidly found to display particularly energetic features unnoticed at other incidence angles. These features became known as Sea Spikes and were reported for the first time by Kalmykov and Pustovoytenko (1976) as sharp discrete "bursts" of energy typical of horizontal polarisation and small grazing angles (< 5 degrees). These Sea Spikes are found to be exclusive to high-resolution radars with pulse lengths much smaller than the dominant ocean wavelength.

Sea Spikes are characterised by high returns, strong HH/VV polarisation ratios reaching up to

12 dB, large Doppler shifts and long decorrelation times (50 ms). In comparison, Bragg-type distributed scatter presents negative HH/VV ratios and coherence times of only a few milliseconds. Due to the high amplitudes and the conditions in which they occur, Sea Spikes are considered sufficiently widespread to significantly modify the average value of NRCS for lower resolution radars and could explain the discrepancies between the Two Scale model and the data at grazing angles.

6.5.2 - Potential scattering mechanisms

The occurrence of these high intensity echoes was associated visually by means of televideo images to steep crested waves on the verge of breaking (Lewis and Olin, 1980). The many water surface features occurring at short time intervals and closely in space in near-breaking conditions made the precise identification of the specific scatterer responsible for Sea Spikes difficult.

It is generally accepted that specular scattering is not likely to occur at grazing angles less than 10 degrees since it would require the water surface steepness to be greater than 80 degrees from the horizontal and this is far beyond the commonly accepted maximum slope of 30 degrees from the horizontal set by the water surface stability criterion. Furthermore, the polarisation ratio for specular scattering is close to unity in clear disagreement with experimental evidence. The hypothesis of volume scattering by spray temporarily suspended above the water surface is equally inappropriate since scattering from symmetric drops of water would also produce HH/VV polarisation ratios close to unity in contradiction with experimental evidence.

Attempts have been made to assimilate Sea Spikes with the enhanced scattering observed at slightly larger grazing angles. This latter scattering has however been associated with turbulence patches or wave crest bound capillary waves on the forward face of breaking waves, which once again result in decorrelation times and polarisation ratios incompatible with those observed for Sea Spikes (Trizna, 1993).

6.5.3 - Scattering models for long waves

The observation that the major feature of the sea surface is "V-shaped" rather than sinusoidal has lead to the development of many models for the scattering from wedge-like waves (Wetzel, 1990). The models generally assume waves crests perfectly aligned with regard to the incident radar wave and the water surface steepness to be limited to 30 degrees. Although these models have shown good agreement with laboratory results, they are unable to explain the high intensity of Sea Spikes and the large HH/VV polarisation ratios observed in the open sea (Trizna, 1991a).

Other models have considered the scattering from waves on the verge of breaking by calculating the scattered fields for a particular geometry of breaking waves. Hence, the Plume model proposed by Wetzel (1986) is based on the geometry of the widespread "spilling" breaker. This type of breaking is characterised by a sharpening of the wave crest up until reaching the point of instability when a plume of water breaks from the crest and slides down the front face of the wave. In the Plume model, the plume front edge is represented by a conducting quarter cylinder which intersects perpendicularly to the long wave face and progresses down the long wave towards the trough as shown in Figure 6.3. The model uses a Physical Optics approach and includes forward-reflected multipath reflections of the incident radiation field from the smooth water surface ahead of the cylinder.

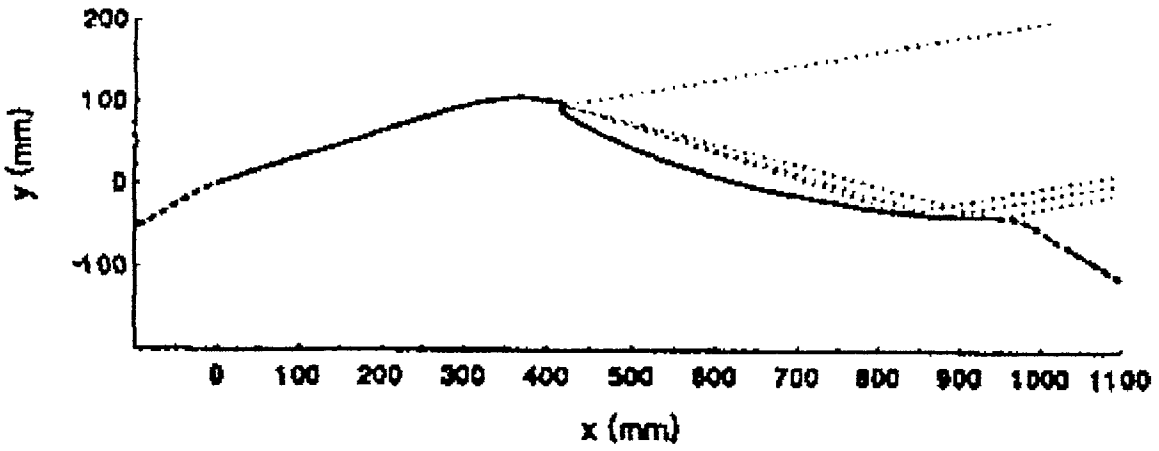

Figure 6. 3 - Spilling breaker plume and multipath scattering (from West et al., 1996)

This model is highly sensitive to grazing angle variations and the radiation polarisation due to the forward-reflected component of the radiation field. The considerable difference in the Fresnel reflection coefficients for sea water between horizontal and vertical polarisation at grazing angles close to the Brewster angle have the potential to produce high radar returns, long decorrelation times and strong HH/VV polarisation ratios comparable to those associated with Sea Spikes.

Recent numerical and experimental investigations (West et al., 1996) have confirmed that the Brewster angle effect on the Fresnel reflection coefficients strongly reduces the forward-scattered scattering component from breaking waves at vertical polarisation. It has been demonstrated that the multiple scattering proposed in the Plume model can lead to positive HH/VV polarisation ratios close to the 12 dB observed experimentally and offers a suitable explanation for the generation of Sea Spikes.

6.6 - Conclusion

The backscatter from the rough sea surface is satisfactorily described at low and intermediate incidence angles by a combination of specular reflections from facets normal to the radar wave and a mechanism of constructive interference between the radar and the ocean waves. Experimental evidence suggests that an additional contribution to the backscatter from sharp-crested waves and breaking waves should also be included to resolve some of the existing differences in backscatter coefficient levels with measurements at all incidence angles.

At low grazing angles, the contribution to the backscatter by sharp-crested and breaking waves becomes significant. The high-energy Sea Spikes events typical of horizontal polarisation and low grazing angle scattering are thought to be able to account for the large discrepancies between the Two-Scale model and experimental data at grazing angles. Hence, the scattering at low grazing angles is considered to consist of a combination of Bragg-type scattering from distributed roughness and enhanced scattering by multiple reflection from steep and near-breaking long waves.

Chapter 7

Influence of Operational Parameters on Ocean Backscatter

Having defined the inherent detection capabilities of the radar system in Part 1, one now considers the influence of the operational parameters on the nature and magnitude of the measured ocean backscatter. Hence, the importance of the pulse length setting and the height of the radar antenna above sea level are examined and where possible quantified. In both cases, experimental observations of the change in NRCS with each parameter are compared to the current understanding in the literature of ocean backscatter at low grazing angles.

7.1 - Influence of the pulse length setting

7.1.1 - Nature of the ocean backscatter at low grazing angles

The backscatter from the ocean at low grazing angles is generally accepted to originate from centimetric scale roughness producing Bragg-type scattering and long sharp-crested waves responsible for high intensity sea spikes (Chapter 6). The backscatter coefficient for individual wave crests is experimentally shown to exceed the scattering contribution from small scale roughness by several orders of magnitude. Typical sea spike NRCS values are equal to -10 dB or more in comparison with values generally smaller than -30 dB for Bragg-type scattering at low grazing angles (Trizna, 1991b, Donelan and Pierson, 1987). Hence, these highly energetic echoes are expected to play an important role in the determination of the mean NRCS.

The two types of scatterers also differ by their decorrelation times which indicate how rapidly the sea surface varies when observed with microwave radiation. The coherence time for the small-scale roughness is estimated at about 10 to 20 ms while Sea Spikes are reported to persist with durations of 50 ms or more (Trizna, 1993).

Radar sea clutter at low grazing angles is generally studied for radar detection applications and therefore focuses on the statistical characteristics of sea clutter. It is now widely recognised that the statistical distribution of the radar backscatter coefficient from the sea is strongly affected by the dimension of the radar's sampling cell (Skolnik, 1970). When the ocean backscatter can be considered to consist of the contribution from a number of independent random scatterers, the ocean backscatter coefficient is best described by a Rayleigh probability distribution function (pdf) given as:

$$P(\sigma_0) = \frac{2 \cdot \sigma_0}{s_\sigma^{\,2}} \cdot \exp\left(-\frac{\sigma_0^{\,2}}{s_\sigma^{\,2}} \right) \qquad \text{Equation 7. 1}$$

where s_σ is the standard deviation of the ocean NRCS. Note that the ocean NRCS is designated here with the symbol σ_0 instead of σ^0 to avoid any confusion between the exponents of the distribution and the variable superscript.

Ocean backscatter with a probability distribution described by Equation 7.1 is known as Rayleigh clutter and is usually observed for low resolution radars. When the resolution of the radar becomes sufficiently high to isolate individual wave crests, the sea clutter pdf deviates from the Rayleigh form following the increased contribution from high energy sea spike echoes. These sea spikes are responsible for the higher probability of observing high echo amplitudes and thereby modify the ocean backscatter pdf at the high amplitude end of the distribution.

The precise analytical form of a suitable pdf for non-Rayleigh clutter is not strictly established as it seems to depend on the complexity of the sea state. Among the most frequently encountered functions is the log-normal pdf given as (Skolnik, 1980):

$$P(\sigma_0) = \frac{1}{\sigma_0 \cdot \sqrt{2\pi} \cdot s_{\ln\sigma}} \cdot \exp\left(-\frac{1}{2 \cdot s_{\ln\sigma}^{\,2}} \cdot (\ln\sigma_0 - m)^2\right) \qquad \text{Equation 7. 2}$$

where m is the mean of $\ln(\sigma^0)$ and $s_{\ln\sigma}$ is the standard deviation of $\ln(\sigma^0)$. The log-normal pdf essentially represents a normal distribution expressed in a logarithmic scale. Another function often applied is the Weibull distribution given as (Chan, 1990):

$$P(\sigma_0) = A \cdot B \cdot \sigma_0^{\,B-1} \cdot \exp\left(-A \cdot \sigma_0^{B}\right) \qquad \text{Equation 7. 3}$$

where A and B are the Weibull scale and shape parameters respectively. The Weibull pdf represents an intermediate between the Rayleigh and the log-normal distribution function. It can be made to resemble either distribution by judiciously choosing the parameters A and B. When fitting the pdf to an experimental dataset, the optimum parameters can be calculated from the NRCS mean $\overline{\sigma^o}$ and standard deviation s_σ via the following relations (Mood et al , 1974):

$$\overline{\sigma^o} = \left(\frac{1}{A}\right)^{1/B} \cdot \Gamma\left(1 + B^{-1}\right) \qquad \text{Equation 7. 4}$$

and

$$s_\sigma = \left(\frac{1}{A}\right)^{2/B} \cdot \left[\Gamma\left(1 + 2 \cdot B^{-1}\right) - \Gamma^2\left(1 + B^{-1}\right)\right] \qquad \text{Equation 7. 5}$$

where Γ is the gamma function.

These non-Rayleigh clutter distributions are compared in Figure 7.1 with the Rayleigh pdf to demonstrate the increased probability density at the high-amplitude end of the distributions. The functions were generated for the same sample of randomly generated numbers. The optimum Weibull parameters were computed numerically by seeking the best fit to the sample's statistical moments. Both the probability density and the signal amplitude are normalised with respect to their maximum values.

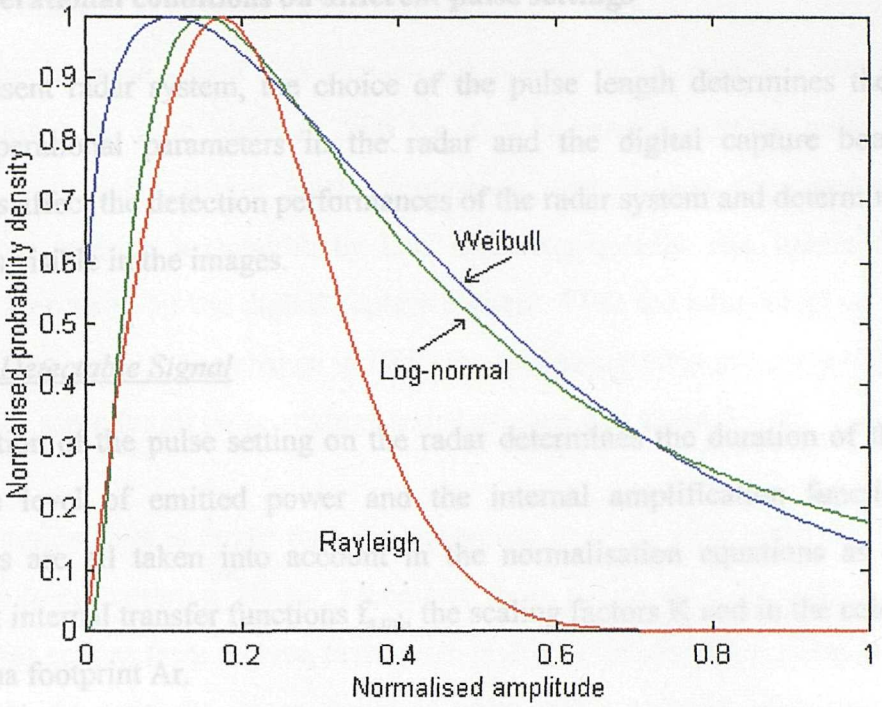

Figure 7. 1 - Rayleigh, log-normal and Weibull probability density functions.

In practice, the Rayleigh pdf is generally found to underestimate the range of ocean backscatter coefficients in the data. The Weibull distribution has proven very successful in describing the ocean backscatter statistics obtained with very high resolution radars (Trizna, 1988). The sea clutter obtained on horizontal polarisation was shown to be perfectly described with two Weibull distributions while vertical polarisation backscatter can be described with one single Weibull distribution. Trizna (1991a) suggested that each Weibull distribution is representative of each particular type of scatterer present on the sea surface.

The criteria defining a high-resolution radar likely to produce non-Rayleigh clutter has been set in relation to the dimension of the radar sampling cell. For pulsed beam radars working at low grazing angles, the surface area of the antenna footprint is determined by the antenna's horizontal beamwidth and the duration of the emitted pulse. Radars are considered to be of high-resolution when the size of the antenna footprint is smaller than the dominant ocean wavelength (Trizna, 1991a). Typically, this condition is taken to correspond to pulse length durations less than 0.1 μs (Skolnik, 1970).

7.1.2 - Operational conditions on different pulse settings

In the present radar system, the choice of the pulse length determines the value of several operational parameters in the radar and the digital capture board. These parameters affect the detection performances of the radar system and determine the type of features visible in the images.

Minimum Detectable Signal

The selection of the pulse setting on the radar determines the duration of the emitted pulse, the level of emitted power and the internal amplification function. These parameters are all taken into account in the normalisation equations as the pulse-dependent internal transfer functions $f_{s,ml}$, the scaling factors K and in the calculation of the antenna footprint Ar.

The impact on the system's detection performances of the different values of these parameters on different pulse settings can be summarised with the calculation of the NRCS equivalent to the system's Minimum Detectable Signal (MDS). The MDS defines the minimum measurable ocean backscatter coefficient at any given range on each pulse setting and was presented previously in Figure 5.12. It is found to increase rapidly with range and decreasing pulse durations. It is therefore expected that for a given ocean backscatter coefficient, images obtained on shorter pulse settings will display receiver noise at closer ranges than longer pulse setting images.

Radar sampling cell

Using the criteria by which pulse durations less than 0.1 μs define a high-resolution radar, the present system features low resolution radar cells when operating on medium and long pulse (pulse durations equal to 0.22 and 0.86 μs respectively). On short pulse, the pulse duration is equal to 0.065 μs and obeys the high resolution cell criteria. Hence, the radar set on short pulse mode is able to isolate individual wave crests and has the potential to measure non-Rayleigh sea clutter.

Integration time

The change in pulse length also changes the radar's pulse repetition rate (PRR). The PRR is largest for short pulse at 2400 Hz, then halved for medium pulse and halved again for long pulse setting. Each decrease in PRR reduces the number of pulses emitted per antenna beamwidth by half and consequently also halves the optimal Azimuth Step value in the digital capture register. With the adjustment of the optimal Azimuth Step value to the change in PRR, the integration time per beamwidth however remains the same for all pulse settings and is estimated at about 0.7 ms.

The integration time is larger than the coherence time for both small scale roughness and wave crest scattering. Hence, successive radar pulses view the surface in a frozen state so that echoes from a given feature are highly correlated from pulse to pulse. This process should result in strong signal to noise ratios and the high intensity echoes reported in the literature. In the present case however, the successive pulses do not view the same part of the frozen surface as the antenna continuously rotates. The distance l between features viewed by successive pulses at a range R from the radar can be estimated from the antenna time per revolution (TPR) and the pulse repetition rate (PRR) as:

$$l = \frac{2\pi \cdot R}{TPR} \cdot \frac{1}{PRR} \qquad \text{Equation 7. 6}$$

For an average TPR of 2.4 seconds and a 2400 Hz PRR on short pulse, the distance between scattering features at 1000 meters is estimated to be over 1 meter and increases with range. The echoes integrated over successive pulses will then generally be decorrelated and should not display any high intensity sea spikes. The range of NRCS values obtained with the present system is therefore expected to be reduced in comparison to those reported for systems performing single pulse NRCS measurements or equipped with staring antennas.

Radiometric resolution

Despite the pulse to pulse decorrelation, the difference in the number of pulses integrated per antenna beamwidth (Azimuth Step) on different pulse settings has

important implications on the signal to noise ratio in the images. Larger values of the Azimuth Step reduce the random noise and result in lower measurement errors. The error analysis performed previously in Chapter 6 confirms that the radiometric resolution is indeed better in shorter pulse images.

7.1.3 - Experimental observations

Experimental measurements of the ocean NRCS at different pulse lengths were carried out to check whether the sea clutter information obtained with the present radar system corresponds to the expected behaviour. The data presented here are part of a larger dataset collected to study both the effect of pulse duration and antenna height. The exploitation of the dataset with regards to the change in antenna height is deferred to the next section. At this stage, the data are exploited solely in terms of changes in pulse length and are therefore limited to images collected with a fixed antenna height. All data presented here were collected with an antenna height of 17 meters above mean sea level.

Experimental set-up

The data were collected over the eastern part of Christchurch Bay from the site in Milford-on-Sea used for the system's absolute calibration (Chapter 4). The location of the radar can be viewed by referring back to Figure 4.2.

Radar images were collected for different pulse settings at a few minutes interval to ensure that similar environmental conditions prevailed. The experiment was repeated from the same site over three days during which the wind and sea conditions changed dramatically. Day 1 was characterised by a light breeze (< 5 m/s) and a very calm sea state, but an overnight storm rapidly increased the wind to 12-15 m/s on Day 2. The sea surface on Day 2 was characterised by long waves developing and strong breaking in the near-shore area. The wind then gradually abated to 7-10 m/s on Day 3; as expected, the sea state took longer to calm down and many long crested waves were still visible. The wind direction on the three days was from the SSW, corresponding to the Bay's widest opening onto the English Channel.

Study area for NRCS measurements

The analysis of the changes in NRCS with pulse length was confined to the western half of the images where the wind field and the sea surface roughness can be assumed to be unaffected by the coastline. The region was further limited to a 60 degree wide angular sector centred on the radar up-wind looking direction. The angular sector was therefore centred on azimuth bearing 210 and ranged between 180 and 240 degrees with respect to geographic North.

The study area is indicated in the calibrated radar image shown in Figure 7.2. The image corresponds to 180 degree coverage in azimuth shown in Cartesian projection. The horizontal axis represent the azimuth angle with respect to geographic North. The vertical axis corresponds to the slant range to the radar. The large dark feature in the top left-hand corner of the image is the Isle of Wight as seen from the mainland. The elongated strip in the bottom left hand corner is Hurst Spit (Figure 4.2).

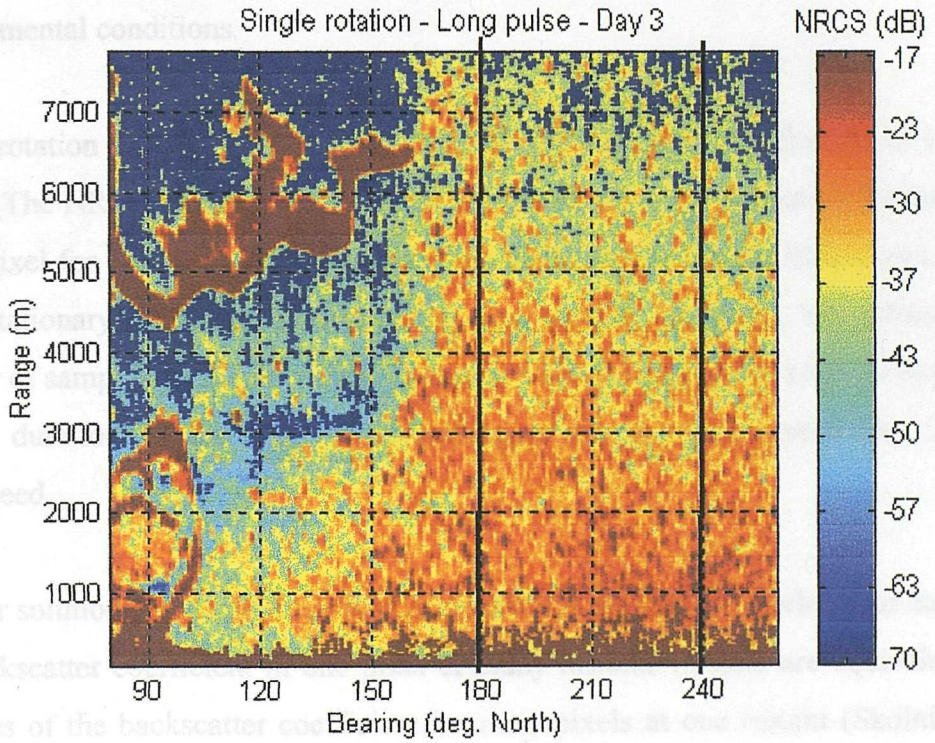

Figure 7. 2 - Location of the study area within a calibrated radar image obtained in Christchurch Bay on Day 3. The radar is set on long pulse and the antenna height is 17m above mean sea level.

The study area selected for the NRCS measurements features a regular bottom topography at an average depth of 15 meters. The sea floor gradient is small over most of the area beyond a range of 1000 meters. Within 1000 meters from the radar, the water depth decreases rapidly and is expected to induce strong wave breaking. Outside this zone, the variation of the sea surface roughness due to changes in the shoaling of ocean waves can however be assumed to be minimal.

Data analysis techniques

For each pulse length, a time-series of 16 successive radar images was collected and the average and standard deviation images were computed. Both single rotation images and the average image were calibrated using the normalisation equations to produce NRCS images. The single rotation images offer a snapshot of the sea surface and help to identify the presence of transient features on the surface. The images averaged over several antenna rotations display the mean NRCS spatial distribution and provided an insight into the long-term dependence of the ocean backscatter on pulse setting and environmental conditions.

Single rotation images were used to compile the statistical distribution of the ocean NRCS. The NRCS statistical distribution can be obtained by extracting the NRCS at a given pixel for a time-series of images. This method calls for the backscatter statistics to be stationary over the duration of the data capture. However, the collection of a number of samples sufficiently large to enable a reliable statistical analysis implies data capture durations of the order of several hours during which stationarity cannot be guaranteed.

Another solution is to exploit the NRCS property of ergodicity by which the statistics of the backscatter coefficient in one pixel at many instants in time are equivalent to the statistics of the backscatter coefficient in many pixels at one instant (Skolnik, 1990). This property derives from the fact that the backscatter coefficient is equally decorrelated from pixel to pixel as it is from rotation to rotation. The NRCS statistical distribution can therefore be computed from the NRCS values in a group of pixels taken from a single rotation image. The area in the image must be sufficiently small for the

ocean backscatter to be assumed homogeneous. Hence, the high spatial resolution in the images enabled over 5000 NRCS values to be obtained over an area 1000 * 1000 meters located at 1500 meters. The collection of an equivalent number of samples in time would entail a minimum capture duration of 3.5 hours on short pulse.

Results

Figure 7.3 shows NRCS transects taken radially across the study area in single rotation images obtained on different pulse settings. Data obtained on short, medium and long pulse are shown respectively as red, green and blue plots. The three subplots correspond to the results obtained on the three successive days characterised by different sea conditions. The arbitrary NRCS value of -70 dB is a data flag attributed to pixels affected by receiver noise.

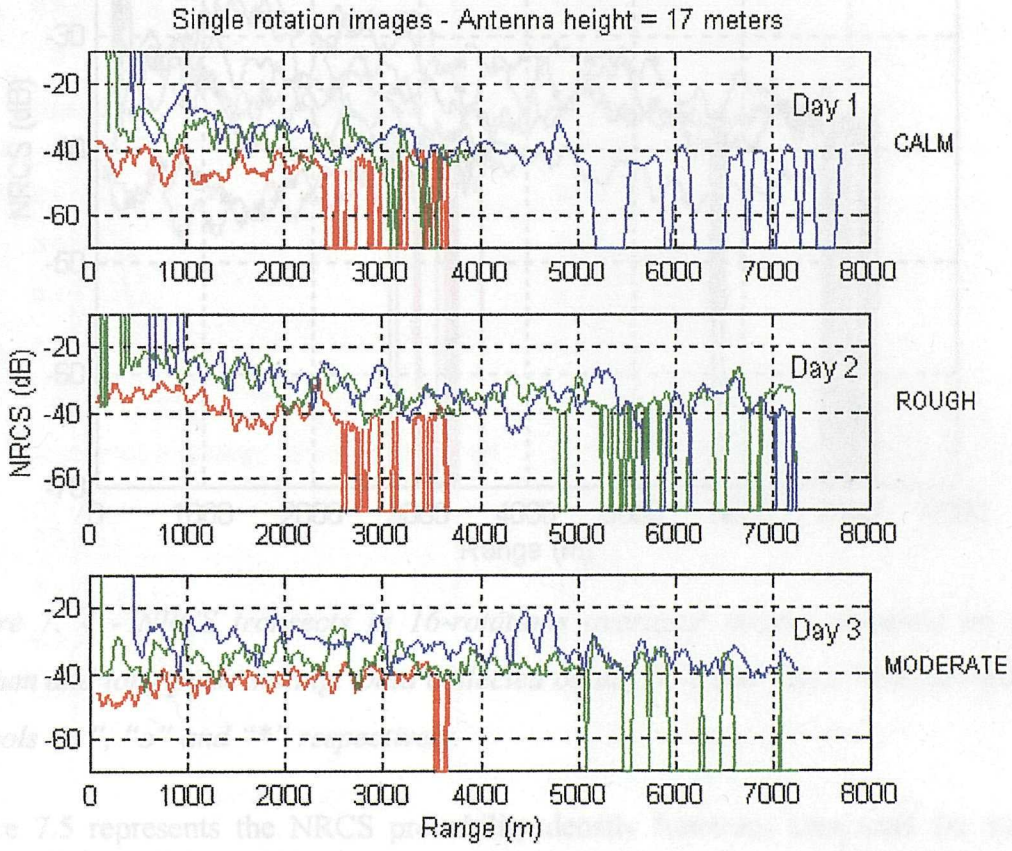

Figure 7. 3 - NRCS transects in single rotation images obtained for different pulse length on three successive days. The red, green and blue plots correspond respectively to short, medium and long pulse data.

Figure 7.4 represents the same type of NRCS transects extracted from the 16-rotations averaged images. The data for all three days are plotted in one single figure to visualise the change in mean NRCS in different sea conditions. The cross "+", circle "o" and star "*" symbols indicate data collected on Day 1, 2 and 3 respectively. The short, medium and long pulse data are identified by red, green and blue plots. The large spikes visible at very close and very far ranges correspond to pixels reaching saturation and noise level respectively.

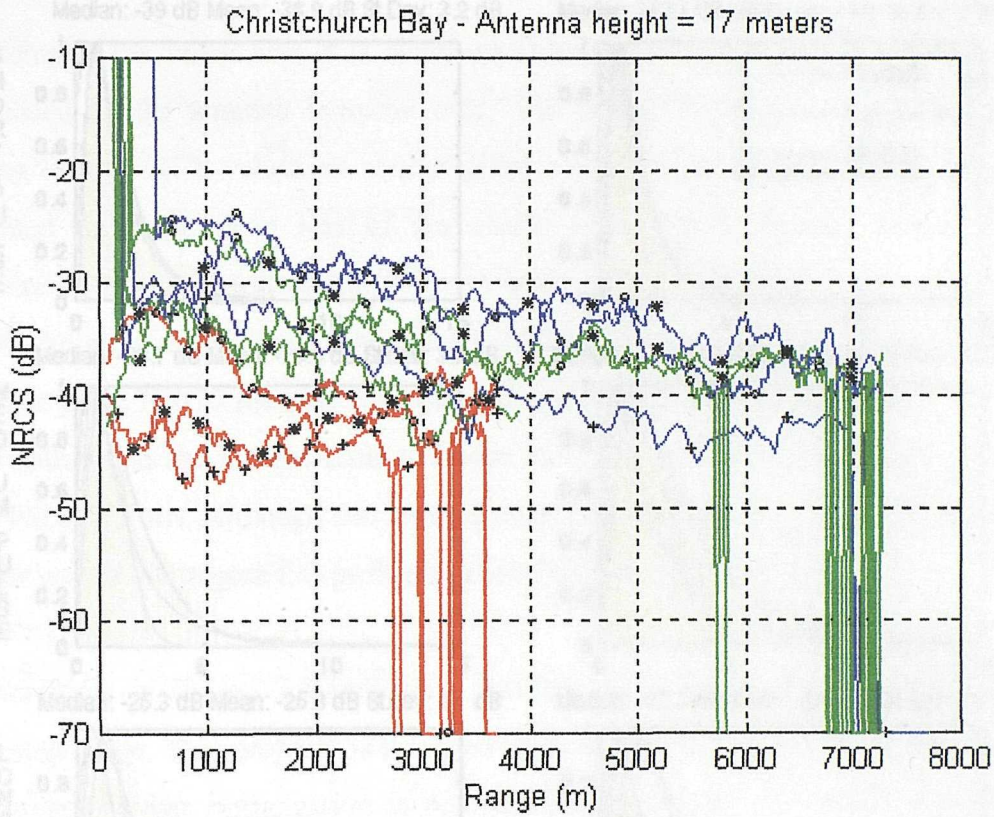

Figure 7. 4 - NRCS transects in 16-rotations averaged images obtained on short, medium and long pulse setting. Data collected on day 1, 2 and 3 are identified with the symbols "+", "o" and "" respectively.*

Figure 7.5 represents the NRCS probability density functions computed for an area 1000 by 1000 meters centred on azimuth bin 150 and a mean range of 1500 meters. The pdf are shown for short, medium and long pulse respectively from top to bottom and for Day 2 and 3 from left to right. The NRCS amplitude on the horizontal axis is normalised with respect to the distribution median to enable comparison between data from different pulse settings while keeping the original distribution shape.

In Figure 7.5, the Rayleigh, log-normal and Weibull distributions were fitted to the NRCS distributions. In some case, the proportion of lower NRCS values in the dataset affected the Weibull distribution too strongly to enable one single distribution to fit the whole range of NRCS values. Under these circumstances, the Weibull parameters were arbitrarily adjusted to get the best fit to the higher tail end. No attempts were made to fit two separate Weibull distributions to the dataset.

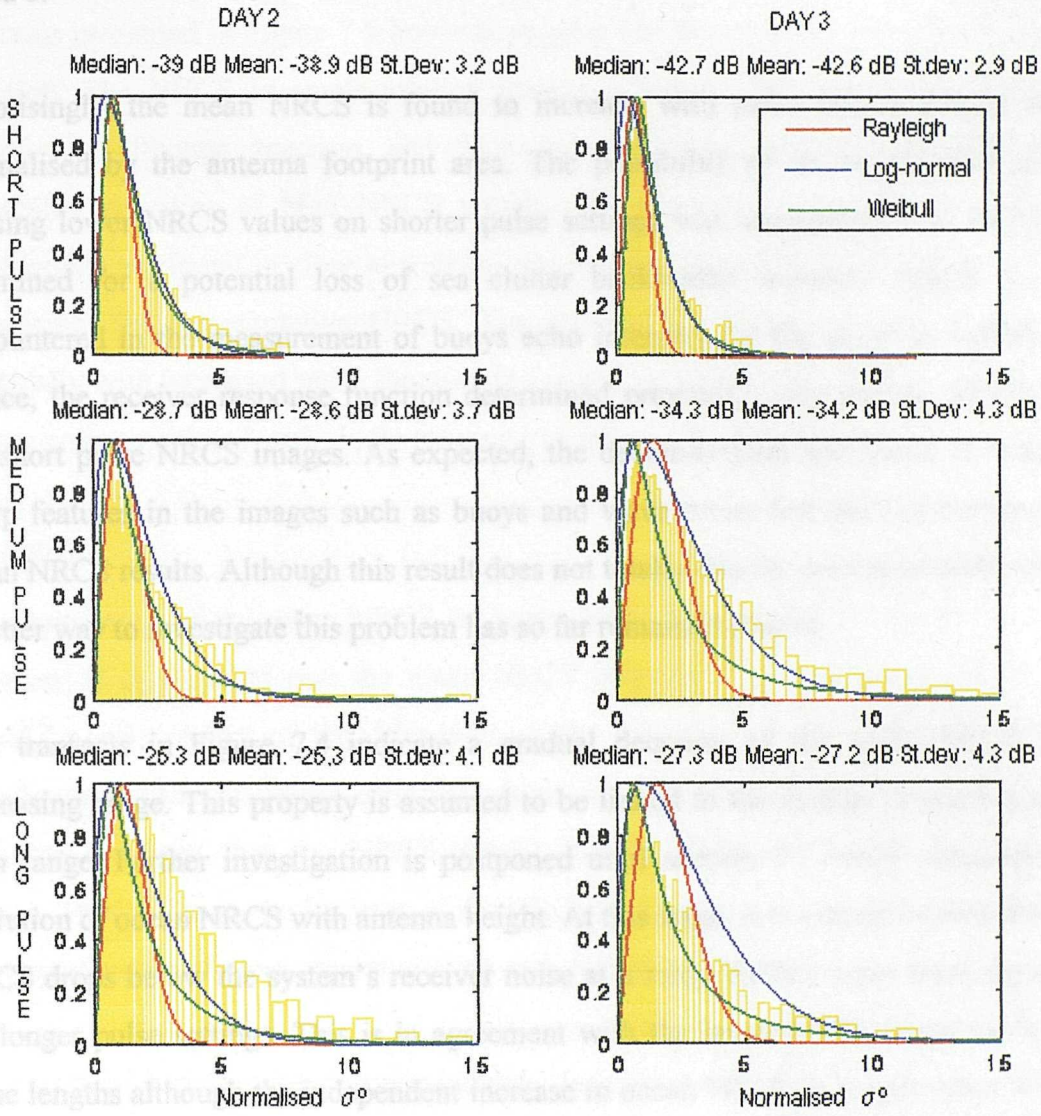

Figure 7. 5 - NRCS probability density functions for a 1000 by 1000 meters area in images obtained on short, medium and long pulse on day 2 and 3. The red, green and blue solid curves correspond to the fitted Rayleigh, log-normal and Weibull pdf respectively.

Data analysis - Mean NRCS

The mean NRCS transects and the statistical distributions in Figure 7.4 and 7.5 indicate a significant increase in ocean backscatter coefficient at all pulse lengths with increasing wind/sea conditions. The NRCS on short and medium pulse appears more sensitive to sea state variations than long pulse setting. This is evidenced by the more immediate drop in NRCS at close range with abating wind/sea conditions between day 2 and 3.

Surprisingly, the mean NRCS is found to increase with pulse length despite being normalised by the antenna footprint area. The possibility of an instrumental defect causing lower NRCS values on shorter pulse settings was considered. The data were examined for a potential loss of sea clutter backscatter intensity similar to that encountered in the measurement of buoys echo intensity for the absolute calibration. Hence, the receiver response function determined previously was used to deconvolve the short pulse NRCS images. As expected, the deconvolution was found to enhance sharp features in the images such as buoys and wave crests but did not increase the mean NRCS results. Although this result does not totally dismiss an instrumental effect, a better way to investigate this problem has so far remained elusive.

The transects in Figure 7.4 indicate a gradual decrease of the mean NRCS with increasing range. This property is assumed to be linked to the change in grazing angle with range. Further investigation is postponed until section 7.2 which considers the evolution of ocean NRCS with antenna height. At this stage, it is enough to note that the NRCS drops below the system's receiver noise at a range further away from the radar for longer pulse settings. This is in agreement with the lower MDS values for longer pulse lengths although the independent increase in ocean NRCS in longer pulse images contributes to further enhance the difference in range coverage for images collected on different pulse lengths.

Data analysis - Single rotation NRCS

The single-rotation NRCS transects in Figure 7.3 confirm the absence on all pulse

lengths of the high energy sea spikes described for high resolution radar systems. The NRCS transects display spatial wave-like features for all pulse lengths but the magnitude at the "spikes" does not exceed the mean NRCS by more than 10 dB, in contrast to the 30 dB difference commonly reported in the literature.

Similarly, the range of measured NRCS in the probability density functions is smaller than those reported for staring antenna systems for example. The probability density functions presented in Figure 7.5 however suggest that the measured sea clutter is non-Rayleigh. The NRCS in single-rotation images is better described by a log-normal distribution although medium and long pulse images generally display higher probability densities of high NRCS values. The median and mean of the NRCS distributions are found in close agreement and suggest that either parameter may serve to estimate the representative NRCS. The standard deviation is shown to increase marginally with increased pulse duration but is not significant with regards to the 1 dB or over error associated with single rotation images.

Discussion

The dependence of the mean NRCS on pulse duration is not well documented in the literature. It is accepted that the mean NRCS generated from distributed roughness should be independent of the dimension of the antenna footprint but when a large contribution to the scattering originates from discrete scatterers, the only accessible reference indicates that the NRCS should behave "differently" with pulse length (Trizna, 1988). Hence, the increase of the NRCS with pulse duration may simply relate to a larger impact of wave crest scattering on longer pulse settings.

The NRCS probability distributions indicate the existence of strong echoes in the sea clutter but at NRCS values much lower than expected. The absence of sea spikes in the single rotation NRCS images recorded on short pulse suggests that the ocean backscatter coefficient is strongly affected by the multi-pulse integration performed during data collection. Thus, it emerges that the ocean backscatter coefficient may not only be affected by the dimension of the antenna footprint but also by differences in the parameters of the data sampling procedure. It was decided that the extent of these

potential differences should be investigated with the help of a model designed to simulate the spatial and temporal integration process carried out by the instrument.

Interpretation - Integration model

The model was designed to reproduce the spatial sampling of the sea surface and the integration of successive pulses in an antenna beamwidth. The model uses statistical information from the literature to randomly generate NRCS samples composed of low intensity Bragg-type scattering and high intensity sea spikes. Typically, the NRCS in dB is taken to be normally distributed and thus follows a log-normal distribution in a linear scale. The mean value of the normal distribution for the Bragg NRCS is set equal to -40 dB while the mean value for the sea spikes distribution was taken equal to -10 dB in accordance with results reported in the literature. The variances of each distribution were reserved as variable parameters of the model.

The random NRCS samples are composed by generating a first series of n random NRCS values with the Bragg distribution, then a second - smaller - series of NRCS values using the sea spikes distribution. The sea spikes samples are then inserted in the Bragg series at regular intervals. The position of the first spike in the Bragg series is changed randomly between each iteration to simulate the decorrelation of the sea surface between successive pulses. The distance "d" between the spikes was chosen as another variable of the model to investigate the effect of different "wave-crest" densities on the surface. An illustration of the NRCS samples is shown in Figure 7.6.

Each NRCS value in the series represent the instantaneous NRCS of the sea surface as originally measured by the high resolution single pulse radar systems from which the NRCS statistics were obtained. According to the definition of the NRCS, each point in the series corresponds to the ratio of the scattered power to the incident power normalised by the dimension of the radar sampling cell. In this 1-dimensional model, each point is assumed to correspond to 1 meter of sea surface, which represents a realistic estimate of the radial dimension of the high resolution radar cells.

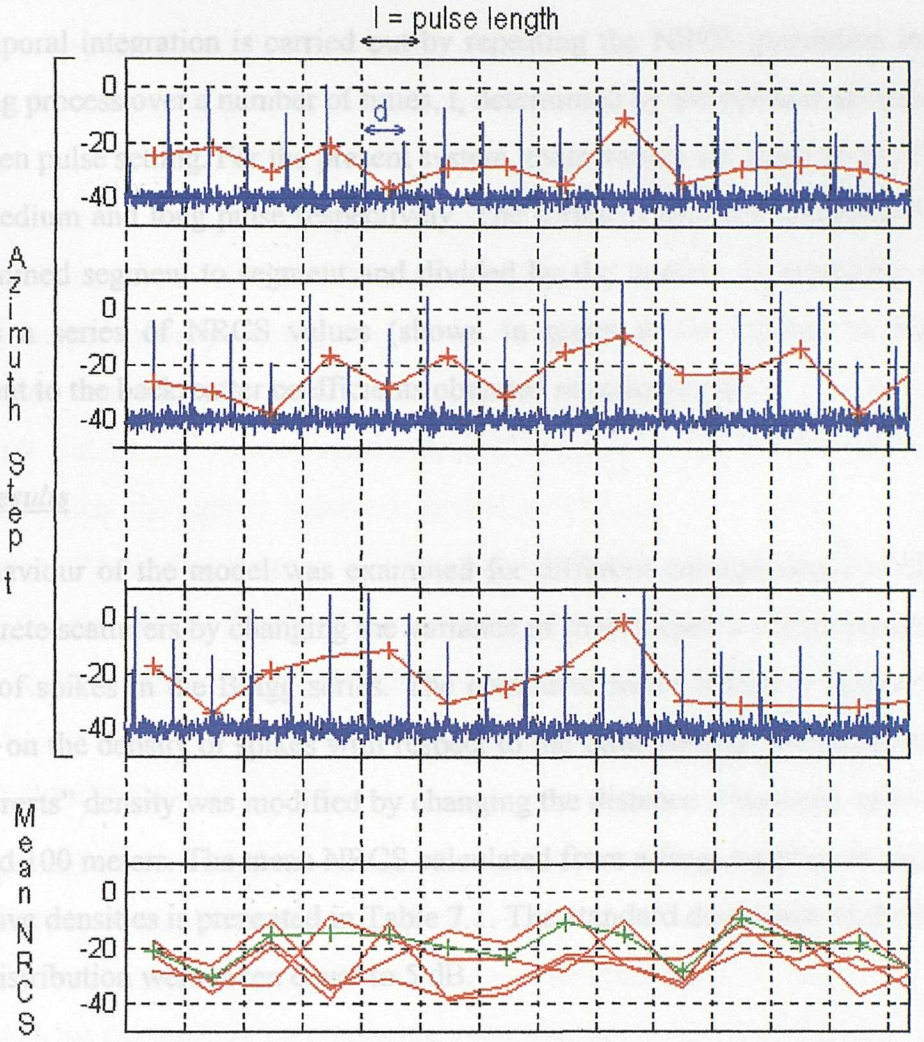

Figure 7. 6 - Spatial averaging and temporal integration of randomly generated NRCS series

The spatial sampling is achieved by dividing the NRCS series in segments of length "l" determined by the duration of the pulse length. Following the specifications of the present system, the length l was taken equal to 10, 30 and 130 meters for short, medium and long pulse respectively. The NRCS for each segment is calculated by assuming the total power scattered by each segment to be equal to the sum of the power scattered by all scatterers in the segment and normalising the sum by the dimension of the segment. Equally, the NRCS for each segment is calculated by taking the mean NRCS value (in linear form) over the length of the segment. The spatially averaged NRCS are shown in red in Figure 7.6.

The temporal integration is carried out by repeating the NRCS generation and spatial averaging process over a number of times, t, determined by the optimal azimuth step for the chosen pulse setting. For the present system, these values are equal to 16, 8 and 4 on short, medium and long pulse respectively. The series of spatially averaged NRCS are then summed segment to segment and divided by the number of iterations. The final result is a series of NRCS values (shown in green at the bottom of Figure 7.6) equivalent to the backscatter coefficients obtained in radar images.

Model results

The behaviour of the model was examined for different configurations of distributed and discrete scatterers by changing the variance of their respective distributions and the density of spikes in the Bragg series. The computed mean NRCS is found to depend strongly on the density of spikes with respect to the dimension of the pulse length. The "wave-crests" density was modified by changing the distance d between spikes from 10 to 50 and 100 meters. The mean NRCS calculated from a large number of segments for these wave densities is presented in Table 7.1. The standard deviations of the Bragg and spikes distribution were taken equal to 5 dB.

Pulse length	Mean NRCS in dB on High wave density (d=10)	Mean NRCS in dB on Moderate wave density (d=50)	Mean NRCS in dB on Low wave density (d=100)
Short	-17.4	-25.6	-29.8
Medium	-17.3	-25.0	-28.6
Long	-17.2	-24.2	-27.4

Table 7. 1 - Computed mean NRCS results for different pulse length for high, moderate and low wave density on the sea surface

In conditions of high wave density when the distance between wave crests is small (d=10), the mean NRCS is found approximately equal at all pulse lengths and the wave crests can be assumed to behave as distributed scatterers. When the wave density is low (d=100), the mean NRCS increases significantly with pulse duration as larger pulse lengths have a better chance to intercept sea spikes. It is interesting to note that the

model also reproduces well the stronger sensitivity of the shorter pulse NRCS to the reduction in wave density which was observed in the experimental results between day 2 and 3.

The magnitude of the NRCS difference on different pulse length is lower than that observed experimentally but this may be the result of unrepresentative spikes statistics. The model was run for varying Bragg and spikes standard deviations comprised between 2 and 10 dB. As anticipated, the difference in mean NRCS with pulse length increases when the spikes standard deviation is large with respect to the Bragg distribution. When the variance of the spikes distribution is smaller or equal to the variance of the Bragg distribution, the difference in NRCS between pulse length vanishes as in the case of uniformly distributed scatterers.

Model's conclusions

The spatial and temporal integration model satisfactorily explains several characteristics of the sea backscatter coefficient obtained with the present system. The absence of large intensity sea spikes from even the short pulse images can be justified by considering the multi-pulse integration taking place in each antenna beamwidth. The higher NRCS observed on longer pulse settings can be attributed to the larger number of spikes intercepted by longer pulse lengths. It is believed that this increase in NRCS is also enhanced by the larger number of iterations on shorter pulse settings which result in a stronger reduction of the spikes influence in the final NRCS values. The model shows the difference in NRCS with pulse length to be strongly dependent on the spatial and statistical distributions of the sea spikes on the sea surface.

7.1.4 - Overall conclusion

The backscatter coefficient measured with the present system displays non-Rayleigh statistical properties but does not reproduce the wide range of NRCS commonly encountered with high resolution single pulse radars. The difference in the magnitude of the backscatter with pulse duration suggests that the ocean backscatter *on all pulse lengths* originates from both small scale distributed roughness and discrete wave crests

scattering. The exact evaluation of the dependence of the ocean backscatter coefficient with pulse length is difficult as most NRCS characteristics - including the mean value - are affected by the temporal and spatial parameters used for the data sampling. The NRCS magnitude ratio between pulse lengths also depends strongly on the spatial and statistical distribution of discrete scatterers on the sea surface with respect to the dimension of the radar sampling cell. In most conditions however, it can safely be assumed that longer pulse images will benefit from larger ocean NRCS values in comparison with shorter pulse lengths.

Combined with lower minimum detectable thresholds (MDS), longer pulse images will allow effective NRCS measurements up to ranges much larger than those observed in shorter pulse images. Longer pulse settings are therefore perfectly adapted for large scale coverage or measurements in low backscatter conditions. It should however be kept in mind that although all pulse settings are sensitive to wave crests scattering, only short pulse setting benefits from a sufficiently high spatial resolution to visually detect long crested waves and other small features in the images.

7.2 - Influence of the antenna height

The height of the antenna above sea level is probably the most difficult operational parameter to accommodate whether on a ship, a coastal site or an offshore platform. The deployment of the antenna is generally restricted by practical considerations. It is therefore particularly important to try to estimate the influence of this parameter on the ocean backscatter coefficient and the radar performances.

7.2.1 - Introduction

The variability of the ocean backscatter coefficient with antenna height is related to the associated change in grazing angle under which the radar wave hits the sea surface. In the normalisation equations, the grazing angle only intervenes in the calculation of the antenna footprint surface area. The dimension of the antenna footprint at any given range can be shown to be quasi-independent of the value of the antenna height for the

range of antenna heights and distances generally considered with the present system. The dependence of the backscatter coefficient on the grazing angle is therefore an intrinsic property of the ocean backscatter.

In the literature, the ocean backscatter coefficient is known to decrease with decreasing grazing angles in the range of low to intermediate incidence angles. This behaviour is well represented with the Two-scale backscatter model shown previously in Figure 6.2. In the region of low grazing angles smaller than 20 degrees, the relationship of the NRCS to the grazing angle changes gradually. The onset of complex propagation phenomena typical of radar radiations travelling close to the sea surface have given this range of incidence angle the denomination of "interference" region.

The evolution of the ocean NRCS with decreasing grazing angle in the interference region is not well understood in view of contradictory experimental evidence. In the past, some authors have reported the existence of a critical angle around 2 degrees from the horizontal below which the ocean NRCS suddenly decreases rapidly (Skolnik, 1990). This phenomenon was then attributed to the onset of destructive interference mechanisms between the incident and scattered radiation resulting in a rapid reduction in returned energy.

More recent investigations have since attributed this behaviour to shadowing effects. It is generally accepted that the electromagnetic scattering from the sea surface at low grazing angles is strongly affected by the shadowing of parts of the surface by higher wave crests. It has been argued that the rapid drop in backscatter coefficient below a certain grazing angle is reminiscent of the decrease in the proportion of ocean surface visible to the eye when viewed under progressively smaller grazing angles. As the look angle decreases, the sea surface has been described to increasingly resemble a "dark plane populated with isolated peaks" (Wetzel, 1977).

7.2.2 - Shadowing models

The effect of shadowing at microwave frequencies has been quantified mathematically in the form of a shadowing function. This function generally expresses the probability that a point on the sea surface is not shadowed by intervening wave crests along the incident path of the radar radiation. Hence the shadowing function is also commonly known as the probability of illumination. Experimental measurements of the sea surface NRCS are expected to include a dependence on the probability of illumination in the form of a multiplying factor comprised between 0 and 1. A probability of illumination equal to 1 signifies the absence of shadowing while a multiplying factor equal to 0 indicates total shadowing.

The approach adopted to estimate the shadowing function has generally been based on the Geometrical Optics approximation using ray tracing principles. The adequacy of the ray tracing approximation was examined by Wetzel (1987) who estimated the importance of diffraction in the shadowed area. He concluded that the Geometrical Optics shadowing theory provided an acceptable solution for the range of frequency, grazing angles and roughness conditions in which radar operations usually occur.

Conventional shadowing function

In the late 60's, several shadowing functions emerged, all developed from purely statistical arguments. Among those, the simplest and most often quoted function is that of Smith (1967). Assuming a normally distributed surface, Smith expresses the probability of illumination of a point at a height z on the surface as a function of the incidence angle and the surface rms height H and rms slope s0 as:

$$S(\zeta,\eta)=\left[1-\frac{1}{2}\cdot \mathrm{erfc}\zeta\right]^{\Lambda(\eta)} \qquad \text{Equation 7. 7}$$

introducing the normalised height ζ as:

$$\zeta=\frac{z}{\sqrt{2}.H} \qquad \text{Equation 7. 8}$$

the normalised grazing angle η defined as:

$$\eta = \frac{\varphi}{s0} \qquad \text{Equation 7. 9}$$

and where the function $\Lambda(\eta)$ reads:

$$\Lambda(\eta) = 0.5 \cdot \left[\sqrt{\frac{2}{\pi}} \cdot \frac{1}{\eta} \cdot \exp\left(-\frac{\eta^2}{2}\right) - \operatorname{erfc}\left(\frac{\eta}{\sqrt{2}}\right) \right] \qquad \text{Equation 7. 10}$$

The function erfc(.) represents the error function complement. Further integration of the original shadowing function permitted to express the probability that a point on the surface is illuminated independently of height and slope at the point. This shadowing function depends only on grazing angle and the surface rms slope $\tilde{s0}$ and essentially represents the percentage of surface area, on average, that will be illuminated at a given grazing angle in a given sea state. The conventional shadowing function reads:

$$S_C = \frac{1 - \frac{1}{2} \cdot \operatorname{erfc}\left(\frac{\eta}{\sqrt{2}}\right)}{\Lambda(\eta) + 1} \qquad \text{Equation 7. 11}$$

The variation of the conventional shadowing function S_C with grazing angle and rms slope is shown in Figure 7.7. The rms slope was chosen to represent a large variety of wind conditions. It was estimated from the ocean surface slope results obtained by Cox and Munk (1954) from sun glitter measurements in light to moderate wind speeds. The rms slope is calculated as a function of wind speed and direction for a clean or slick surface. For winds speeds between 5 and 15 m/s, the rms slope in the upwind direction for a clean surface is found to vary between 0.1 and 0.2 radians.

Figure 7.7 confirms that the shadowing function reproduces the behaviour intuitively expected. Points at higher grazing angles are only shadowed in very rough sea conditions while points at very low grazing angles will almost always lie in shadow. The rapid decrease in NRCS with decreasing grazing angles below 5 degrees also endorses the idea of a possible critical angle in the interference zone.

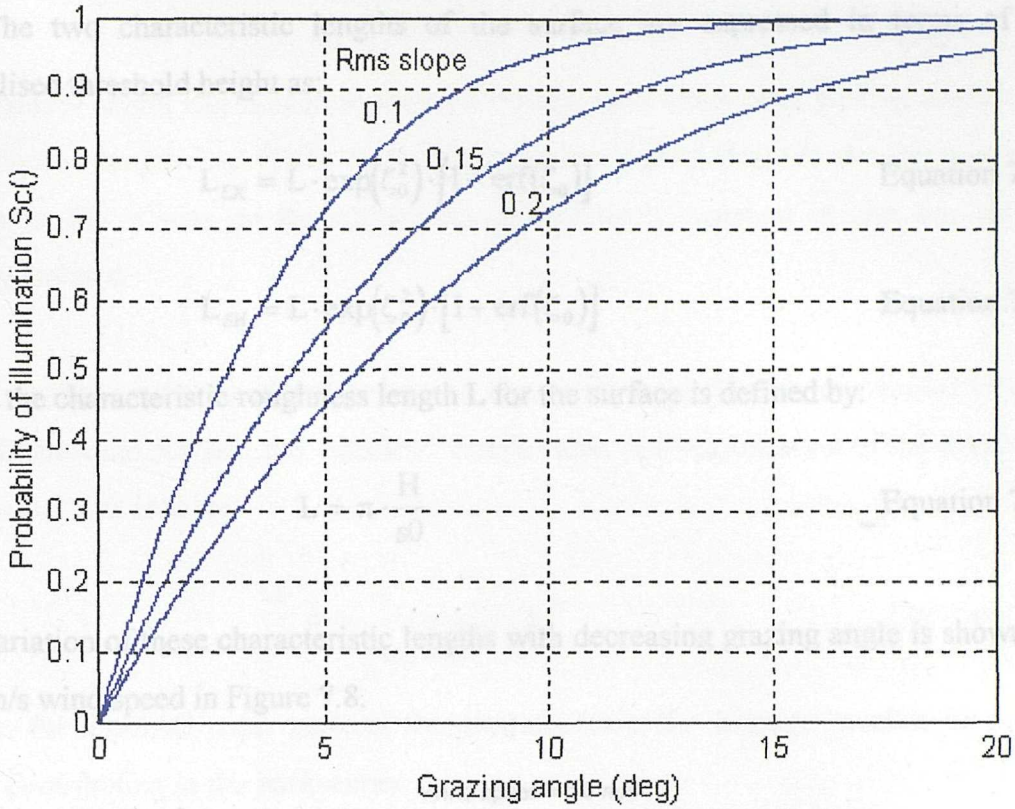

Figure 7. 7 - Conventional shadowing function versus grazing angle for a rms surface slope between 0.1 and 0.2 corresponding to wind speeds between 5 and 15 m/s.

Threshold shadowing model

The threshold shadowing function was developed by Wetzel (1977) and is based on the results from the conventional shadowing function. Using equation 7.7 to express the probability of illumination at a given point, Wetzel introduces the concept of normalised threshold height ζ_0 defined as the normalised height ζ for which the probability of illumination S_C (ζ_0,η) = 0.5. The threshold height is found to be a decreasing function of the normalised grazing angle η and can be approximated for small normalised grazing angles by:

$$\zeta_0 \approx 0.6 \cdot \left[\ln(0.275) - \ln(\eta)\right]^{3/4} \qquad \text{for } \eta \leq 0.275 \quad \text{Equation 7. 12}$$

Extending principles of temporal signal processing to the spatial domain, Wetzel also introduces the idea of "exposure length" L_{EX} and "shadow length" L_{SH} which allow him to describe the ocean viewed at low grazing angles as a surface on which isolated scattering "islands" of mean length L_{EX} are separated in a dark plane by a mean distance

L_{SH}. The two characteristic lengths of the surface are expressed in terms of the normalised threshold height as:

$$L_{EX} = L \cdot \exp\left(\zeta_0^2\right) \cdot \left[1 - \mathrm{erf}\left(\zeta_0\right)\right] \qquad \text{Equation 7. 13}$$

$$L_{SH} = L \cdot \exp\left(\zeta_0^2\right) \cdot \left[1 + \mathrm{erf}\left(\zeta_0\right)\right] \qquad \text{Equation 7. 14}$$

where the characteristic roughness length L for the surface is defined by:

$$L = \pi \cdot \frac{H}{s0} \qquad \text{Equation 7. 15}$$

The variation of these characteristic lengths with decreasing grazing angle is shown for a 10 m/s wind speed in Figure 7.8.

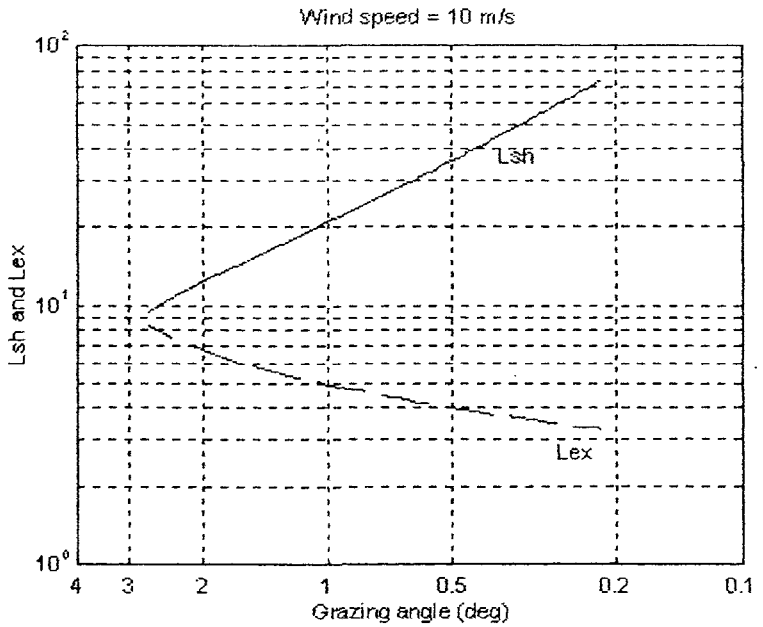

Figure 7. 8 - Characteristic length L_{EX} and L_{SH} in logarithmic scale against decreasing grazing angle at 10 m/s wind speed.

Once again, the surface rms slope s0 is calculated from Cox and Munk's (1954) empirical relationship to the wind speed. The rms height is calculated with respect to wind speed using the calculation of the surface variance based on a Phillips (1977) wave number spectrum for a one-sided uniform surface. The rms height (m) can be approximated by (Wetzel, 1977):

$$H \approx 0.005 \cdot U^2 \qquad \text{Equation 7. 16}$$

The shadow length L_{SH} is seen to increase rapidly with decreasing grazing angle while the exposed length L_{EX} varies little. This result suggests that, as the grazing angle decreases, the islands on the surface remain relatively constant in size but become rapidly isolated.

Assuming the scattering islands to be well separated and uniformly distributed over the two-dimensional surface, the "shadow" length leads to the estimation of the number of islands per unit area as:

$$n = \frac{1}{L_{SH}^2} \text{ peaks} / m^2 \qquad \text{Equation 7. 17}$$

Hence, for a pulsed radar antenna footprint Ar (m^2), the average number of surface peaks contributing to the backscatter is:

$$N_p = n \cdot Ar = \frac{Ar}{L_{SH}^2} \qquad \text{Equation 7. 18}$$

The factor N_p is defined as the "intermittency index" which characterises the scattering conditions. For N_p much larger than 1, the sea clutter comes from many independent islands and displays fluctuations about a mean value. The ocean backscatter intermittency is then said to be "high". For N_p much smaller than 1, the clutter signal is intermittent, consisting of receiver noise most of the time with an occasional sharp echo from an isolated island. This type of clutter corresponds to low intermittency conditions and appears in radar images as regions strongly affected by receiver noise featuring occasional spiky returns.

From these definitions, Wetzel (1990) suggests that for intermittency indexes much larger than 1, the average NRCS of the ocean at extreme grazing angles is equal to the average number of islands per unit area multiplied by the average cross section per island:

$$\sigma(\varphi) = \overline{\sigma}^{0}_{island}(\varphi) \cdot \frac{1}{2} \cdot \left(\frac{L_{EX}}{L_{SH}}\right)^2 \qquad \text{Equation 7. 19}$$

which leads him to the definition of the threshold shadowing function:

$$S_T = \frac{1}{2} \cdot \left[\frac{L_{EX}}{L_{SH}}\right]^2 = \frac{1}{2} \cdot \left[\frac{1 - \mathrm{erf}(\zeta_0)}{1 + \mathrm{erf}(\zeta_0)}\right]^2 \qquad \text{Equation 7. 20}$$

The threshold function is shown as a function of grazing angle and surface rms slope in Figure 7.9. The threshold shadowing function is defined only for extremely grazing angles and the precise range of grazing angles is determined by the surface rms slope via the condition expressed in equation 7.12. The grazing angles are generally found smaller than 5 degrees and in this range the probability of illumination decreases much more rapidly with decreasing grazing angle than the conventional shadowing function.

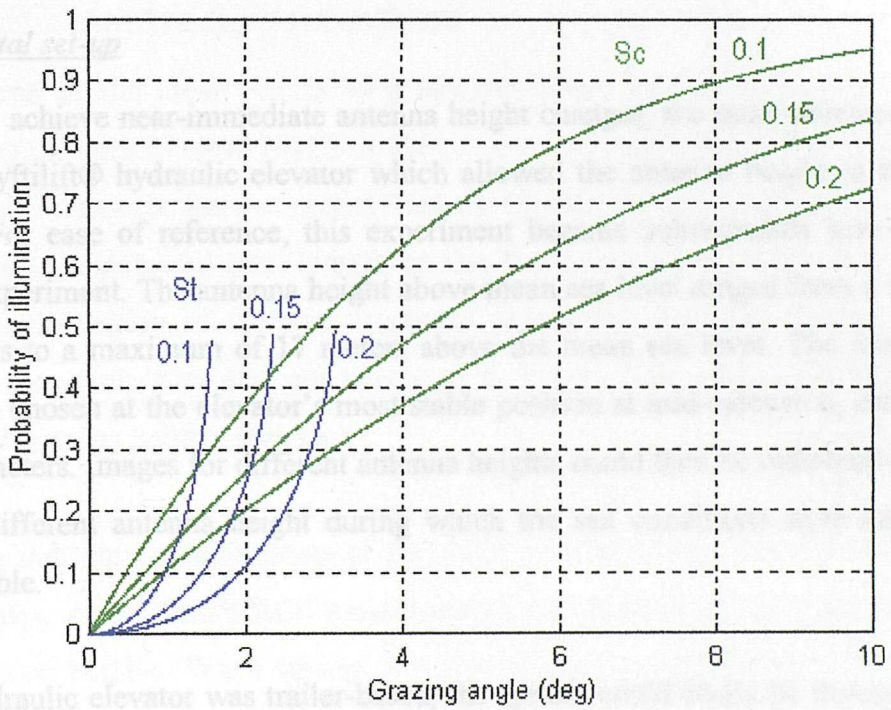

Figure 7. 9 - Threshold (blue) and conventional (green) shadowing functions versus grazing angle for rms slopes associated with wind speeds between 5 and 15 m/s.

This larger shadowing effect results from the threshold shadowing function representing more than just the backscatter reduction due to the geometrical shadowing of a proportion of the surface. It also includes the loss of backscatter caused by the receding

number of scattering islands intercepted by the antenna footprint with decreasing grazing angle. Hence, the threshold shadowing function is valid only for high intermittency indexes when the sea clutter originates from many scattering islands in the antenna footprint. At higher grazing angles and in conditions of low intermittency index, the shadowing is purely geometrical and the conventional shadowing function is expected to produce a better estimate of the loss of backscatter.

7.2.3 - Experimental observations: the Nyftilift® experiment

Experimental measurements of the ocean NRCS were taken using the present marine radar system. The aim of the experiment was to collect radar images over the same area with different antenna heights above mean sea level and with environmental conditions as similar as possible.

Experimental set-up

In order to achieve near-immediate antenna height changes, the radar antenna was set-up on a Nyftilift® hydraulic elevator which allowed the antenna height to be rapidly changed. For ease of reference, this experiment became subsequently known as the Nyftilift experiment. The antenna height above mean sea level ranged from a minimum of 7 meters to a maximum of 17 meters above the mean sea level. The intermediate height was chosen at the elevator's most stable position at mid-extension, estimated at about 13 meters. Images for different antenna heights could then be collected closely in time for different antenna height during which the sea conditions were assumed to remain stable.

As the hydraulic elevator was trailer-based, the system could easily be transported and was set up in Milford-on-Sea overlooking Christchurch Bay. Radar images were collected from the same site on three successive days characterised by rapidly changing environmental conditions. Details of the geographical area, the radar's field of view and the weather conditions have already been given in section 7.1 when part of this dataset was applied to examining NRCS changes with respect to pulse length setting.

Data collection

On all three days, images were collected for all pulse lengths from antenna heights equal to 7, 13 and 17 meters, resulting in a minimum of 27 images. For each image, a time series of 16 single rotation images was collected and the average and standard deviation images were computed. The average image was then calibrated using the normalisation equations.

For reasons of limited power supply, the antenna height could only be changed a limited number of times on each day. Hence, the antenna height was changed only after a complete set of images for all pulse lengths was obtained and the time between images collected on a same pulse setting with different antenna height could vary from 30 to 90 minutes.

Results - NRCS variation with antenna height

The variation of the mean NRCS with antenna height was examined to determine whether any changes in mean NRCS could be observed with a small change in antenna height. NRCS transects were extracted from the 16-rotations averaged images obtained for all antenna heights and pulse lengths on Day 2. Transects were taken at azimuth bin 100 within the region of uniform roughness previously identified during the pulse setting investigation. The data are presented in Figure 7.10 with the different pulse lengths and antenna heights indicated.

The results indicate a clear increase of the NRCS with increasing antenna height for all pulse settings. Also, valid NRCS measurements are obtained up to larger ranges for larger antenna heights. When viewed in terms of grazing angles, these results are in good agreement with a reduction in shadowing with increasing grazing angles.

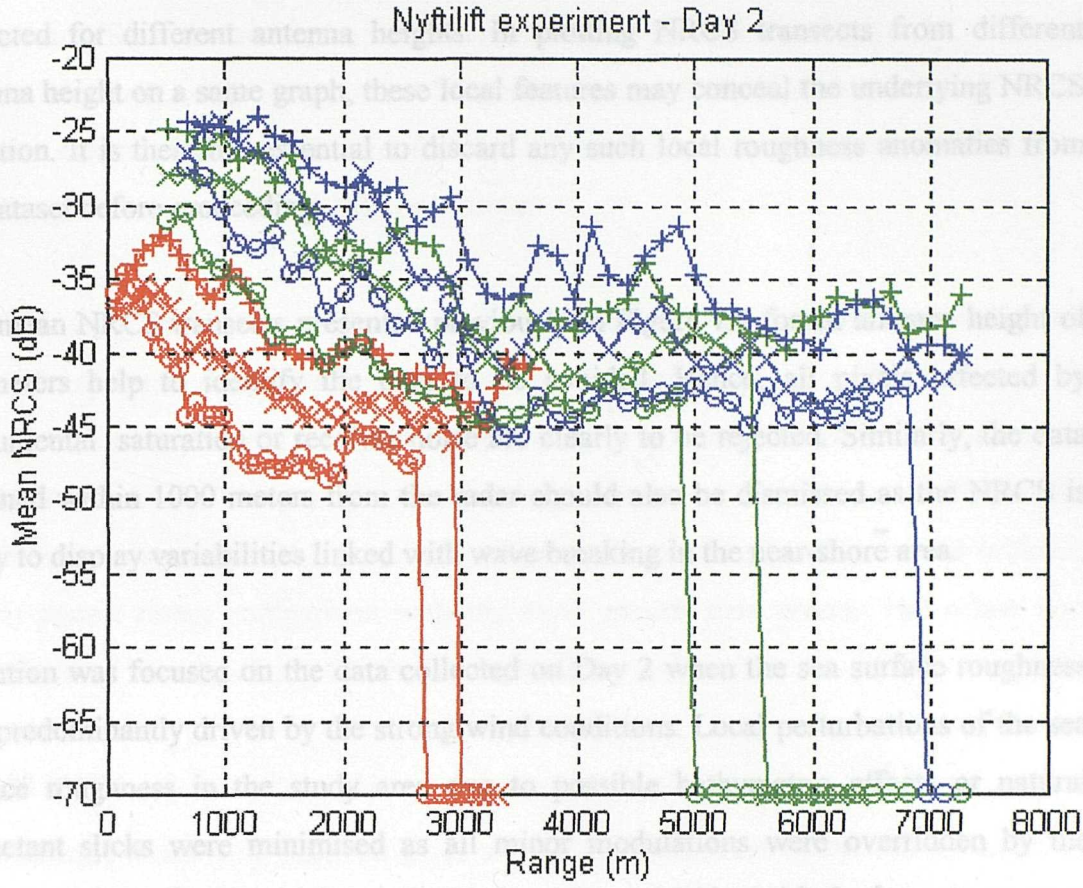

Figure 7. 10 - Mean NRCS transects for images obtained on Day 2 with short (red), medium (green) and long (blue) pulse setting. The symbol "o", "x" and "+" indicate antenna heights respectively equal to 7, 13 and 17 meters.

7.2.4 - Comparison of the shadowing functions with the Nyftilift experimental results

Both shadowing functions were compared with the Nyftilift data to determine whether they constitute a suitable tool to describe the variation with grazing angle of the ocean NRCS measured with the present system. For each image, the NRCS is represented by a mean radial transect computed by averaging in azimuth all transects between azimuth bearing 180 and 220 in the average NRCS images.

Data selection for comparison with shadowing functions

Because of the dependency of the grazing angle on antenna height, any surface feature located at a given range will be displayed at a different grazing angle in images

collected for different antenna heights. In plotting NRCS transects from different antenna height on a same graph, these local features may conceal the underlying NRCS variation. It is therefore essential to discard any such local roughness anomalies from the dataset before proceeding.

The mean NRCS transects presented previously in Figure 7.4 for an antenna height of 17 meters help to identify the data to be avoided. Hence, all pixels affected by instrumental saturation or receiver noise are clearly to be rejected. Similarly, the data obtained within 1000 meters from the radar should also be dismissed as the NRCS is likely to display variabilities linked with wave breaking in the near-shore area.

Attention was focused on the data collected on Day 2 when the sea surface roughness was predominantly driven by the strong wind conditions. Local perturbations of the sea surface roughness in the study area due to possible bathymetric effects or natural surfactant slicks were minimised as all minor modulations were overridden by the action of the wind on the surface. This dataset also coincides with the largest coverage in range for which valid NRCS measurements were obtained during the experiment. The data therefore cover an extensive range of grazing angles ideally suited for a comparison with the shadowing models.

Results

The mean NRCS transects for all images obtained on Day 2 of the Nyftilift experiment were plotted against grazing angle. The grazing angle for each pixel in the transect was calculated from the pixel range R and the antenna height h as:

$$\varphi = \mathrm{a}\sin\left(\frac{\mathrm{h}}{\mathrm{R}}\right) \qquad \text{Equation 7. 21}$$

The conventional and the threshold shadowing functions were computed for the range of grazing angles covered by each image. The rms surface slope values were calculated from the wind speed using the Cox and Munk (1954) results for a clean surface. For an approximate wind speed of 12 m/s, the rms slope is found equal to 0.195.

The mean NRCS transects are shown against grazing angle in Figure 7.11. In the interest of clarity, only 1 in every 10 pixels was plotted. The data obtained with different antenna heights are identified by different symbols while the difference in pulse length is represented by different colours.

The shadowing functions are plotted in dB and appear as straight lines in the log-log scale. The offset of each function changes with the surface rms slope but the slope of each particular shadowing function is invariable. The threshold shadowing function appears as the line of steepest slope indicating the more rapid increase in NRCS with increasing grazing angle. The shadowing functions were linearly offset on the ordinate axis to permit direct comparison with the experimental data points. The offset was determined by visually fitting the shadowing functions to the data.

Data analysis

The threshold shadowing function gives a good approximation of the NRCS variation with grazing angle for most of the medium and long pulse datasets and for short pulse at large grazing angles. The NRCS data diverge from the threshold shadowing function at very small grazing angles, corresponding to data collected at far ranges. In this region, the slower decay in NRCS with decreasing grazing angle is better represented by the conventional shadowing function.

The deviation from the threshold shadowing model occurs at different grazing angles for NRCS measured with different pulse lengths and antenna heights. For a given antenna height, the point of divergence is observed at a smaller grazing angle for longer pulse data and thus occurs at a larger range from the radar. For a given pulse length, the divergence also appears at smaller incidence angles for smaller antenna heights but this time corresponds to a point located at a smaller distance from the radar.

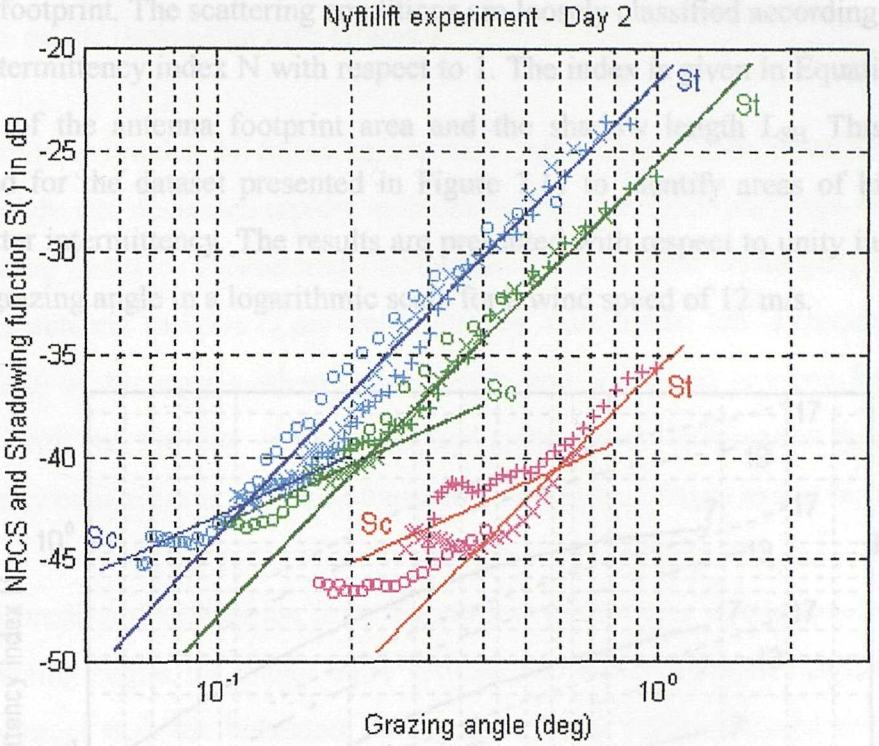

Figure 7. 11 - Mean NRCS transects against grazing angle for data obtained on day 2 on all pulse lengths. The symbols "o", "x" and "+" correspond to data collected with antenna height equal to 7, 13 and 17 meters respectively. The data collected on short, medium and long pulse are represented in red, green and blue.

The possibility of anomalous propagation conditions during the experiment was considered. This phenomenon, also known as atmospheric ducting, causes radar waves to be trapped in the near-surface evaporative layer and changes the dependency of the grazing angle on antenna height and range. Further details and the new expression for the calculation of the grazing angle is given in appendix C. Hence, the difference in the location of the divergence point may be a result of atmospheric effects. The data in Figure 7.11 were therefore plotted against the modified grazing angle calculated for various propagation conditions. No significant change was observed in the location of the deviation points as the effect of ducting only becomes important for ranges beyond 10 km.

Discussion - Backscatter intermittency conditions

The threshold shadowing function has been defined for conditions of high backscatter intermittency when the backscatter originates from many scattering islands in the

antenna footprint. The scattering conditions are loosely classified according to the value of the intermittency index N with respect to 1. The index is given in Equation 7.18 as a function of the antenna footprint area and the shadow length L_{SH}. This index was computed for the dataset presented in Figure 7.11 to identify areas of high and low backscatter intermittency. The results are presented with respect to unity in Figure 7.12 against grazing angle in a logarithmic scale for a wind speed of 12 m/s.

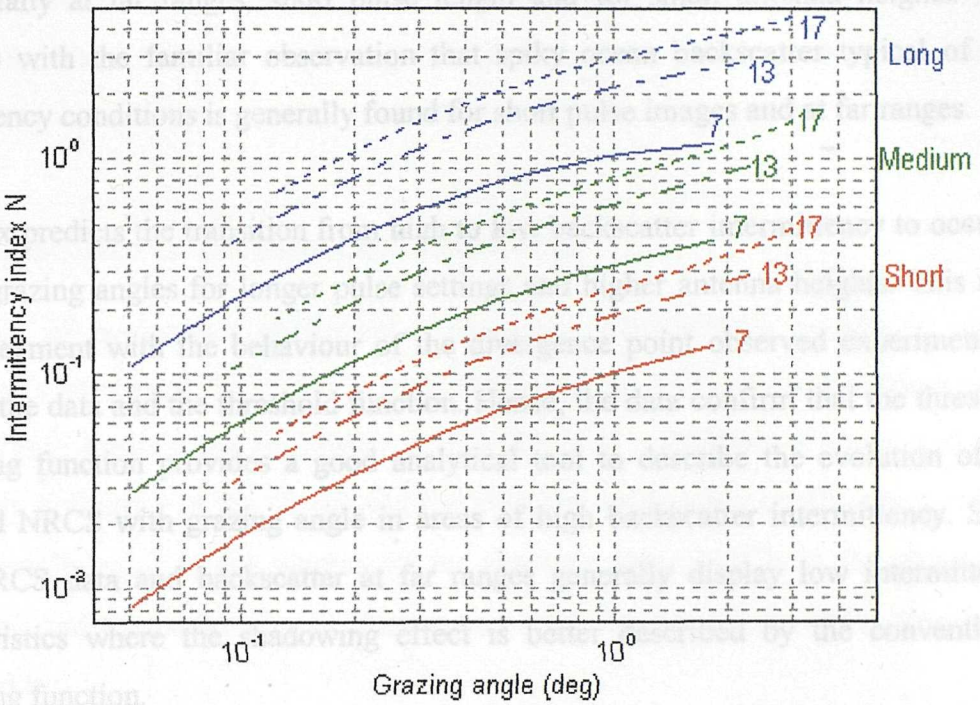

Figure 7. 12 - Intermittency index calculated for all pulse lengths and antenna heights and a 12 m/s wind speed. The solid, dash-dotted and dashed plots correspond to antenna heights equal to 7, 13 and 17 meters respectively.

The intermittency index calculated for the dataset is generally smaller than unity except on long pulse and large grazing angles. It should be noted here that the absolute value of the intermittency index is probably not representative of the real number of scattering islands in the antenna footprint. Aside from any possible doubts about the validity of the model, the rms slope parameter, critical in the calculation of the index's absolute value, was obtained from a rough wind speed estimate. Furthermore, the empirical relationship between the rms slope and wind speed proposed by Cox and Munk applies to the surface roughness in the open ocean and is not rigorously valid in coastal waters. Nevertheless, the index N gives a correct estimate of the relative importance of various

parameters on the backscatter intermittency.

The intermittency index is found to increase significantly with pulse duration and antenna height and decreases rapidly with decreasing grazing angle. High intermittency conditions are therefore characteristic of backscatter measured on longer pulse settings and large antenna heights. Low intermittency conditions are expected to occur preferentially at far ranges, short pulse length and for small antenna heights. This conforms with the familiar observation that spiky ocean backscatter typical of low intermittency conditions is generally found for short pulse images and at far ranges.

The index predicts the transition from high to low backscatter intermittency to occur at smaller grazing angles for longer pulse settings and higher antenna heights. This is in good agreement with the behaviour of the divergence point observed experimentally between the data and the threshold function. Hence, the data confirm that the threshold shadowing function provides a good analytical tool to describe the evolution of the measured NRCS with grazing angle in areas of high backscatter intermittency. Short pulse NRCS data and backscatter at far ranges generally display low intermittency characteristics where the shadowing effect is better described by the conventional shadowing function.

7.2.5 - Conclusion

The influence of the antenna height on the ocean NRCS is related primarily to the associated change in grazing angle under which the radar views the sea surface. The precise nature of the shadowing regime in the interference zone has been shown to depend on the ocean backscatter intermittency conditions. The variation of the ocean backscatter coefficient with grazing angle is well reproduced by the threshold shadowing model in conditions of high backscatter intermittency while the conventional model is better suited to describe the shadowing regime in regions of low backscatter intermittency.

High backscatter intermittency conditions are generally expected to prevail at close ranges while low intermittency regions are confined to far ranges. The transition range from high to low intermittency is dependent on the pulse setting, the antenna height and the environmental conditions. The occurrence of low backscatter intermittency is identified in images by the onset of receiver noise as the ocean backscatter level approaches the lower detection limit of the instrument at that range. Hence, the detection performances of the system on different pulse settings must be redefined to account for the effect of shadowing for given antenna height and environmental conditions.

7.3 - Absolute detection performances

The range of backscatter coefficient measurable experimentally is defined by the instrument's Minimum Detectable Signal (MDS) and the SATuration equivalent NRCS (SAT). These limits were established in Chapter 5 as a function of range and pulse length. By definition of the shadowing function, the backscatter coefficient measured experimentally σ_{mes}^{0} is the product of the absolute ocean NRCS in the absence of shadowing and the probability of illumination $S(\varphi)$. In logarithmic scale, this can be expressed as:

$$\sigma_{mes}^{0}(\mathrm{dB}) = \sigma_{abs}^{0}(\mathrm{dB}) + 10 \cdot \log_{10} S(\varphi) \qquad \text{Equation 7. 22}$$

The absolute ocean NRCS σ_{abs}^{0} is a measure of the sea surface roughness independently of the viewing angle. In presence of shadowing, the minimum σ_{abs}^{0} required to exceed the receiver noise level needs to be larger to allow for the loss of backscatter with shadowing. Hence, the detection performances of the system when accounting for shadowing are redefined as the absolute MDS and SAT. These minimum and maximum detectable absolute ocean NRCS are then expressed in dB as:

$$\mathrm{MDS}_{\mathrm{absolute}} = \mathrm{MDS}_{\mathrm{instrument}} - 10 \cdot \log_{10} S(\varphi) \qquad \text{Equation 7. 23}$$

$$\mathrm{SAT}_{\mathrm{absolute}} = \mathrm{SAT}_{\mathrm{instrument}} - 10 \cdot \log_{10} S(\varphi) \qquad \text{Equation 7. 24}$$

The reduction of the absolute SAT by shadowing is generally beneficial as it reduces the risk of saturation. In contrast, the backscatter loss caused by shadowing is detrimental to the system's lower limit of detection capabilities. Hence, the most important aspect of shadowing to be quantified is its impact on the system's absolute MDS. The following argument is therefore entirely focused on the definition of the absolute MDS, although all results can be readily applied to the definition of the absolute SAT.

7.3.1 - Graphical representation of the absolute MDS

The diagrammatic representation of the absolute MDS is difficult because of the many variables involved in the estimation of the shadowing. It was decided to retain the format used for the instrumental MDS whereby the MDS is displayed against range. Hence, the shadowing function is first calculated as a function of grazing angle for different environmental conditions and subsequently expressed against range by applying different values of antenna height.

An example of the graphical representation to be adopted hereafter is given in Figure 7.13. In the interest of clarity, the absolute MDS is presented for short pulse only, in relation to the instrumental MDS and the shadowing function. In this example, the absolute MDS is calculated from both conventional and threshold shadowing models to illustrate the change in the increase of the absolute MDS with range for different shadowing regimes. The probability of illumination is estimated for a 50 m antenna height and 5 m/s wind speed.

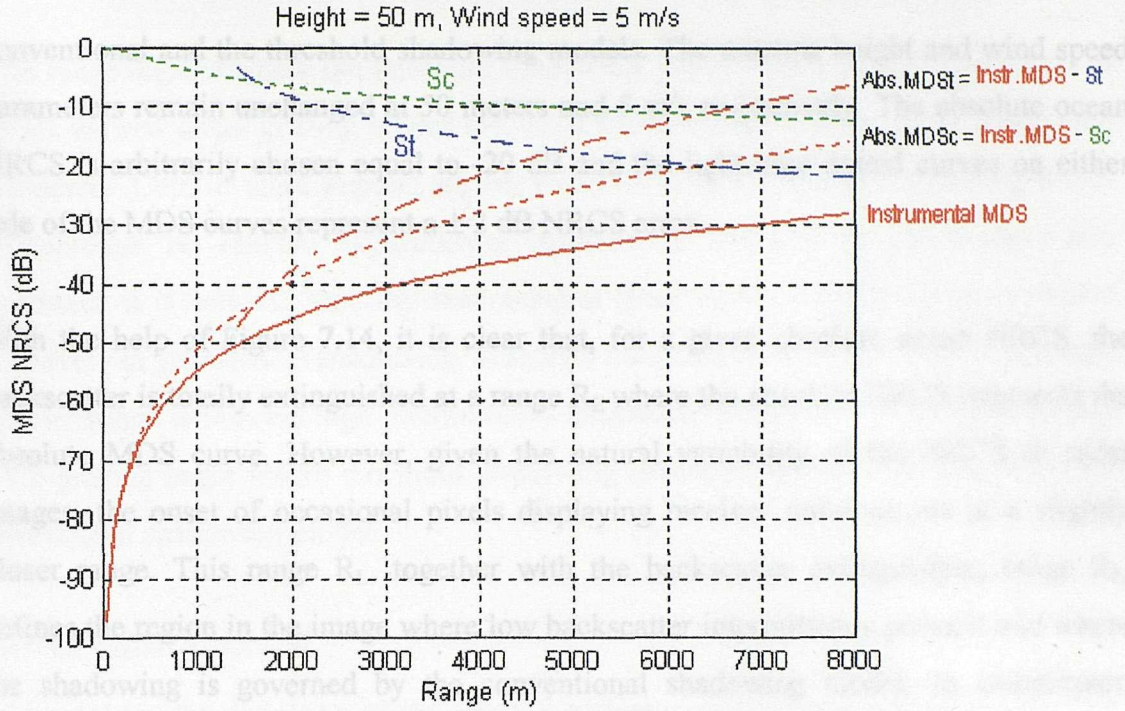

Figure 7. 13- Absolute MDS calculated for short pulse setting with the conventional (dashed line) and the threshold (dotted line) shadowing model. The antenna height is 50 meters and the wind speed is 5 m/s. The solid line represent the instrumental MDS.

7.3.2 - Shadowing regimes at different ranges

It was established earlier that the most appropriate shadowing model for the description of the ocean NRCS with range is determined by the backscatter intermittency conditions. The dependency of intermittency with range has indicated that regions located at close ranges are generally governed by the threshold shadowing regime while far range regions will exhibit the slower decay of NRCS with range predicted by the conventional shadowing model.

Transition range

By definition, the transition range from high to low backscatter intermittency corresponds to the area where the received power approaches the system's MDS. Expressed in terms of absolute sea surface backscatter coefficient, this transition occurs where the absolute ocean NRCS becomes close to the absolute MDS at that range. Figure 7.14 represents the absolute MDS for short pulse calculated as for Figure 7.13 from the instrumental MDS and the probability of illumination obtained with both the

conventional and the threshold shadowing models. The antenna height and wind speed parameters remain unchanged at 50 meters and 5 m/s respectively. The absolute ocean NRCS is arbitrarily chosen equal to -20 dB and the light-blue dotted curves on either side of the MDS curves represent a ± 2 dB NRCS error.

With the help of Figure 7.14, it is clear that, for a given absolute ocean NRCS, the backscatter is totally extinguished at a range R_E where the absolute NRCS intersects the absolute MDS curve. However, given the natural variability of the NRCS in radar images, the onset of occasional pixels displaying receiver noise occurs at a slightly closer range. This range R_L, together with the backscatter extinguishing range R_E, defines the region in the image where low backscatter intermittency prevails and where the shadowing is governed by the conventional shadowing model. In counterpart, regions located at ranges smaller than R_L benefit from high backscatter intermittency and obey the threshold shadowing function when viewed under sufficiently low grazing angles.

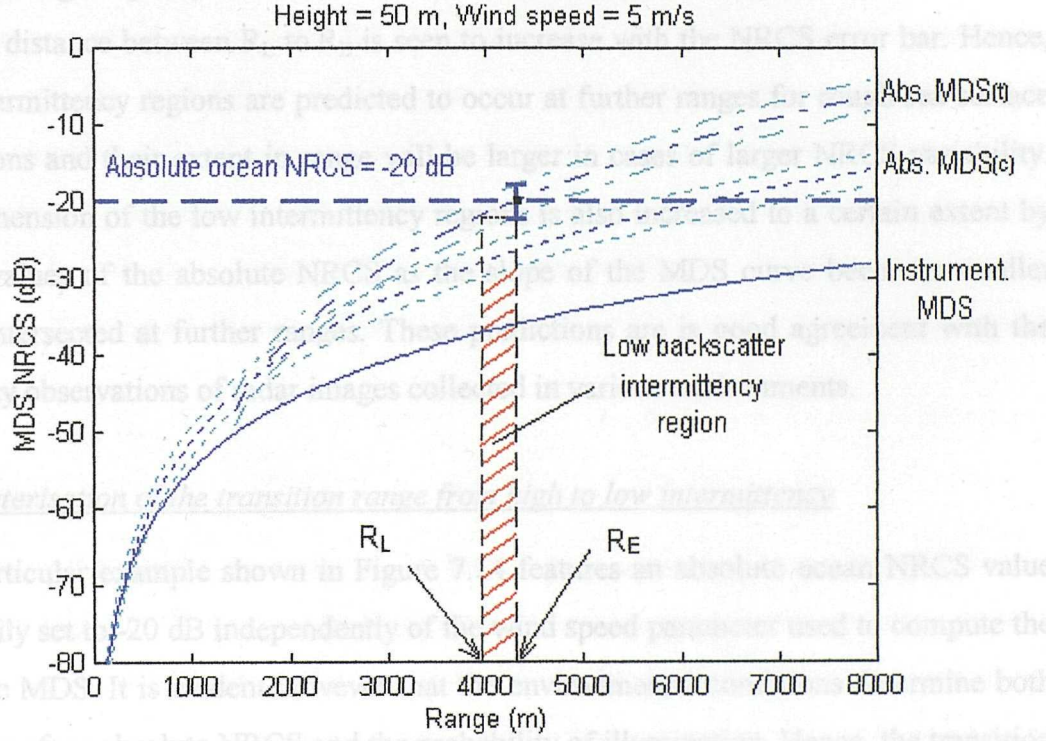

Figure 7. 14 - Determination of the low backscatter intermittency region for short pulse images with an absolute ocean NRCS of -20 dB and a NRCS standard deviation of ± 2 dB.

Close range regions where the threshold shadowing model is not defined correspond to regions viewed under grazing angles too large to experience the threshold shadowing mechanism. Data in these regions are not expected to display large shadowing losses and although no reliable experimental evidence is available to substantiate this hypothesis, it is believed that any shadowing at these higher grazing angles is related exclusively to geometrical shadowing. A second transition point is therefore anticipated at closer range within the high intermittency backscatter conditions which corresponds to the grazing angle where threshold shadowing becomes dominant and replaces the conventional shadowing model.

Low intermittency region

The model for the definition of the low intermittency region presented in Figure 7.14 indicates that the absolute ocean NRCS and the NRCS variability, represented by the error bar at range R_E, determine the location and dimension of this region. Indeed, the extinguishing range R_E is clearly determined by the magnitude of the absolute NRCS, and the distance between R_L to R_E is seen to increase with the NRCS error bar. Hence, low intermittency regions are predicted to occur at further ranges for rough sea surface conditions and their extent in range will be larger in cases of larger NRCS variability. The dimension of the low intermittency regions is also increased to a certain extent by larger values of the absolute NRCS as the slope of the MDS curve becomes smaller when intersected at further ranges. These predictions are is good agreement with the everyday observations of radar images collected in various environments.

Parameterisation of the transition range from high to low intermittency

The particular example shown in Figure 7.14 features an absolute ocean NRCS value arbitrarily set to -20 dB independently of the wind speed parameter used to compute the absolute MDS. It is evident however that the environmental conditions determine both the sea surface absolute NRCS and the probability of illumination. Hence, the transition range can only be estimated and compared with experimental results after a relationship between the absolute ocean NRCS and environmental conditions is obtained. This topic is investigated in Chapter 8.

The transition range was seen from experimental evidence to increase rapidly with pulse duration. Part of this can be attributed to the lower instrumental MDS on longer pulse setting which extends the range where receiver noise becomes apparent. In addition, the ocean NRCS has been found to increase with the pulse duration as a result of the non-uniform distribution of scatterers on the sea surface. The parameterisation of the transition range must therefore account for this intrinsic increase in the absolute NRCS with pulse length. The relationship defining the absolute ocean NRCS with environmental conditions must therefore be established for each pulse length individually.

Quantitative evaluation of the shadowing models

So far, the shadowing theories have been compared successfully with experimental results from a qualitative point of view. The models reproduce the rate of change of the ocean NRCS with grazing angle. The existence of a transition point visible in radar images which marks the passage from a threshold to a conventional shadowing regime provides a method to evaluate the validity of the shadowing models' quantitative estimate of the probability of illumination. In particular, the suitability of the parameterisation of the shadowing with the surface rms slope (via the wind speed) may be examined by comparing the transition range estimated from the model shown in Figure 7.14 with the location of the transition point seen in radar images. This validation relies on an estimate of the absolute ocean NRCS and is therefore covered in Chapter 8.

Conclusion

The shadowing regime experienced for low grazing angle radars is generally divided into three regions: (1) a far range region where low backscatter intermittency prevails and the ocean NRCS obeys the conventional shadowing model, (2) a closer range region at grazing angles less than 1 degree where backscatter intermittency is high and threshold shadowing dominates, and (3) a close range region at larger grazing angles where shadowing losses are small and data are expected to follow the conventional shadowing model.

Both transition points from zone 1 to 2 and zone 2 to 3 are determined by the threshold shadowing function. The shadowing regime is therefore entirely defined by the absolute ocean NRCS and the absolute MDS values calculated with the threshold shadowing function for different antenna height, pulse length and environmental conditions. This modelling of the shadowing regime relies strongly on the evaluation of the probability of illumination by the threshold shadowing model. The validity of this model can only be examined after a relationship between the absolute ocean NRCS on different pulse lengths and environmental conditions is obtained and is consequently investigated in Chapter 8.

7.3.3 - Dependence of the absolute MDS model on wind speed and antenna height

This section establishes the relative importance of the wind speed and the antenna height parameters on the value of the absolute MDS. The absolute MDS is computed from the instrumental MDS and the threshold shadowing function (Equation 7.23). In the interest of clarity, the effects of wind speed and antenna height are examined separately. The absolute MDS results are shown only for short pulse as the detection performances for medium and long pulse differ only by the value of their respective instrumental MDS. The absolute MDS for medium and long pulse for different winds and antenna heights can therefore be deduced by simply lessening the results for short pulse by 5 and 12 dB respectively, representing the reduction in instrumental MDS.

The selected range of wind speed varies from 1 to 15 m/s to coincide with the domain of validity of the Cox and Munk slope statistics. The antenna height varies from 3 to 100 meters to represent the range of antenna heights typical for a coastal site on the south coast of England.

Antenna height

The effect of antenna height on the absolute MDS is presented in Figure 7.15 for a 7 m/s wind speed.

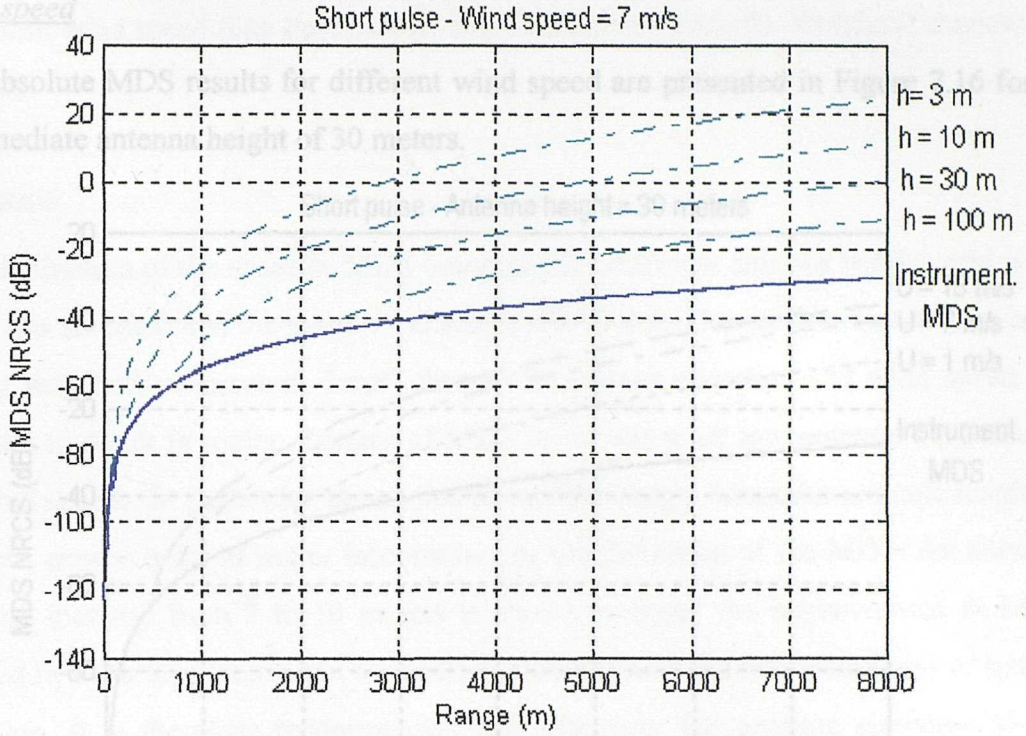

Figure 7. 15 - Modelled absolute MDS equivalent NRCS on short pulse setting for different antenna heights and a 7 m/s wind speed.

The predicted absolute MDS decreases with increasing antenna height in accordance with the larger probability of illumination associated with larger grazing angles. The transition range where receiver noise starts to appear is predicted to increase for larger values of the antenna height. The threshold shadowing mechanism is expected to occur at closer ranges for lower antenna heights thus causing the NRCS to decrease more rapidly at close ranges. The improvement of the absolute MDS with increasing antenna height is non-linear as demonstrated by the 8 dB decrease in MDS observed for both a 7 m increase from 3 to 10 m and a 70 m increase from 30 to 100 m.

These predictions are well supported by the experimental evidence obtained during the Nyftilift campaign. The increase of the transition range with antenna height, the faster reduction of the ocean NRCS at close ranges and the non-linear increase of the transition range with increasing antenna height were all clearly exhibited in the data shown in Figure 7.10 and 7.11.

Wind speed

The absolute MDS results for different wind speed are presented in Figure 7.16 for an intermediate antenna height of 30 meters.

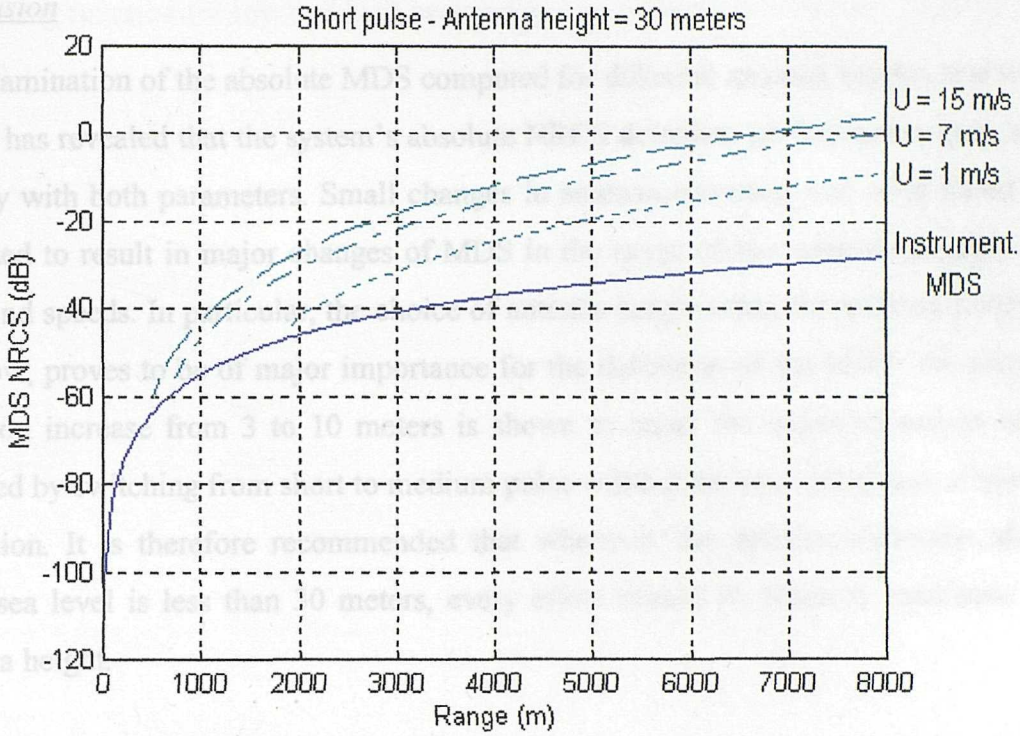

Figure 7. 16 - Modelled absolute MDS equivalent NRCS on short pulse setting for different wind speeds and a 30 meters antenna height.

The absolute MDS increases with wind speed following the decrease in the probability of illumination with higher sea states, and the threshold shadowing mechanism is predicted to occur at closer ranges for higher wind speeds. The predicted increase in MDS with wind speed is non-linear as demonstrated by the large discrepancy in MDS improvement between a similar magnitude wind increase from 1 to 7 m/s and 7 to 15 m/s.

The increase in MDS with wind speed suggests that the transition range should be smaller for larger wind speeds. This is in apparent contradiction with experimental evidence shown in Figure 7.4 which indicates that the transition range occurs further away from the radar for high wind speed conditions. This inconsistency implies that the increase in the absolute ocean NRCS with wind speed must compensate for the increase in absolute MDS. The absolute ocean NRCS is therefore expected to increase much

faster with wind speed than the absolute MDS calculated with the threshold shadowing function.

Conclusion

The examination of the absolute MDS computed for different antenna heights and wind speeds has revealed that the system's absolute NRCS detection performances vary non-linearly with both parameters. Small changes in antenna elevation and wind speed are predicted to result in major changes of MDS in the range of low antenna heights and low wind speeds. In particular, the choice of antenna height when the antenna height is very low, proves to be of major importance for the definition of the MDS. An antenna elevation increase from 3 to 10 meters is shown to equal the improvement in MDS obtained by switching from short to medium pulse without the associated loss of spatial resolution. It is therefore recommended that whenever the antenna elevation above mean sea level is less than 30 meters, every effort should be made to maximise the antenna height.

7.4 - Overall conclusion

The investigation into the effect of pulse setting and antenna height has revealed that these operational parameters change not only the mean ocean NRCS measurements but also the whole nature of the ocean backscatter at different ranges. Both parameters were indeed shown to have a profound effect in defining the backscatter intermittency conditions which govern the NRCS statistics and determine the shadowing regime.

The pulse length examination has established that the NRCS data obtained with the present system do not feature the high energy sea spikes described in the literature for high resolution radars. The observed increase in ocean NRCS with pulse duration however indicates that the ocean backscatter measured on all pulse settings comprises a strong contribution from non-uniformly distributed wave crests. The precise increase in NRCS with pulse duration was found to depend on the parameters of the data collection procedure and the spatial density of waves on the surface with respect to the dimension of the antenna footprint. The examination into the effect of the antenna height has

revealed that the NRCS changes with antenna height are entirely related to the associated change in grazing angle. The variation of the NRCS with grazing angle has been successfully compared with predictions from the conventional and the threshold shadowing function for low and high backscatter intermittency conditions respectively.

Chapter 8

The Relationship between Environmental Conditions and the Ocean Backscatter

This final chapter sets out to answer several questions regarding the role of environmental parameters in the absolute ocean backscatter coefficient. Firstly, the principal environmental variables responsible for changes in ocean backscatter are examined and empirical relationships for the estimation of the ocean NRCS are investigated. Then, these relationships are applied to validate the quantitative accuracy of the shadowing model presented in Chapter 7. Finally, examples of oceanographic applications are presented where the marine radar system provides key information on physical ocean processes.

8.1 - Principal environmental parameters: the Portland experiment

The principal environmental parameters influencing the ocean backscatter are identified from experimental results of a long-term deployment of the radar system in a fixed location. The experiment took place in Autumn 1994 to experience as wide as possible a range of environmental conditions and enable empirical relationships to be derived.

This section provides details of the experimental set-up and the environmental data collected. Background oceanographic information is given for the area observed with the radar system and the environmental conditions encountered during the experiment are examined.

8.1.1 - Experimental set-up

Marine radar deployment

The marine radar system was deployed over a period of 4 weeks on the west coast of the Isle of Portland in Dorset, UK. The geographical location of the radar site is presented in Figure 8.1. The western coast of the island consists of a near vertical cliff reaching nearly 60 meters above mean sea level. Hence, for safety and security reasons associated with the hazardous surroundings and the duration of the deployment, the marine radar system was granted access to the secure perimeter belonging to the Defence Research Agency (DRA) in Southwell, Portland.

The radar system was deployed from a Portacabin positioned along the DRA perimeter fence which resulted in the radar antenna being located less than 5 meters from the edge of the cliff. The radar antenna was secured on a frame on top of the Portacabin resulting in a total antenna height of 60 metres. The radar location provided 180 degree coverage in azimuth over the sea surface. The maximum surface area imaged with the radar is indicated in Figure 8.1 for a maximum range of 4.2 nautical miles (c. 7600 meters).

Environmental data collection

In addition to the radar data, *in situ* meteorological and oceanographic data were collected from instrumented buoys situated within the radar observation area. Three buoys were deployed by the Institute of Oceanographic Sciences (IOS) on behalf of DRA Portland to provide information on the near surface wind field, air and sea temperature, ocean wave spectra and oceanic current. The buoys were moored in 40 metres of water approximately 1.5 nautical mile (2700 meters) offshore almost directly west of the radar site. The approximate location of the three buoys is indicated in Figure 8.1. To facilitate the detection and location of the buoys in the radar images, one of the three buoys was fitted with a radar reflector.

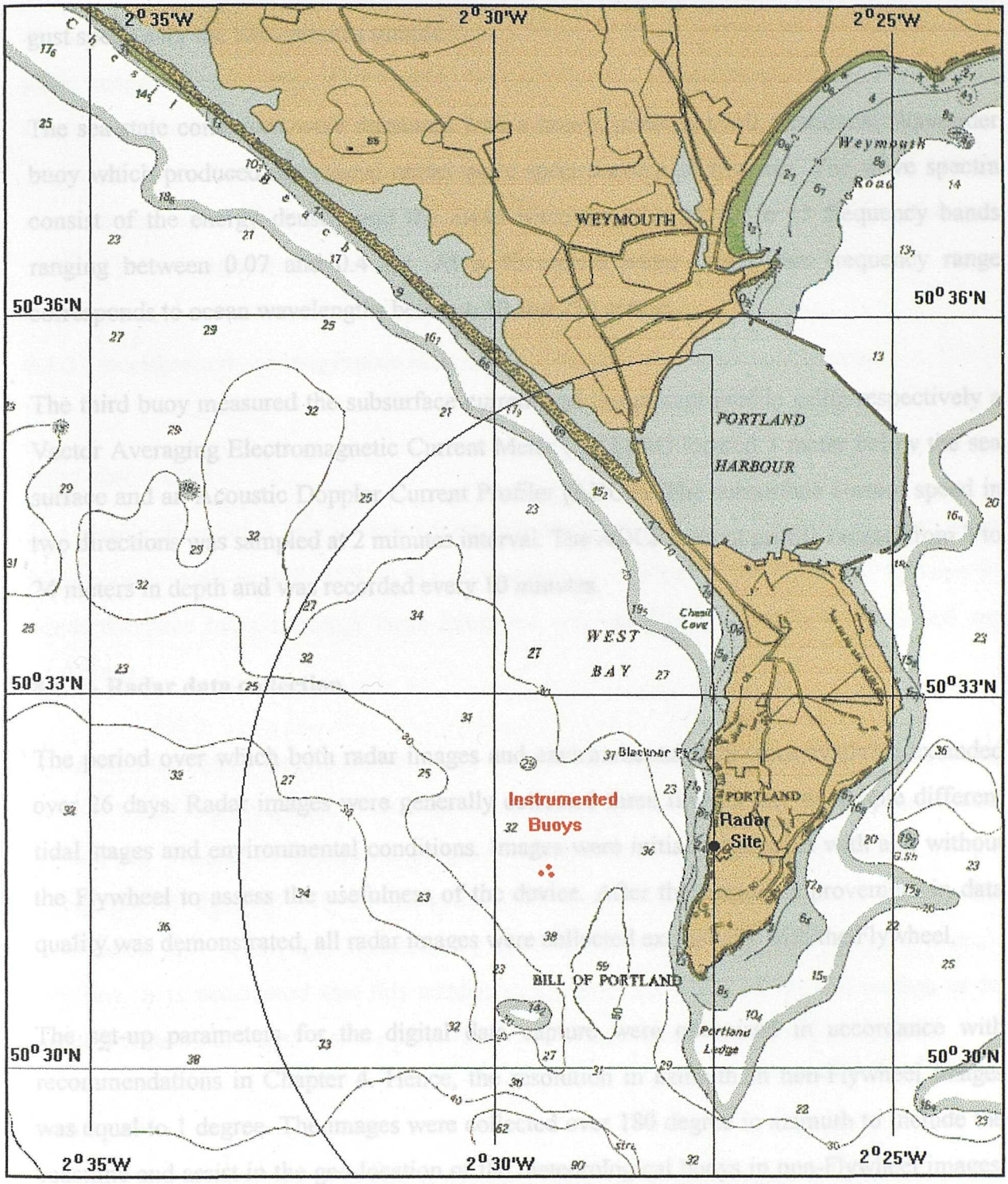

Figure 8. 1 - Radar site and observation area during the Portland experiment (adapted from Admiralty Chart 2615)

The meteorological buoy provided wind measurements at 2.5 meters above the sea surface and information on air and sea temperature. The data were sampled continuously and averaged over two-minutes records. The wind speed record included both the average and the

gust speed over the two-minutes sample.

The sea state conditions were measured with a heave, pitch and roll directional Waverider buoy which produced directional ocean wave spectra every 30 minutes. The wave spectra consist of the energy density and the mean wave direction given in 15 frequency bands ranging between 0.07 and 0.4 Hz. At a 40 meters water depth, this frequency range corresponds to ocean wavelengths between 10 and 250 meters.

The third buoy measured the subsurface current and the current profile using respectively a Vector Averaging Electromagnetic Current Meter (VAECM) located 1 meter below the sea surface and an Acoustic Doppler Current Profiler (ADCP). The subsurface current speed in two directions was sampled at 2 minutes interval. The ADCP current profile ranged from 3 to 24 meters in depth and was recorded every 10 minutes.

8.1.2 - Radar data collection

The period over which both radar images and environmental data were available extended over 26 days. Radar images were generally collected three times a day to sample different tidal stages and environmental conditions. Images were initially collected with and without the Flywheel to assess the usefulness of the device. After the overall improvement in data quality was demonstrated, all radar images were collected exclusively with the Flywheel.

The set-up parameters for the digital data capture were optimised in accordance with recommendations in Chapter 4. Hence, the resolution in azimuth in non-Flywheel images was equal to 1 degree. The images were collected over 180 degree in azimuth to include the coastline and assist in the geo-location of the meteorological buoys in non-Flywheel images. Short, medium and long pulse images were collected on short range setting (maximum range ~ 3800 meters) with the maximum radial resolution of 7.5 m. Large coverage images (maximum range ~ 7600 meters) were collected with a lower radial resolution of 15 m for medium and long pulse setting only as the performances on short pulse were not deemed sufficient to generally provide effective NRCS measurements at ranges beyond 3800 m.

A total of 359 radar images were obtained, consisting of 87 short pulse images, 145 medium pulse images and 127 long pulse images. For each image, a time-series of a minimum of 16 single-rotation images was collected. The average and standard deviation images were computed and the 16-rotation average image was normalised. Hence, the NRCS measurement error in the average normalised images is better than 0.6 dB in short and medium pulse images and better than 0.8 dB in long pulse images.

8.1.3 - Background oceanographic information for the radar observation area

Wind distribution

The radar's observation area is open widely onto the English Channel and the Atlantic ocean from a south-south-westerly (SSW) to a north-westerly (NW) direction. Southerly to westerly winds therefore benefit from a large fetch and will rapidly result in fully developed sea conditions.

The area is limited by land to the north and the east which reduces the fetch for northerly and easterly winds to a minimum. Wind from these sectors are therefore expected to produce less typical sea conditions especially sensitive to the wind direction with respect to the topography of the coast. In the particular case of easterly winds, the wind field in the observation area is strongly disturbed by the high altitude of Portland island's western coastline. It is anticipated that this sudden step causes the wind on the sea surface to be strongly reduced in the near-shore part of the radar images due to sheltering by the cliff.

Bathymetry

The sea bottom topography in the radar observation area can be seen in Figure 8.1. The underwater approach to the island is characterised by an abrupt step in the sea floor at 500 meters from the shore but is otherwise uniform at an average water depth of 35 meters. The southern half of the observation area includes a striking bathymetric feature located immediately west of the southern tip of the island. It consists of an underwater mound juxtaposed to a sudden cavity in the sea bed. The variation in water depth between the mean

depth in the observation area and the bottom of the trough reaches 20 meters while the difference from the underwater mound to the trough is over 40 meters. It is anticipated that these features will strongly affect the strength and direction of the tidal flow in this region and may be responsible for dramatic changes in the radar signature of the sea surface.

Tidal regime

The Portland region is famous for its hazardous tidal regime characterised by complex tidal streams and strong currents. South of Portland island is a region of extreme water turbulence known as the Portland Race, located alternatively to the south-east and south-west of the Bill of Portland at high and low water respectively. At low water, the tidal race lies slightly south of the radar observation area and is therefore not considered in this study.

The tidal stream in the radar observation area is illustrated in Figure 8.2 for several tidal stages with regards to the time of high water (HW) at Portland Harbour. The ebbing flow globally moving from east to west can result in the formation of an eddy in the observation area around HW - 4 hours. The tidal flow is generally stronger in the southern half of the study area, particularly in the near-shore region where the bathymetry encourages a high speed tidal channel close to the southern tip of the island. The tidal current can be considered slack from HW + 4 hours to HW - 5 hours when the maximum spring tide current is predicted to be less than 0.5 m/s in the northern half of the region and less than 1 m/s in the south. The current speed reaches its maximum intensity at HW - 2 hours when current speeds between 2 to 3 m/s can be obtained in the southern area.

The variation in tidal elevation between high and low water is estimated from tidal predictions to vary between 1 and 2.5 meters for neap and spring tide respectively. Given the high altitude of the radar antenna above the mean sea level, the variation in the actual sea level represents a small error in height. Hence, the change in the height of the antenna above mean sea level at different tidal stages can be neglected.

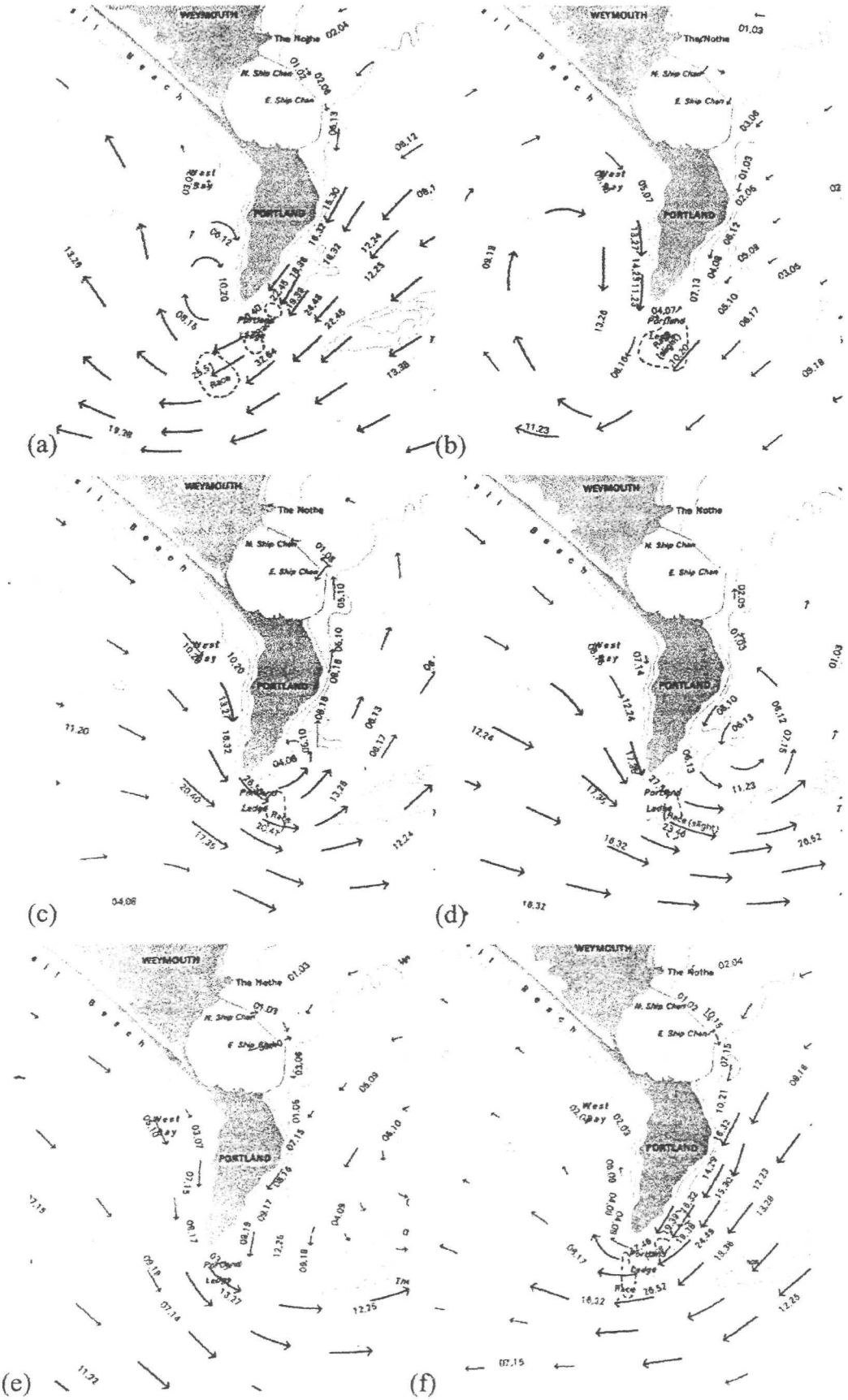

Figure 8. 2 - Tidal stream at HW-5 (a), HW-3 (b), HW-1 (c), HW+1 (d), HW+3 (e) and HW+5 (f) hours where HW is High Water at Portland Harbour(from Admiralty Stream Atlas NP 257)

8.1.3 - Environmental conditions during the Portland experiment

The environmental parameters measured by the buoys during the experiment are presented in the form of time series in Figure 8.3. The plots show successively from top to bottom: the two-minute averaged wind speed (m/s), the wind direction (degree), (3) the air-sea temperature difference (degree C), the significant wave height (m), the zero-crossing period (s), the mean wave direction of travel (degree), the current magnitude (cm/s) and the current direction (degree). Following the oceanographic convention, the wind and wave direction are expressed as the direction the wind and waves are coming "from" while the current direction indicates the direction the current is flowing "to" with respect to geographic North.

The horizontal time axis is given in Julian days as the day number counted from the 1st of January. The beginning and end of the period when both digital marine radar images and environmental data are available is indicated by the vertical boundaries on day 279 and day 305, corresponding to midnight on respectively the 6th of October and the 2nd of November 1994. Some data on the environmental conditions a few days prior to the start of the experiment are also presented to provide information on the wind history and help characterise the type of conditions experienced on the first few days.

Air-Sea temperature difference

The air to sea temperature difference characterises the stability of the atmospheric boundary layer over the ocean. Unstable atmospheric conditions identified by negative air-sea temperature differences have been associated with an increase in the transfer of energy from the atmosphere to the ocean by wind. This results in enhanced wind wave generation and is related by some authors to observations of increased microwave ocean NRCS in cases of unstable stratification (Keller *et al.*, 1985).

The air-sea temperature difference during the experiment is presented in Figure 8.3. c where it varies between -4 and +1° C. The atmospheric conditions were weakly unstable over most of the experiment with short periods of weak or neutral stability. Hence, with near-neutral stability conditions persisting throughout the experiment, little ocean NRCS variation due to changes in atmospheric stratification is anticipated.

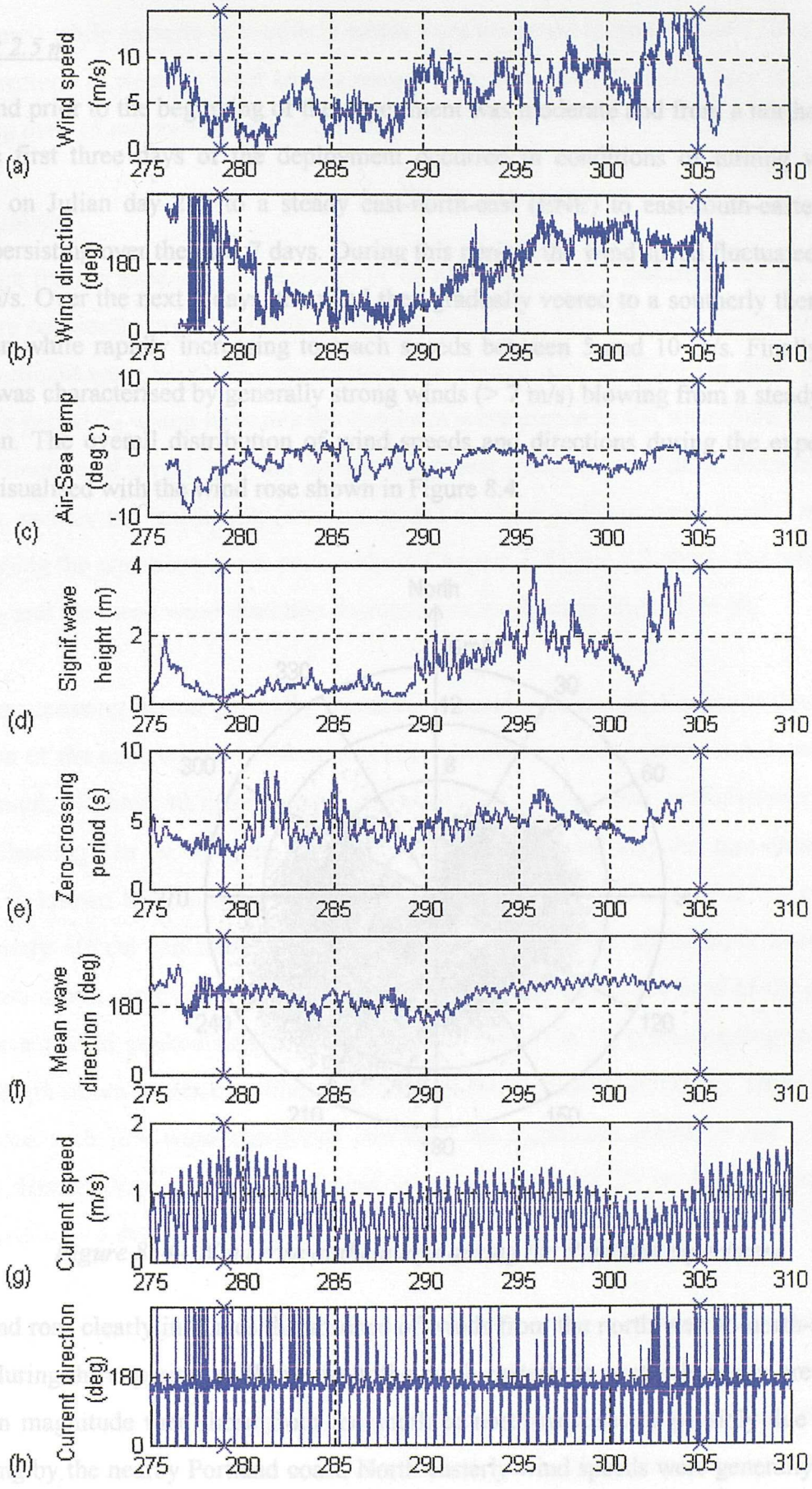

Figure 8. 3- Environmental conditions during the Portland experiment

Wind at 2.5 m

The wind prior to the beginning of the experiment was moderate and from a northerly sector and the first three days of the deployment occurred in conditions of turning wind until settling on Julian day 282 to a steady east-north-east (ENE) to east-south-easterly (ESE) sector persisting over the next 7 days. During this period, the wind speed fluctuated from 0.5 to 10 m/s. Over the next 7 days, the wind then gradually veered to a southerly then westerly direction while rapidly increasing to reach speeds between 5 and 10 m/s. Finally, the last period was characterised by generally strong winds (> 7 m/s) blowing from a steady westerly direction. The overall distribution of wind speeds and directions during the experiment is better visualised with the wind rose shown in Figure 8.4.

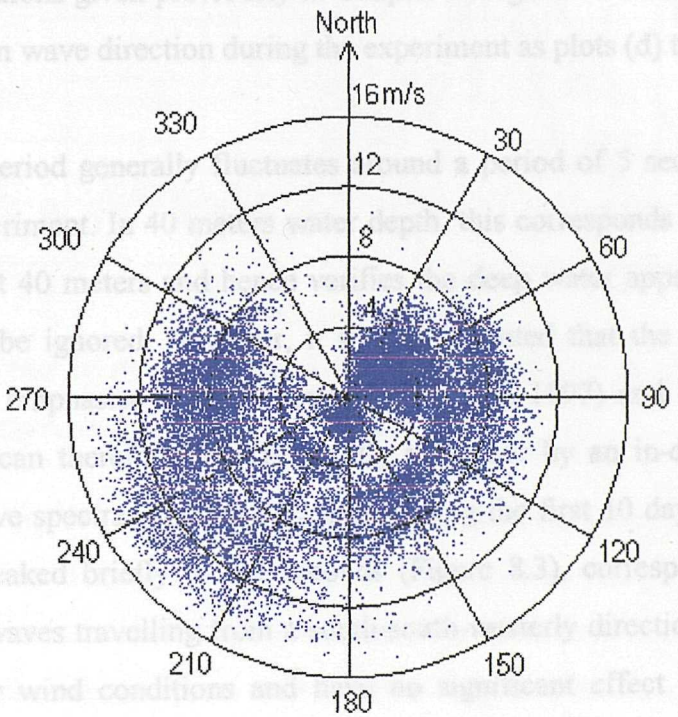

Figure 8. 4 - Wind rose at the buoys during the Portland experiment

The wind rose clearly indicates the absence of winds from the north-west to north-north-east sector during the experiment. Winds from the north-easterly to southerly sector are generally lower in magnitude than those from the south to north-west sector possibly due to partial sheltering by the nearby Portland coast. North-easterly wind speeds were generally low (less

than 5 m/s) while easterly to southerly winds were moderate (between 5 and 10 m/s). Finally south-westerly to westerly wind speeds ranged from very low (<2m/s) to very high (> 12m/s) reaching over 15 m/s average speed on many occasions.

Wave climate

Although the sea state is best described by its directional wave spectrum, the sea conditions are more compactly expressed with a few statistical quantities. The parameters used here are the significant wave height $H_{1/3}$ representing the energy content of the sea state, the zero up-crossing period Z_0 which indicates the dominant wave period in the wave field and the mean wave direction of travel. The sea surface roughness statistics were also computed from the spectra, namely the rms height (directly related to the significant wave height) and the rms slope using the equations given previously in Chapter 2. Figure 8.3 shows the time series for $H_{1/3}$, Z_0 and the mean wave direction during the experiment as plots (d) to (f).

The zero-crossing period generally fluctuates around a period of 5 seconds throughout the duration of the experiment. In 40 meters water depth, this corresponds to a dominant ocean wavelength of about 40 meters and hence verifies the deep water approximation for which wave shoaling can be ignored. However, it should be noted that the zero-crossing period record is known to emphasise higher frequencies (Wyatt, 1997) and that the existence of bathymetry effects can therefore only be totally ruled out by an in-depth analysis of the complete ocean wave spectra. On two occasions during the first 10 days of the experiment, the wave period peaked briefly to 8.5 seconds (Figure 8.3), corresponding to 110-meter wavelength ocean waves travelling from a south-south-westerly direction. These long waves coincided with low wind conditions and have no significant effect on the overall wave energy. Hence, these waves are not wind waves generated locally but swell waves generated presumably by a distant storm in the Atlantic ocean.

The energy content of the sea spectrum before the start of the experiment was moderate with a significant wave height around 1 meter. The sea state remains generally low ($H_{1/3} < 1$ m) for the first 10 days of the experiment but starts to increase from Julian day 289 when the wind strengthens and veers to a south to westerly direction. The sea state then steadily

increases up to Julian day 296 as a direct result of larger wind speeds and longer fetches. Outside the two instances associated with the presence of swell, the significant wave height is well correlated with wind speed for the duration of the experiment as shown in Figure 8.5. In the last period characterised by westerly winds, the time lag between sharp wind bursts in the wind speed time-series and the associated increase in significant wave height was found to be in the order of 6 hours.

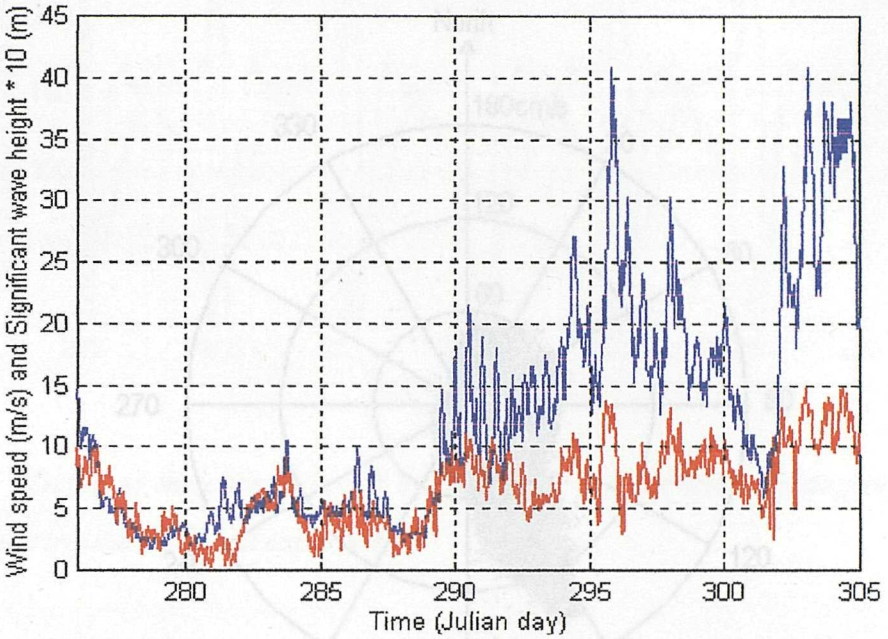

*Figure 8. 5 -Time series of the wind speed (red) and significant wave height * 10 (blue) illustrating the good correlation between wind and sea state.*

The mean wave direction is stable throughout the duration of the experiment around a south-south-westerly direction. The waves' direction of travel is only marginally affected by the gradual change in wind direction from an easterly to a westerly sector. The time-series however indicates a clear semi-diurnal modulation of the wave direction presumably linked to the alternating tidal flow advecting the ocean waves.

Current

The current speed and direction measured by the current meter at a 1 meter depth are plotted as plots (g) and (h) in Figure 8.3. The experiment covers nearly two complete tidal cycles and includes two spring and two neap tides. The modulation of the current speed indicates the strong fortnightly and semi-diurnal tidal modes dominating the area.

The current speed in the region of the buoys ranges from less than 0.1 m/s at low water to over 1.5 m/s at high water. The maximum current speed occurs at high water on spring tide on Julian day 280 when it reaches up to 1.7 m/s. The direction of the tidal flow is better illustrated with the help of Figure 8.6 and 8.7 which respectively present the current rose at the buoys and an extract over three days of the current speed and direction time-series.

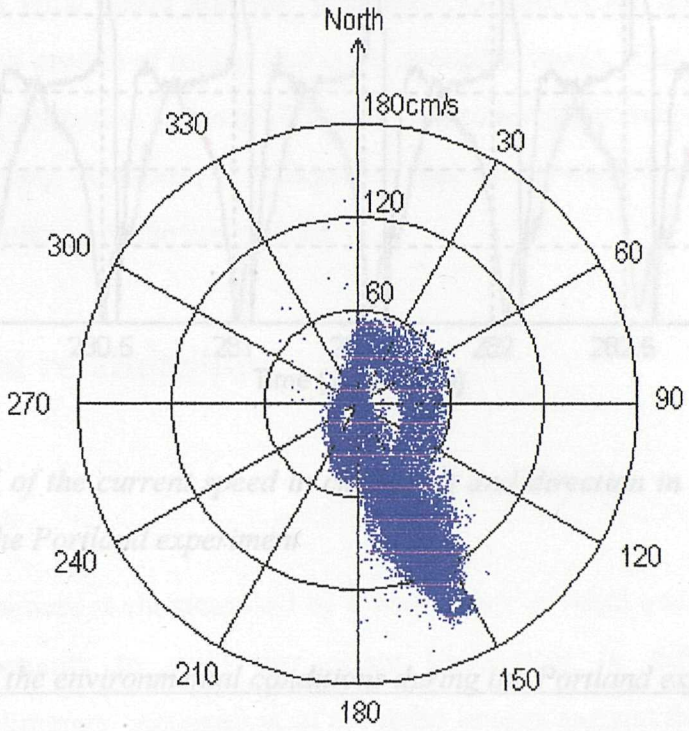

Figure 8. 6 - Current rose at buoys during the Portland experiment

The tidal flow consists of an extended flood in a steady south-south-easterly direction followed by a rapid ebbing in a northerly direction. Hence, for most of the tidal cycle, the current at the buoys is larger than 0.5 m/s and travelling in a south-south-easterly direction. The ebbing flow corresponding to currents less than 0.5 m/s and travelling to the north represent only 20 % of the tidal cycle duration. As the westerly winds become strong towards the end of the experiment, the time-series in Figure 8.3 indicates that the ebbing loop of the current towards a northerly direction can occasionally disappear altogether.

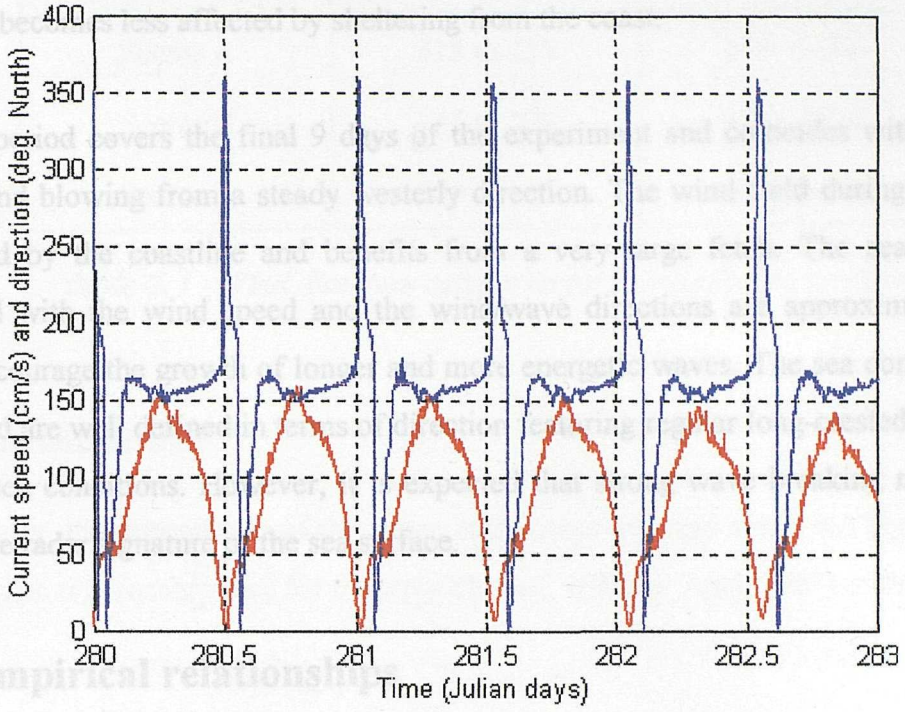

Figure 8. 7 - Detail of the current speed in cm/s (red) and direction in degree North (blue) time-series during the Portland experiment

Overall summary of the environmental conditions during the Portland experiment

Globally, three major periods can be distinguished during the Portland experiment: the first period covers the first 10 days and is characterised by a low to moderate fetch-limited easterly wind blowing over a low energy sea surface with ocean waves travelling in from a south-south-westerly direction. The tidal current at the buoys is generally orientated in the cross-wind direction and is not foreseen to contribute significantly to the surface roughness. The opposing wind/wave directions however may steepen the waves on the sea surface and result in increased surface roughness and ocean NRCS.

The second period ranges over 7 days between Julian day 289 and 296 and is characterised by turning wind conditions from an easterly to a westerly direction accompanied by a rapid increase in magnitude. Benefiting from longer fetches, these moderate winds lead to a gradual increase in sea state. The sea conditions over this period are expected to be confused

as the wind field in the observation area continually changes direction and intensity and gradually becomes less affected by sheltering from the coast.

The last period covers the final 9 days of the experiment and coincides with moderate to strong wind blowing from a steady westerly direction. The wind field during this period is unaffected by the coastline and benefits from a very large fetch. The sea state is well correlated with the wind speed and the wind/wave directions are approximately parallel, which encourage the growth of longer and more energetic waves. The sea conditions during this period are well defined in terms of direction featuring regular long-crested waves typical of open sea conditions. However, it is expected that strong wave breaking may occur and change the radar signature of the sea surface.

8.2 - Empirical relationships

8.2.1 - Introduction

The Portland experiment is characterised by a wide range of wind and sea conditions which provide the opportunity to study the ocean backscatter in different environmental circumstances. Preliminary examination of the radar images suggest that wind speed plays a fundamental role in the generation of radar backscatter from the sea surface. The ocean NRCS is observed to respond instantaneously to any change in wind magnitude in contrast to any change in sea state which generally lags behind by a few hours or more. The wind direction is also anticipated to be of major importance for the ocean backscatter if only for its impact on coastal sheltering and fetch which have already been pointed out.

Consequently, the analysis initially proceeds by seeking an empirical relationship between the ocean NRCS and the wind speed only. The wind direction is accounted for by splitting the dataset into three subsets corresponding to the wind blowing from three different sectors. These sectors are determined in view of wind sheltering by the coast and fetch considerations. The three sectors are defined with respect to geographic North as shown in Table 8.1.

	Angular Range	Wind sector
Sector A	315 to 135	NW to SE
Sector B	135 to 200	SE to SSW
Sector C	200 to 315	SSW to NW

Table 8. 1 - Wind direction categories for Portland data analysis

8.2.2 - Literature review

Traditionally, the dependence of the ocean backscatter on wind speed has been modelled by a logarithmic relationship (see for example Stewart, 1985, or Apel, 1987) of the form:

$$\sigma^0(\mathrm{dB}) = A + B \cdot \log_{10} W_{10} \qquad \text{Equation 8. 1}$$

where W_{10} is the wind speed measured at 10 meters above sea level. With this model, the ocean NRCS increases logarithmically with wind speed up to a wind speed around 10-15 m/s when the ocean backscatter shows signs of saturation and starts to level off.

One such empirical model has been proposed by Sittrop (1985) based on four series of experimental measurements obtained at low grazing angles for medium to long radar pulse durations between 0.5 and 10 μs (Nathanson, 1969). The ocean NRCS is expressed with respect to wind speed W_{10} and grazing angle φ as:

$$\sigma^0(\mathrm{dB}) = \alpha + \beta \cdot \log_{10}\left(\frac{\varphi}{\varphi_0}\right) + \left[\delta \cdot \log_{10}\frac{\varphi}{\varphi_0} + \gamma\right] \cdot \log_{10}\frac{W_{10}}{W_0} \qquad \text{Equation 8. 2}$$

where α, β, δ, γ are empirical constants determined for different frequency and polarisation in the upwind and crosswind direction. The parameters φ_0 and W_0 are the reference grazing angle and reference wind speed respectively equal to 0.5 degrees and 10 knots. The accuracy of the model is estimated at ± 5 dB on average.

Some authors have suggested that the radar backscatter also features a low wind speed

threshold below which no sea echo can be observed (Donelan and Pierson, 1987). The lower and upper wind speed threshold values are however known only approximately as large discrepancies are common from one author to the next. It is thought that this variability is linked in part to different measurement techniques and errors in the estimation of the incidence angle and the wind speed. Also, information on the type of sea conditions encountered at the time of the measurements is rarely available to help compare results from different datasets and is generally ignored.

The directional variation of the ocean backscatter is expressed in terms of the direction of the radar look angle in azimuth relative to the wind direction. The radar look direction is known as upwind, downwind and crosswind corresponding to the radar looking respectively "into", "along" and "across" the wind. Experimentally, the ocean backscatter is found largest in the upwind direction and weakest in the crosswind direction while reaching an intermediate strength in the downwind direction (Skolnik, 1990).

8.2.3 - Experimental measurements

Sample area

The ocean backscatter coefficient used for the determination of the empirical relationships with environmental parameters was measured in the vicinity of the instrumented buoys in the radar images. A sample area centred on the buoys was selected and the distribution of NRCS values in the box was computed. As the sample area includes direct echoes from the buoys, the dimension of the box was chosen sufficiently large to ensure that the NRCS values from the buoys do not interfere with the ocean NRCS measurements. The box must also be sufficiently small to guarantee that the environmental parameters measured by the buoys are representative of the whole box area. Hence, the sample area was chosen as a square area 1000 meters in range by 1000 meters in azimuth, centred on the location of the buoys 2500 meters from the radar site. Given the 60 meters antenna elevation, the radar views the sea surface in the sample box with a grazing angle equal to nearly 1.4 degrees.

NRCS measurement

The ocean NRCS taken to be representative of given environmental conditions was chosen as the median of the NRCS distribution in the sample area. This method was preferred to the traditional calculation of the mean NRCS which would be corrupted by integrating the higher NRCS values obtained from the buoys. The difference between the mean and the median of the NRCS distribution of sea clutter echoes has previously been shown to be of minor importance (Figure 7.5).

Conversion from wind at 2.5 m to wind at 10 m

In order to compare our results with previous studies, the wind speed measurements obtained with the anemometer at 2.5 meters need to be converted to wind values at 10 meters above sea level. In neutral stratification, the vertical wind speed profile is given by (Geernaert, 1990):

$$u(z) = \frac{u_*}{K} \cdot \ln\left(\frac{z}{z_o}\right) \qquad \text{Equation 8. 3}$$

where u_* is the wind friction velocity, K is the von Karman constant (K = 0.4), z is the height above the sea level and z_o is the roughness length. The friction velocity is given with respect to the drag coefficient C_{D10} and the wind speed W_{10} at 10 meters by:

$$u_*^2 = C_{D10} \cdot W_{10}^2 \qquad \text{Equation 8. 4}$$

and the roughness length z_o is given by the Charnock relation (1955) as:

$$z_o = \frac{a_{Ch} \cdot u_*^2}{g} \qquad \text{Equation 8. 5}$$

where a_{Ch} is the Charnock constant equal to 0.0144 and g is the gravitational acceleration.

The drag coefficient at 10 meters has been determined experimentally by many authors. Garratt (1977) compiled an expression for C_{D10} using the composite results of many investigations. The drag coefficient in neutral stratification is expressed with respect to the wind speed at 10 meters as:

$$C_{D10} \cdot 10^3 = 0.75 + 0.067 \cdot W_{10} \qquad \text{Equation 8. 6}$$

This expression is valid for open ocean and wind speeds between 4 and 21 m/s (Geernaert, 1990). The drag coefficient is expected to be larger in coastal areas but no parameterisation is so far available. These expressions were used in conjunction with the wind speed measurements at 2.5 meters above sea level to numerically compute the wind speed at 10 meters.

8.2.4 - Ocean NRCS dependence on wind speed

The median ocean NRCS was measured in the sample box for all images collected during the Portland experiment. The data are plotted against wind speed in a log-log scale in Figure 8.8. For sake of clarity, the data are represented in separate subplots for the different pulse settings and data points falling below the receiver noise threshold are not displayed. The usual colour convention applies whereby short, medium and long pulse are respectively shown in red, green and blue.

The data are identified by different symbols to indicate the wind sector for which the NRCS measurement was obtained. Given the fixed radar bearing when measuring the NRCS at the buoys, the data associated with wind sector A correspond to the radar looking mostly downwind and are represented by the symbol "o". The data obtained for wind sector B correspond to the radar looking crosswind and are represented by the symbol "x" and the data measured for wind sector C correspond to the radar looking upwind and are represented by the symbol "+".

For each plot, the experimental data are compared with the Sittrop empirical model in the upwind and the crosswind direction. Given the 0.5 to 10 μs pulse duration used as a basis for the model's development, the modelled NRCS are expected to compare best with the long pulse dataset. The model output is represented in Figure 8.8 by the magenta lines. The dotted magenta lines represent the modelled upwind and crosswind NRCS output at 2500 meters range corresponding to the distance from the sample box to the radar. The solid magenta lines represent the model output for a hypothetical 100 meters range which will be discussed

later.

Due to the important scatter in the NRCS measurements, a least-mean-square method was used to fit logarithmically the data and allow a rapid assessment of the agreement between the model and the data. The data were therefore divided into two subsets representing respectively the "upwind" dataset and the "crosswind and downwind" dataset. Each dataset was then fitted in a least-mean-square method with logarithmic functions which are depicted as the red, green and blue solid lines in Figure 8.8.a to 8.8.c respectively.

8.2.5 - Discussion

The experimental NRCS measurements are found to clearly display the expected logarithmic dependence on wind speed, especially in the upwind direction. The NRCS data obtained when the radar is looking crosswind and downwind show a greater variability which may be related to secondary environmental influences such as varying current speed for example. The NRCS scatter may also result from the extensive differences in sheltering and fetch conditions associated with the wide range of wind direction covered by this subset.

As expected, the short pulse dataset includes fewer valid data points in the crosswind direction and low wind speed following the reduced detection performances on this setting compared to longer pulse lengths. On medium and long pulse setting, valid crosswind NRCS are measured down to wind speeds of 3.2 and 2.5 m/s respectively when the system reaches the receiver noise threshold (MDS) for that range. This dataset therefore indicates that valid NRCS measurements are obtainable down to very low wind speeds but the performances of the instrument do not allow us to comment on the existence of a lower wind speed threshold.

The NRCS data show a large upwind to crosswind ratio at low wind speed which gradually decreases towards unity for high wind speed as the ocean roughness becomes more isotropic. The crosswind NRCS appears to increase much faster with wind speed that the upwind component in good agreement with observations reported in the literature for moderate grazing angles (Skolnik, 1970).

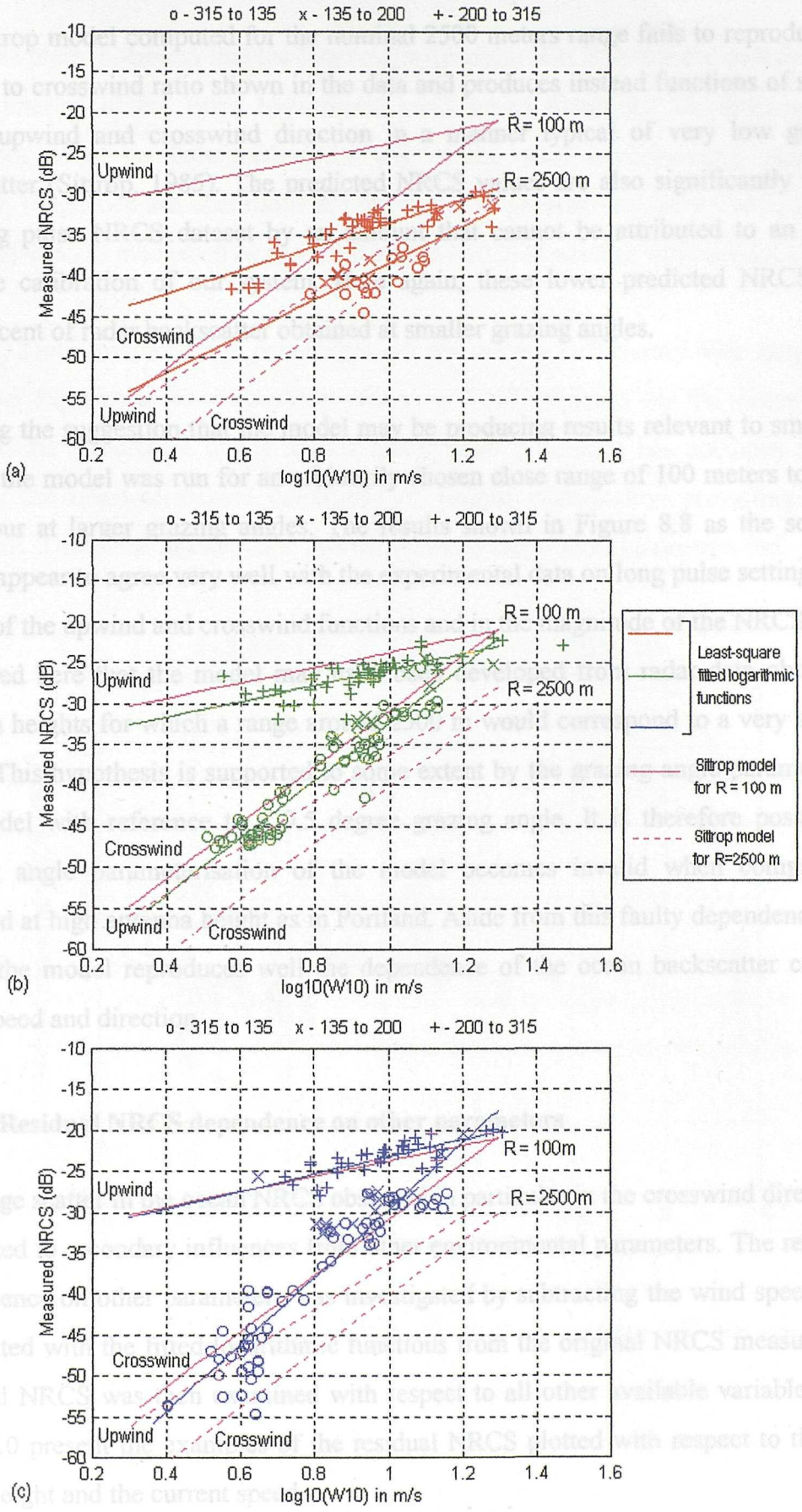

Figure 8. 8 - Median NRCS obtained during the Portland experiment plotted against wind speed at 10 meters in logarithmic scale for short (a), medium (b) and long (c) pulse setting

The Sittrop model computed for the nominal 2500 meters range fails to reproduce the large upwind to crosswind ratio shown in the data and produces instead functions of similar slope in the upwind and crosswind direction in a manner typical of very low grazing angle backscatter (Sittrop, 1985). The predicted NRCS values are also significantly smaller than the long pulse NRCS dataset by an amount that cannot be attributed to an error in the absolute calibration of our system. Here again, these lower predicted NRCS values are reminiscent of radar backscatter obtained at smaller grazing angles.

Pursuing the suggestion that the model may be producing results relevant to smaller grazing angles, the model was run for an arbitrarily chosen close range of 100 meters to examine its behaviour at larger grazing angles. The results shown in Figure 8.8 as the solid magenta curves appear to agree very well with the experimental data on long pulse setting, both in the slopes of the upwind and crosswind functions and in the magnitude of the NRCS. Hence, it is suggested here that the model may have been developed from radar data obtained at low antenna heights for which a range around 2500 m would correspond to a very small grazing angle. This hypothesis is supported to some extent by the grazing angle parameterisation of the model with reference to a 0.5 degree grazing angle. It is therefore possible that the grazing angle parameterisation of the model becomes invalid when compared to data obtained at high antenna height as in Portland. Aside from this faulty dependence on grazing angle, the model reproduces well the dependence of the ocean backscatter coefficient on wind speed and direction.

8.2.6 Residual NRCS dependence on other parameters

The large scatter in the ocean NRCS observed in particular in the crosswind direction may be attributed to secondary influences from other environmental parameters. The residual NRCS dependence on other parameters was investigated by subtracting the wind speed component calculated with the fitted logarithmic functions from the original NRCS measurements. The residual NRCS was then examined with respect to all other available variables. Figure 8.9 and 8.10 present the examples of the residual NRCS plotted with respect to the significant wave height and the current speed.

From these plots, it appears that the large majority of the NRCS values are contained within a ± 5 dB interval of the fitted logarithmic wind speed functions. No obvious secondary dependence could be distinguished for any of the other environmental parameters. In particular, roughened sea conditions are not found to generate any ocean backscatter in the absence of wind as evidenced by the rapid loss in NRCS in abating wind conditions.

Arguably, some environmental parameters did not cover a sufficiently wide range of values during the experiment to draw conclusions on their influence on the ocean NRCS. In particular, the importance of the air-sea temperature difference has not been investigated following the quasi-permanent conditions of neutral stratification prevailing during the experiment. Therefore, at this stage, this temperature factor must be disregarded.

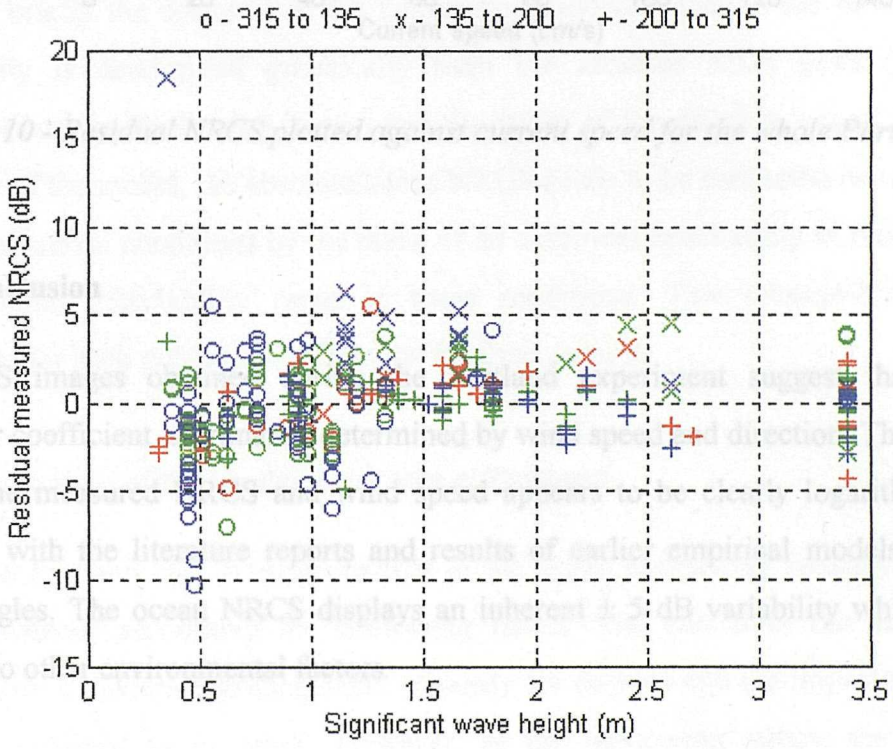

Figure 8. 9 - Residual NRCS plotted against significant wave height for the whole Portland dataset

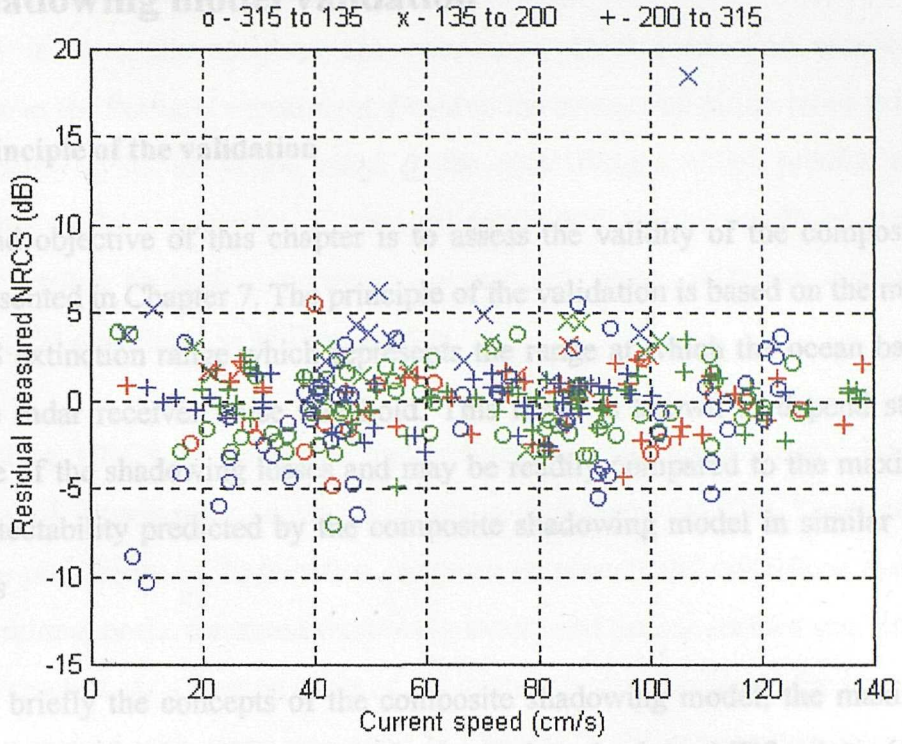

Figure 8. 10 - Residual NRCS plotted against current speed for the whole Portland dataset

8.2.7 - Conclusion

The NRCS images obtained during the Portland experiment suggest that the ocean backscatter coefficient is primarily determined by wind speed and direction. The relationship between the measured NRCS and wind speed appears to be clearly logarithmic in good agreement with the literature reports and results of earlier empirical models at moderate grazing angles. The ocean NRCS displays an inherent ± 5 dB variability which cannot be attributed to other environmental factors.

8.3 - Shadowing model validation

8.3.1 - Principle of the validation

The second objective of this chapter is to assess the validity of the composite shadowing model presented in Chapter 7. The principle of the validation is based on the measurement of the NRCS extinction range which represents the range at which the ocean backscatter falls below the radar receiver noise threshold. This range is known to depend strongly on the magnitude of the shadowing losses and may be readily compared to the maximum range of NRCS detectability predicted by the composite shadowing model in similar environmental conditions

Recalling briefly the concepts of the composite shadowing model, the maximum range of detectability is determined graphically from the absolute MDS plots (which include compensations for shadowing losses) and the value of the absolute ocean NRCS. For the validation of the model, the absolute ocean NRCS needs to be estimated independently from the environmental conditions by the mean of an empirical relationship in order to determine the maximum detectability range in these conditions. This relationship needs to be established for each pulse setting from the Portland dataset.

8.3.2 - Estimation of the shadowing losses at Portland

So far, the Portland NRCS values consist of the ocean backscatter measured at the buoys' location without accounting for shadowing losses. The NRCS in the sample box was measured for a moderate grazing angle of nearly 1.4 degrees and the impact of shadowing is therefore expected to be small. However, as the shadowing affects the data unevenly depending on surface roughness statistics, the value of each NRCS data point must be compensated for these losses.

It is noted here that the data must regrettably be corrected with the same shadowing model that will later be validated using results derived from this data. Ideally, the measured NRCS

should be obtained at a grazing angle sufficiently large not to require any shadowing correction in even the roughest sea conditions. Such measuring conditions were not achievable in the Portland experiment. Besides, the model validation relies principally on the measurements of the extinction range in the radar images which provide an independent check of the model's suitability. Further validation will also be sought by integrating results from the earlier Nyftilift experiment carried out under different antenna height and environmental conditions in Milford-on-Sea.

The absolute NRCS is computed by adding the shadowing losses, estimated as the probability of illumination expressed in dB, to the measured NRCS values (see equation 7.22). The probability of illumination for given environmental conditions is calculated from the conventional or the threshold shadowing model and the sea surface rms slope and the rms height parameters. At a grazing angle of 1.4 degrees and according to the classification of the shadowing regime with range presented in Chapter 7, the sample box belongs to the close range area. In this area, shadowing losses are generally described by the conventional shadowing model except for rough sea conditions when the surface rms slope is sufficiently large to obey the criteria of the threshold model at this grazing angle. Hence, the probability of illumination is derived from the threshold model when the roughness conditions are fulfilled, or else from the conventional shadowing model.

8.3.3 - Sea surface roughness parameters

The surface roughness parameters have so far been computed from the Cox and Munk (1954) slope relations to wind speed and a simple Phillips (1977) equilibrium spectrum. The measurement of the ocean wave spectrum by the Waverider buoy during the Portland experiment provides the opportunity for a direct estimate of the surface roughness properties. The rms height and slope were therefore computed from the spectral data using the method described in Chapter 2. Figure 8.11 compares the rms slope derived experimentally from the wave spectrum with the rms slope calculated from the Cox and Munk relation for the measured wind speed.

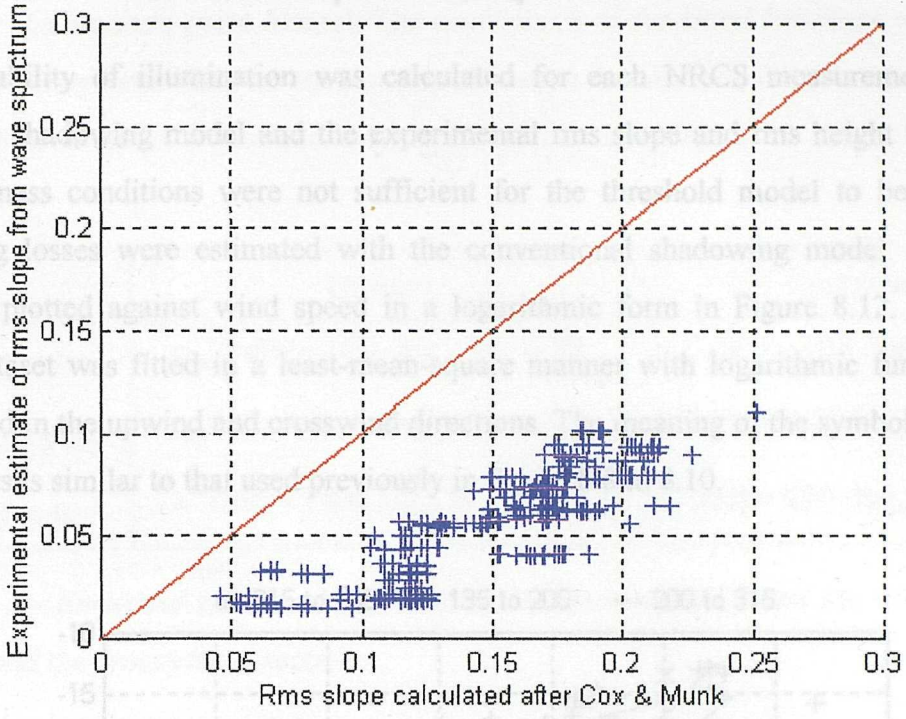

Figure 8. 11 - Experimental rms slope versus rms slope calculated from Cox and Munk (1954)

The result in Figure 8.11 clearly indicates that the experimental rms slope is systematically smaller than the rms slope computed with the Cox and Munk formula, especially at higher sea state when the discrepancy is seen to increase. The origin of this discrepancy lies essentially in the Cox and Munk relations having been developed for open oceans and fully developed sea conditions and are consequently not representative of the sea surface statistics in the coastal zone. Also, the Cox and Munk slope statistics were derived from sun glitter measurements originating predominantly from short steeper waves which do not affect the motion of the Waverider buoy and do not appear in the spectral record. Hence, as the shadowing mechanism is concerned mostly with larger waves, the shadowing losses at the NRCS sample box were estimated using the experimental rms slope and rms height measurements.

8.3.4 - Absolute NRCS relationship with wind speed

The probability of illumination was calculated for each NRCS measurement using the composite shadowing model and the experimental rms slope and rms height values. When the roughness conditions were not sufficient for the threshold model to be defined, the shadowing losses were estimated with the conventional shadowing model. The absolute NRCS is plotted against wind speed in a logarithmic form in Figure 8.12. The absolute NRCS dataset was fitted in a least-mean-square manner with logarithmic functions of the wind speed in the upwind and crosswind directions. The meaning of the symbols and colours in the plots is similar to that used previously in Figure 8.8 to 8.10.

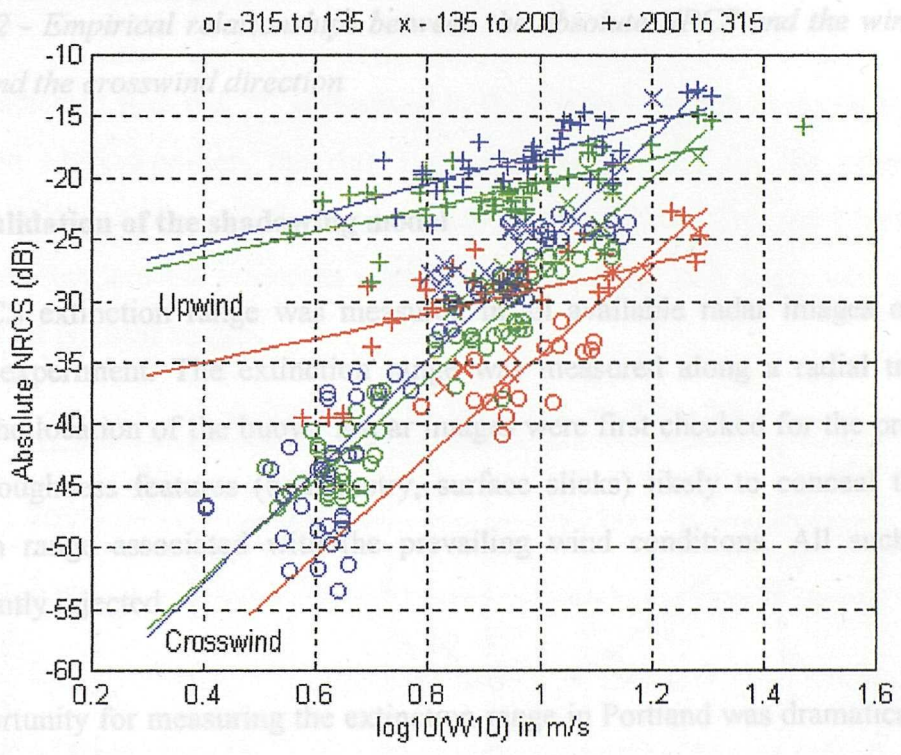

Figure 8. 12 - Absolute NRCS against wind speed at 10 meters in logarithmic scale

The magnitude of the shadowing losses is found to range between 2 and 6 dB. The scatter of the absolute NRCS can be shown to remain confined to a ± 5 dB interval around the fitted logarithmic functions. The slopes of both upwind and crosswind fitted lines were found to agree closely for the medium and long pulse dataset. However, the lack of data points at low wind speed in the short pulse dataset resulted in widely differing results. The slope of the

logarithmic functions fitted to the short pulse dataset were therefore forced to equal those found for the medium pulse dataset. The coefficients of the fitted functions are presented in Table 8.2. They determine the relationships between the absolute NRCS and the wind speed for the different pulse lengths and radar look direction to the wind.

	Upwind	Crosswind
Short pulse	$\sigma_{up}^{0}(\mathrm{dB}) = 10.0 \cdot \log_{10} W_{10} - 39$	$\sigma_{cr}^{0}(\mathrm{dB}) = 40.5 \cdot \log_{10} W_{10} - 75$
Medium pulse	$\sigma_{up}^{0}(\mathrm{dB}) = 10.0 \cdot \log_{10} W_{10} - 30.4$	$\sigma^{0}(\mathrm{dB}) = 40.5 \cdot \log_{10} W_{10} - 68.7$
Long pulse	$\sigma^{0}(\mathrm{dB}) = 12.4 \cdot \log_{10} W_{10} - 30.4$	$\sigma^{0}(\mathrm{dB}) = 45.0 \cdot \log_{10} W_{10} - 70.8$

Table 8. 2 - Empirical relationships between the absolute NRCS and the wind speed in the upwind and the crosswind direction

8.3.5 - Validation of the shadowing model

The NRCS extinction range was measured in all available radar images obtained in the Portland experiment. The extinction range was measured along a radial transect passing through the location of the buoys. Radar images were first checked for the presence of local surface roughness features (bathymetry, surface slicks) likely to conceal the real NRCS extinction range associated with the prevailing wind conditions. All such images were consequently rejected.

The opportunity for measuring the extinction range in Portland was dramatically reduced by the number of images failing to reach the receiver noise threshold within the 8000 meters maximum range covered by the radar system. This was particularly evident for the upwind dataset when few valid images with visible receiver noise could be found as a direct result of generally strong westerly winds and high antenna height. Consequently, most of the extinction range measurements were obtained in the downwind and the crosswind directions.

The maximum range of NRCS detectability was predicted for each Portland image from the

absolute MDS plots and the absolute ocean NRCS computed for the measured wind (Figure 7.14). The absolute MDS was plotted for each image according to the pulse setting and the measured rms slope and height. The Portland dataset was divided into "upwind" and "crosswind-and-downwind" subsets for the calculation of the absolute NRCS with the empirical relationships.

The measured and predicted extinction ranges are compared in Figure 8.13. The symbols "o", "x" and "+" correspond again to the wind sectors A, B and C defined previously. The data shown in magenta correspond to the extinction range obtained with the conventional shadowing model, while the data shown in blue indicate results obtained when the threshold shadowing model was applicable.

The data indicated with red "*" correspond to the Nyftilift dataset. Since no buoy data were available in Milford-on-Sea, the rms slope and height used for the estimation of the shadowing in the absolute MDS plots were calculated with the Cox and Munk relation, the Phillips spectrum and the estimated wind speed. The radar look angle was assumed to be upwind for all Nyftilift images.

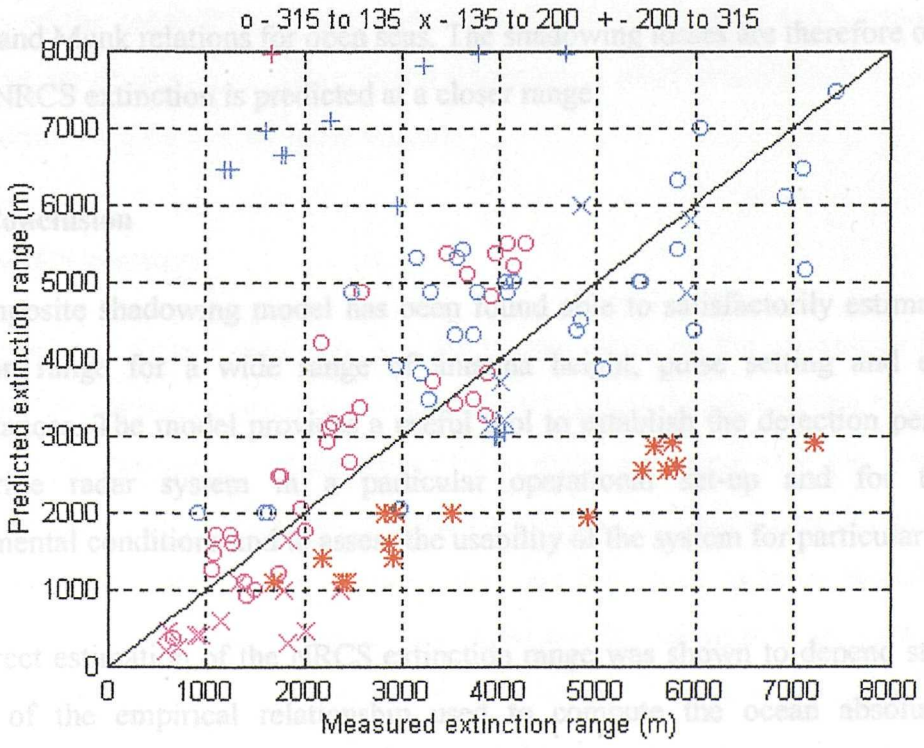

Figure 8. 13 - Predicted versus measured NRCS extinction range for the Portland experiment. The red "" correspond to the Nyftilift dataset collected in Milford-on-Sea*

The extinction range predicted for the Portland dataset is found well correlated to the measured extinction range. The threshold shadowing model is shown to give good results in rough sea conditions when the maximum range of NRCS detectability is large while the conventional shadowing model gives a good estimate of the extinction range in low sea states.

The dataset obtained in the upwind direction (sector C) shows maximum scatter with a distinct cluster of "+" points at the top left of the figure. These data were identified with wind directions in the vicinity of the 200 degree boundary between crosswind and upwind directions. Hence, the discrepancy may be explained by recognising that the predicted extinction range is over-estimated by applying the empirical relationship in the upwind direction to data obtained in a near crosswind direction.

The predicted extinction range for the Nyftilift dataset is found systematically smaller than the measured extinction range. The data show however a clear correlation with the measurements for the whole range of environmental conditions, pulse settings and antenna heights encountered in Milford-on-Sea. The under-estimation of the extinction range by the model may therefore be attributed to the over-estimated rms slope statistics computed with the Cox and Munk relations for open seas. The shadowing losses are therefore over-estimated and the NRCS extinction is predicted at a closer range.

8.3.4 - Conclusion

The composite shadowing model has been found able to satisfactorily estimate the NRCS extinction range for a wide range of antenna height, pulse setting and environmental circumstances. The model provides a useful tool to establish the detection performances of the marine radar system in a particular operational set-up and for the dominant environmental conditions and to assess the usability of the system for particular applications.

The correct estimation of the NRCS extinction range was shown to depend strongly on the validity of the empirical relationship used to compute the ocean absolute NRCS. In

particular, the parameterisation of these relationships considering the radar look angle with respect to the wind direction, needs to be further explored. It is expected that a more detailed analysis of the wind direction factor would also help to reduce the large NRCS scatter observed in the data used for the definition of the empirical relationships.

The calculation of the shadowing losses from purely meteorological parameters was shown to be strongly dependent on an accurate estimate of the surface slope and height statistics in the coastal zone. This dependence of the NRCS extinction range on the surface roughness properties suggests that, once reliable empirical relationships are available, it may be possible to invert the problem and extract information on the surface roughness statistics from the measurement of the NRCS extinction range and an estimate of the wind speed and direction.

8.4 - Oceanographic applications

Besides the applications related to the study of the relations between ocean backscatter and the surface roughness properties, a marine radar system can yield complementary information in the investigation of many oceanographic processes. This final section gives an overview of the capabilities of this instrument for oceanographic applications using a non-exhaustive set of examples where useful information otherwise difficult to obtain could be extracted from digital marine radar images.

8.4.1 - NRCS contrast

The principle of feature detection in radar images relies on the existence of a sufficiently strong NRCS contrast between the feature of interest and the background backscatter. It was established in Chapter 2 that the ocean backscatter measured with the present system is determined primarily by the physical roughness of the sea and to a much lesser extent by its temperature and composition. Hence, any oceanographic process which results in a modulation of the surface roughness is theoretically detectable in radar images. The modulation of the ocean roughness may be positive when the surface roughness is enhanced, or negative when the roughness is reduced with respect to the surrounding area. Positive

roughness modulation results in positive contrast with features appearing brighter in the images with higher NRCS than the surrounding area, while negative modulation shows up as negative contrast with features appearing darker (lower NRCS) than the surrounding backscatter.

The nature and magnitude of oceanographic features' contrast determine the detection capabilities of the radar system for that feature. The system's detection performances for negative contrast features are restricted by the need for sufficiently strong background backscatter to ensure detection. The limitation of the ocean backscatter extinction range implies that negative contrast features are detectable only within this range which depends on operational and environmental parameters. Positive contrast features on the contrary are generally detectable over larger regions as they may be discerned beyond the extinction range against a background of receiver noise. The suitability of the system for the detection of a given feature in given operational and environmental circumstances can now be assessed using the composite shadowing model proposed for the calculation of the absolute detection performances and the maximum NRCS extinction range.

8.4.2 - Example of positive contrast features: Ocean waves

Directional ocean wave spectrum

The imaging of ocean waves by marine radars is a well documented example of an application to oceanography. As early as 1965, Wright suggested that qualitative information on the directional distribution of ocean gravity waves may be obtained with such instrumentation. Later, the emergence of digital sampling systems able to produce computerised radar images resulted in many investigations into the measurement of the ocean directional spectra from marine radar images (see for example Hirakuchi *et al.*, 1990, Trask *et al.*, 1994). In these studies, the directional information is obtained by performing a Fast Fourier Transform (FFT) in the spatial domain on sections of the radar image.

Such an example is given in Figure 8.14 for an image obtained in Shoreham-on-Sea on the

southern coast of England. The lower figure shows the two-dimensional spectrum of the selection highlighted in the upper radar image. The axis represent the two components of the ocean wave number counted from the origin at the central point. The spectral peaks determine the wave vector which magnitude and direction represent the wave number and wave direction of a particular ocean wavelength.

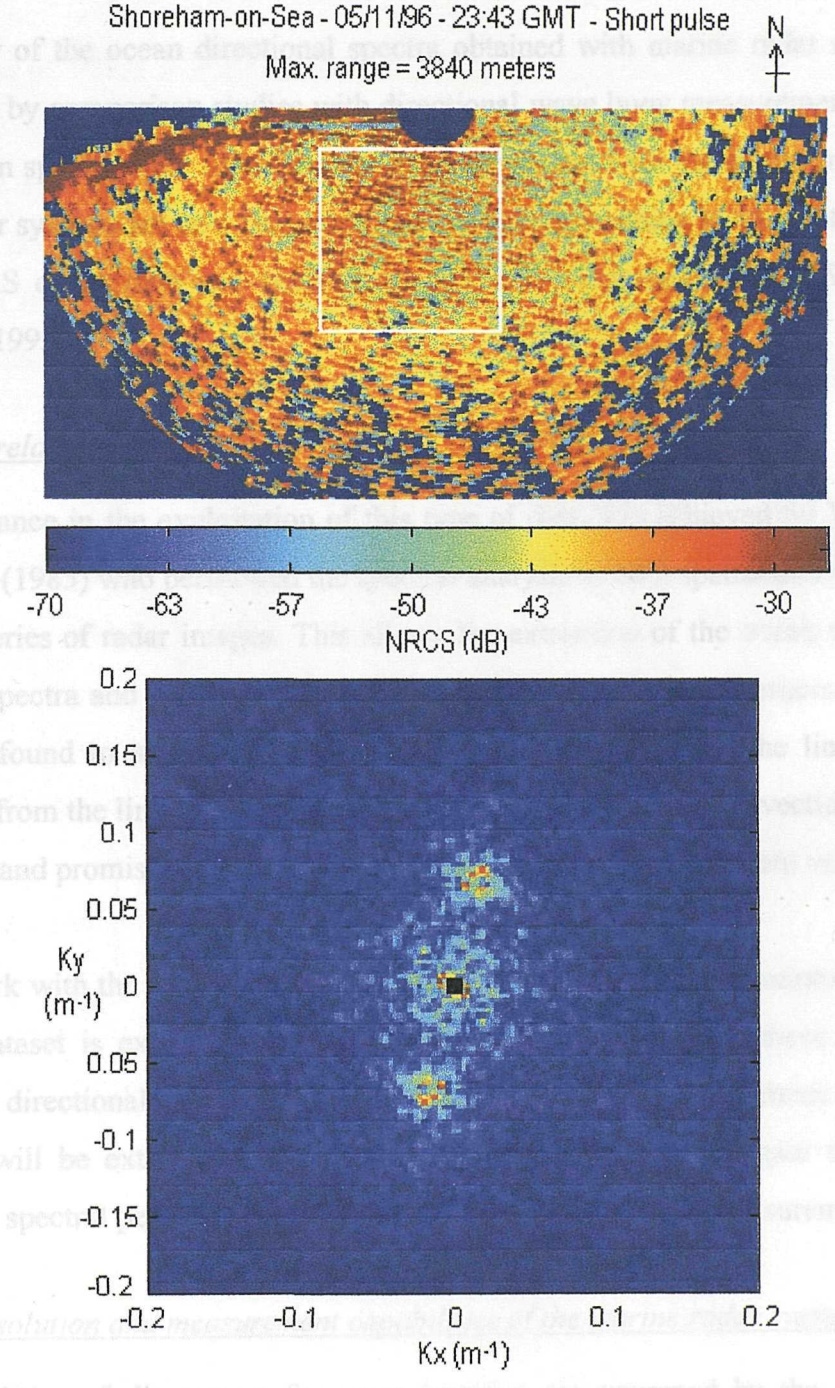

Figure 8. 14 - Imaging of surface gravity waves in Shoreham-on-Sea (top) and unscaled two-dimensional wave spectrum (bottom)

In this example, the ocean wave associated with the strongest spectral peak corresponds to a wavenumber of about 0.07 m^{-1} (wavelength ~ 90 meters) and a SSW-NNE direction of propagation. The wave direction displays a 180 degree ambiguity which can be resolved with additional information on the wave field. In Shoreham, the presence of the nearby coast is sufficient to infer that the wave direction of travel is from the SSW to the NNE.

The validity of the ocean directional spectra obtained with marine radar systems has been investigated by comparison studies with directional wave buoy measurements. The remotely sensed ocean spectra were found in very good agreement with the in-situ measurements and marine radar systems are now frequently used as ground truthing instruments to calibrate and validate ERS ocean data and geophysical products (Henschel *et al.*, 1994, Kleijweg and Greidanus, 1993).

Dispersion relation

Further advance in the exploitation of this type of data was achieved by Young, Rosenthal and Ziemer (1985) who performed the spectral analysis in both spatial and temporal domains of a time-series of radar images. This allows the extraction of the ocean wave number and frequency spectra and enables the computation of the ocean wave dispersion relation. This relation is found to agree well with the theoretical results from the linear wave theory. Deviations from the linear dispersion relationship are related to the advection of ocean waves by currents and promise a reliable method to estimate the surface current velocity.

Similar work with the present system is currently underway at Southampton University. The Portland dataset is expected to provide the opportunity to verify these results using the coincident directional wave buoy and surface current measurements. Ultimately, the technique will be extended to calibrated NRCS images to investigate the possibility for meaningful spectral peak intensities and quantitative wave height measurements.

Spectral resolution and measurement capabilities of the marine radar system

The capabilities of the system for wave imaging are governed by the dimension of the antenna footprint with respect to the dominant ocean wavelength and this application is

generally restricted to measurements on short pulse setting. The spatial resolution is less than 10 meters in the radial direction and therefore limits the spectral analysis to ocean wavelengths larger than 20 meters. In terms of frequency spectrum, the temporal resolution is at best equal to 2.4 seconds and limits the spectral analysis to frequencies over 4.8 seconds, corresponding to an ocean wavelength of 36 meters.

The detection of waves is optimal when the radar looks perpendicularly to the wave crests and becomes quasi-impossible for azimuth-travelling waves when the radar looks along the crests. Figure 8.15 clearly illustrates this point with an image obtained in Portland showing long-crested ocean waves travelling from a south-westerly direction. The waves are well distinguished in the lower half of the image but appear gradually fuzzier and eventually disappear as they become parallel to the radar look angle in the top half of the image.

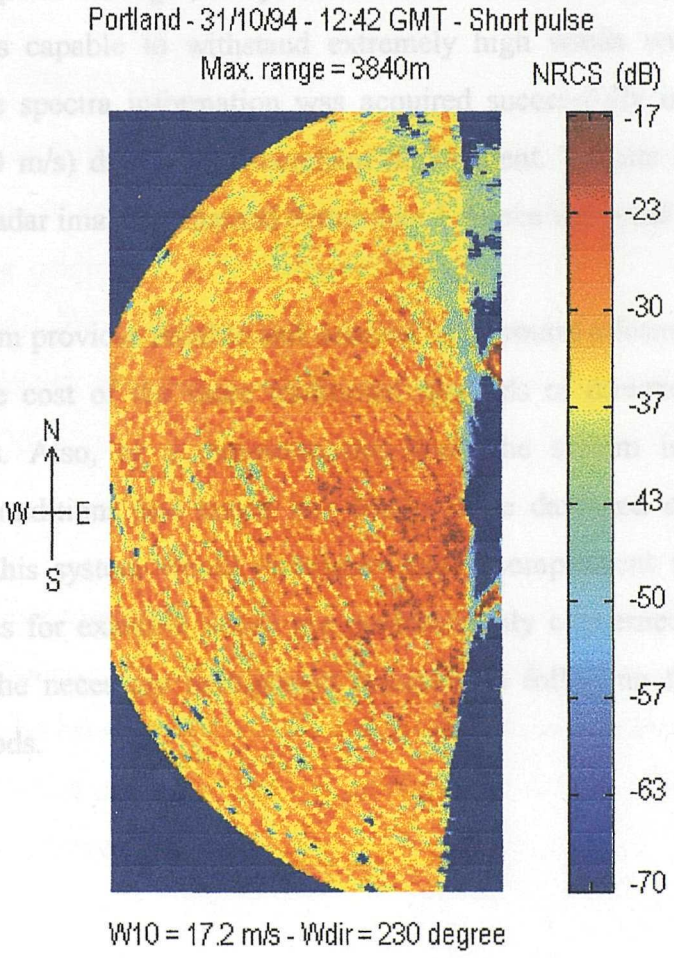

Figure 8. 15 - Ocean waves imaging in Portland depicting the reduction in wave crest sharpness as the waves become parallel to the radar look angle.

The reduced imaging of wave crests parallel to the radar look angle has previously been attributed to the distribution and orientation of small scale roughness on the longer wave crests. However, a more likely explanation lies in the dimension of the radar sampling cell being much larger in azimuth than in range. Hence, as waves become parallel to the radar look direction, the spatial resolution used to sample perpendicularly to the waves is strongly degraded and is no longer able to discriminate individual wave crests. This hypothesis is further confirmed by the observation in Figure 8.15 that the azimuth travelling waves are clearly imaged at close range but become gradually confused at far range as the dimension of the antenna footprint in azimuth becomes larger than the dominant ocean wavelength.

The possibility of ocean directional spectra measurements is strongly dependent on antenna height considerations and wind conditions, especially given the lesser performances of the system on short pulse setting. The system is not well suited to measurements in low wind conditions but is capable to withstand extremely high winds without loss of accuracy. Directional wave spectra information was acquired successfully in Beaufort 9 conditions (wind speed >30 m/s) during the Shoreham deployment. Despite high winds, the angular accuracy in the radar images remained better than 1 degree using the electronic Flywheel.

Hence, this system provides reliable and detailed background information on wave climate at a fraction of the cost of the more traditional methods of directional buoys or arrays of pressure sensors. Also, as a remote-sensing tool, the system is unaffected by stormy environmental conditions and hence less likely to be damaged or lost. The information produced with this system would therefore clearly complement investigations of coastal erosion processes for example which are predominantly concerned with storm events and generally lack the necessary background information following the failing of traditional measuring methods.

8.4.3 - Negative contrast features: Surfactant slicks

Surface roughness damping

The detection of natural and man-made surfactant slicks with marine radar systems has been reported by many investigators (Kerry, 1984, Tennyson, 1989, Atanassov, 1991) but is generally limited to qualitative results on the oil detection feasibility. The detection of surfactant slicks by microwave radar has been related to the attenuation of short scale capillary waves (Alpers and Huhnerfuss, 1989) in areas of lower surface tension. Oil slicks are known to reduce the momentum transfer from the atmosphere to the ocean by impeding the generation of wind ripples on the surface (Mitsuyasu and Honda, 1986) and also reduce wave breaking. The imaging of slicks at low grazing angles is therefore associated with an overall reduction in surface roughness and appear as dark features in radar images.

Surfactant slick experiment

The surfactant detection capabilities of the system were tested experimentally with the opportunity to participate in a series of four "oil" deployment trials during the Portland experiment. The controlled spills were carried out by DRA Portland within the system's observation area with a biodegradable surface active material known as Emkarox. This surfactant reproduces the physical properties of a mono-molecular slick and was specially developed by DRA to study the signature of thin surfactant slicks in microwave radar imagery.

The successful detection rate was only 50% and highlighted the strengths and weaknesses of the technique. The imaging of the slick during one successful trial is presented in Figure 8.16 where the artificial oil slick is highlighted by an arrow. The figure represents a time-series of four images collected on either short or medium pulse setting, which were averaged over 16 antenna rotations before normalisation.

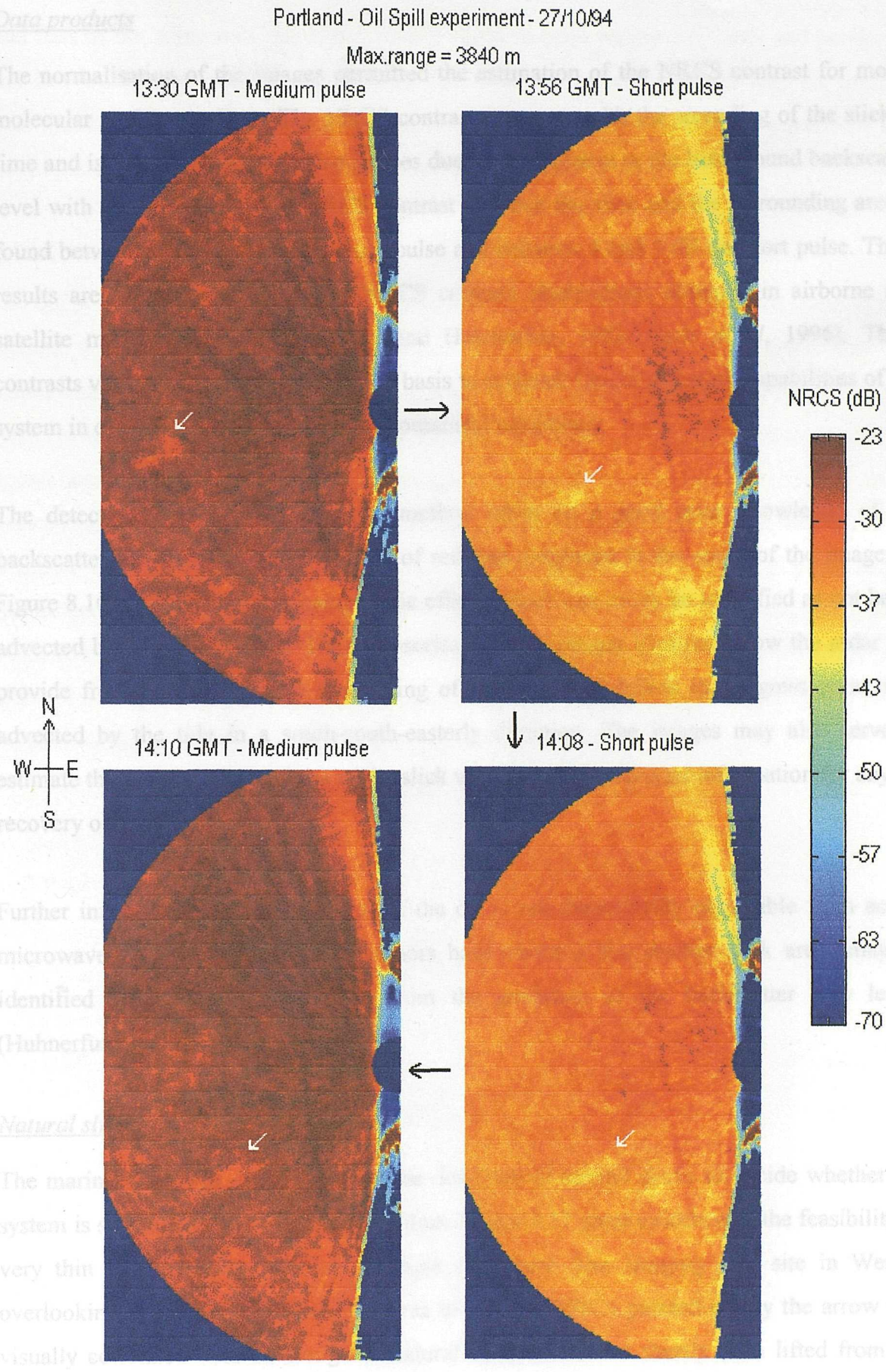

Figure 8. 16 - Imaging of an artificial oil spill in Portland

Data products

The normalisation of the images permitted the estimation of the NRCS contrast for mono-molecular surfactant slicks. The NRCS contrast increases with the spreading of the slick in time and is larger in medium pulse images due to the increase in the background backscatter level with pulse duration. The NRCS contrast between the slick and the surrounding area is found between 6 and 8 dB on medium pulse and between 4 and 5 dB on short pulse. These results are of similar order to the NRCS contrast observations obtained in airborne and satellite microwave imagery (Alpers and Huhnerfuss, 1988, Gade *et al*, 1996). These contrasts values can therefore serve as a basis to estimate the oil detection capabilities of the system in different operational and environmental conditions.

The detection of oil slicks with this method relies on a good prior knowledge of the backscatter in the region. Hence, areas of reduced roughness in the south of the images in Figure 8.16 are attributable to bathymetric effects which can easily be identified as not being advected by the tidal current. The time-series of radar images illustrates how the radar can provide frequent and accurate positioning of the slick and follow its progression as it is advected by the tide in a south-south-easterly direction. The images may also serve to estimate the dimension and shape of the slick which constitute crucial information for any oil recovery operation.

Further information on the thickness of the oil is not theoretically obtainable from active microwave images although some authors have claimed that thicker slick areas may be identified in airborne SAR images from the gradation of the backscatter grey levels (Huhnerfuss *et al*, 1989).

Natural slicks

The marine radar was also applied to the detection of natural slicks to decide whether the system is sensitive to very thin surface films. Figure 8.17 gives evidence of the feasibility of very thin film detection with an example of natural film imaging at a site in Weston overlooking Southampton Water. The area of reduced NRCS pointed out by the arrow was visually correlated with an elongated natural slick which had shortly been lifted from the

mud flats by the rising tide. However, natural slicks in open waters only form and persist in very low wind speed conditions (< 4 m/s). The detection of natural slicks with the marine radar system is therefore unlikely given the contradiction between the optimal conditions for the formation of natural slicks and their successful detection by radar.

Limitations and applications

Two out of the four oil release trials in Portland were unsuccessful and underline some of the inherent weaknesses of the technique. Once again, wind speed plays a major role as demonstrated by the first failed detection trial performed under very low wind conditions (< 2 m/s) when not enough background backscatter was generated to allow detection. The second unsuccessful trial was performed at high water shortly after a storm when many other surface roughness features linked to bathymetric effects were present and made the objective detection of the artificial slick impossible. Hence, these trials suggest that in some circumstances the system can provide a useful tool for the detection, monitoring and assessment of oil spills but as for all microwave radar instruments, the oil detection capabilities of the system are strongly dependent on suitable wind conditions and rely on a good knowledge of background backscatter patterns in the region.

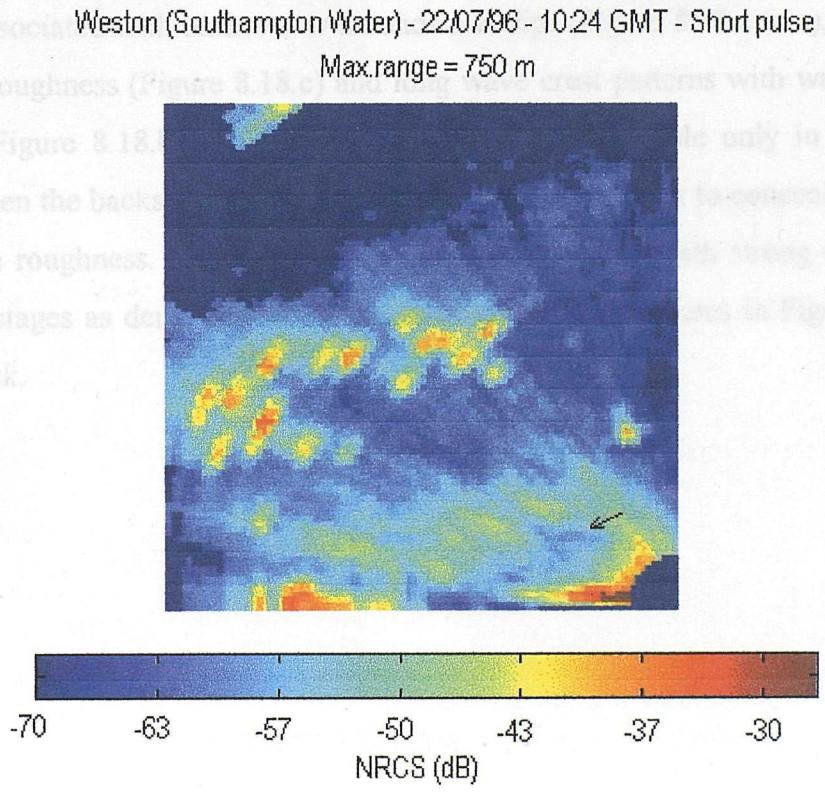

Figure 8. 17 - Natural slick imaging in Southampton Water

Finally, the limited spatial coverage of the present system is unsuited for large scale surveying but offers a good alternative for routine monitoring of particularly sensitive areas such as the vicinity of oil platforms or sensitive natural reserves. Another potential use of the oil detection capabilities of the marine radar system is on-board oil spill recovery vessels which would greatly benefit from its slick positioning capabilities.

8.4.4 - Mixed contrast features: Bathymetry/current interactions

Bathymetric features and their interaction with ocean currents in shallow waters are responsible for many different types of NRCS signatures in radar images. The Portland dataset offers particularly good examples of surface roughness modulation caused by bathymetry/current interactions. The variety of these features is associated with the unusual sea bed layout and the strong and complex tidal currents in the region (Figure 8.1 and 8.2). Figure 8.18 illustrates the rapidly changing surface roughness configurations observed at different tidal stages. All images were obtained on a medium pulse setting for wind speeds between 5 and 8 m/s.

Three types of features can be identified in Figure 8.18: areas of reduced and enhanced backscatter associated with underwater mounds and dips (Figure 8.18.a to c), elongated lines of increased roughness (Figure 8.18.c) and long wave crest patterns with wavelengths up to 400 meters (Figure 8.18.b and c). These features are observable only in moderate wind conditions when the backscatter is neither too strong nor too weak to conceal the modulation of the surface roughness. Each feature is uniquely associated with strong tidal currents at various tidal stages as demonstrated by the total absence of features in Figure 8.18.d when the tide is slack.

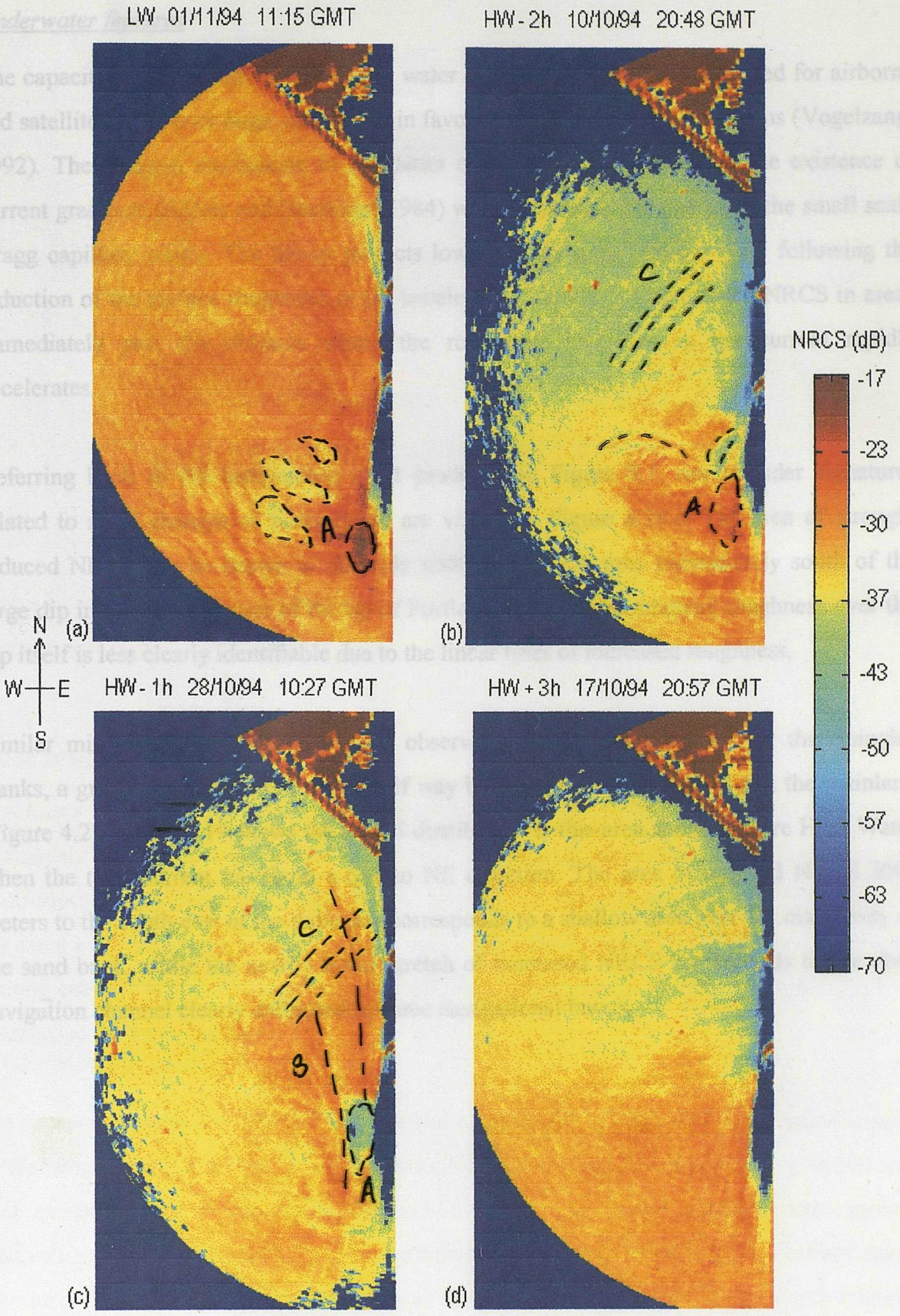

Figure 8. 18 - Imaging of bathymetry/current interactions in Portland. The maximum range in the images is 7740 meters.

A: Underwater features

B: Increased roughness lines

C: Long wave crest patterns

Underwater features

The capacity to detect sudden changes in water depth is similar to that reported for airborne and satellite radars over large sand dunes in favourable tide and wind conditions (Vogelzang, 1992). The imaging mechanism in this latter case has been attributed to the existence of current gradients (Alpers and Hennings, 1984) which modulate the energy of the small scale Bragg capillary waves. The theory predicts lower NRCS over shallow areas following the reduction of the surface roughness in the accelerating current, and increased NRCS in areas immediately past the obstacle where the roughness increases as the current rapidly decelerates.

Referring back to the bathymetric chart produced in Figure 8.1, mixed radar signatures related to rapid changes of water depth are visible in Figure 8.18.c. The area of strongly reduced NRCS can be shown to coincide with the shallow area immediately south of the large dip in the sea bed west of the tip of Portland island. The increased roughness over the dip itself is less clearly identifiable due to the linear lines of increased roughness.

Similar mixed contrast signatures were observed in Christchurch Bay over the Shingles Banks, a group of sand banks located half way between the Isle of Wight and the mainland (Figure 4.2). Figure 8.19 shows the NRCS distribution is this area shortly before High Water when the tidal current travels in a SW to NE direction. The area of reduced NRCS 3000 meters to the south-east of the radar site corresponds to a shallow area over the main body of the sand bank, while the nearby linear stretch of increased NRCS corresponds to the deep navigation channel clearly delimited by three navigational buoys.

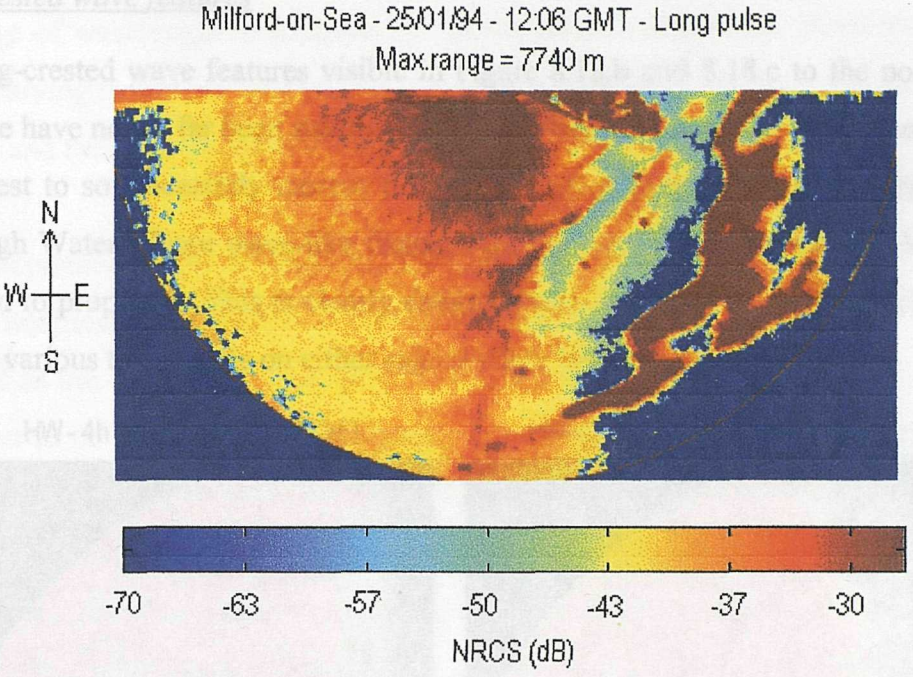

Figure 8. 19 - Mixed NRCS signature of bathymetric features in presence of tidal currents in Christchurch Bay

Linear roughness features

The linear features of increased roughness seen in Figure 8.18.c have been associated exclusively with the occurrence of strong tidal currents travelling in a north-north-west to south-south-easterly direction. The NRCS contrast of these linear features dramatically increased after a period of rough weather and were visually correlated with bands of foam running parallel to the coast. In calmer conditions, linear bands of reduced NRCS can be observed at the same location.

The apparent accumulation of surface material suggests the existence of convergence zones of tidal origin. Such a tidal front has previously been identified during the ebbing tide to the west of the Isle of Wight in Christchurch Bay and was well correlated with similar observations in ERS-1 imagery. It is thought that the particular bathymetry in Portland may encourage the channelling of the strong tidal current and result in these water-depth related areas of convergence.

Long-crested wave features

The long-crested wave features visible in Figure 8.18.b and 8.18.c to the north-west of the radar site have not so far been strictly identified. They have however been associated with the north-west to south-easterly current flow conditions prevailing for a few hours before and after High Water. These wave-like features are also restricted to a specific location and do not seem to propagate. This is clearly demonstrated in the series of images shown in Figure 8.20 for various tidal stages on either side of High Water.

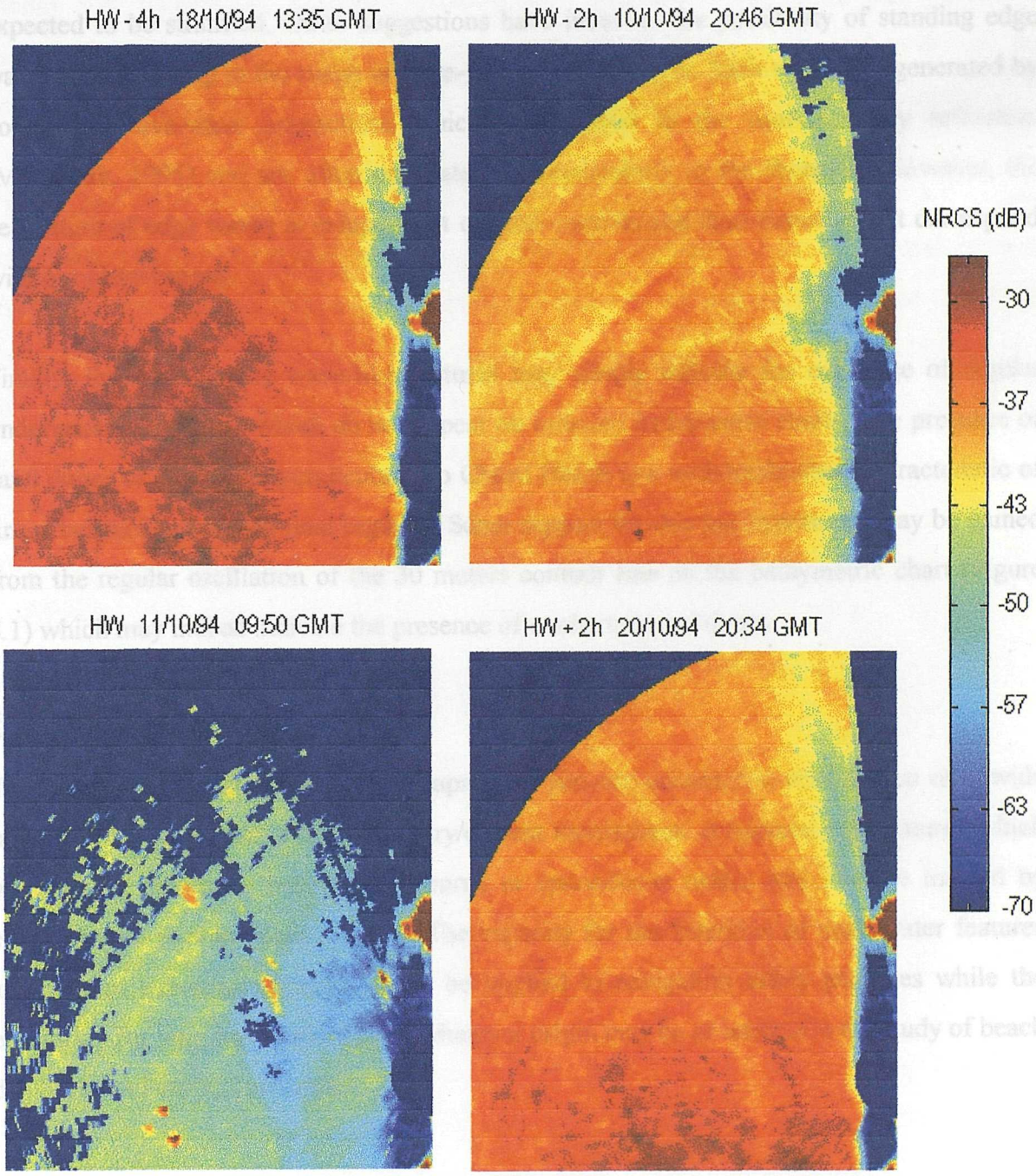

Figure 8. 20 - Long-crested wave features at various tidal stages in Portland

The apparent wavelength of these features has been estimated at 380 meters and fall beyond the range of wavelength measurable by the directional wave buoy. Multi-rotation averaging over a varying number of antenna revolution confirmed that these features are not a sampling artefact and that their position remains unchanged in all images.

The interpretation of these features proves difficult due to the complexity of the area and the lack of additional information. However, the hypothesis of internal wave oscillations can be rejected as the experiment took place in autumn and the water column in this area was not expected to be stratified. Other suggestions have involved the possibility of standing edge waves which belong to the range of infra-gravity wavelengths. Such waves are generated by non-linear wave-wave interactions which get trapped in the near-shore by refraction (Masselink, 1995) and are often orientated perpendicularly to the shoreline. However, the generation of edge waves is independent of tidal currents and does therefore not correspond with our observations.

Finally, these long scale wave-like features may simply indicate the existence of regular underwater sand dunes which do not appear on ordinary bathymetric charts. The presence of sand dunes orientated perpendicularly to Chesil Beach is a well-established characteristic of linear beaches and strong tidal regimes. Some support for this last hypothesis may be gained from the regular oscillation of the 30 meters contour line on the bathymetric chart (Figure 8.1) which may indeed indicate the presence of uncharted sand dunes.

Potential applications

The marine radar system has proved capable to provide quantitative information on a wide range of processes related to bathymetry/current interactions. It appears that features which were so far detectable only from airborne or space-borne radars may also be imaged by coastal based or ship based systems. The capacity for the detection of underwater features and current convergence zones could be applied to navigation safety purposes while the possibility for long wave detection of whatever origin may be of interest in the study of beach dynamics and erosion processes.

8.5 - Conclusions

This chapter has established the basic relationships between the ocean backscatter and environmental conditions. The ocean backscatter level has been found to be governed primarily by wind speed and direction and was found to closely follow a logarithmic dependence. The detection performances of the radar system were shown to depend strongly on wind conditions and on sea state which determines the shadowing losses and defines the maximum NRCS extinction range. The proposed model based on the composite shadowing model and preliminary empirical relationships with the wind speed has proven to satisfactorily predict the system's detection performances and may be used to deduce the capabilities of the system in a wide range of operational and environmental conditions.

The marine radar system was found able to provide important complementary information for a wide range of oceanographic applications. The quantitative measuring capabilities of the system remain to be fully exploited as for example in the investigation of the possibility for remotely measuring the ocean wave height. The system was however found already able to contribute to practical applications as diverse as directional wave climate estimation, surfactant detection and monitoring and bathymetric features detection.

Chapter 9

Conclusion and Future Work

9.1 - Synopsis

The original aim of the thesis was to examine the capabilities of a digital marine radar system for quantitative sea surface roughness measurements and application to oceanography. The thesis was divided into two parts which aimed respectively at defining the performances of the system and investigating the relation between ocean backscatter measurements and operational/environmental parameters. A summary will now be provided recalling the principal results achieved in each part:

Part 1 - Instrumentation, Calibration and Performances

- The spatial and radiometric resolution in the marine radar images were optimised by identifying the best combination of parameters in the digital capture register.

- The antenna heading error responsible for large positioning inaccuracies in azimuth was substantially reduced with the development and implementation of the electronic Flywheel.

- The end-to-end calibration of the radar system was performed to provide the means to meaningful quantitative measurements of the sea surface roughness.

- A full error analysis of the normalisation equations resulted in the estimation of the total relative error in the quantitative measurements of the sea surface NRCS. This NRCS error was found to be of the order of 0.6 dB given adequate averaging and established that the

radiometric resolution in the marine radar images compares well with that of traditional research radar systems.

- The lower and upper limits of the instrument's detection performances were established and revealed that the marine radar system is particularly well adapted to sea clutter measurements at low grazing angles.

Part 2 - Ocean Backscatter at Low Grazing Angles

- The ocean backscatter at low grazing angles originates from both small scale distributed roughness scattering and discrete high energy returns from longer ocean waves crests.

- The differences in spatial and temporal sampling on different pulse settings and the non-uniform spatial distribution of wave crests on the surface are responsible for larger ocean backscatter coefficients on longer pulse settings.

- The increase in ocean backscatter coefficient with antenna height is related primarily to the associated change in viewing angle and is well predicted by analytical models of the shadowing processes at low grazing angles.

- A composite shadowing model is proposed to describe the observed variation in shadowing regime with range, antenna height, pulse length and environmental conditions.

- Experimental results establish that the ocean backscatter at low grazing angles is entirely determined by wind conditions and follows a logarithmic dependence on wind speed.

- The combination of the composite shadowing model and the empirical relationships to wind speed provides a satisfactory method to predict the extinction range of the ocean backscatter and determine the detection capabilities of the system in a wide range of operational and environmental conditions.

9.2 - Conclusion and future work

In conclusion, the key objectives of the thesis have been achieved and have clearly established the great potential of a marine radar system as a tool for oceanographic research. The system is capable of providing complementary information for a wide range of oceanographic applications including beach erosion studies, oil pollution control and navigation safety. The full capabilities of the marine radar system are only just starting to unfold as the system is only now sufficiently well defined to serve as a reliable investigative tool.

The work in the immediate future should aim towards a better definition of the ocean backscatter's dependence on wind direction to improve the accuracy of the model for ocean backscatter extinction range predictions. Later work will concentrate on the quantitative measuring capabilities of the system which still remain to be fully exploited. In particular, the combination of ocean backscatter coefficient measurements with the system's capabilities for space-time analysis of sea clutter is likely to constitute one of our future challenges.

Appendix A

Experimental Data Points for the System Calibration

A.1 - Two-step calibration

A.1.1 - Marine radar calibration experiment

Short Pulse		Medium/Long Pulse	
Power input (dBm)	Voltage output (V)	Power input (dBm)	Voltage output (V)
-101.0 (noise level)	0.22	-104.00 (noise level)	0.35
-99.00	0.25	-92.00	0.50
-81.00	0.50	-80.00	0.75
-69.70	0.75	-69.50	1.00
-59.70	1.00	-61.30	1.25
-52.00	1.25	-53.90	1.50
-44.50	1.50	-46.70	1.75
-36.60	1.75	-37.80	2.00
-28.60	2.00	-30.10	2.25
-20.90	2.25	-22.00	2.50
-9.00	2.50	-	-

Table A. 1 - Experimental results for the marine radar in the Two-step calibration experiment

Voltage correction for noise voltage:

Corrected Voltage = Vmesured - Vnoise

Transformation from dBm into dB:

Power in dB = Power in dBm - 30

A.1.2 - Digital capture board calibration

Voltage input (V)	Intensity in image (counts)
1.58	255
1.57	254
1.56	253
1.55	251
1.50	244
1.40	229
1.30	214
1.20	198
1.10	184
1.00	168
0.90	154
0.80	140
0.70	123
0.60	108
0.50	94
0.40	77
0.30	64
0.20	48
0.10	32
0.01	20
0.00	18
-0.005	17
-0.030	13

Table A. 2 - Experimental results for the digital capture board in the Two-step calibration experiment

A.2 - One-step calibration

Short Pulse		Medium/Long Pulse	
Power input (dBm)	Image Intensity (counts)	Power input (dBm)	Image Intensity (counts)
-102	18	-	-
-100	19	-100	18
-95	22	-95	20
-90	30	-90	24
-85	48	-85	42
-80	67	-80	60
-75	85	-75	88
-70	108	-70	110
-65	132	-65	140
-60	156	-60	163
-55	179	-55	191
-50	200	-50	215
-45	228	-45	243
-40	251	-40	255
-35	255	-	-

Table A. 3 - Experimental results for the One-step calibration experiment

Transforming dBm into dB:

$$\text{Power in dB} = \text{Power in dBm} - 30$$

Appendix B

Calibration and Averaging Programs

B.1 - Calibration routine - CALIB.C

```
#include <stdio.h>
#include <stdlib.h>
#include <math.h>

int noiserr,noiseaverage;

main()
{
/*****************************************************************
THIS PROGRAMME READS RAW OR AVERAGED IMAGES AND CALIBRATES
THEM EXTERNALLY OR INTERNALLY TO PRODUCE FILES CALLED
IMAGERAW.EXT, IMAGERAW.INT, IMAGEAVE.EXT OR IMAGEAVE.INT
*****************************************************************/
/*INITIALISING VARIABLES*/

FILE *fsetup,*fin,*foutwax;
FILE *foutreal;

char imagetype,pulselength,radarset,caltype,setting,modfly;
int i,data=0,im,imcalinteger,noi=0;
long j=0;

float heightinput;
long pixelrad,pixelaz,pixelnum;

double pi,omega,pulse,height;
double range,phi,footsize,Klog;
double C,D,sigmat;
double imcal,logp;

int rescale(double);
double logpowershort(int),logpowerlong(int);
```

```
struct wbr
{
double sr,id,bd,azs,azi;
unsigned int azst,noi,mux;
};

struct rr
{
double prf,tpr;
};

struct sr
{
unsigned int yr,mo,dy;
unsigned int hr,mn,ss;
unsigned int ms,us;
char site[65];
};

struct all
{
struct wbr wx;
struct rr rx;
struct sr sx;
};

union ip
{
struct all ax;
char ic[142];
} imp;

/*********************************************************************/
/*READING RADAR IMAGE PARAMETERS IN SETUP FILE*/
fsetup = fopen("setup.wax","rb");
if(fsetup==NULL)
    {
    printf("\nError in opening file:64");
    return(0);
    }
for(i=0;i<142;i++)
        imp.ic[i]=getc(fsetup);
fclose(fsetup);

printf("\nSampling Rate=%f",imp.ax.wx.sr);
printf("\nInitial Delay=%f",imp.ax.wx.id);
```

```
printf("\nBurst Duration=%f",imp.ax.wx.bd);
printf("\nAzimuth Start Angle=%f",imp.ax.wx.azs);
printf("\nAzimuth Interval=%f",imp.ax.wx.azi);
printf("\nAzimuth Step=%u",imp.ax.wx.azst);
printf("\nNumber of Images=%u",imp.ax.wx.noi);
printf("\nMux=%u",imp.ax.wx.mux);
printf("\nPulse Repetition Frequency=%f",imp.ax.rx.prf);
printf("\nTime per Revolution=%f",imp.ax.rx.tpr);
printf("\nYear=%u",imp.ax.sx.yr);
printf("\nMonth=%u",imp.ax.sx.mo);
printf("\nDay=%u",imp.ax.sx.dy);
printf("\nHour=%u",imp.ax.sx.hr);
printf("\nMinutes=%u",imp.ax.sx.mn);
printf("\nSeconds=%u",imp.ax.sx.ss);

if(imp.ax.rx.prf==1300||imp.ax.rx.prf==700||imp.ax.rx.prf==300)
        {
        printf("\nAre you using the modified Flywheel? (Y/N) ");
        scanf("%c%c",&modfly);
        modfly=toupper(modfly);
        if(modfly=='Y')
                imp.ax.wx.id = imp.ax.wx.id + 1.59;
        else
                imp.ax.wx.id = imp.ax.wx.id + 2.4;
        }

/*********************************************************************/
/*IMAGE SIZE */
pixelrad = imp.ax.wx.sr * imp.ax.wx.bd;
printf("\npixelrad=%i",pixelrad);
pixelaz = imp.ax.wx.azi*imp.ax.rx.prf/(imp.ax.wx.azst*(360/imp.ax.rx.tpr))+0.5;
printf("\npixelaz=%i",pixelaz);
pixelnum = pixelrad * pixelaz;
printf("\npixelnum=%ld",pixelnum);

/*********************************************************************/
/*TYPE OF IMAGE TO BE CALIBRATED*/
printf("\nDo you want to calibrate a raw (R) or an averaged (A) image?");
scanf("%c%c",&imagetype);
imagetype=toupper(imagetype);

if(imagetype=='A')
        {
        printf("\nNumber of images averaged?");
        scanf("%i%c",&noi);
        }
else
```

```
        noi=1;
/*************************************************************************/
/*CONSTANTS AND CALIBRATION PARAMETERS*/
pi=4*atan(1);
omega=1.3*pi/180; /*antenna horizontal beamwidth in radians*/
sigmat=10;
noiseaverage=19;

printf("\nEnter antenna height (in meters): ");
scanf("%f",&heightinput);
height=heightinput;

if(imp.ax.rx.prf==2400||imp.ax.rx.prf==1300)
        {
        printf("\nYou are in the short pulse setting");
        setting='S';
        pulse=0.065*150;
        Klog=31.6;
        /*noiserr=Standard Deviation of thermal noise in counts*/
        if(imagetype=='A')
                {
                if(noi<4)
                        noiserr=2;
                else
                        noiserr=1;
                }
        else
                noiserr=2;
        }

else if(imp.ax.rx.prf==1200||imp.ax.rx.prf==700)
        {
        printf("\nYou are in the medium pulse setting");
        setting='M';
        pulse=0.22*150;
        Klog=33.1;
        C=-0.206;
        D=170;
/*noiserr=Standard Deviation of thermal noise in counts*/
        if(imagetype=='A')
                {
                if(noi<4)
                        noiserr=4;
                else if(noi<16)
                        noiserr=2;
                else
                        noiserr=1;
```

```
                }
        else    noiserr=4;
        }

else if(imp.ax.rx.prf==600||imp.ax.rx.prf==300)
        {
        printf("\nYou are in the long pulse setting");
        setting='L';
        pulse=0.86*150;
        Klog=33.7;
        /*noiserr=Standard Deviation of thermal noise in counts*/
        if(imagetype=='A')
                {
                if(noi<4)
                        noiserr=6;
                else if(noi<8)
                        noiserr=3;
                else if(noi<24)
                        noiserr=2;
                else
                        noiserr=1;
                }
        else    noiserr=6;
        }
else    exit(1);

noiserr = noiserr + 1;

printf("\nPulse length=%f m\nPRR=%f Hz\n\nHeight=%f m",pulse,imp.ax.rx.prf,height);
printf("\nNumber of images averaged=%i \n\nNoise Average=%i \nNoise
Error=%i",noi,noiseaverage,noiserr);

/*****************************************************************/
/*TYPE OF CALIBRATION*/
printf("\nDo you want an External (E) or Internal (I) calibration: ");
scanf("%c%c",&caltype);
caltype=toupper(caltype);

if(caltype=='E'&&setting=='S'||caltype=='E'&&setting=='L')
        {
        printf("\nSorry! No external calibration available for short and long pulse settings!");
        exit(1);
        }

/*****************************************************************/
/*OPENING INPUT AND OUTPUT FILES*/
if(imagetype=='R')
```

```
        {
        fin = fopen("image.raw","rb");
        if(caltype=='E')
                foutwax=fopen("imageraw.ext","wb");
        else
                foutwax=fopen("imageraw.int","wb");
        }
else if(imagetype=='A')
        {
        fin = fopen("image.ave","rb");
        if(caltype=='E')
                {
                foutwax=fopen("imageave.ext","wb");
                foutreal=fopen("imavreal.ext","wb");
                }
        else
                {
                foutwax=fopen("imageave.int","wb");
                foutreal=fopen("imavreal.int","wb");
                }
        }
else
        printf("\nInvalid Entry:107");

if(fin==NULL||foutwax==NULL)
   {
   printf("Error in opening file:125");
   exit(1);
   }

/*********************************************************************/
/*CALIBRATION*/

switch(caltype)
{

/*********************************************************************/
/* EXTERNAL CALIBRATION */
case 'E':
while((data !=EOF) && (j<pixelnum))
        {
        data=getc(fin);
        im=255-data;
        if(i>pixelrad-1)i=0;
        range=((i/imp.ax.wx.sr)+imp.ax.wx.id)*150;
        phi=acos(height/(range+pulse)) - acos(height/range);
        footsize=phi*omega*pow(range,3)/height;
```

```
        if(im>=255)
                imcal=15;
        else
                imcal= -C*im -D +10*log10(sigmat) +10*log10(pow(range,4)) -
10*log10(footsize);
        fprintf(foutreal,"%f",imcal);
        imcalinteger=rescale(imcal);
        imcalinteger=255-imcalinteger;
        fprintf(foutwax,"%c",imcalinteger);
        i++;
        j++;
        }
printf("\n\ni=%i,j= %ld",i,j);
break;

/*****************************************************************/
/* INTERNAL CALIBRATION */
case 'I':
if(setting=='S')
        {
        i=0;
        while((data !=EOF) && (j<pixelnum))
                {
                data=getc(fin);
                im=255-data;
                if(i>pixelrad-1)i=0;
                range=((i/imp.ax.wx.sr)+imp.ax.wx.id)*150;
                phi=acos(height/(range+pulse)) - acos(height/range);
                footsize=phi*omega*pow(range,3)/height;
                if(im<=noiseaverage+noiserr)
                        imcal=-70;
                else if(im==255)
                        imcal=15;
                else
                        {
                        logp=logpowershort(im);
                        imcal= logp - Klog + 10*log10(pow(range,4)) - 10*log10(footsize);
                        }
                fprintf(foutreal,"%f",imcal);
                imcalinteger=rescale(imcal);
           imcalinteger=255-imcalinteger;
                fprintf(foutwax,"%c",imcalinteger);
                i++;
                j++;
                }
        printf("\n\ni=%i,j= %ld",i,j);
        }
```

```
else
        {
        i=0;
        while((data !=EOF) && (j<pixelnum))
                {
                data=getc(fin);
                im=255-data;
                if(i>pixelrad-1)i=0;
                range=((i/imp.ax.wx.sr)+imp.ax.wx.id)*150;
                phi=acos(height/(range+pulse)) - acos(height/range);
                footsize=phi*omega*pow(range,3)/height;
                if(im<=noiseaverage+noiserr)
                        imcal=-70;
                else if(im==255)
                        imcal=15;
                else
                        {
                        logp=logpowerlong(im);
                        imcal= logp - Klog + 10*log10(pow(range,4)) - 10*log10(footsize);
                        }
                fprintf(foutreal,"%f",imcal);
                imcalinteger=rescale(imcal);
                imcalinteger=255-imcalinteger;
                fprintf(foutwax,"%c",imcalinteger);
                i++;
                j++;
                }
        printf("\n\ni=%i,j= %ld",i,j);
        }
break;

default:
printf("\nInvalid entry:271");
break;

}
fclose(fin);
fclose(foutwax);
fclose(foutreal);
return(0);

}
/*END OF MAIN PROGRAM*/

/*****************************************************************/
```

```
/*****************************************************************/
/*SUBROUTINES*/

double logpowershort(int im)
        {
        double logp,imdouble;
        imdouble=im;
        if(imdouble>noiseaverage+noiserr&&imdouble<31)
                logp= 2.6777E-03*pow(imdouble,3) - 2.8129E-01*pow(imdouble,2) +
                9.7829*imdouble - 2.3262E+02;
        else if(imdouble>=31&&imdouble<251)
                logp= 1.0973E-06*pow(imdouble,3) - 6.2997E-04*pow(imdouble,2) +
                3.2499E-01*imdouble - 1.2919E+02;
        else if(imdouble>=251&&imdouble<255)
                logp= 6.8152E-04*pow(imdouble,3) - 4.6199E-01*pow(imdouble,2) +
                1.0414E+02*imdouble - 7.8814E+03;
        return (logp);
        }

double logpowerlong(int im)
        {
        double volt,logp,imdouble;
        imdouble=im;
        if(imdouble>noiseaverage+noiserr&&imdouble<25)
                logp= 6.8392E-03*pow(imdouble,3) - 6.3237E-01*pow(imdouble,2) +
                1.9116E+01*imdouble - 3.0909E+02;
        else if(imdouble>=25&&imdouble<245)
                logp= 1.4922E-06*pow(imdouble,3) - 7.3008E-04*pow(imdouble,2) +
                3.0260E-01*imdouble - 1.2657E+02;
        else if(imdouble>=245&&imdouble<255)
                logp= 1.0195E-04*pow(imdouble,3) - 6.6737E-02*pow(imdouble,2) +
                1.4685E+01*imdouble - 1.1656E+03;
        return(logp);
        }

int rescale(double imcal)
        {
        int imcalinteger;
        double imcaldouble,imcaldecimal,*imcalintptr;
        imcaldouble=3*imcal+210;
        /*imcaldouble: imcal rescaled -70->15dB to 0->255counts but still double*/
        /*Rescales (-70dB-->15dB) to (0-->255counts)*/
        imcalintptr=&imcaldouble;
        imcaldecimal=modf(imcaldouble,imcalintptr);
        /*imcaldecimal: fractionnal part of imcaldouble*/
        if(imcaldecimal>0.5) *imcalintptr=*imcalintptr + 1;
```

```
        /* imcalintptr: pointer to the integral part of imcaldouble*/
        imcalinteger=*imcalintptr;
        if((imcalinteger<0) || (imcalinteger>255)) imcalinteger=0;
        return (imcalinteger);
        }
/*END OF SUBROUTINES*/
/*************************************************************************/
```

B.2 - Averaging routine - WAVER.C

```
#include <stdio.h>
#include <math.h>
#include <graphics.h>
#include <string.h>
#include <alloc.h>

/*************************************************************************/
/*THIS PROGRAMME IS ADAPTED FROM A PROGRAM WRITTEN BY NICHOLAS
WARD. THE ROUTINE READS IMAGE.RAW AND COMPUTES THE AVERAGE AND
STANDARD DEVIATION IMAGES FOR A GIVEN NUMBER OF ROTATIONS TO BE
SPECIFIED. THE  OUTPUT FILES ARE CALLED IMAGE.AVE AND IMAGE.STD*/
/*************************************************************************/

FILE *fn,*fnp,*fng;

int nol,nil,noi,noitotal;
unsigned int map[512];
unsigned char inm[512],inm2[512];
unsigned long dev[512];

float ang;
double inmreal[512],inm2real[512],temp;

struct wbr
  {
  double sr,id,bd,azs,azi;
  unsigned int azst,noi,mux;
  };

struct rr
  {
  double prf,tpr;
  };

struct sr
```

```
  {
  unsigned int yr;
  unsigned int mo,dy,hr,mn,ss;
  unsigned int ms,us;
  char site[65];
  };

struct all
  {
  struct wbr wx;
  struct rr rx;
  struct sr sx;
  };

union ip
  {
  struct all ax;
  char ic[142];
  } imp;

/*************************************************************************/
main()

{
int x;
char ch;
fn=fopen("setup.wax","rb");
if(fn==NULL)
  {
  printf("set up file not found\n");
  exit(-1);
  }
for(x=0;x<142;x++)
  imp.ic[x]=getc(fn);
imp.ax.sx.site[64]='\0';
fclose(fn);
fn=fopen("image.raw","rb");
fnp=fopen("image.ave","wb");
fng=fopen("image.std","wb");
if(fn==NULL)
  {
  printf("no image file");
  exit(-1);
  }
ave();
}
/*END OF MAIN PROGRAM*/
```

```
/*************************************************************************/

/*SUBROUTINES*/
ave()
{
int x,y,z;
int n;
noitotal=imp.ax.wx.noi;

printf("\nEnter number of images to average:");
scanf("%i",&noi);
while(noi>noitotal)
        {
        printf("\nSorry! Maximum Number of images is %i",noitotal);
        return(0);
        }
printf("\nNumber of images=%i",noi);
nil=imp.ax.wx.bd*imp.ax.wx.sr;
ang=360.0/imp.ax.rx.tpr/imp.ax.rx.prf*imp.ax.wx.azst;
nol=imp.ax.wx.azi/ang+0.5;
printf("\nAveraging program\n\n\n");
printf("Number of images = %d\n",noi);
printf("Number of lines  = %d\n",nol);
printf("Number of pixels = %d\n\n",nil);

for(x=0;x<nol;x++)
  {
  printf("%d -",x);
  if(kbhit()!=0)
        if(getch()==27)
          exit(-1);
  for(y=0;y<nil;y++)
        {
        dev[y]=0;
        map[y]=0;
        }
  for(y=0;y<noi;y++)
        {
        fseek(fn,((long)y*nol+x)*nil,SEEK_SET);
        fread(inm,1,nil,fn);
        for(z=0;z<nil;z++)
                {
                inm[z]=255-inm[z];
                dev[z]+=(unsigned long)inm[z]*inm[z];
                map[z]+=inm[z];
                }
        }
```

```
  for(y=0;y<nil;y++)
    {
    inmreal[y]=(double)map[y]/noi;
    temp=((double)dev[y] - (double)map[y]*map[y]/noi);
    if(temp>=0)
        inm2real[y]=sqrt(temp/(noi-1));
    else
        inm2real[y]=0;

    inm[y]=inmreal[y]+0.5;
    inm2[y]=inm2real[y]+0.5;

    inm[y] = 255 - inm[y];
    inm2[y]= 255 - inm2[y];
    }
  fwrite(inm,1,nil,fnp);
  fwrite(inm2,1,nil,fng);
  }
printf("\nFinished\n\n");
fclose(fn);
fclose(fnp);
}
/*END OF SUBROUTINES*/
/*************************************************************************/
```

Appendix C

Atmospheric Ducting

Atmospheric ducting is a propagation effect typical of radar waves travelling near the earth or sea at low grazing angles. The phenomenon is linked with the presence of strong refractivity index gradient near the surface which traps the radar waves and changes the dependency of the grazing angle on antenna height and range. The propagation conditions have been shown to be anomalous over the sea surface for at least 85% of the time due to the persistent presence of an evaporative layer about 10 m thick over the sea surface (Skolnik,1980).

Electromagnetic radiation travel in straight lines in free space, but are refracted in the earth's atmosphere because of the change in refractive index with altitude. The problem of electromagnetic waves following bent path in the earth atmosphere can be reformulated in the flat earth approximation by replacing the actual earth radius a by an equivalent earth radius r_e and replacing the actual atmosphere by an homogeneous atmosphere in which electromagnetic rays travel in straight lines (Skolnik, 1970). The equivalent earth radius is then given by:

$$r_e = \frac{a}{1 + a \cdot \frac{dn}{dz}}$$ **Equation C. 1**

where dn/dz is the vertical gradient of the atmosphere's refractive index n. The standard refraction condition assumes that the index of refraction gradient to be constant with altitude and equal to $-40.10^{-6}\ m^{-1}$.

The grazing angle at any given range R can then be calculated using (Nathanson, 1969):

$$\varphi = \operatorname{asin}\left[\frac{h}{R} \cdot \left(1 + \frac{h}{2 \cdot r_e}\right) - \frac{R}{2 \cdot r_e}\right]$$ **Equation C. 2**

where h is the height of the radar antenna. Figure C.1 shows the grazing angle with range for two antenna heights (10 and 50 m) and values of the refractivity index gradient equal to 0, -40.10^{-6} and -100.10^{-6} m^{-1}. The results are shown only for the range of distances accessible to the present radar system (i.e. maximum range = 8000 m).

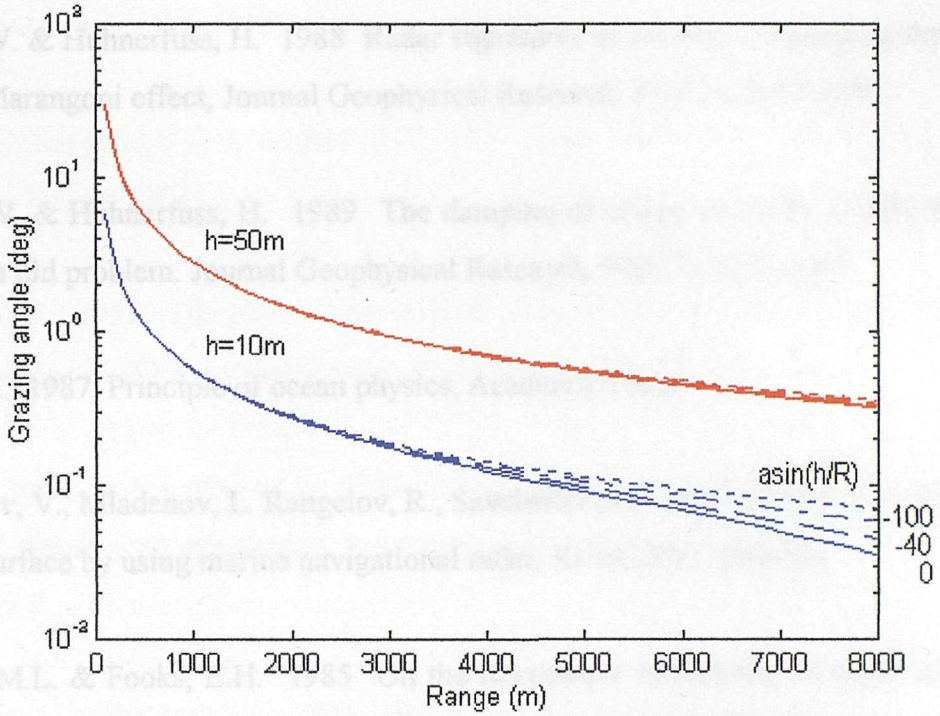

Figure C. 1 - Atmospheric ducting effect on grazing angle shown in logarithmic scale versus range for different antenna heights and dn/dz equal to 0 (solid line), -40.10^{-6} (dashed line) and -100.10^{-6} m^{-1} (dash-dotted line). The dotted line correspond to the traditional calculation of the grazing angle as asin(h/R).

The effect of anomalous propagation conditions on the grazing angle is more noticeable at far ranges and for low antenna heights. Strong refractive index gradients tend to limit the minimal value of the grazing angle, which can becomes constant at far ranges. However, for ranges smaller than 8000 meters as considered by the present radar system, the change in grazing angle due to atmospheric ducting is negligible, even for strong refractive index gradients.

List of References

Alpers, W. & Hennings, I. 1984 A theory of the imaging mechanism of underwater bottom topography by real and synthetic aperture radar, 89(C), 10529-10546.

Alpers, W. & Huhnerfuss, H. 1988 Radar signatures of oil films floating on the sea surface and the Marangoni effect, Journal Geophysical Research, 93(C4), 3642-3648.

Alpers, W. & Huhnerfuss, H. 1989 The damping of ocean waves by surface films: a new look at an old problem. Journal Geophysical Research, 94(C5), 6251-6265.

Apel, J.R. 1987 Principle of ocean physics, Academic Press.

Atanassov, V., Mladenov, L. Rangelov, R., Savchenko, A. 1991 Observation of oil slicks on the sea surface by using marine navigational radar, IGARSS'91, Helsinki.

Banner, M.L. & Fooks, E.H. 1985 On the microwave reflectivity of small scale breaking water waves, Proceedings Royal Society London, Series A, 399, 93-109.

Beckmann, P. & Spizzichino, A. 1963 The scattering of electromagnetic waves from rough surfaces, Pergamon Press.

Boalch, C.R. & McManus, J. 1989 Wave refraction pattern recognition off North Sea coasts using X-band radar, p.79-84 in, Radar Refraction of waves.

Boas, M.L. 1983 Mathematical methods in the physical sciences, 2nd edition, John Wiley & Sons, Inc.

Chan, H.C., 1990 Radar sea-clutter at low grazing angles, IEE Proceedings F: Radar and signal processing, 137(2), 102-112.

Charnock, H. 1955 Wind stress on a water surface, Quarterly Journal Royal Meteorological Society, 81, 639-640.

Crombie, D.D. 1955 Doppler spectrum of sea echo at 13.56 Mc/s, Nature, 175, 681-682.

Cox, C. & Munck, W. 1954 Statistics of the sea surface derived from the sun glitter, Journal Marine Research, 13, 198-227.

Daley, J.C, Ransone, J.T.Jr., Burkett, J.A. 1971 Radar sea return - JOSS1, Naval Research Laboratory Report 7268.

DeLoor, G.P. 1981 The observation of tidal patterns, currents and bathymetry with SLAR imagery of the sea, IEEE Journal Oceanic Engineering, OE-6, 124-129.

Donelan, M.A. & Pierson, W.J. 1987 Radar scattering and equilibrium ranges in wind-generated waves with application to scatterometry, Journal Geophysical Research, 92(C5), 4971-5029.

Fiuza, A.F.G. 1990 Physics of Remote Sensing of Sea Surface Temperature, p. 215-242 in, Space Oceanography, Eds. A.P. Cracknell, World Scientific.

Garratt, J.R. 1977 Review of drag coefficients over oceans and continents, Monthly Weather Review, 105, 915 -929.

Gade, M., Alpers, W., Bao, M. & Huhnerfuss, H. 1996 Measurements of the radar backscattering over different oceanic surface films during the SIR C/X-SAR campaigns, IGARSS'96, 2, 860-862.

Geernaert, G.L. 1990 Bulk parameterisations for the wind stress and heat fluxes, p 91-172 in, Surface Waves and Fluxes, Volume 1 - Current theory, eds. G.L. Geernaert and W.J. Plant.

van Hasselma, D. & Teewen, J.H.M. 1992 Tracking of oil-spills at sea with the shipborne SHIRA radar: Summary of results during NEDGER 1992, TNO-FEL report 92-B328.

Henschel, M.D., Paul, R.A. & Eid, B.M 1994 Use of satellite synthetic aperture radar for operational measurement of ocean wave spectra, ERIM 2nd Thematic Conference: Remote sensing for marine and coastal environments, New Orleans, USA.

Hirakuchi, H. & Ikeno, M. 1989 Wave direction measurements using Marine X-band radar, ABIKO Research Laboratory Report No. U89007.

Holliday, D., St-Cyr, G. & Woods, N.E. 1986 A radar ocean imaging model for small to moderate incidence angles, International Journal Remote Sensing, 7(12), 1809-1834.

Huhnerfuss, H., Alpers, W. & Witte, F. 1989 Layers of different thicknesses in mineral oil spills detected by grey level textures of real aperture radar images, International Journal Remote Sensing, 10(6), 1093-1099.

Jeynes, P.L.C. 1989 Limitations of the two-scale theory for microwave backscatter from the ocean, p.41-47 in, Radar scattering from modulated wind waves, eds. G.J.Komen and W.A.Oost.

Kalmykov, A.I & Pustovoytenko, V.V 1976 On polarisation features of radio signals scattered from the sea surface at small grazing angles, Journal Geophysical Research, 81, 1960-1964.

Keller, W.C., Plant, W. & Weissman, D.E. 1985 The dependence of X-band microwave sea return on atmospheric stability and sea state, Journal Geophysical Research, 90 (C1), 1019-1029.

Kerry, N.J., Burt, R.J., Lane, N.M. & Bagg, M.T. 1984 Simultaneous radar observations of surface slicks and in situ measurements of internal waves, Journal Physical Oceanography, 14, 1419-1423.

Kleijweg, J.C.M & Greidanus, H. 1993 Validation of directional wave spectra from the ERS-1 during the ESA Cal/Val campaign, Proceedings 1st ERS-1 Symposium, Space at the service of our environment, Cannes, France.

Knott, E.F., Shaeffer, J.F. & Tuley, M.T. 1985 Radar Cross Section - Its prediction, measurement and reduction, Artech House.

Komen, G.J. & Hasselmann, K. 1994 The action balance equation and the statistical description of wave evolution, p. 5-48 in, Dynamics and modelling of ocean waves, eds. G.J. Komen, L. Cavaleri, M. Donelan, K. Hasselmann, S. Hasselmann and P.A.E.M. Janssen.

Kwoh, D.S.V & Lake, B.M. 1981 Microwave scattering from short gravity waves: deterministic, coherent, dual polarised study of the relationship between backscatter and water wave properties, p.273-281 in, Wave Dynamics and Radio Probing of the Ocean Surface, eds. O.M Phillips and K. Hasselmann.

Kwoh, D.S.V & Lake, B.M. 1984 A deterministic, coherent and dual-polarised laboratory study of microwave backscattering from water waves: Part 1 - Short gravity waves without wind, IEEE Journal Oceanic Engineering., OE-9, 5, 291-308.

Kwoh, D.S.V & Lake, B.M. 1985 The nature of microwave backscattering from water waves, p. 249-256 in, The ocean surface: wave breaking, turbulent mixing and radio probing, eds. Y.Toba and H.Mitsuyasu.

Lee, P.H.Y., Barter, J.D., Beach, K.L., Hindman, C.L., Lake, B.M., Rungaldier, H., Shelton, J.C., Williams, A.B., Yee, R. & Yuen, H.C. 1995 X-band microwave backscattering from ocean waves, Journal Geophysical Research, 100 (C2), 2591-2611.

Lewis, B.L. & Olin, I.D. 1980 Experimental study and theoretical model of high-resolution radar backscatter from the sea, Radio Science, 15, 815-828.

Masselink, G. 1995 Group bound long waves as a source of infragravity energy in the surf zone, Continental shelf research, 15, 1525-1547.

Meadows, P.J. & Wright, P.A. 1994 ERS-1 SAR analogue to digital converter saturation, Proceedings of the CEOS SAR calibration workshop, Ann Arbor, Michigan, 28-30 September 1994.

MIROS 1991 Operation manual for Wavex radar data capture system, GD/037/91/dB/-/D.

Mitsuyasu, H. & Honda, T. 1986 The effects of surfactants on certain air-sea interaction phenomena, p. 95-115 in, Wave Dynamics and Radio Probing, eds. O.M. Phillips and K. Hasselmann.

Mood, A..M., Graybill, F.A. & Boes, D.C. 1974 Introduction to the theory of statistics, McGraw Hill.

Nathanson, F.E. 1969 Radar Design Principles - Signal Processing and the Environment, McGraw-Hill.

Ogilvy, J.A. 1991 Theory of wave scattering from random rough surfaces, IOP Publishing Ltd.

Phillips, O. M. 1977 The dynamics of the upper ocean, 2d ed., Cambridge University Press.

Phillips, O.M. 1988 Radar returns from the sea surface - Bragg scattering and breaking waves, Journal Physical Oceanography, 18(8), 1065-1074.

Plant, W.J. & Keller, W.C. 1990 Evidence of Bragg Scattering in microwave Doppler spectra of sea return, Journal Geophysical Research, 95(C9), 16299--16310.

Rees, W.G. 1990 Physical principles of remote sensing, Cambridge University Press.

Rice, S.O. 1951 Reflection of electromagnetic waves from slightly rough surfaces, Communications Pure Applied Mathematics, 4, 351-378.

Robinson, I.S. & Ward, N. 1990 A numerical phase summation model of radar backscatter from a rough sea surface, Electronics Division Colloquium on the Interaction of radiowaves with the sea surface, 21 February 1990, London, p.7/1-7/6.

Simmons, J. 1994 Director of Engineering, Trinity House Lighthouse Service, private communication.

Sittrop, H. 1985 On the sea clutter dependency on wind speed, p. 245-249 in, Advances in Radar Techniques, IEE Electromagnetic Waves Series 20, eds. J.Clarke.

Skolnik, M.L. 1970 Radar Handbook, McGraw Hill.

Skolnik, M.L. 1980 Introduction to Radar Systems, McGraw Hill.

Skolnik, M.L. 1990 Radar Handbook, 2nd edition, McGraw Hill.

Smith, B. G. 1967 Geometrical shadowing of a random rough surface. IEEE Transactions Antennas Propagation, AP-15, 668-671.

Stewart, R.H. 1985 Methods of satellite oceanography, University of California Press.

Tennyson, E.J. 1989 Shipboard navigational radar as an oil spill tracking tool, Oil Spill Conference 1989.

Tenorio, M.A. 1992 The Southampton University Wavex System, Internal report, September 1992.

Trask, J., Henschel, M. & Eid, B. 1994 Analysis of marine radar image spectra collected during the Grand Banks ERS-1 SAR wave experiment, Atmosphere-Ocean, 32 (1).

Trizna, D.B. 1985 Preliminary results of dual polarised radar sea scatter, p. 297-302 in, The ocean surface: wave breaking, turbulent mixing and radio probing, eds. Y.Toba and H.Mitsuyasu.

Trizna, D.B. 1988 Measurement and interpretation of North Atlantic ocean marine radar sea scatter, US Naval Research Laboratory, NRL Report 9099.

Trizna, D.B. 1989 Pacific marine radar sea scatter experimental results, US Naval Research Laboratory, NRL Memorandum Report 6506.

Trizna, D.B. 1991a Statistics of low grazing angle radar sea scatter for moderate and fully developed ocean waves, IEEE Transactions Antennas Propagation, 39, 1681-1690.

Trizna, D.B., Hansen, J.P., Hwang, P. & Wu, J. 1991b Laboratory studies of radar sea spikes at low grazing angles. Journal of Geophysical Research, 96(C7), 12529-12537.

Trizna, D.B., Hansen, J.P., Hwang, P. & Wu, J. 1993 Ultra-wideband radar studies of steep crested waves with scanning laser measurements of wave slope profiles, Dynamics Atmosphere Ocean, 20, 33-53.

Ulaby, F.T., Fung, A.K. & Moore, R.K. 1982 Microwave remote sensing: active and passive - Volume 2: Radar remote Sensing and Surface Scattering and Emission Theory, Addison-Wesley Publish. Co.

Valenzuela, G.R. 1978a Theories for the interaction of electromagnetic and ocean waves - A review, Boundary Layer Meteorology, 13, 61-85.

Valenzuela, G.R. 1978b Scattering of electromagnetic waves from the ocean, p. 199-226 in, Surveillance of environmental pollution and resources by electromagnetic waves, eds.T. Lund. Reidel.

Valenzuela, G.R. 1985 Microwave sensing of the ocean surface, p. 233-244 in, The ocean surface: wave breaking, turbulent mixing and radio probing, eds. Y.Toba and H.Mitsuyasu.

Vesecky, T.V. & Strewart, R.H. 1982 The observation of ocean surface phenomena using imagery from the SEASAT Synthetic Aperture Radar: An assessment, Journal Geophysical Research, 87 (C5), 3397-3430.

Vogelzang, J., Peters, H.C., Deloor, G.P., Pouwels, H. & Wensink, G.J. 1992 Sea bottom topography with X-band SLAR: the relation between radar imagery and bathymetry, International Journal Remote sensing, 13(10), 1943-1958.

Ward, N. & Vennings, D.A.S. 1989 Radar reflector trials, Annexe 6, Development report n° 12 - 1989/NW, May 1989.

Watson, G. & Robinson, I.S. 1990 A study of internal wave propagation in the Strait of Gibraltar using shore-based marine radar images, Journal Physical Oceanography, 20, 374-395.

West, J.C., Sturm, J.M. & Sletten, M. 1996 Small grazing angle radar scattering from a breaking water wave: demonstration of Brewster angle damping, IGARSS'96, 4, 2207-2209.

Wetzel, L.B. 1977 A model for sea backscatter intermittency at extreme grazing angles, Radio Science, 12, 749-756.

Wetzel, L.B. 1986 On microwave scattering by breaking waves, p.273-281 in, Wave Dynamics and Radio Probing of the Ocean Surface, eds. O.M Phillips and K. Hasselmann.

Wetzel, L.B. 1987 Models for electromagnetic scattering from the sea at extremely low grazing angles, US Naval Research Laboratory, NRL Memorandum Report 6098.

Wetzel, L.B. 1990 Electromagnetic scattering from the sea at low grazing angles, p. 109-171 in, Surface waves and fluxes, volume 2 - Remote sensing, eds. G.L. Geernaert and W.L.Plant.

Wheeler, G.J. 1963 Radar Fundamentals, Prentice-Hall, Inc.

Wright, J,W. 1965 Wave observation by shipboard radars, Ocean Science Ocean Engineering, 1, 506-514.

Wright, J,W. 1968 A New Model for Sea Clutter, IEEE Transactions Antennas Propagation, 16, 217-223.

Wyatt, L. 1997 University of Sheffield, private communication.

Young, I.R., Rosenthal, W. & Ziemer, F. 1985 A three-dimensional analysis of marine radar images for the determination of ocean wave directionality and surface currents, Journal Geophysical Research, 90(C1), 1049-1059.

Young, I.R., Rosenthal, W. & Ziemer, F. 1985 Marine radar measurements of waves and currents during turning winds, Deutsche Hydrographische Zeitschrift, 38(1), 23-38.

Zink, M. 1995 Results of X-SAR calibration, IGARSS'96, 1, 590-592.